UNIVERSITY OF
NEWCASTLE UPON TYNE

THE EFFECT OF HYDROGEN ON THE MECHANICAL BEHAVIOUR OF DUPLEX STAINLESS STEEL

by

A. A. EL-YAZGI

Materials Division
Department of Mechanical, Materials & Manufacturing Engineering

A Thesis submitted in partial fulfilment of the
requirements for the degree of Doctor of Philosophy

1995

CONTENTS

Page

CHAPTER 1: INTRODUCTION 1
CHAPTER 2: LITERATURE REVIEW 4
2.1 Material Properties 4
2.1.1 The Development and Classification of Stainless Steels 4
2.1.2 The Iron-Chromium-Nickel Ternary System 6
2.1.3 Duplex Stainless Steels 9
2.1.3.1 The Development of Duplex Stainless Steels 9
2.1.3.2 Solidification of Duplex Stainless Steels 13
2.1.3.3 The Microstructure of Commercial Duplex Stainless Steels 15
2.1.3.4 Microstructure of Duplex Stainless Steel Welds 17
2.1.3.5 Other Phases in Duplex Stainless Steels 18
2.1.4 The Role of Alloying Elements 24
2.2 Stress Corrosion Cracking 35
2.2.1 Introduction.....35
2.2.2 Mechanism of Stress Corrosion Cracking 38
2.2.2.1 Film Rupture 38
2.2.2.2 Pre-existing Active Path 41
2.2.2.3 Embrittlement Mechanism 43
2.2.2.4 Stress Corrosion Cracking Spectrum.....47
2.2.3 Chloride SCC of Austenitic stainless Steels 49
2.2.4 Chloride SCC of Ferritic stainless Steels 51
2.2.5 Chloride SCC of Duplex stainless .....53.
2.2.6 Sulphide Stress Corrosion Cracking 57
2.3 Hydrogen Embrittlement 65
2.3.1 Introduction 65
2.3.1.1 Internal (Reversible) Hydrogen Embrittlement (IHE) 65
2.3.1.2 Hydrogen Environment Embrittlement (HEE) 66
2.3.1.3 Hydrogen Reaction Embrittlement (HRE).....66
2.3.2 The Process of Hydrogen Embrittlement 67
2.3.2.1 The Entry of Hydrogen into Metals 67
2.3.2.2 Source of Hydrogen 70
2.3.2.3 The Transport of Hydrogen 73
2.3.3 Mechanisms 78
2.3.3.1 Internal Pressure Theory 78
2.3.3.2 Hydrogen/Lattice Bond Interaction 82
2.3.3.3 Dislocation Interaction Theory 84
2.3.3.4 Hydride Formation 87

2.3.4 Trapping of Hydrogen in Metals 87
2.3.5 Distinction Between SCC and Hydrogen Embrittlement 90
CHAPTER 3 : EXPERIMENTAL PROCEDURE 93
3.1 Material Composition and Microstructure 93
3.2 Specimen Design and preparation.....104
3.3 Heat Treatement of Specimen 104
3.4 Thermal Charging with Hydrogen 109
3.5 Slow Strain Rate Testing 113
3.5.1 Straining Uncharged and Charged Specimens in Air 113
3.5.2 Straining in Gaseous Hydrogen Atmosphere ..... .115
3.5.3 Straining Cathodically Polarized Specimens in Aqueous Environments 115
3.6 Hydrogen sulphide Testing 116
3.7 Pitting Tests ..... .120
3.8 Polarization Curves 121
3.9 Microstructure and Fractographic Examinations.....123
CHAPTER 4: RESULT AND DISCUSSION 126
4.1 The Effect of Strain Rate on Mechanical Behaviour 126
4.1.1 Uncharged Material Strained to Failure in Air 126
4.1.2 Uncharged Material Strained to Failure in Hydrogen Gas 126
4.1.3 Thermally Charged Specimens (Strained to Failure in Air).....143
4.2 Hydrogen Sulphide 159
4.2.1 The Effect of Temperature 159
4.2.2 The Effect of Chloride Ion Concentration 182
4.3 Straining Cathodically Polarized Specimens 184
4.4 The Effect of Microstructure 196
CHAPTER 5: CONCLUSIONS 204
REFERENCES 207

PREFACE

This thesis describes original work which has not been submitted for a degree at any other University. The investigations was carried out in the Materials Division of the Department of Mechanical, Materials, and Manufacturing Engineering of The University of Newcastle upon Tyne, under the supervision of Professor Donald Hardie.

ABSTRACT

Duplex stainless steels are commonly used in environments that are expected to produce hydrogen i.e. in sour environments and sea water applications, often under cathodic protection. Under these conditions there is a concern about their susceptibility to hydrogen embrittlement.

The effect of hydrogen, both external and internal, on the mechanical properties and the fracture characteristics of duplex stainless steels Type 2205 and 2507 have been studied by slow strain rate techniques using smooth tensile specimens. Specimens were strained to failure in air after high pressure hydrogen thermal charging, in a hydrogen atmosphere, in a hydrogen sulphide environment under open circuit potential condition, and whilst cathodically polarized at different potentials in distilled water with 100 wppm potassium sulphate added, in 3.5% aqueous sodium chloride, or in NACE solution.

All the environments produced a major reduction in ductility that increases linearly with decrease in strain rate. The severity of the embrittlement depended upon whether the supply of hydrogen was external or internal. Internal hydrogen, as in thermally charged specimens, produced a more profound loss in ductility than straining in a hydrogen atmosphere and prolonged room temperature aging of these specimens, for up to 3 years, resulted in insignificant recovery of ductility, emphasizing the role of the austenite as a hydrogen reservoir. Provision of hydrogen at very high fugacities (cathodic polarization) during straining indicated that the potential at which loss in ductility is first noted corresponds to the hydrogen evolution potential for the particular solution involved. The presence of chloride ion seems to have no significant effect on the loss in ductility.

The presence of hydrogen sulphide in the environment, however, introduced the complication of extensive chemical attack during and after crack propagation. The loss in ductility increased as the pH of the solution decreased and, irrespective of pH, maximum embrittlement occurred at some particular temperature between 20 and 90°C. The latter is attributed to the two competing processes of hydrogen

embrittlement and corrosion. A minimum chloride ion concentration of 300 wppm seems necessary to maintain the maximum embrittlement.

The ultimate tensile strength of the steel is not affected by hydrogen ,since cracking only occurs after it is exceeded. Cracks initiate and grow preferentially through the ferrite phase, with fracture surfaces exhibiting quasi-cleavage features; the austenite often failed in a ductile mode. The proportion and distribution of the two phases has a significant effect on the degree of embrittlement. The presence of greater amounts of austenite seems to inhibit crack propagation, but may act as a hydrogen source or reservoir for the embrittlement of the ferrite phase.

Straining of the as received weldments, which had been annealed after welding, showed no evidence of hydrogen embrittlement, but an attempt was made to simulate via heat-treatment the structures that could occur in the heat affected zone of the weld and these structures had inferior mechanical properties in the presence of hydrogen.

Chapter 1

Introduction

In recent years, the increasing demand for fossil energy and exhaustion of existing oil and gas reservoirs has led to the development of deeper wells that contain harsh "sour" environments with substantial amounts of hydrogen sulphide, carbon dioxide, and chlorides, usually in the absence of dissolved oxygen. Each of these species has a role to play in the degradation of iron-base materials that come into contact with such an environment. The role of hydrogen sulphide is, in the presence of moisture, to produce high hydrogen fugacities by dissociation at the metal surface and, equally important, to suppress the recombination of atomic hydrogen/1,2/. This leads to a high concentration of adsorbed hydrogen and hence to a higher permeation rate. Carbon dioxide, on the other hand, dissolves in water to form carbonic acid that reduces the pH of the solution, which reduces the protective properties of the surface film and also increases the hydrogen evolution potential. Chloride concentration in the solution also plays a significant part, particularly for those materials for which it has an adverse effect on passivity, e.g. stainless steels, by local removal of the protective film, which facilitates the entry of hydrogen. Careful selection of the materials to be used in such a hostile environment is therefore needed.

Austenitic stainless steels, for example, offer good general corrosion resistance , depending on alloy content, but are of inherently low strength, and are susceptible to various forms of selective corrosion, particularly in chloride environments. On the other hand, ferritic stainless steels have relatively high strength and excellent resistance to

stress corrosion cracking, but they lack ductility and are prone to hydrogen embrittlement. Clearly austenitic stainless steels are not as easily embrittled by hydrogen as ferritic stainless (which are long known to suffer loss in ductility at much lower hydrogen concentrations /3,4/). However, the occurrence of some embrittlement is now well established where hydrogen is introduced at high fugacities at the surface, i.e. cathodic charging /5-7/ and hydrogen sulphide bearing environments /8,9/, or simply if straining is carried out in a hydrogen atmosphere /10/.

Duplex stainless steels having approximately equal proportions of ferrite and austenite are being used very extensively under such conditions, in the oil, gas, and petrochemical industries. This is basically because they combine the high strength and excellent resistance to chloride-induced stress corrosion cracking of ferritic stainless steels and the excellent toughness and resistance to hydrogen embrittlement of austenitic stainless steels. Their yield strengths are double those of austenitic stainless steels with good ductility and weldability (providing that a reasonable phase balance is maintained). Alloying with nitrogen, a potent austenite stabilizer, has facilitated the use of these steels in the as welded condition.

Despite their good corrosion resistance, however, they may be expected to suffer damage due to hydrogen, because of the high susceptibility of the ferritic phase, if this is available internally, as a dissolved element, after thermal charging, or externally, as in cathodic charging, in a hydrogen sulphide solution or in a low pressure hydrogen atmosphere. The degree of embrittlement introduced depends

upon many factors: i) hydrogen content, ii) strength level, iii) strain rate, iv) temperature, v) pH of the environment, vi)chloride ion concentration, and vii) microstructure of the material.

The aim of this work is to assess the contribution of many of these factors to embrittlement induced in commercial duplex stainless steel by such hydrogen environments, and to gain a better understanding of the effects of internal and external hydrogen on the mechanical properties of such steels by employing the slow strain rate technique.

Chapter 2

Literature review

2.1 Material properties

The term stainless steel is generally used to describe a class of alloy with a minimum of 11.5% chromium. Such chromium content makes the alloy capable of forming an adherent film of surface oxide which is responsible for the enhanced corrosion resistance of these alloys in many environments.

2.1.1 The development and classification of stainless steels

The first industrial development of a stainless steel is often accredited to Brearley some 80 years ago /11,12/. However, some of the pioneering works were carried out, about 100 years earlier, by Stodart and Faraday /13/ and Berthier (1821) in which they noted that the addition of a small amount of chromium to iron enhances the atmospheric corrosion resistance of the resultant alloy. It was reported that Berthier actually suggested the use of chromium steels for cutlery /11/. These observations did not receive the attention they deserved, mainly because of the detrimental effect of carbon causing the formation of chromium carbide, which was not realized at that time, and also because chromium decreases the corrosion resistance of steel in sulphuric acid, as demonstrated by the extensive research work of Hadfield /14/. By the end of the 19th century the detrimental effect of carbon was recognized and Monnartz /15/ finally demonstrated the corrosion resistance of chromium steels. In Germany in 1912, Maurer and Strauss were working on developing corrosion resistant iron alloys but

their alloy was discarded, again due to the chromium carbide formation. Later on, Maurer realized that water quenching of these alloys retarded the chromium carbide formation and the result is an alloy with enhanced corrosion resistance /16/. At about the same time (1912) in England, Brearley was working on the prevention of fouling and erosion of rifle barrels using iron chromium alloys and he noted the resistance of these alloys to etching with acids. In 1915, he produced a 0.25% carbon-13% chromium steel which was introduced to the public as cutlery material. Between 1904 and 1914 several workers /17-19/ investigated the metallurgy of chromium and chromium-nickel steels having variously austenitic, ferritic, and martensitic structures.

The development of various types of stainless steel accelerated very rapidly after the early 1920s and today more than 170 different alloys can be recognized and classified in five different classes:

i) ferritic stainless steels, containing 12-30% chromium and low carbon,
ii) martensitic stainless steels, with 12-17% chromium and 0.1-1.0%carbon,
iii) austenitic stainless steels, containing 17-25% chromium and 8-20% nickel,
iv) precipitation hardening alloys, which can have an austenitic or martensitic base, with addition of copper, aluminum, titanium, molybdenum, niobium, or nitrogen, and
v) duplex stainless steels, containing 20-30% chromium, 2.5-7.0% nickel, with addition of molybdenum, copper, and nitrogen.

2.1.2 The iron-chromium-nickel ternary system

The first comprehensive investigation of the iron-chromium-nickel ternary system was carried out by Bain and Griffiths /20/, who observed an α+γ mixture in their examination of the Fe-Cr-Ni system. They also observed (γ+martensite), (α+martensite), and (α+γ+martensite) as well as the existence of carbides and σ phase, which they identified only as an unanalysed brittle phase that they called β. They also published isothermal sections (for 900°C, 1050°C, 1200°C, and 1300°C)of the Fe-Cr-Ni ternary phase diagrams. More recently, isothermal sections have also been published by Pugh and Nisbet /21/ and Colombier and Hochman /22/. Even though the isothermal ternary diagrams (Figure 2.1) can give valuable information about phases present at a specific temperature, it is easier to consider vertical sections (at specific iron content) which are known as pseudo-binary diagrams (Figure 2.2). The latter provide a much clearer picture of the phases that can be expected during heat treatment of such alloys. An increase in Fe content results in a change in the shape of α and γ phase fields and the α/(α+γ) and γ/(α+γ) phase boundaries become curved, restricting the α field at high temperatures and broadening it and the (α+γ) fields at low temperatures. At an iron content of 90% the high temperature ferrite δ is separated from the low temperature ferrite α due to an expansion of the γ phase field. It should be emphasized here that both of these phases have exactly the same body centred cubic structure and it is only the convention adopted in the iron-carbon system that caused the higher temperature bcc phase to be denoted δ while the lower temperature phase was denoted α.

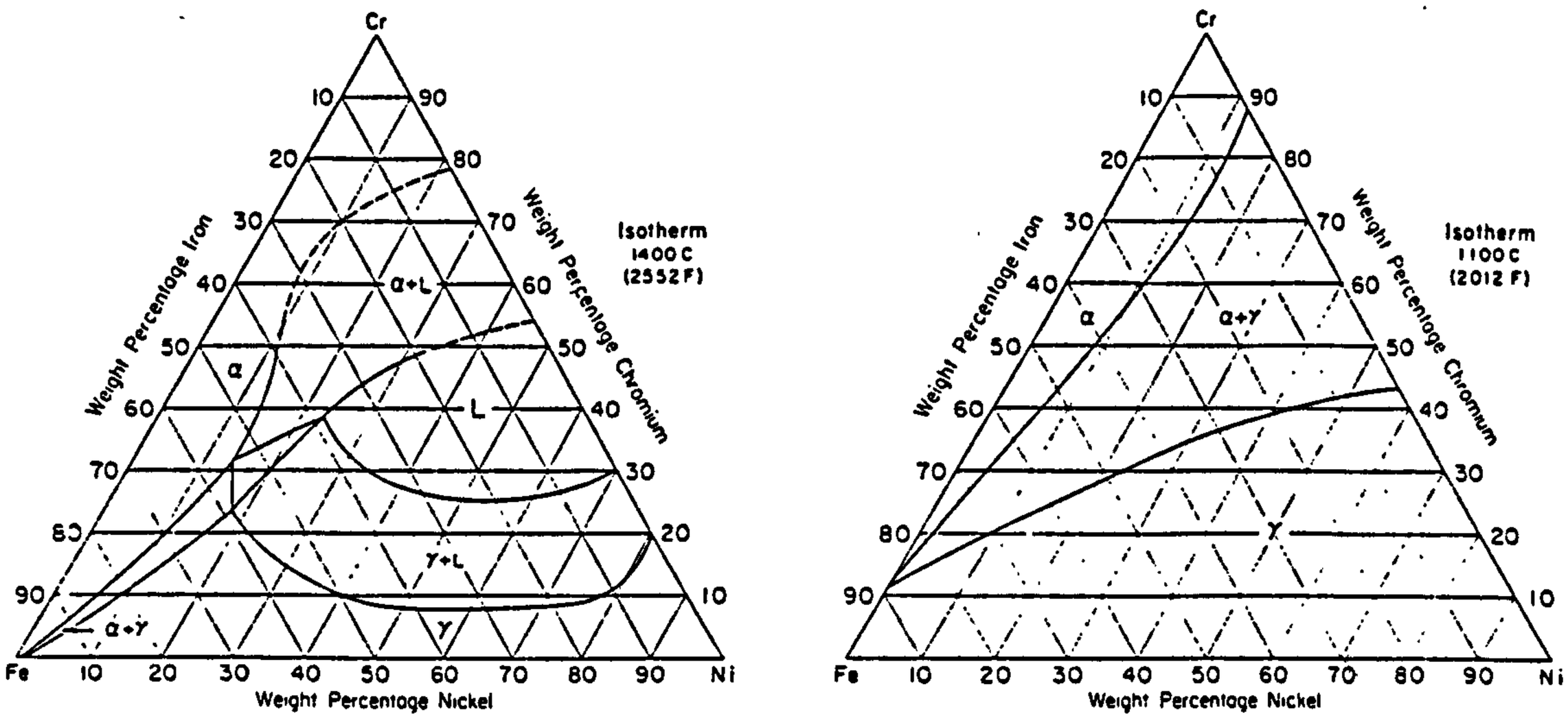

Figure 2.1 Isothermal sections of the iron-chromium-nickel ternary system at **(a)** 1400°C, **(b)** 1100°C and **(c)** 650°C. /23/

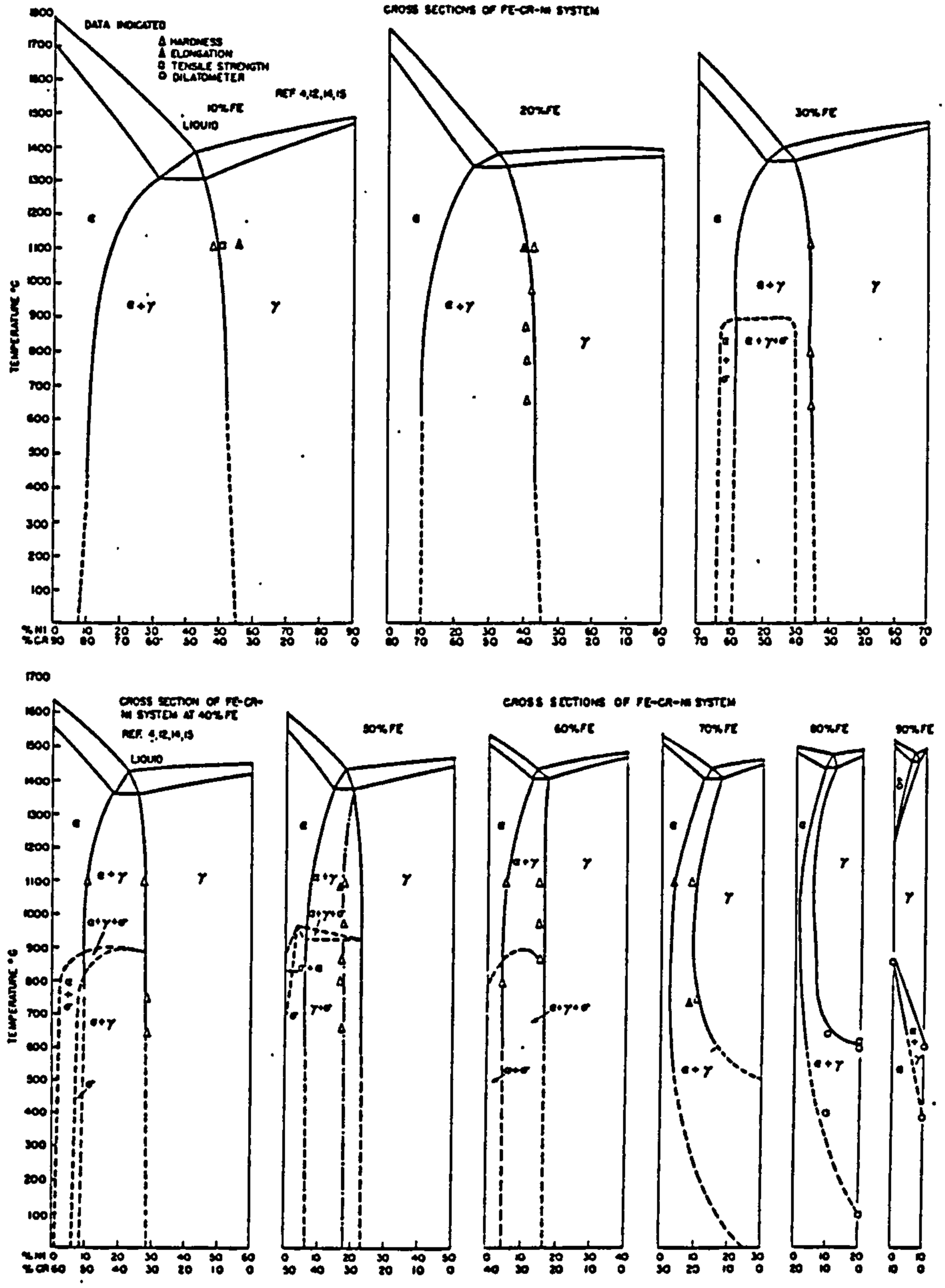

Figure 2.2 Series of pseudo-binary diagrams of the iron-chromium-nickel system. /21/

Most commercial duplex stainless steels have iron content in the range 60-70%. Therefore, it should be noted from Figure 2.2 that with iron contents ≥ 70% the austenite phase is unstable at low temperatures and could transform to martensite. This martensite is different from that formed in carbon steels due to the much lower carbon content of stainless steels (0.03-0.08 wt% carbon) and this means that martensite formed in duplex stainless steels is not as hard and brittle as that observed in carbon steels, though the nature of the transformation is the same.

2.1.3 Duplex stainless steels

Duplex stainless steels are a class of alloys whose annealed structure consists of two phases, ferrite α and austenite γ. This term is generally reserved for alloys in which the phases are present in substantially separate volume fractions, typically of equal proportions, in contrast to the situation were one phase is present as a fine precipitate within a major phase. Although not formally defined, it is generally accepted that the lesser phase will be at least 30% by volume. Although most of the following discussion will be confined to the two phases, the bcc ferrite and the fcc austenite, some discussion will be offered for the other possible phases that may form during heat-treatment or mechanical deformation (e.g. σ phase, α' phase, carbide precipitate, martensite phase ...)

2.1.3.1 The development of duplex stainless steels

Duplex stainless steels have been known since the late 1920's, when Griffiths and Bain demonstrated the existence of the two phase alloy in 1927. In the early 1930's, it was found that the introduction of ferrite into austenitic

stainless steel increased the resistance to sensitization, which was significant in view of the high carbon content prevalent in stainless steels at that time. In France (in J. Holtzer Co.) in 1933, an alloying error to produce 18%Cr-8%Ni-2.5%Mo led to a 20%Cr-8%Ni-2.5%Mo steel containing a large volume fraction of ferrite in an austenitic matrix /24/. The resultant alloy was found to resist intergranular attack in various corrosive environments and this was shown at the time to be due to the fact that the carbide formation was discontinuous, in contrast to the continuous precipitation observed in austenitic stainless steels /25/. Another early use of ferrite in austenitic stainless steels was to improve the mechanical properties of castings. Nevertheless it was not until the 1950's, when nickel shortages were being experienced, that duplex development gained reasonable momentum. It was realized that improvement of the strength and corrosion resistance could be achieved at a reasonable price (with low nickel content). Alloys developed at this time, involving a 26%Cr-4%Ni base with or without molybdenum addition, proved difficult to machine (brittle) /26/. Furthermore, the addition of sulphur to the alloy, to improve machinability, considerably reduced corrosion resistance in 10% sulphuric acid at room temperature. It was found, however, that an addition of 3% copper improved the corrosion resistance of the alloy in this environment. The manganese content was also found to affect the corrosion resistance and a low manganese alloy with 0.1% manganese maximum was found to have superior corrosion resistance. This new base alloy (25%Cr-4%Ni-2% to 3%Cu) was brittle even after the relatively slow air cooling employed at the time (water quenching of such alloys being considered too severe for

practical application), and it was essential to improve the ductility of the alloy. Thus, the effect of chromium and nickel contents on ductility was investigated and, with a maximum nickel content of 5 wt% (kept low because of its high price), it was found that the maximum level of ductility was obtained with a chromium content of 22-23 wt% /26/ (Figure 2.3). Towards the end of the 1950's the grade CD4MCu (25%Cr-5%Ni-2%Mo-3%Cu) was developed by the Alloy Casting Institute but, because of brittleness of the castings obtained, the chromium content was reduced to 22-23 wt% and a quench-annealing treatment was adopted to increase ductility /27,28/. Even though the strength level was reduced it is still about twice that of the austenitic grades and with a superior corrosion resistance.

The introduction, in the 1970's, of the argon-oxygen decarburization (AOD) process facilitated precise and economical control of carbon and, perhaps more importantly, nitrogen in stainless steels, which in turn led to the introduction of a new class of duplex steels containing 0.2-0.3 wt%N. Nitrogen was first used because it was an inexpensive austenite former, replacing some of the nickel, but it was quickly found that it had other beneficial effects, such as improving tensile properties and resistance to pitting and crevice corrosion. Moreover, nitrogen was also recognized for its high temperature austenite stabilizing effect /24/ (Figure 2.4), which facilitated the restoration of an acceptable balance of austenite and ferrite after a rapid thermal cycle in the heat-affected zone (HAZ) during welding and enables the use of duplex grades in the as-welded condition.

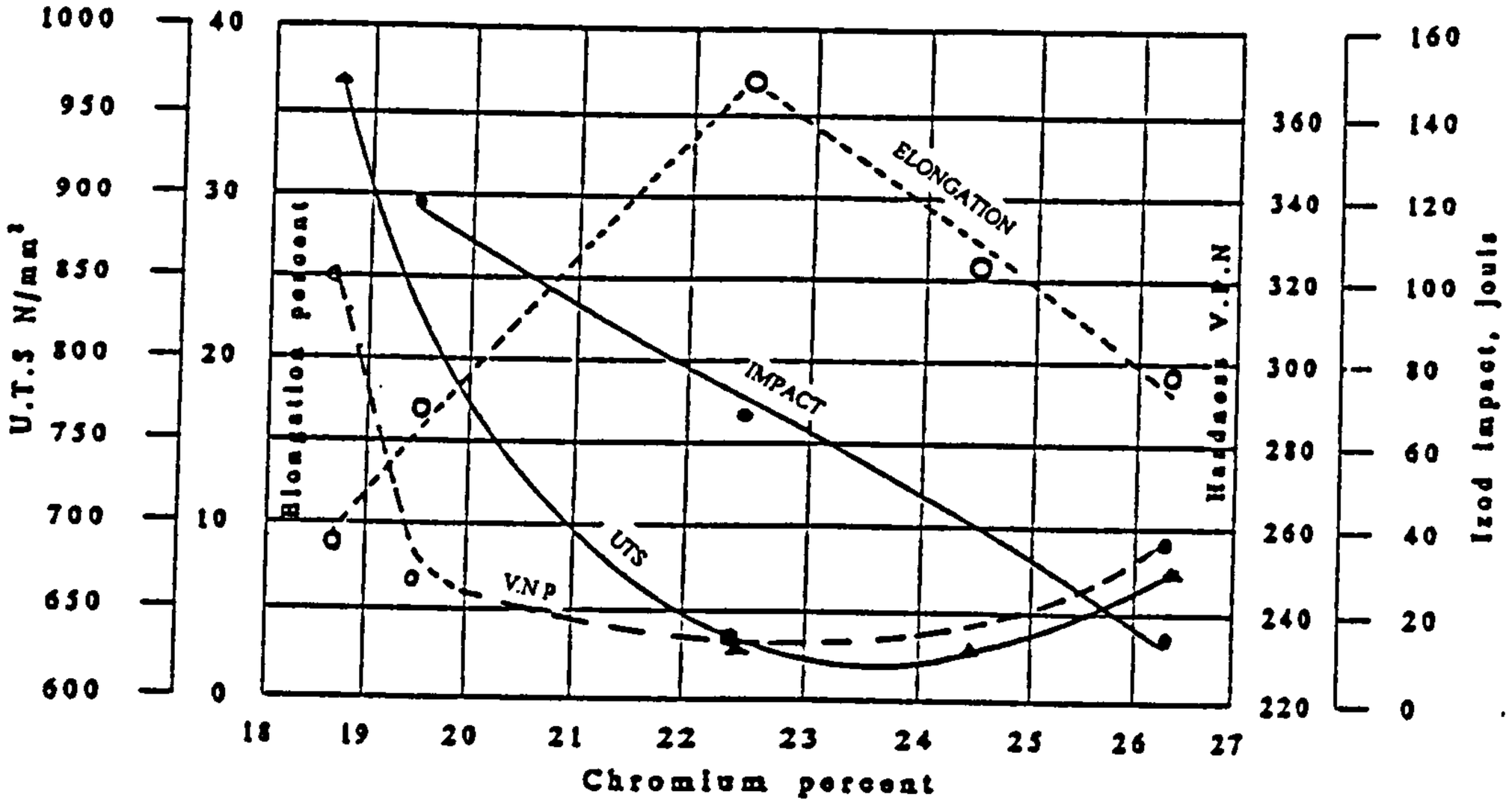

Figure 2.3 The effect of chromium on the mechanical properties of 5% nickel base stainless steel alloy.

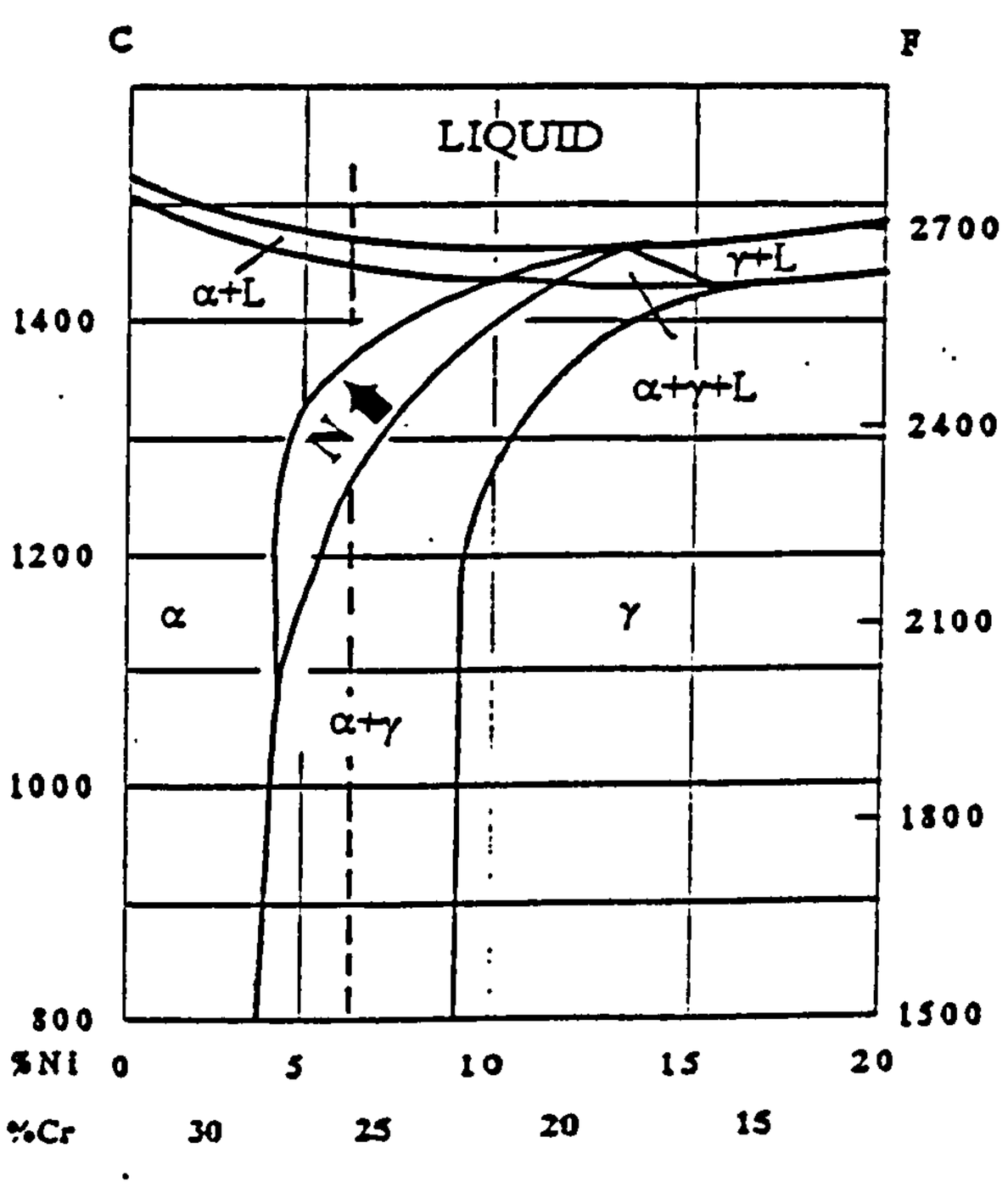

Figure 2.4 Schematic effect of nitrogen addition on the pseudo-binary Cr-Ni-68Fe phase diagram /24/.

2.1.3.2 Solidification of duplex stainless steels

Depending upon their composition, duplex stainless steels can solidify in two different modes (Figure 2.5). Those alloys with a composition that places them to the left of the pseudo-eutectic composition (hypo-pseudo-eutectic) (region 1) solidify as dendritic austenite and, because of the flat liquidus (i.e. almost independent of composition), this primary austenite should have very high nickel and low chromium content (the Cr is rejected to the remaining liquid) /29/. The final liquid will solidify as a ($\gamma+\alpha$) divorced eutectic structure between the primary γ dendrites. The ferrite formed in the divorced structure is unstable and eventually it will transform to austenite upon cooling. Therefore, the resulting structure at room temperature will be austenitic, except for a very small region of interdendritic ferrite. Such alloys with low residual ferrite content (< 5%) can be prone to hot-cracking due to the fact that impurities (particularly sulphur and phosphorus) tend to partition preferentially to the ferrite, which is the last phase to solidify. This expands the freezing temperature range and promotes solidification cracking, referred to as hot cracking /30/. On the other hand, alloys with hyper-pseudo-eutectic compositions (regions 2,3, and 4) will solidify as ferrite. This primary ferrite is very high in chromium and low in nickel content (Ni is rejected to the remaining liquid). Again the final liquid solidifies as $\alpha+\gamma$ divorced eutectic structure. The primary ferrite, with high chromium content, will be stable at room temperature while ferrite of the divorced structure (with low chromium content) is less stable and will transform to austenite. The resultant structure will be predominantly austenitic with ferrite retained at the original dendrite cores. The exact structure depends on the volume of the ferrite phase that has a chromium

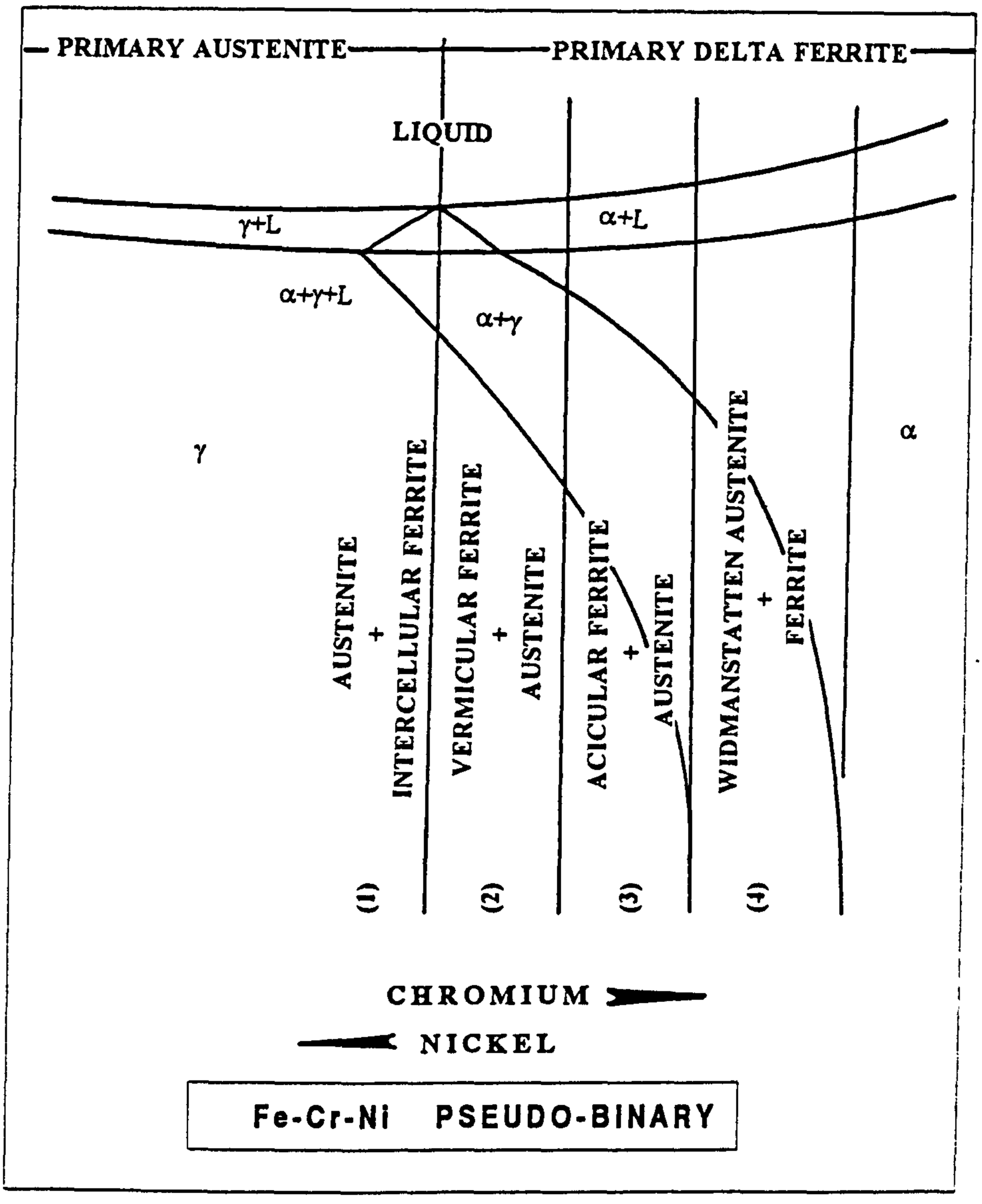

Figure 2.5 Schematic pseudo-binary diagram for 70%Fe showing the structure developed in Fe-Cr-Ni alloy.

content high enough to be stable at room temperature. Hyper-pseudo-eutectic alloys are not prone to solidification cracks, mainly due to the fact that ferrite, the first phase to solidify, is enriched in sulphur and phosphorus. This enrichment results in a decrease in the freezing point rather than expanding the freezing temperature range /30/.

It has to be noted here that the quantity of each phase present in the final structure can not be predicted from pseudo-binary diagrams such as Figure 2.5, mainly for two reasons: firstly, we are not dealing with a true binary system and thus the lever rule is not applicable and secondly, these diagrams do not take into account the influence of alloying elements other than chromium and nickel.

2.1.3.3 The microstructure of commercial duplex stainless steels

Commercial duplex stainless steels, including that investigated here, have compositions that put them in the $\alpha+\gamma$ phase field at elevated temperatures (typically 1000°C-1150°C) where they are hot worked in order to produce a banded structure of ferrite and austenite particles elongated in the working direction. After the hot working operation they are normally quenched to prevent the formation of any of the detrimental phases that exist at lower temperatures, in particular the σ phase (Figure 2.6). Morini and Bettinelli /31/ recommend that the final heat-treatment should not increase the amount of ferrite and that the cooling rate should be fast enough to prevent σ phase formation, yet slow enough to prevent quench-cracking. For the duplex steels studied they therefore suggested a final heat-treatment of homogenization at 1120°C, followed by furnace cooling to 1000°C and water quenching. The resultant

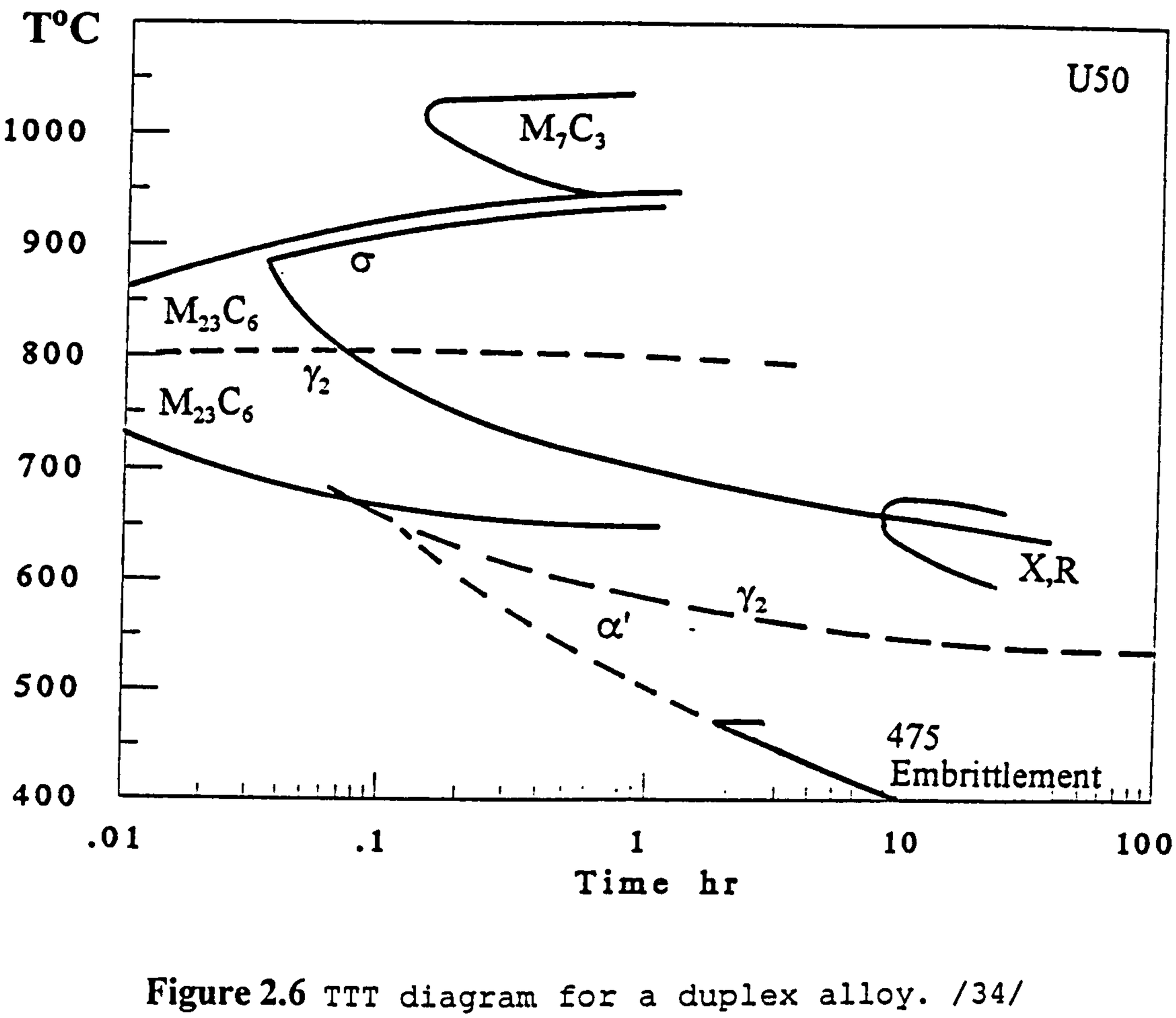

Figure 2.6 TTT diagram for a duplex alloy. /34/

microstructure, therefore, consists entirely of α+γ and the steels are expected to be highly anisotropic. Hot working of these alloys can be complicated by the formation of edge cracks, which are believed to be caused by the nucleation of chromium carbide at the α-γ grain boundaries /32/. These can be eliminated by lowering the carbon content or by the addition of titanium and niobium to tie up the carbon as TiC and NbC. However, the degree of element partitioning and the coring effect of solidification can be reduced by hot working in this temperature range.

2.1.3.4 Microstructure of duplex stainless steel welds

The desirable properties, corrosion and mechanical, exhibited by duplex stainless steels are achieved through the careful balance of austenite and ferrite. In the base material this balance is achieved by controlling both the composition and the thermo-mechanical treatment conditions. During welding, however, it is difficult to maintain the optimum ferrite/austenite balance because the thermal conditions experienced by the weld metal and the heat affected zone (HAZ) are more difficult to control. The HAZ region will be heated to the single phase ferrite region and then cooled rapidly, resulting in a very large-grained ferritic structure with very little austenite. This region will therefore have inferior mechanical and corrosion properties as compared with the parent metal or the weld pool. The weld metal microstructure is controlled by composition and the cooling rate through the α+γ phase region. Lippold et al /33/ proposed the use of a modified Fe-Cr-Ni pseudo-binary diagram, by replacing the Cr and Ni equivalent by $[Cr/Ni]_{eq}$, to predict the weld structure (Figure 2.7). From this diagram it can be seen that the duplex stainless steels will

solidify as delta ferrite and the structure remains fully ferritic until the two phase boundary is reached where partial transformation of ferrite to austenite occurs. To preserve an acceptable phase balance in the weld, therefore, filler metals with low $[Cr/Ni]_{eq}$ are generally used to promote the ferrite to austenite transformation by shifting the weld metal composition to the left (Figure 2.7). Unlike the weld fusion zone which can be adjusted via filler metal composition and thermal conditions, the HAZ microstructure is solely subject to the thermal conditions and thus depends upon the thickness of the material, the weld heat input, and preheat temperature. It is evident from Figure 2.7 that there is a significant variation in microstructure across the weld HAZ in duplex stainless steel. Next to the fusion zone will exist a fully ferritic structure. The width of this region will depend upon the composition of the alloy, since increasing the $[Cr/Ni]_{eq}$ stabilizes the ferrite phase over a wider temperature range (Figure 2.7).

Recently, the advantages of nitrogen on the high temperature stability of the austenite phase were recognised, which led to the development of super duplex stainless steels of the 2507 type, with >0.2 wt% nitrogen. Charles /34/ investigated the effect of nitrogen content on the stability of the duplex structure at a high temperatures and indicated that alloying with ≥0.22 wt% nitrogen would maintain a high proportion of the austenite phase (up to 40% at 1300°C) (Figure 2.8) thus maintaining the favourable properties of the duplex structure after welding.

2.1.3.5 Other phases in duplex stainless steels

In addition to ferrite (α) and austenite (γ) a variety of other phases may form in duplex stainless steels upon aging

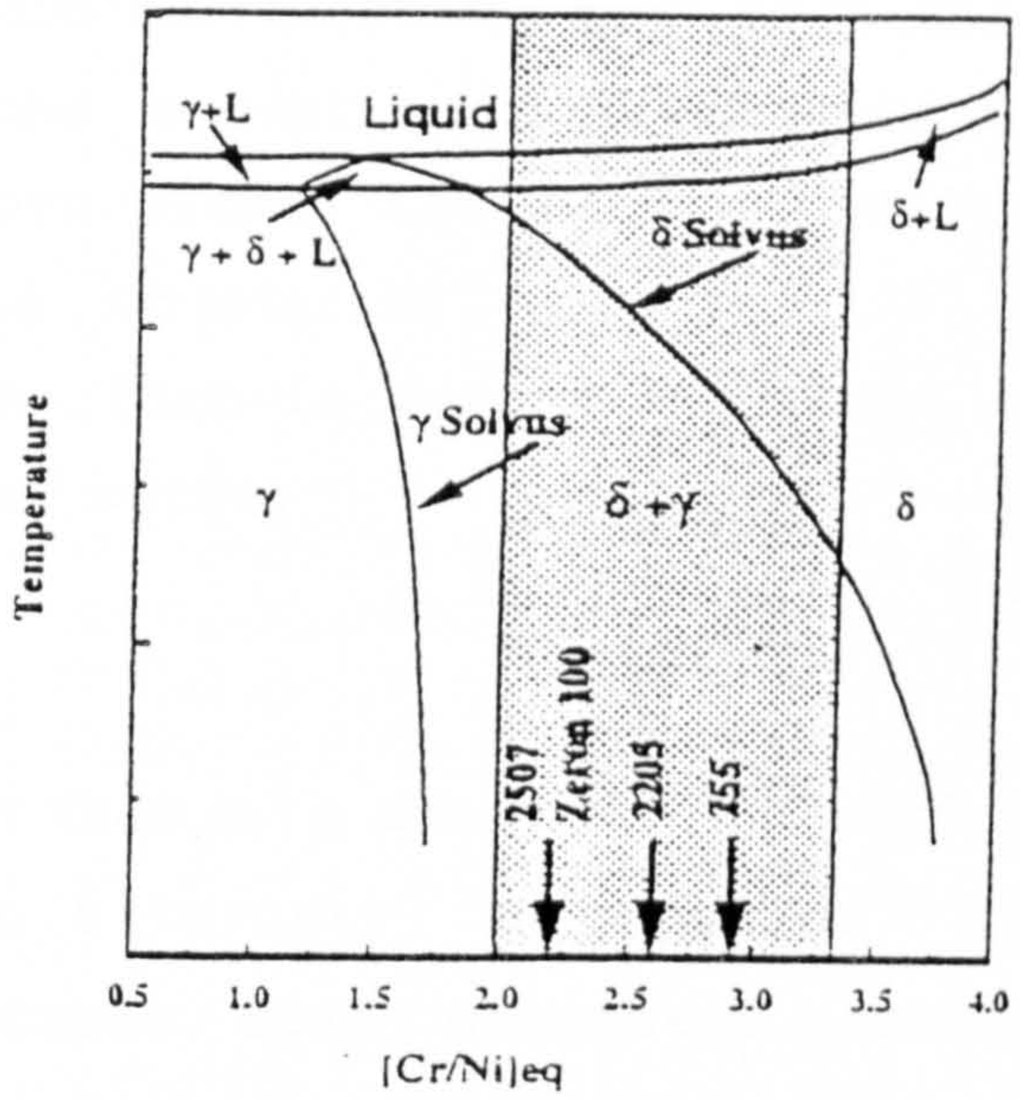

Figure 2.7 A modified ternary section of the Fe-Cr-Ni phase diagram. The location of a number of commercial alloys is indicated /33/.

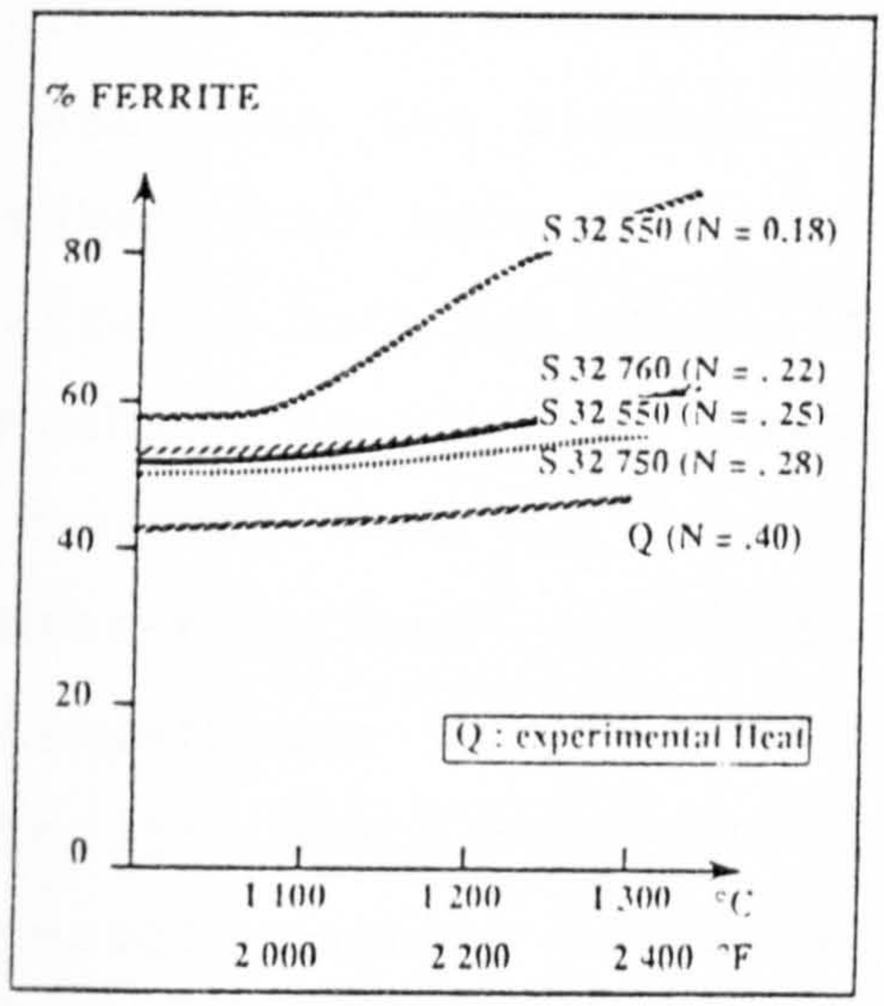

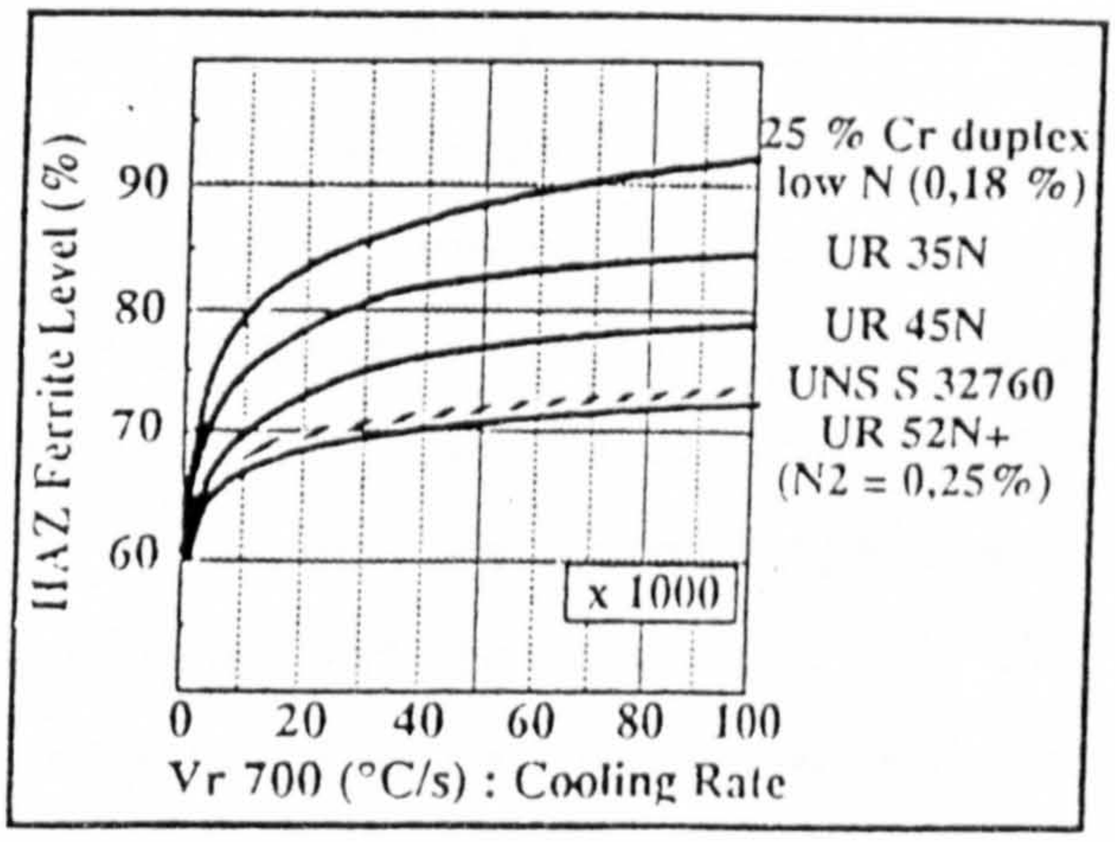

Figure 2.8 The effect of Nitrogen addition on the duplex structure. a)variation of ferrite content with increasing temperature. b)variation of the HAZ maximum ferrite content as a function of cooling rate /34/.

at different temperatures. Among these, σ, M_7C_3, $M_{23}C_6$, Cr_2N, X, R', γ_2 , α' and martensites, have been observed /31,32,35-37,50/. With the exception of martensite all of these precipitates form within the ferrite phase or at ferrite-austenite grain boundaries. Figure 2.6 illustrates the phases that can form in duplex stainless steel, U50, with different cooling rates.

i) Sigma phase σ

It is known that σ, a chromium and molybdenum rich phase, is formed in a variety of duplex stainless steels /29,38,50/. Because most of these contain substantial amounts of Mo, which is believed to promote the formation of σ, the temperature range of stability of σ is extended as compared to Fe-Cr binary alloys. In duplex stainless steels, molybdenum in the α phase tends to stabilize σ phase and allow it to form at temperature in excess of 950°C. Thus, to prevent the precipitation of σ, one must cool past 900°C in less than two minutes (Figure 2.6). This fact has to be taken into account during production because σ adversely affects both hot ductility and room temperature ductility. Maehare et al /39/ investigated 25%Cr-7%Ni-3%Mo steel and observed that the precipitation of σ can be influenced by heat-treatment temperature. A high solution treatment temperature tends to increase the volume fraction of the ferrite which will consequently be diluted with respect to ferrite-forming elements. As a consequence the rate of σ formation will be reduced. They showed that, in extreme cases, the σ nose in a CCT diagram could be shifted to longer times by about a factor of 5 by employing a higher solution treatment temperature. Quantitative chemical

analysis of the σ phase showed that it was enriched with Cr, Mo and Si, which are bcc stabilizing elements. Therefore, once σ phase is formed the adjacent ferrite will be depleted of Cr and Mo, which will adversely affect its corrosion properties /40/. Microanalysis, performed by Redjaimia et al /41/, undertaken across the σ particles formed at different temperatures between 650°C and 970°C indicates that the temperature of formation has no effect on the chemical composition described by the formula:

$[Fe_{0.95} Ni_{0.04} Mn_{0.01}]_{0.61}\ [Cr_{0.88} Mo_{0.09} Si_{0.03}]_{0.39}$.

ii) M_7C_3 and $M_{23}C_6$

Carbides of the type M_7C_3 precipitate in the temperature range 950-1050°C and can be avoided by cooling past this temperature range in less than 10 minutes. The other carbide type, $M_{23}C_6$, forms below 950°C very rapidly, in less than 1 minute (Figure 2.6). Both carbides precipitate preferentially at the α/γ grain boundaries /29/, but precipitation at the α/α and γ/γ grain boundaries has also been observed /42/. A variety of morphologies has been noted by many authors (i.e. triangular, rod-like, cuboidal and lamellar). The crystal structure is complex face centered cubic /42/. The formation of $M_{23}C_6$ is deleterious to the corrosion properties, and several investigations have shown that pits form in the chromium-depleted regions. Since most of the carbides form at the γ/α interface and because of the higher chromium content and faster diffusion rate in the ferrite phase, most of the corrosion is confined to the austenite side. However, due to the fact that the new generation duplex steels contain much less carbon (≤.015%), carbide formation seems to be less important as compared with the early class of duplex steels.

iii) Cr_2N

With the increasing use of N as an alloying element in duplex steels, the precipitation of chromium nitride Cr_2N (a hexagonal superlattice) has been recognized /42,50/. The kinetics of nitride precipitation depend strongly on the solution treatment conditions. A high temperature treatment (1200-1300°C) can lead to greater dissolution of nitrogen in the ferrite, and, consequently, abundant precipitation of nitride can occur during cooling or subsequent heat-treatment /38/. Cr_2N forms at austenite-ferrite grain boundaries, around dislocations, and also intragranularly in the ferrite phase as thin plates. The precipitate of Cr_2N depletes the adjacent material of Cr which understandably, as in the case of σ phase, will have an adverse effect on corrosion properties.

iv) Chi(χ) phase

Aging of duplex stainless steel at 700-900°C results in the precipitation of chi(χ) phase /42/. It has a body centred cubic structure with the composition $Fe_{36}Cr_{12}Mo_{10}$ /36/. Chi, like σ, is a brittle phase and is undesirable because of its adverse effect on ductility. However, its effect on ductility is difficult to assess since χ and σ often coexist. Chi phase is not as important as σ phase because it occurs as very small volume fractions.

v) R phase

R is a molybdenum-rich intermetallic compound that precipitates, in the ferrite as entangled platelets attached to γ_2 needles, in the temperature range 550-650°C. Solomon and Devine /29/ found that it has a composition of approximately Fe_2Mo, but recent investigation of 22%Cr-8%Ni-

3%Mo weld metal indicates that it has the approximate composition 30% Fe, 25% Cr, 6% Ni, 35% Mo and 4% Si /43/. It was also found in this investigation that toughness and pitting temperature were reduced by the formation of R phase. Both intergranular and intragranular precipitates have been observed. The intergranular precipitates are thought to be more deleterious with regard to pitting as they may contain as much as 40% Mo.

vi) γ_2 secondary austenite

At higher temperature (hot working temperatures) the fraction of ferrite in duplex steels is higher than in the finished product. It is upon cooling and aging at lower temperatures in the range 600-900°C that ferrite decomposes to austenite and the desired phase proportion is attained. This newly formed γ_2 has exactly the same composition as the bulk austenite (rich in Ni and low in Cr) and this will result in enrichment of the surrounding ferrite with Cr, which in turn will cause nucleation of σ phase /29/. The γ_2 phase is characterized as being lenticular with a mid-rib and being too fine to be clearly resolved by optical microscopy.

vii) Martensite Phase

The austenite phase, γ, of duplex stainless steel is metastable at low temperatures. Figure 2.2 indicate that for ≥70%Fe alloy the γ should transform to α at low temperature. This transformation occurs martensitically, i.e. via diffusion-less shear transformation. The martensite transformation temperature, M_s, depends upon the specific composition of the

alloy and is generally below room temperature. Deformation, however, causes martensite to form at room temperature and above /44/. Wakasa and Nakamura /45,46/ studied the formation of martensite in the austenite phase of duplex stainless steel and found both lath shape α' (bcc) and ε (hcp) martensite. The ε martensite was found to be a low temperature transitional phase that transforms to α' martensite with increasing strain. The ε martensite was not observed when the straining was carried out at temperatures above -50°C, the transformation being directly to the lath, α', martensite.

2.1.4 The role of alloying elements

All duplex stainless steels contain alloying elements other than chromium and nickel, such as carbon, nitrogen, molybdenum, silicon, copper, manganese and many others [Table 2.1]. Certain elements such as nickel, manganese, nitrogen, and carbon segregate preferentially into the austenite while others such as chromium, molybdenum, and silicon preferentially partition into the ferrite phase which, in turn, influences the phase equilibrium considerably and their effect can not be ignored. It is inconceivable, however, to construct a phase diagram that accommodates the effect of all the alloying elements.

Different alloying elements have been recognized as having specific influences on the resultant microstructure in terms of their effectiveness in stabilizing the ferrite or the austenite phases and their combined effect may be expressed in terms of chromium and nickel equivalents. Silicon (a ferrite stabilizer) for example, was assigned a

Table 2.1 Composition of some commercial duplex stainless steels

Alloy	Composition, wt.%									Others
Trade Name	Fe	Cr	Ni	Mo	Mn	C	Si	S	P	
AF 22	Bal.	21-23	4.5-6.5	2.5-3.5	<2.0	<0.03	<1.0			
FMN	Bal.	25.0	5.0	2.2	0.7	0.04	0.7			0.2 N
Ferrallium 225	Bal.	24-27	44.5-6.5	2.0-4.0	2.0 max	0.08 max	0.2 max	0.04 max	0.04 max	min 0.1 N 1.3-4.0 Cu
7Mo	Bal.	23-28	2.5-5.0	1.0-2.0	1.0 max	0.08 max	0.75 max	0.03 max	0.04 max	
Uranus 50	Bal.	20-22	5.5-8.5	2.0-3.0	2.0 max	0.03 max	1.0 max	0.03 max	0.04 max	max 0.2 N 0.5 Cu
3RE60	Bal.	18.5	4.7	2.7	1.5	0.03 max	1.7	0.03 max	0.03 max	
SAF 2205	Bal.	22.0	5.5	3.0	2.0 max	0.03 max	0.8 max	0.02 max	0.03 max	Approx. 0.14
DP 3	Bal.	24-26	5.5-7.5	2.5-3.5	1.0 max	0.03 max	1.0 max	0.03 max	0.04 max	0.1-0.3 N 0.2-0.8 Cu 0.1-0.5 W
44 LN	Bal.	25.0	6.2	1.7	1.7	0.03 max	0.4			0.17 N
Zeron 25	Bal.	24.4	5.5	2.5	0.54	0.04	0.57			0.12 N

magnitude of 1.5, which indicates that it is 1.5 times as powerful as chromium in stabilizing the ferrite phase. Nitrogen, on the other hand, is a potent austenite former and was assigned a value of 16 which indicates that it is 16 times as powerful as nickel in stabilizing the austenite phase. Experimental observations of the amount of ferrite present could then be correlated with the composition of the steel. A diagram relating the amount of ferrite present in the structure and the Cr and Ni equivalents was developed by Schaeffler /47/ (Figure 2.9) for predicting the amount of delta ferrite in weld metals. The Schaeffler diagram was later modified by Delong /48/ by taking into consideration the important influence of nitrogen in the stabilization of austenite. The Delong diagram, however, was essentially developed for austenitic stainless steels and was only intended for ferrite contents up to 18%, and thus can not be used for predicting the amount of ferrite in the duplex alloys. More recent, Siewart /49/ published a new diagram for fast cooling of duplex stainless steels (Figure 2.10) which incorporates ferrite contents up to 100%. It should be noted here that all of these diagrams indicate the structure obtained in fast cooled alloys and should not be used to define precisely the percent of phases present in wrought alloys.

Several equations have been developed to calculate the chromium and nickel equivalents in stainless steels /47,51-53/. The most recent are those proposed by Pickering /52,53/:

For steels with 12 weight% Cr:

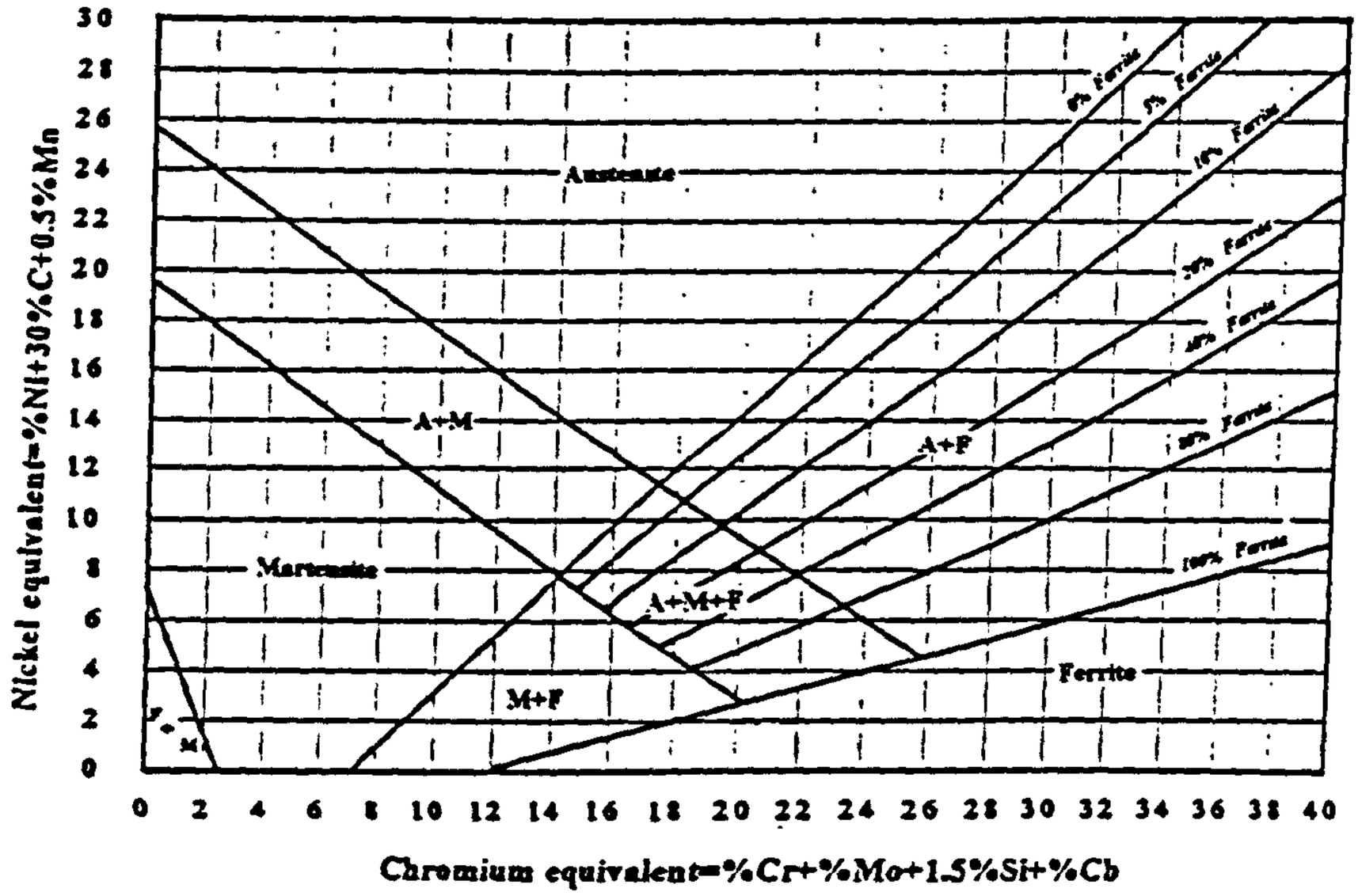

Figure 2.9 Schaeffler diagram showing the amount of ferrite and austenite present in weldment as a function of chromium and nickel equivalents.

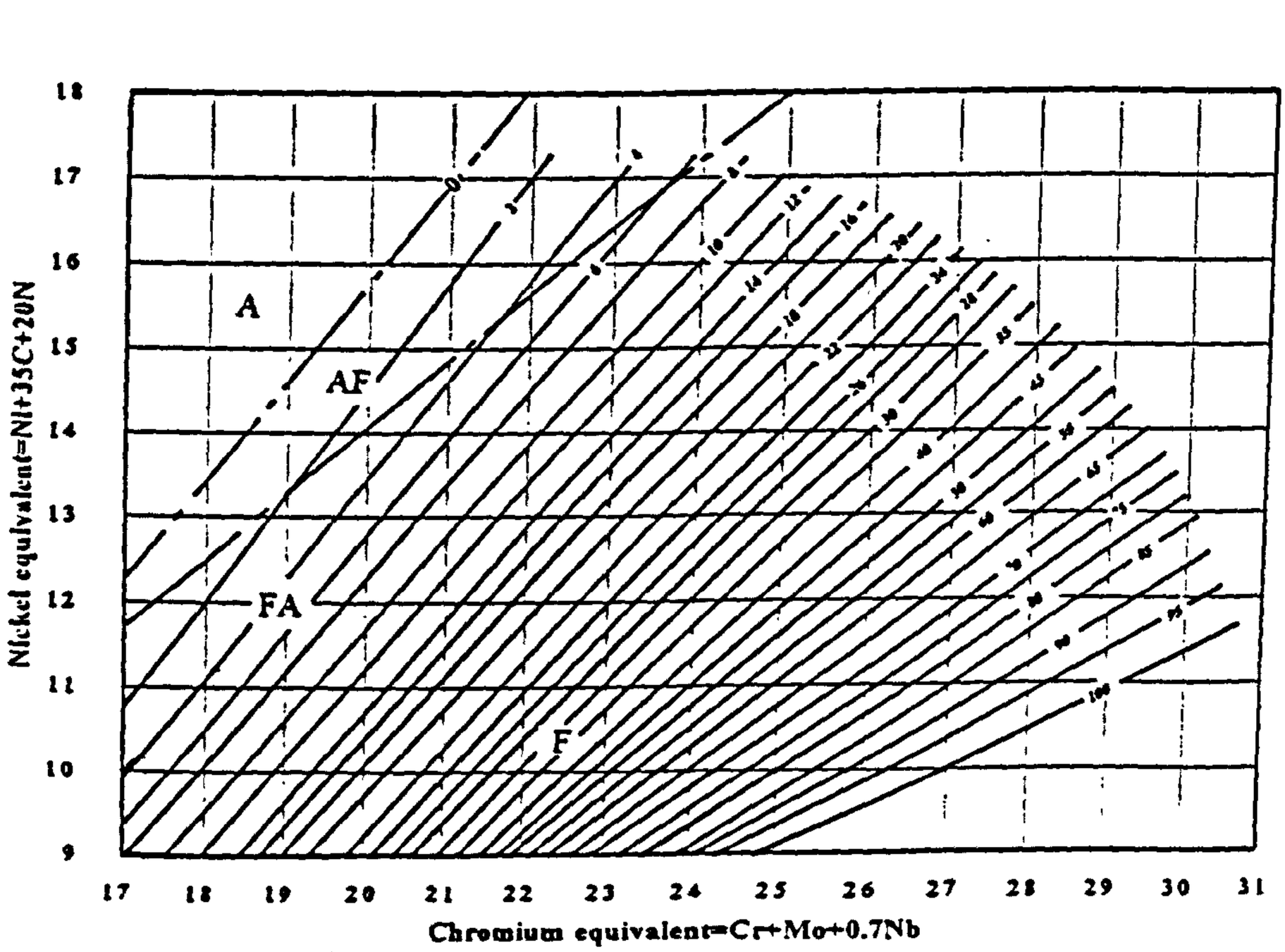

Figure 2.10 Modified Schaeffler diagram incorporating the effect of nitrogen.

$$Cr_{eq} = \%Cr + 2(\%Si) + 1.5(\%Mo) + 5(\%V) + 5.5(\%Al) + 1.75(\%Nb) + 1.5(\%Ti) + 0.75(\%W) \quad 2.1$$

$$Ni_{eq} = \%Ni + (\%Co) + 0.5(\%Mn) + 0.3(\%Cu) + 25(\%N) + 30(\%C) \quad 2.2$$

For steels with more than 17 weight %Cr:

$$Cr_{eq} = \%Cr + 3(\%Si) + \%Mo + 10(\%Ti) + 4(\%Nb) \quad 2.3$$

$$Ni_{eq} = \%Ni + 0.5(\%Mn) + 21(\%C) + 11.5(\%N) \quad 2.4$$

Difficulty may be encountered in dealing with elements such as Nb and Ti in terms of their Cr equivalent values, as they are not only ferrite formers but they also remove the potent austenite formers, namely carbon and nitrogen, from solution in the form of NbC and NbN or TiC and TiN. Thus he proposed equations to take into account the carbide and nitride forming tendencies of titanium and niobium:

$$\%Ti(effective) = \%Ti - 4[(\%C - 0.03) + \%N] \quad 2.5$$

$$\%Nb(effective) = \%Nb - 8[(\%C - 0.03) + \%N] \quad 2.6$$

Recently, Hertzman et al /54/ have derived a mathematical expression relating the amount of austenite present as a function of temperature and the amount of alloying elements present:

$$Weight\ \%\ austenite = 75 - 6.8 \times 10^{-5}\ (T + 273)^3 + 190\ (\%C - 0.03) + 6(22 - \%Cr) + 9(\%Ni - 5) + 6.5(3 - \%Mo) + 160(\%N - 0.15) \quad 2.7$$

Where T is the temperature in Celsius and the elements are in weight%. Their findings, based on a computer simulation that calculated the thermodynamic equilibria by minimizing the Gibbs free energy, showed good agreement with experimental data.

Alloying elements also affect the stability of the austenite phase. Austenite with a low Ni equivalent, and therefore unstable, may undergo partial transformation to martensite either by cooling or by deformation. This may be expressed by M_s, the temperature of spontaneous formation of martensite on cooling, and M_d, the highest temperature at which martensite is formed when the austenite undergoes plastic deformation. Eichelmann and Hull /55/ have derived an equation relating M_s to the composition of the alloy. For 18/8 stainless steels:

$$M_s\alpha'(°C) = 1305 - 6.1(\%Ni) - 41.7(\%Cr) - 33.3(\%Mn) - 27.8(\%Si) - 1667(\%C + \%N) \qquad 2.8$$

In the derivation of this equation they assumed that the effect of each element varies linearly with its weight percentage and that there is no interaction between elements. Angel /44/ determined the effect of alloying elements on the temperature at which 50% of the austenite transforms to martensite under the action of a true strain of 0.3:

$$M_d\alpha'_{30}(°C) = 413 - 462(\%C + \%N) - 9.2(\%Si) - 8.1(\%Mn) - 13.7(\%Cr) - 9.5(\%Ni) - 18.5(\%Mo) \qquad 2.9$$

These equations indicate that the general effect of the alloying elements is to lower both $M_s\alpha'$ and $M_d\alpha'$ and that some elements, namely carbon and nitrogen, have a much stronger effect.

The stacking fault energy (SFE) of the austenite in the duplex stainless steels is also affected by the alloying additions. Nickel, copper, and carbon increase the stacking fault energy whilst many other elements, especially

nitrogen, decrease it. Several equations have been proposed to enable the prediction of the stacking fault energy and these include that by Pickering /56/:

$$SFE\ (mJ\ m^{-2}) = 25.7 + 2(\%Ni) + 410(\%C) - 0.9(\%Cr) - 77(\%N) - 13(\%Si) - 1.2(\%Mn) \qquad 2.10$$

The SFE is important in view of the strengthening mechanism (work hardening rate), the type and mechanism of martensite formed and, according to some workers, the susceptibility of the austenite to transgranular stress corrosion cracking.

In addition to the influence of alloying elements on the phase balance and stability, they also have a profound influence on the mechanical properties of the alloy. The potencies of alloying elements in solution strengthening fall into three groups: (i) interstitial alloying elements that have a very large strengthening effect. (i.e. C and N), (ii) substitutional (ferrite-forming) alloying elements with a moderate strengthening effect (W, Mo, V, Si), and (iii) substitutional (austenite-forming) elements that have low or no strengthening effect. (i.e. Mn, Co, Ni) (Figure 2.11).

Since alloying with carbon to increase the strength of stainless steels is out of the question due to the detrimental effect of the precipitation of chromium carbides, the other obvious effective solution strengthening element is nitrogen (Figure 2.11). In duplex stainless steels, most of the dissolved nitrogen segregates into austenite, the softer phase, and thus has a profound effect in increasing the strength of the alloy via strengthening of the softer phase (austenite).

Alloying elements also influence the corrosion properties of stainless steels and this is summarized in Figure 2.12.

Chromium obviously has a beneficial effect on the stability of the passive film and thus on the resistance to uniform and localized corrosion. Increasing the chromium content raises the pitting potential and the critical pitting temperature of duplex stainless steels /57-59/. An increase of chromium beyond a certain limit, however, is known to promote the precipitation of undesirable carbides and sigma phase. Therefore, chromium addition to duplex stainless steels should not exceed 27%.

Molybdenum has an even stronger beneficial effect on localized corrosion resistance. A molybdenum content in excess of 3.0% was required to induce a high level of resistance to localized corrosion of 25%Cr duplex stainless steels in chloride solutions /58,59/, and a hydrogen-sulphide-containing environment at 80°C /60/. It was also reported that molybdenum is more efficient in high chromium duplex stainless steels than in austenitic steels/61/. Like chromium the molybdenum content cannot be increased beyond a certain limit because it promotes the precipitation of the intermetallic phases. In modern duplex stainless steels the molybdenum content rarely exceeds 4%.

On the other hand, it was found that the main role of nickel in duplex stainless steels is to control the ferrite/austenite phase ratio to about 50/50 /62/, rather than modify the corrosion resistance itself. In 25%Cr-3%Cu-2.5%Mo-0.15%N duplex steel for example, the maximum pitting potential, in 3% NaCl solution, was achieved with a nickel

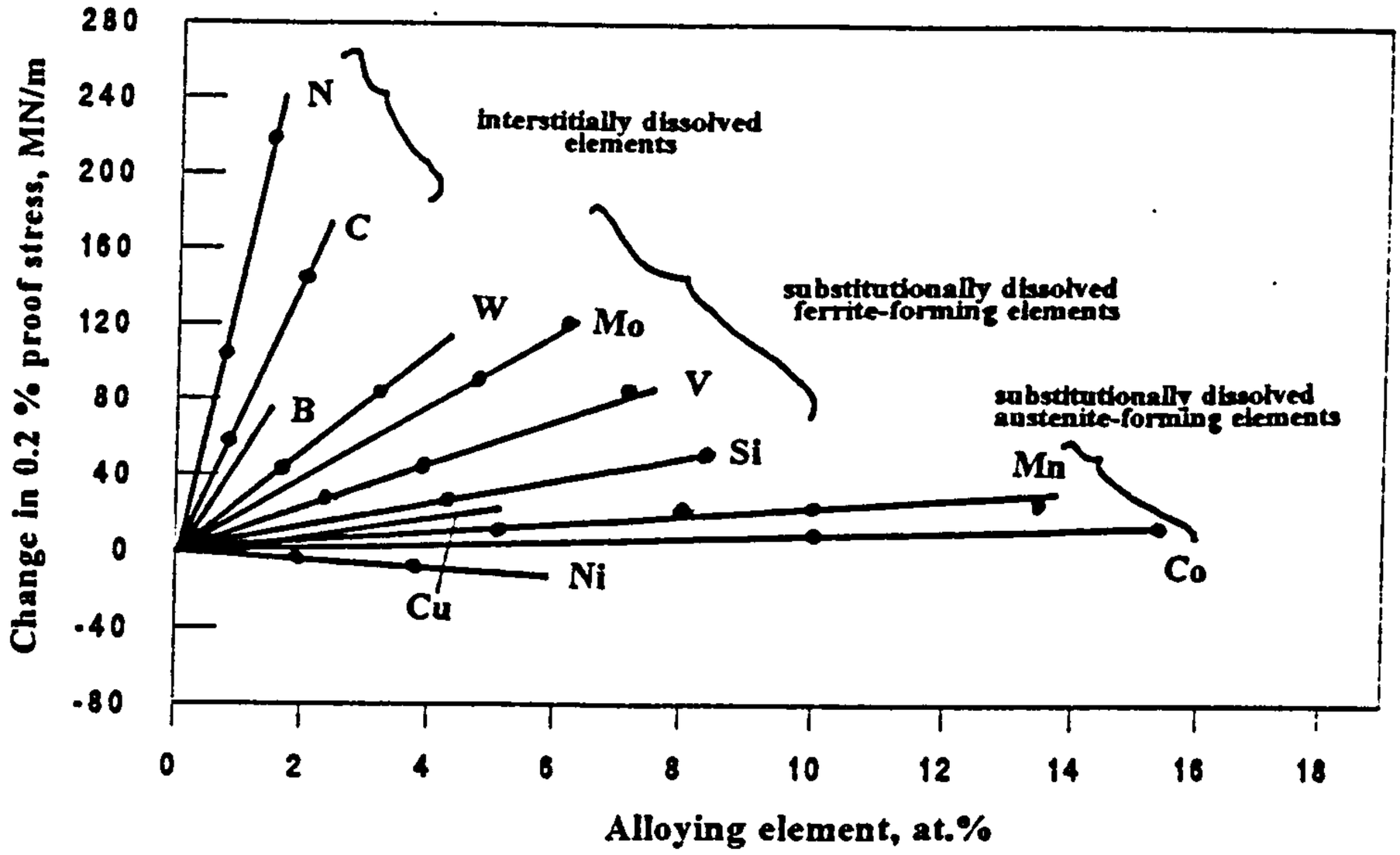

Figure 2.11 The effect of solid solution hardening in austenite

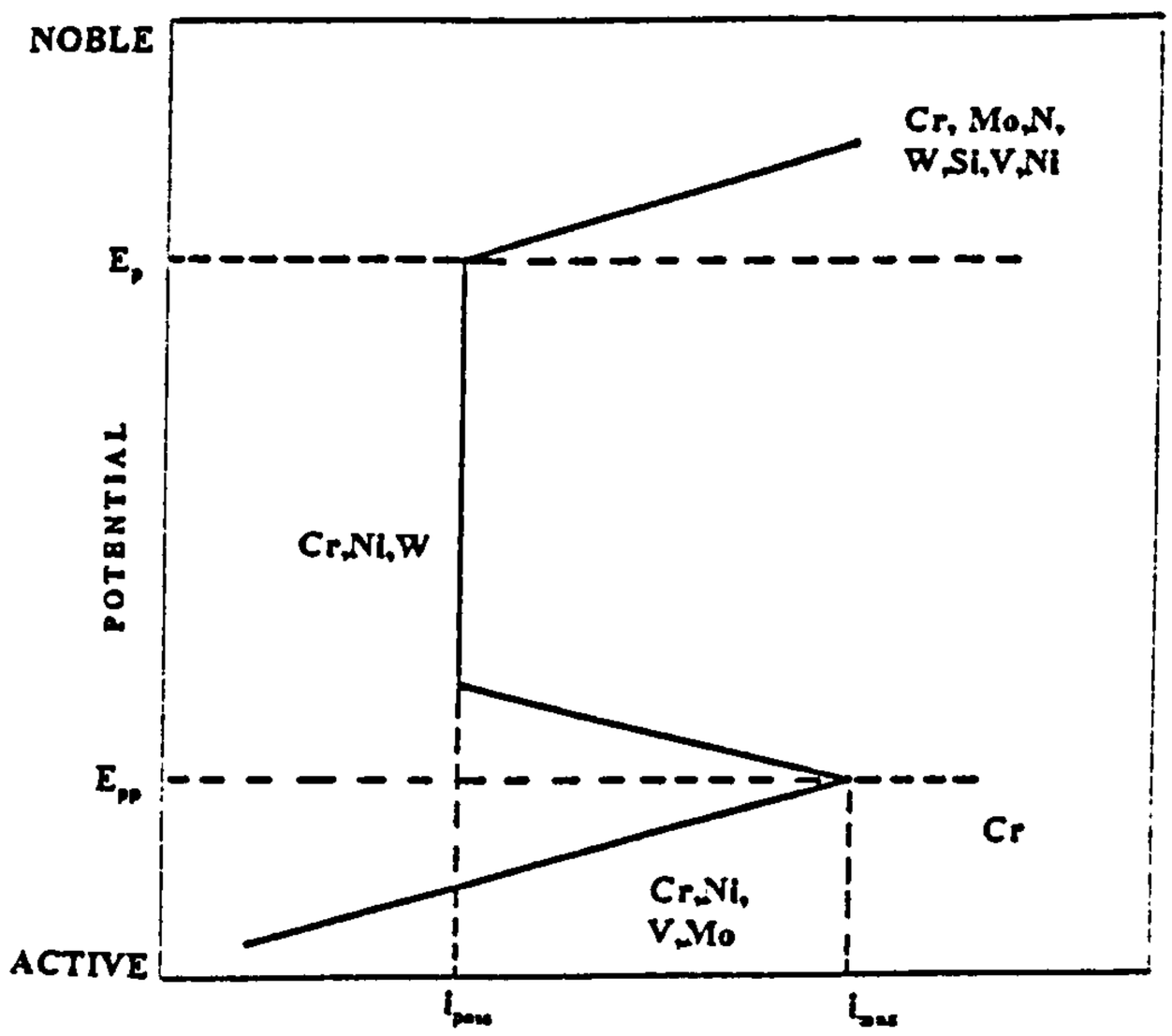

Figure 2.12 Schematic summary of the effect of alloying elements in stainless steels on the anodic polarization curve.

content of about 5.2% and associated with equal amounts of ferrite and austenite. Increasing the nickel content above this optimum value would increase the volume of the austenite phase and so alter the distribution of the alloying elements between the two phases. In particular the greater austenite phase will be diluted of nitrogen, thus lowering its resistance to pitting and crevice corrosion /62,63/.

Nitrogen efficiently increases the resistance of duplex stainless steels to localized corrosion. It increases the resistance to pit initiation as demonstrated by pitting potential measurements in NaCl solution and critical pitting temperature measurement in $FeCl_3$ solution /62/. It also reduces pit propagation and crevice corrosion. It is important to note here that, because nitrogen preferentially segregates to the austenite, the phase with less Cr and Mo, it plays an important role in increasing the resistance to localized corrosion of the inherently more susceptible phase.

Other alloying elements, such as copper, tungsten , manganese, and silicon, also have certain effects on the corrosion of duplex stainless steels, ranging from beneficial to detrimental. Table 2.2 summarizes some of these effects.

From the few previous paragraphs it becomes clear that the most profound influence on the corrosion properties of duplex stainless steels is exerted by three alloying elements, namely chromium, molybdenum, and nitrogen. In fact the assessment of resistance to pitting is often made by use of a pitting resistance equivalent number (PRE_N) which is proportional to the content of these three elements in the

Table 2.2 Influence of different alloying elements and the microstructure on the pitting and crevice corrosion resistance of duplex stainless steels /64/.

Alloying elements	Effect	Reason	Practical limitation
C	Negative	Causes precipitation of chromium carbides with accompanying chromium depicted zones	Abt 0.03% maximum
Si	Positive	Si stabilizes the passive film of the alloy	Abt 2% maximum due to its effect on structural stability and on nitrogen solubility
Mn	Negauve	Mn-rich sulphides act as initiation points for pitting. Mn may also destabilize the passive film	Abt 2%. Higher amounts might also increase the risk for precipitation of intermetallics
S	Negauve	Sulphides, if not Cr-, Ti- and Ce-rich, tend to initiate pitting attacks	Abt 0.003% if maximum pitting resistance required. If reasonable machinability required, up to say 0.020% allowed
Cr	Posiuve	Cr stabilizes the passive film	Abt 25-28% maximum depending on the Mo-content. Higher Cr-content increases the risk for precipitation of intermetallics too much.
Ni	Negauve	Increased Ni, other elements constant, dilutes the γ phase with regard to N, which in turn decreases the PRE of the γ-phase. If the alloy is very sensitive to precipitation of chromium nitrides, Ni can have a positive effect.	Ni should primarily be used to give the alloy the desired austenite content.
Mo	Positive	Mo stabilizes the passive film, either directly or through enrichement beneath the film	Abt 4-5% maximum depending on the Cr-content of the alloy. Mo enhances the precipitation of intermetallics.
N	Positive	N increases the PRE-number of the γ phase dramatically, both by increasing the N-content of that phase, but also by increasing the Cr- and Mo-contents through their partitioning coefficients.	Abt 0.15% in Mo-free DSS, abt 0.3% in 25Cr high-Mo ones, and some 0.40% in 25Cr high-Mo, high-Mn alloys
Cu	Disputed	Marginal positive or negative effect	Abt 2.5% maximum more than that reduces hot workability and causes undesired hardenability.
W	Positive	Probably the same as for Mo	Increases the tendency to precipitation of intermetallics.
Volume fraction ferrite	Positive	Increased ferrite content increases the N, Cr and Mo contents of the γ phase	Too high ferrite content can cause precipitation of chromium carbides and nitrides in a coarse microstructure.
Intermetallic phases (σ, χ, ...)	Negauve, if any	Precipitates with accompanying depletion of alloying elements (Cr, Mo)	If steel manufacturers recommendations are followed, precipitation of intermetallics will not occur during heat treatment or welding.
Chromium carbides and nitrides	Negauve in oxidizing and corrosive chloride-containing environments	Precipitation of carbides/nitrides causes Cr-depleted zones which are selectively attacked in certain corrosive environments.	In older generations of DSS, nitrides have frequently been present in welded joints and in the base metal of material with a coarse microstructure. This has rarely been the reason for a corrosion failure.

steel:

$$PRE_N = \%Cr + 3.3\%Mo + 16\%N \qquad 2.11$$

It must be appreciated, however, that the PRE_N is not an absolute measure of pitting resistance, rather it is a broad method of material grading, since it does not take into account the influence of other alloying elements on phase balance and corrosion properties.

2.2 Stress corrosion cracking

2.2.1 Introduction

Stress corrosion cracking (scc) refers to cracking of an alloy by the simultaneous presence of tensile stress (applied or residual) and a specific corrosive environment. These cracks can be either intergranular or transgranular. The seriousness of this type of cracking lies in its unexpected occurrence which can prove to be catastrophic in its consequences.

The history of the subject goes back to the last century in which reports were concerned with the "season cracking" of cold-drawn brass cartridge cases in ammoniacal atmospheres /65/ and early this century with the caustic cracking of rivetted boilers /66/. Since then the problem has received widespread attention from both scientists and engineers. Many alloys have been found to be susceptible to scc in a wide variety of environments, but the phenomenon is often considered to be alloy/environment specific and frequently the result of a particular chemical species in the environment. For example, the scc of copper alloys (season

cracking) is usually attributed to the presence of ammonia in the environment, and chloride ions cause cracking in aluminum and stainless steels. That is to say, an environment that causes scc in one alloy may not cause it in another. Moreover, the temperature, degree of aeration and the concentration of ionic species may change a harmless environment to one that cause scc failure. Changes in the microstructure of the material via heat treatments may also effect the susceptibility to scc. As a result the list of the possible alloy/environment combinations that cause scc is continually expanding and some are listed in Table 2.3.

Advances in the understanding of the scc phenomenon have occurred in three distinct phases. The first was the "identification" of the problem in the 1940's, which involved categorization in terms of a specific alloy/environment combination. The second was the "mechanistic" phase in the 1960's and 1970's, in which various mechanisms were proposed to explain the crack morphology, the dependency of cracking on the environmental and metallurgical parameters, and the wide range of crack propagation rates observed. It was during this phase that numerous combinations of alloys and environment were investigated and it was realised that most alloys are susceptible to scc under appropriate conditions. The present (third) phase involves the application of the mechanistic knowledge, specifically in improving predictive capabilities through knowledge of the rate-determining steps involved in the cracking mechanism, in establishing guidelines for the development of material compositions and micro-structures that improve scc resistance, in controlling the environment, and in developing test techniques that are more relevant to practical situations.

Table 2.3 Alloy/Environment systems exhibiting scc /67/.

Alloy.	Environment.
Carbon steel.	Hot nitrate, hydroxide and carbonate/bicarbonate solutions
High strength steels.	Aqueous electrolytes, particularly when containing H_2S.
Austenitic stainless steels.	Hot concentrated chloride solutions, chloride- contaminated steams.
High nickel alloys.	High purity steam.
α-Brass.	Ammoniacal solutions.
Aluminium.	Aqueous Cl^-, Br^- and I^- solutions.
Titanium alloys.	Aqueous Cl^-. Br^- and I^- solutions and organic liquids; N_2O_4.
Magnesium alloys.	Aqueous Cl^- solutions.
Zirconium alloys.	Aqueous Cl^-solutions.

2.2.2 Mechanisms of stress corrosion cracking

The mechanisms of stress corrosion cracking have been reviewed in detail by many authors /68-71/ but there are so many variables that it is unlikely that a universal mechanism could explain all known cases. However, some general classification may be attempted into two basic categories involving either dissolution or embrittlement.

2.2.2.1 Film rupture

Transgranular scc is a characteristic of this model, which is based on the fact that most metals and alloys, in aqueous solutions, develop a surface film that is characteristic of the environment. Before any form of corrosion reaction can occur between the bulk alloy and any of the constituents of the solution, the two must come into contact and this can only happen if the surface film, whatever its nature, is disrupted locally by either chemical or mechanical means. Chemically, film breakdown may occur due to the activity of a certain aggressive anion in the environment (i.e. Cl^- for stainless steels). Mechanically, however, the breakdown process in stressed specimens is commonly thought to be caused directly by the action of the stress in producing plastic deformation at a particular surface strain rate.

In the film rupture model, which was originally proposed by Champion /72/, the basic hypothesis is that the protective film is ruptured by localized plastic deformation at a crack tip, permitting rapid anodic dissolution of the freshly exposed substrate while the undeformed crack walls remain passivated by the film, thus concentrating the chemical activity at the minute crack tip region /73/ (Figure 2.13). Staehle /74/ argued that the film rupture

event is the result of the emergence of slip steps through the passive film and that the crack tip does not become completely repassivated at any stage during propagation, so that crack advance is essentially continuous. It has been suggested /73/ that during an increment of crack growth a certain rate of charge must pass in order to cause sufficient corrosion damage and initiate a further crack increment. The nature and properties of the film are very important since, in the extreme case, if the film were very ductile it might deform and stretch without causing any exposure of fresh metal surface to the corrosive environment. The thickness of the film, t, in relation to the height of the slip step, h, will also be important. If t/h is relatively high, fresh metal may not be revealed at all, and therefore, thick films may be more beneficial than thin films providing that their mechanical properties are unchanged. As this mechanism involves rupture of a passive film by plastic deformation it might be expected that the slip mode of the alloy would play an important role in the cracking phenomenon. Alloys exhibiting lamellar slip are, therefore, less susceptible to scc because of relatively easy cross slip and have low slip step height /75/. It is, however, the characteristic of fcc and hexagonal alloys, susceptible to transgranular scc, that they exhibit co-planar arrays of dislocations, indicative of a tendency not to cross slip easily (i.e. large slip steps). Once bare metal is exposed to the environment and cracking has started, the chemistry of the solution at the crack tip may differ greatly from the bulk solution chemistry due to the restricted migration of ionic (i.e. Cl^-) species into the crack tip region to maintain charge neutrality. Brown et al /76/ showed that the pH at the crack tip region of steel in

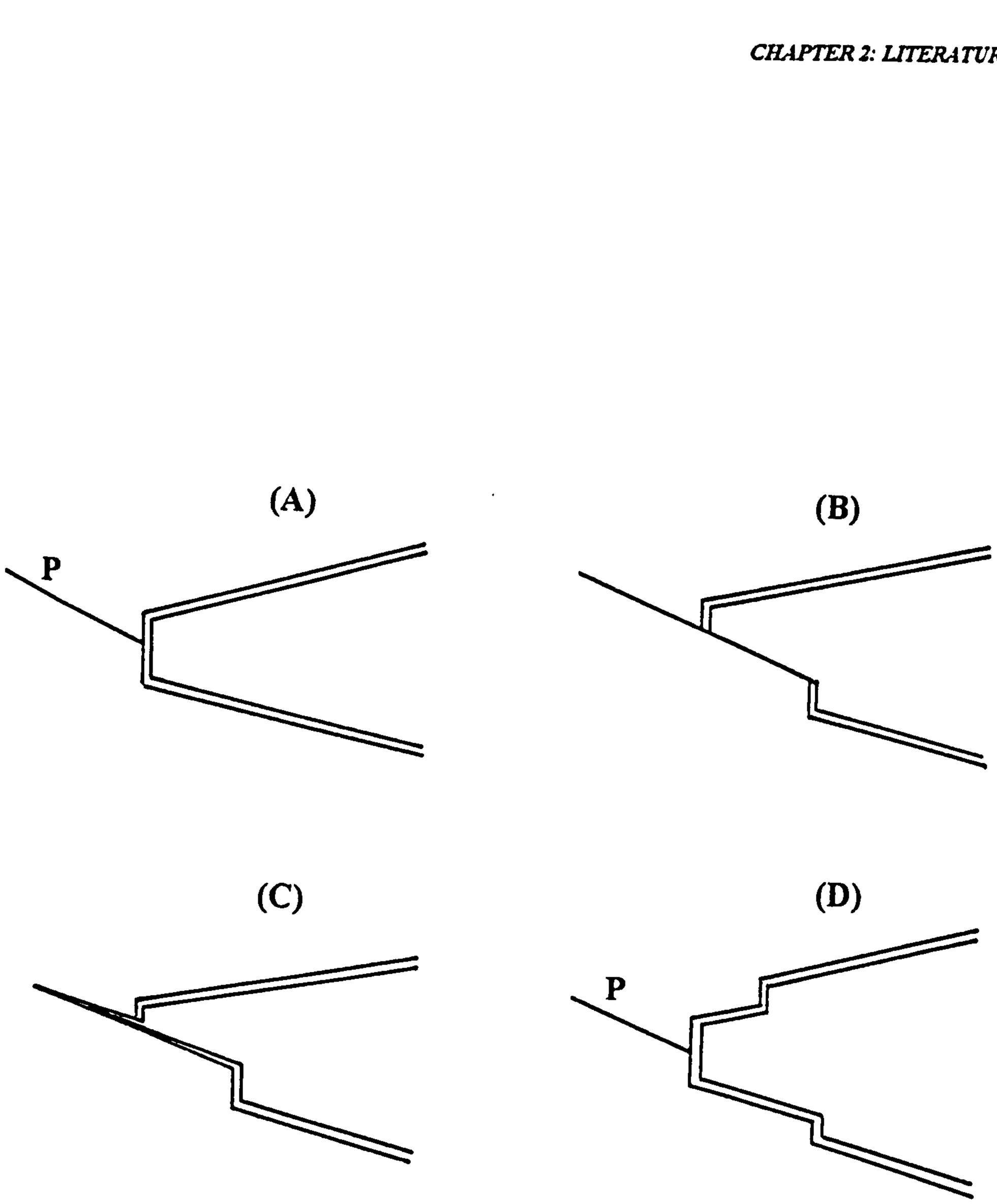

A) The tip of a crack. The surface is covered by protective film.(P is a slip plane)

B) The slip plane undergoes a shear and a new, unfilmed, reactive surface is created.

C) Corrosion attack occurs on the reactive surface while repassivation begins on the outer-edge. The morphological aspects of the attack may vary from alloy to alloy and it is not necessary that it occurs preferentially along the slip plane.

D) Depassivation occurs but not until sufficient corrosion attack and plastic deformation have occurred to ensure that an increment of crack growth occurs and will recur.

Figure 2.13 Schematic diagram of the sequence of events occuring at the tip of a propagating crack.

chloride solutions has a value corresponding to that of the saturated chloride ≈3.8, which is similar to the value observed inside pits on steels. This severe crack tip environment undoubtedly enhances the corrosion reactions and thus the production of hydrogen and most probably will retard the repassivation of the crack tip because of low pH.

Repassivation rate is also of prime importance to the stress corrosion crack propagation. Scully /73/ argued that, if repassivation is relatively high then insufficient charge will flow to sustain cracking and crack arrest will occur. On the other hand, if repassivation is relatively slow then corrosion will not be localized but will spread laterally, causing crack blunting. Cracking therefore, can only occur with a repassivation rate within some defined narrow range. It should be noted here that, if hydrogen absorption plays any part in the crack propagation process, rapid repassivation is also likely to retard cracking since the formation of the film will hinder hydrogen entry and may affect hydrogen discharge rate. Figure 2.14 represents a schematic explanation of the effect of the electrochemical condition present at a propagating stress corrosion crack for 18%Cr-8%Ni steel exposed to chloride solution.

2.2.2.2 Pre-existing active path

This mechanism, originally proposed by Dix /77/, is mostly applicable to intergranular cracking and relates the cracking to the chemical activity of the grain boundary. Grain boundaries possess relatively higher energy than the bulk grains, due to the fact that they are regions of disorder

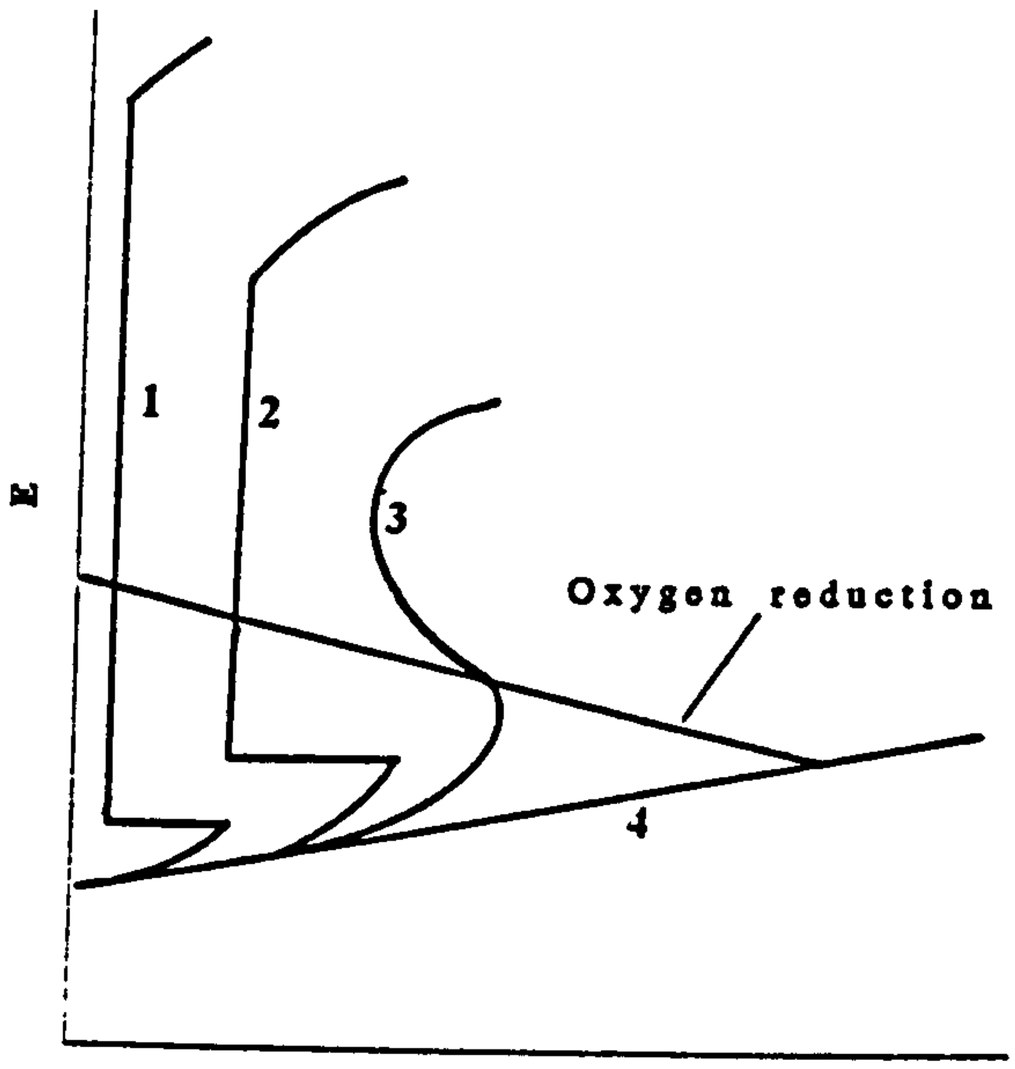

(a)

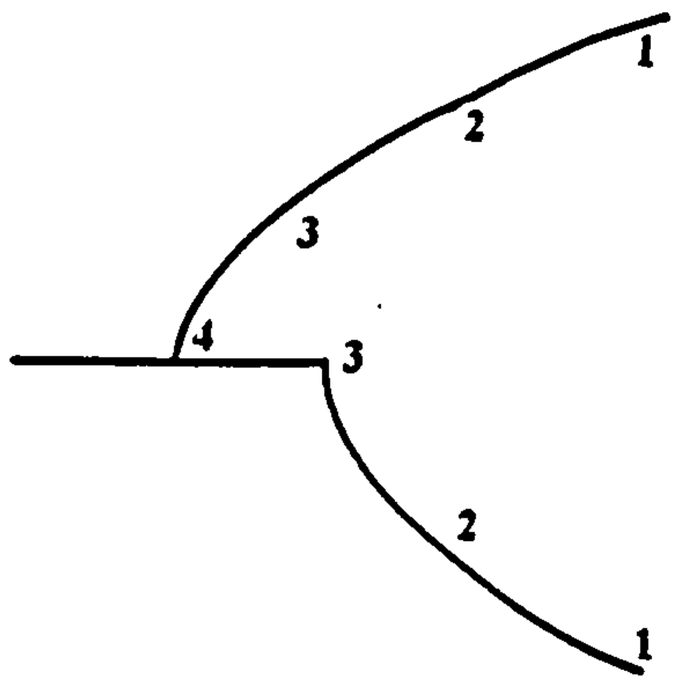

(b)

(a) Schematic polarization curves for 18Cr-8Ni steel exposed to solutions of increasing chloride concentration, falling pH and decreasing dissolved oxygen.

(b) A schematic drawing of the tip of a stress corrosion crack. The numbers correspond to the curves in (a).

(1) Normal polarization curve in low chloride solution, high pH and high dissolved oxygen concentration.	*Crack sides covered with protective film (passivated)*
(2) and (3) Polarization curve in high chloride solution, lower dissolved oxygen (raises the critical current density for passivation)	*Crack sides near the tip covered with defective film.(higher dissolution and, because potential is low, hydrogen may evolve).*
(4) Polarization curve in even higher chloride solution, very low pH, and very low dissolved oxygen concentration (no passivation occurs).	*Bare metal at the crack tip, dissolution of the active metal (potential is very low and hydrogen will be discharged).*

Figure 2.14 Schematic representation of the electrochemistry of stress corrosion cracking.

or misfit and are thus favourite sites for segregation of various solute elements, or precipitation of metal compounds such as carbides and σ phase. This results in grain boundaries having different chemical composition from the bulk of the grain. In certain corrosive environments the grain boundary, or the area immediately adjacent to it (as in the case of the chromium-depleted zone in some sensitized stainless steels) may be preferentially attacked, depending upon whether it is anodic or cathodic with respect to the rest of the grain (Figure 2.15). The actual polarity of these areas might change in different environments /78/. With no stress of appreciable magnitude present, the initial attack may not extend before filming prevents further penetration. Thus, the rupture of the protective film at the crack tip plays an essential role for further crack advancement.

2.2.2.3 Embrittlement mechanisms

This model proposes that adsorption of a specific species from the environment decreases the mechanical integrity at the crack tip and various mechanisms for the degradation of mechanical properties have been proposed /79,80/. This surface energy reduction model relies on chemisorption of an environmental species, i.e. hydrogen atoms, at the crack tip (Figure 2.16), which reduces the surface energy term in the Griffith equation /81/ for brittle fracture and thereby reduces the stress to cause brittle fracture:

$$\sigma_f = \left(\frac{2 E \gamma_s}{\pi c} \right)^{1/2} \qquad 2.12$$

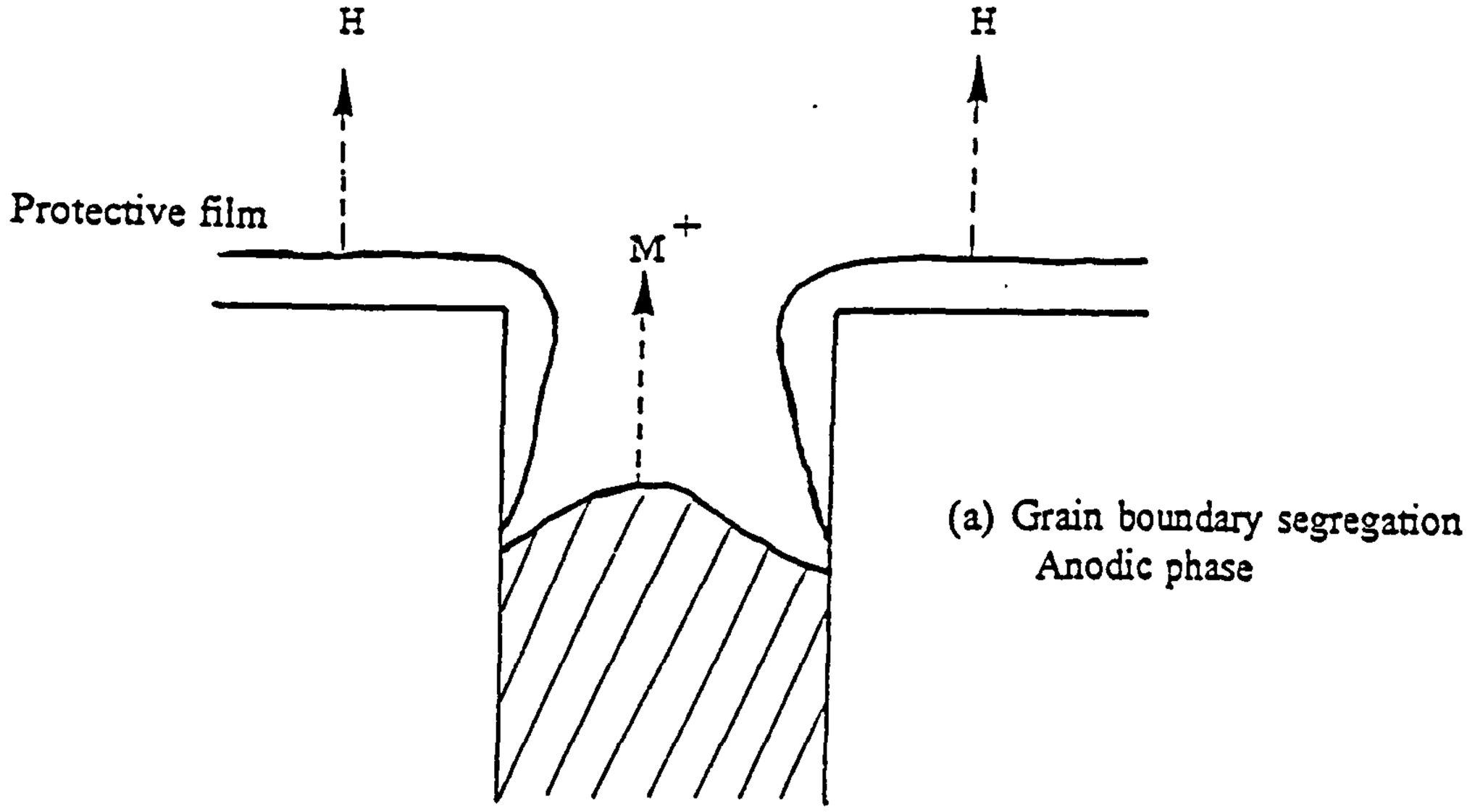

Figure 2.15 The galvanic cell mechanism

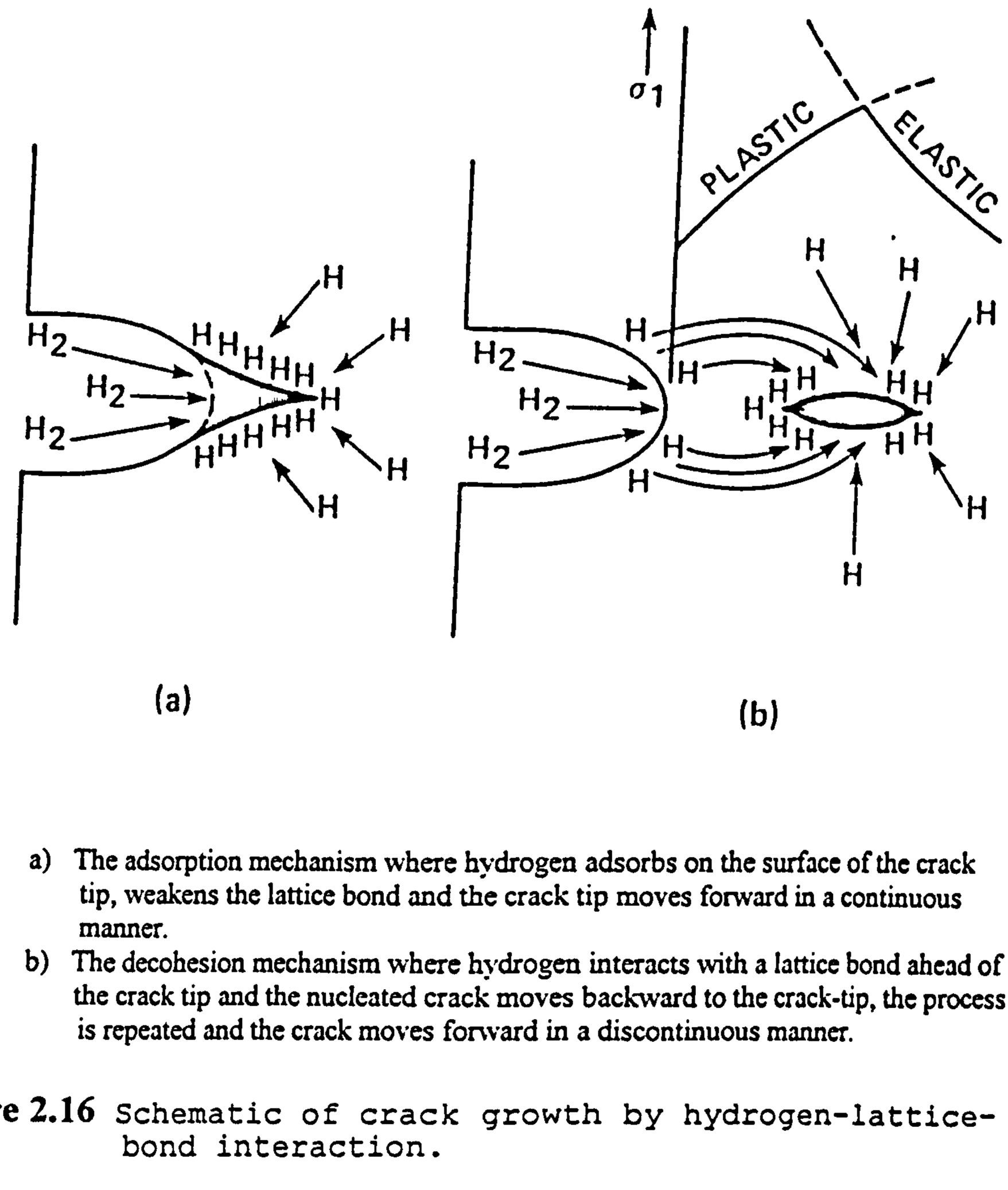

a) The adsorption mechanism where hydrogen adsorbs on the surface of the crack tip, weakens the lattice bond and the crack tip moves forward in a continuous manner.
b) The decohesion mechanism where hydrogen interacts with a lattice bond ahead of the crack tip and the nucleated crack moves backward to the crack-tip, the process is repeated and the crack moves forward in a discontinuous manner.

Figure 2.16 Schematic of crack growth by hydrogen-lattice-bond interaction.

where σ_f is the fracture stress to cause the spread of an elliptical crack with a length of $2c$, E and γ_s are the Young's modulus and specific surface energy respectively. Clearly any process that lowers γ_s reduces the stress for brittle fracture and γ_s may be lowered by the adsorption of appropriate species at the fracture surface. Such an argument has been used to explain hydrogen embrittlement /79/ and liquid metal embrittlement /82/. However, this model has difficulty in explaining the significant plastic deformation associated with stress corrosion crack propagation, particularly for hydrogen-related scc in tougher alloys. Orowan /83/ suggests that the surface energy term in Equation 2.12 needs to modified to take into account the work done in plastic deformation, so that to γ_s should be added γ_p, the work for plastic strain. However, γ_p is several order of magnitude larger than γ_s and therefore any reduction in the latter by adsorption will have little effect on the fracture stress.

Decohesion models /84-87/ have been proposed specifically for hydrogen embrittlement and temper embrittlement, where subsurface atom-atom rupture is facilitated by local concentration of hydrogen or temper embrittling elements that modify the electron d-band structure or expand the lattice. Such effects can lead to a loss in tensile ductility following hydrogen charging (either thermally or electrochemically) or from heat treatments that allow segregation of temper embrittling elements to the grain boundary. Oriani /87/ argued that the difference in mechanism of atom-atom rupture between the surface energy and the decohesion model is minor, and the main difference is that in the former, rupture occurs at the crack tip

surface, whereas in the latter, subcritical crack propagation is governed by the diffusion of the "aggressive" atom to the critical point beneath the surface where rupture occurs. Such subcritical crack propagation, therefore, is expected in hydrogen-bearing environments (environments where hydrogen atoms can be produced at the crack tip surface by H^+ reduction, hydrogen molecule dissociation,...etc) because of the high mobility of the hydrogen atom in most metal lattices. The propagation of the crack is envisaged as a discontinuous cycle involving production of an adsorbed hydrogen atom at the crack tip, surface diffusion, absorption, and matrix diffusion to a region in front of the crack tip where localized mechanical fracture occurs when the hydrogen content reaches some critical value. From the standpoint of fractography this model proposes brittle fracture and is thus consistent with the general cleavage-like appearance of the transgranular fracture, which sometimes exhibits crack arrest marks.

2.2.2.4 Stress corrosion spectrum

From the review of the models for stress corrosion cracking presented in the previous sections it is clear that no single mechanism can explain all observed failures. Parkins /88,89/ proposed the concept of a continuous spectrum of failure mechanisms (Table 2.4). He characterised the scc in terms of the relative importance of the parameters involved;(i.e. stress, electrochemistry, metallurgy,..) Thus, corrosion may be the dominant parameter, with the stress only playing a minor role (a mechanism associated with pre-existing active paths), corrosion and stress may be of roughly equal importance (strain-generated active path), or the cracking process may be stress-dominated (specific adsorption). It should be emphasized here that the

Table 2.4 Stress corrosion spectrum: " a gradual transition from one mechanism of fracture to another."

corrosion-dominated solution specificity.	**Intergranular corrosion**		
	Stress-associated intergranular corrosion.	Dissolution-controlled intergranular fracture along pre-existing active path.	C steels in NH_4NO_3 C steels in nitrate solutions. Al, Zn, and Mg in chloride solutions. C steels in Na_2CO_3+$NaHCO_3$
	Slip step dissolution.	Transgranular fracture along strain-generated active paths.	C steels in CO_3-HCO_3 (high strain rate) Ni steel in $MgCl_2$ C steels in CO-CO_2-H_2O C and low alloy steels in liquid NH_3 Ti steels in CO_3-HCO_3 (high stress low strain rate tests).
	Surface energy lowering.	Mixed crack path by H adsorption at subcritically stressed sites	C steels in OH or CO_3-HCO_3^- (slow strain rate tests at low potential) medium strength steels in OH, CO_3 acetates, ...etc at low potentials. High strength steel in H_2O, Cl^-, ...etc.
stress dominated	**Brittle fracture**		

spectrum is continuous with no abrupt change from one mechanism to another but a gradual change of emphasis between the mechanisms involved through the spectrum.

2.2.3 Chloride SCC of austenitic stainless steels

Austenitic stainless steels exhibit stress corrosion cracking in hot chloride solutions and there is a long history of such failures in chemical plants and many other industries /90/. In concentrated chloride solutions, cracking is predominantly transgranular while in high-temperature pressurized water and steam intergranular cracking predominates. Although most scc investigation of austenitic steels employed $MgCl_2$ solution at 154°C, which is a very severe environment, many others have been conducted in much less severe solutions (e.g. NaCl or LiCl solutions of varying concentrations). A film exists on the surface in this type of solution and cracking is associated with its localized rupture. Many investigators believe that the transgranular cracking of austenitic steels is associated with the slip step dissolution model, while others have nominated the embrittlement model to be the operative mechanism. Neilsen /91/, using dual-image oxide replicas, has demonstrated that the features on both fracture surfaces are exactly matching. If the dissolution model is the operative mechanism, the dissolution events should result in different features on opposite faces of the fracture and, since this is not the case, the operative mechanism is most probably the embrittlement model.

It is well established that transgranular cracks are crystallographic in nature and there have been several

attempts to identify the orientation of the fracture facets. Reed and Paxton /92/ have reported that cracking occurs on {110} planes in high nickel austenitic steel. For 304 type the orientation of the facets were reported to be either {110} or {210} /105,112/. No explanations have, however, been put forward for the fracture orientation. The possible role of hydrogen in promoting transgranular fracture in stress corrosion cracking environments has been emphasized by many workers; especially in the light of the fact that, in chloride solutions, the pH measured in the region of the crack tip is 3.8 regardless of the pH of the bulk solution /76/. Many workers believe that absorbed hydrogen promotes the formation of ε and α' martensite in some austenite lattices /93/. Birley and Tromans /94/ have observed the formation of α' phase on the scc fracture surface. It has been argued that such a transformation is not an essential part of the fracture mechanism, since scc occurs well above the M_s temperature of some austenitic steels. Liu et al /95/ have investigated the cracking of the stable 310 and the less stable 304 austenitic steels in boiling $MgCl_2$ solution. They found that the fracture orientation of 310 type was at or near {100} planes, while that of 304 was near {211} and {110} planes. Both α' and ε martensites were found on the fracture surface of the 304 steel while none was found on the 310 steels (considered to be more stable). When they tested the 304 steel at a higher temperature (above M_s) no martensite phases were detected.

The influence of alloying elements on the susceptibility of austenitic stainless steels to scc is complicated because of the interaction between individual elements /96/. Nickel has long been recognized as beneficial and chloride

scc is not usually observed in alloys with a Ni content at or above 42% in boiling $MgCl_2$. Other elements designated beneficial to chloride scc resistance include copper, zinc and silicon, while, phosphorus and carbon and nitrogen are found to be detrimental /90/.

2.2.4 Chloride SCC of ferritic stainless steels

For a long time, ferritic stainless steels were thought to be immune to scc. In 1945, Scheil /97/ demonstrated the high resistance of the 405 (13% chromium) and the 430 (17% chromium) grades to chloride scc and this has subsequently been confirmed by many investigations /98,99/. These findings have led to the misleading impression that all ferritic stainless steels are immune to scc in chloride environments. However, more recent investigations have demonstrated the susceptibility of this class of alloys to chloride scc. Bednar /100/ showed that the 434, the 430, and the Fe-18Cr-2Mo ferritic grades can be cracked in lithium chloride solutions; also, sensitized 446 and 430 were shown to be prone to cracking in sodium chloride environments /101/.

Many factors were identified as increasing the susceptibility of ferritic stainless steels to chloride scc and among these are: the presence of certain alloying elements, sensitization (induced by heat treatment or welding), cold work, high temperature embrittlement, and precipitation of α' chromium-rich phase (475°C embrittlement). However, because of the metallurgical complexity of ferritic stainless steels, it is not well understood whether all of these factors are related to the phenomenon

identified as chloride scc in austenitic stainless steels or represent manifestations of other phenomena such as hydrogen embrittlement.

Many alloying elements have been identified as detrimental to chloride scc resistance of ferritic stainless steels. These include copper, nickel, molybdenum (in the presence of nickel), cobalt (in the presence of molybdenum), and carbon. Bond and Dundas /102/ carried out many investigations of the effect of steel composition on the resistance to chloride scc and their findings show that varying the chromium content in the range 17-25% and molybdenum in the range 0-5% in steel otherwise containing only residual elements does not induce susceptibility to cracking, even when they are present conjointly. Nickel up to 1.7% in 17% chromium steel did not cause susceptibility but was detrimental in the presence of up to 5% molybdenum. A similar effect of nickel was also shown in 25% chromium ferritic stainless steel. Shimodaira et al /103/ used the constant strain rate technique in studying the effect of nickel addition to 23% chromium ferritic stainless steel on the susceptibility to chloride scc. The steel had been hot forged, cold rolled, and annealed. They found that as the nickel content increased the susceptibility to scc increased (Figure 2.17). Copper and cobalt were also shown to have similar, but more potent, effects to nickel. The presence of titanium appears neither beneficial nor detrimental, as does that of carbon and nitrogen, providing that no sensitization has occurred, although data related to the latter are limited.

Ferritic stainless steels that are not of extremely low carbon and nitrogen can easily become sensitized toward intercrystalline corrosion after heating to temperatures near 900-1000°C (a condition that naturally occurs near welds). The sensitization is due to the formation of chromium, and possibly molybdenum, carbonitrides at grain boundaries. Selective attack in these areas, and intergranular scc is expected in the presence of tensile stress .

There is much evidence that cold working of ferritic stainless steels can make them prone to chloride scc. Newberg and Uhlig /104/ tested a series of high purity 18% chromium steels with nickel contents of up to 8%, in both the annealed and cold-rolled conditions, in boiling magnesium chloride solution. The results (Figure 2.18) demonstrated the detrimental effect of cold-working. Increasing the nickel content of such steels, however, will increase the austenite content at the annealing temperature (815°C), which will make it debatable whether the higher nickel types really qualify to represent ferritic steels.

2.2.5 Stress corrosion cracking of duplex stainless steels

The positive effect of the introduction of ferrite on the resistance to scc of austenitic stainless steel has long been recognised /99/. Since then, a large number of investigations have recognized the superior scc resistance of the duplex grades as compared with the austenitic stainless steels and the accumulated data from practical experience have confirmed these findings /106-110/.

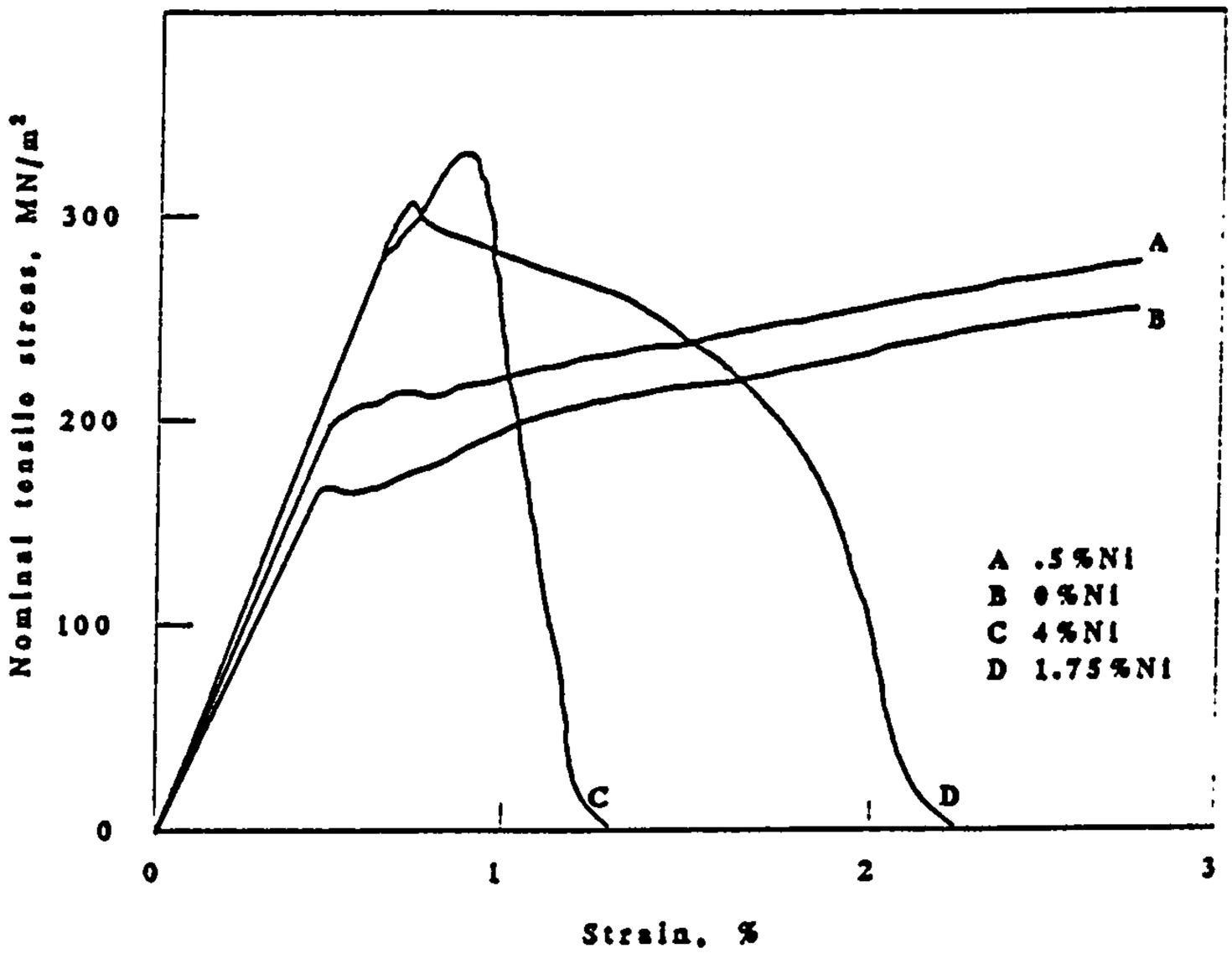

Figure 2.17 Stress strain curves for 23% chromium stainless steels with 0-4% nickel determined in boiling (140° C) de-aerated $MgCl_2$ solution at a strain rate of $4.6x10^{-6}$ /s /103/.

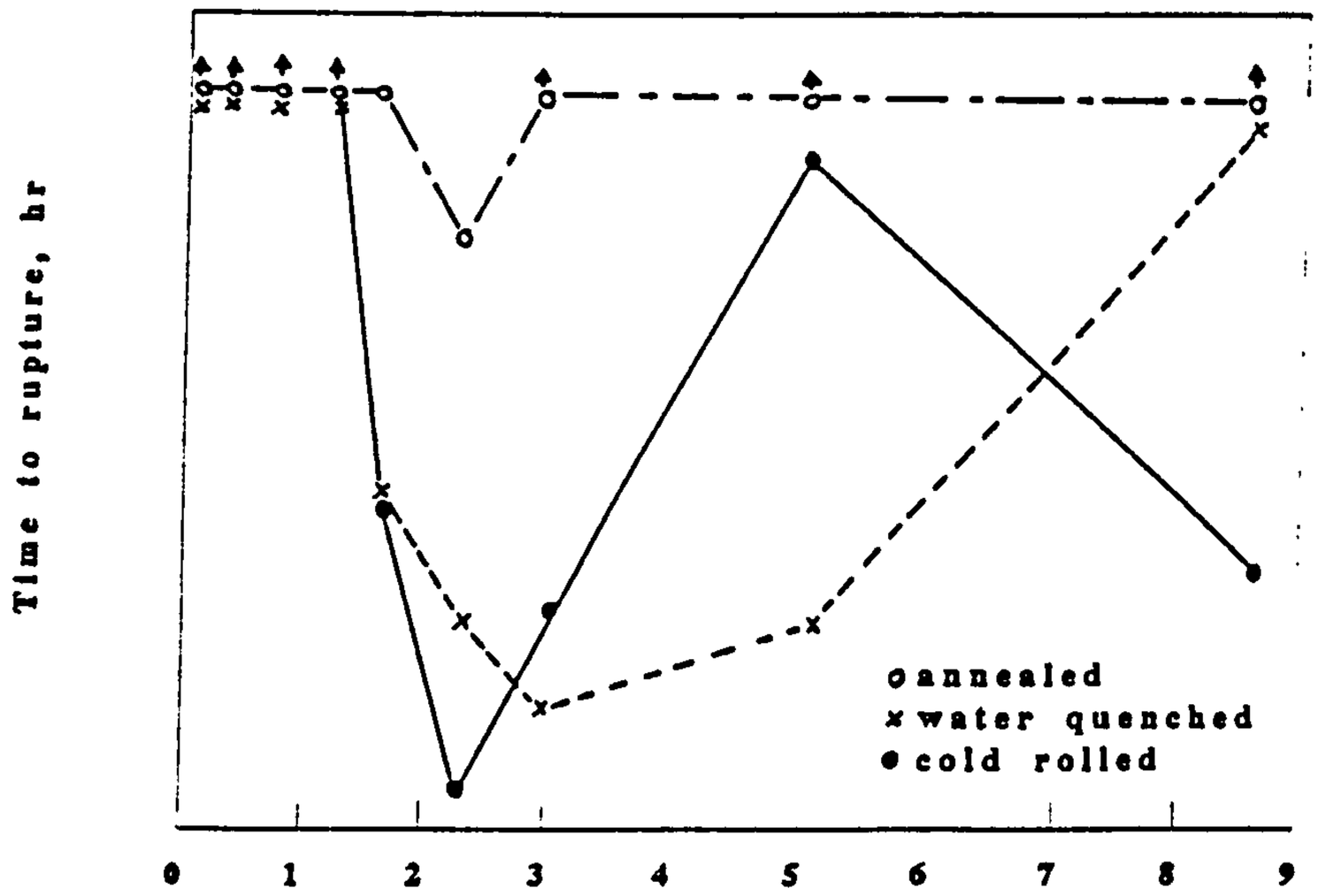

Figure 2.18 Effect of alloyed nickel in 18% chromium high-purity stainless steels in several conditions; U-bend specimens tested in $MgCl_2$ solution at 130°C /104/.

Commercial duplex stainless steels, either austeno-ferritic (with austenitic matrix) or ferrito-austenitic (with ferritic matrix), in fact, are more resistant to scc than either austenitic or ferritic grades (Figure 2.19). Flowers et al /106/, attributed this enhancement of scc resistance in austeno-ferritic stainless steels, to the "keying" action of the ferrite phase. (The propagating crack stopped at the ferrite particle and propagated in the austenite phase around the ferrite and emerged again on the other side of the ferrite particle). Kudo et al /111/ have observed a similar "keying" effect in ferrito-austenitic stainless steel by the austenitic phase. Shimodaira et al /103/ suggested that in ferrito-austenitic stainless steels the resistance to scc is due to the mechanical crack arrest by the austenitic phase while in austeno-ferritic stainless steels the keying effect by the ferritic phase is due to both the mechanical and electrochemical (cathodic protect-ion) effects. Hochmann et al /107/ investigated the characteristics of duplex alloys as well as ferritic and austenitic alloys whose composition corresponds to those of the phases present in the duplex alloy. They found that the duplex structure offers a superior resistance to scc in boiling $MgCl_2$ partially due to the mechanical keying effect which effectively places the ferrite in compression and to the protection of the austenitic phase by the more anodic ferrite (ferrite is about 10 mV more active to the austenite). However, many other investigations have shown that the austenite is the anodic phase.

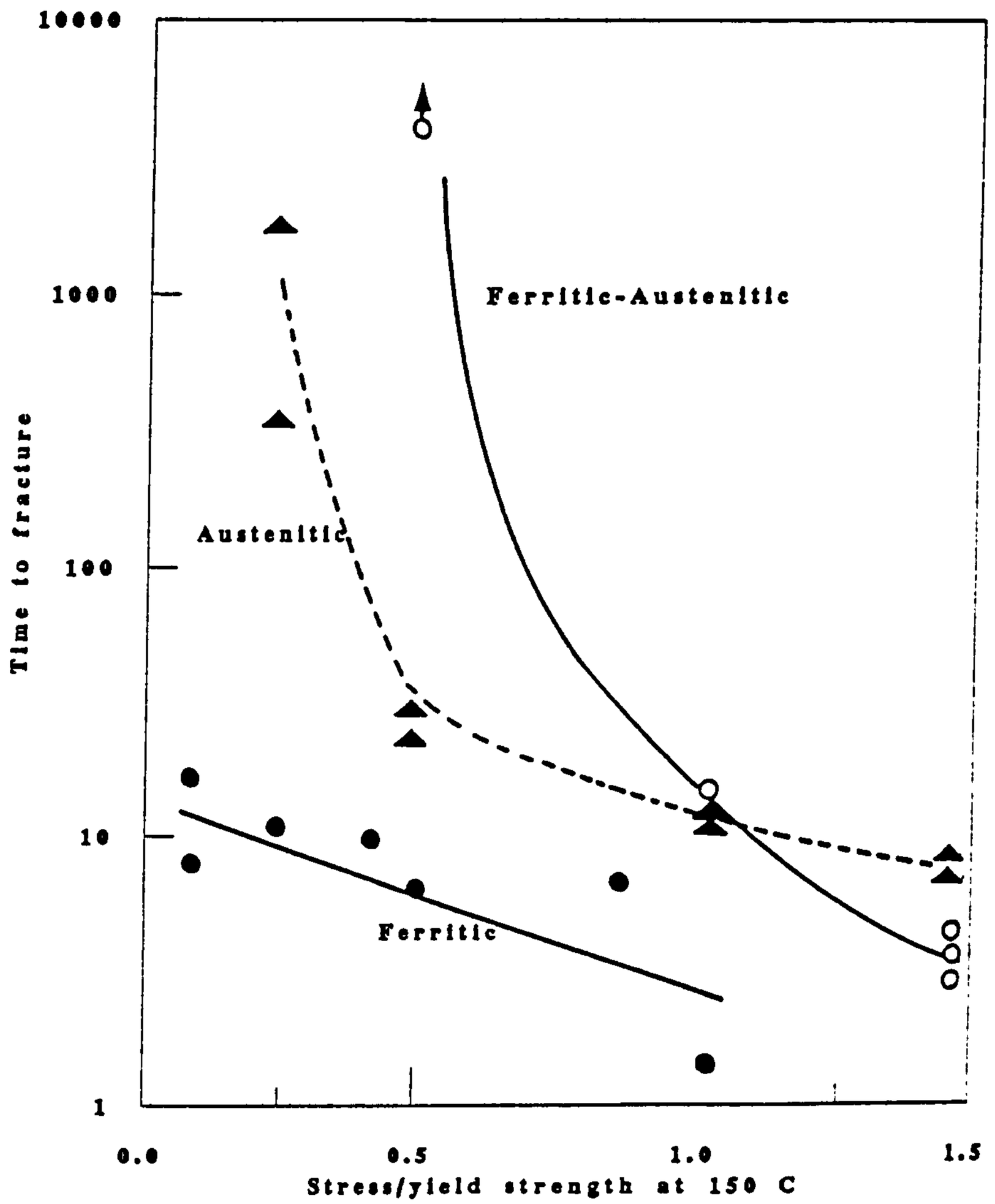

Figure 2.19 The performance of the duplex alloy 21%Cr-8%Ni-2%Mo-0.5%Cu and of alloys with comparable composition to its austenite and ferrite phases.
Constant load tests in 44% $MgCl_2$ solution (153°C).

2.2.6 Sulphide stress corrosion cracking

Sulphide stress corrosion cracking (sscc) has long been recognised as a serious problem for the petroleum and petrochemical industries, particularly in high strength and stainless steels /113-118/. In recent years the rising energy demand, increasing oil and gas prices, and dwindling reserves have led to the development of deeper oil and gas wells (often > 6000 m). The environments often encountered in such deep wells contain substantial amounts of salt water, hydrogen sulfide, and carbon dioxide (sour wells). This hostile environment, depending upon its composition and temperature, may cause general corrosion, localized corrosion, and stress corrosion cracking of the material used. One way of combating these problems is to inject inhibiting agents, but it was soon realized that these were not wholly effective and were economically ill suited. Another solution relied on the use of highly alloyed materials that can withstand the corrosiveness of the well fluids. Among the various special materials that can be utilized in such hostile environments, duplex stainless steels represent an optimum technical-economic choice.

When H_2S is present in aqueous solution, it dissociates to form a weak acid according to the reactions :

$$H_2S \rightleftharpoons HS^- + H^+ \qquad 2.13$$

$$H_2S \rightleftharpoons 2H^+ + S^{--} \qquad 2.14$$

Corrosion reaction takes place between these ions and iron alloys resulting in the formation of ferrous ion Fe^{++} at the

anodic sites, according to the anodic reaction :

$$Fe \rightarrow Fe^{++} + 2e^{-} \qquad 2.15$$

Meanwhile at the cathodic sites on the surface of the steel, the hydrogen ion is reduced to atomic hydrogen according to the cathodic reaction:

$$2H^{+} + 2e^{-} \rightarrow 2H \qquad 2.16$$

$$2H \rightleftharpoons H_2 \qquad 2.17$$

Thus the overall reaction can be represented as :

$$Fe + H_2S(aq) \rightarrow FeS + 2H \qquad 2.18$$

The recombination of atomic hydrogen is inhibited by the presence of the dissociated hydrogen sulphide, which results in a greater hydrogen fugacity and therefore facilitates penetration of hydrogen into the steel, hence intensifying the embrittlement.

Many variables are known to influence sscc of iron base alloys and these may be classified into two broad categories :

i) Environmental variables that include hydrogen sulphide concentration (pressure), chloride concentration, temperature and applied potential.

ii) Mechanical and metallurgical variables such as alloy composition, microstructure, heat treatment, cold work, hardness or strength level, and surface condition.

Many investigations have shown that hydrogen induced cracking (HIC) of metals increases with increasing hydrogen sulphide concentration of the environment. Ikeda et al /119/ tested line pipe steels to study the effect of hydrogen sulphide concentration in synthetic seawater by long term exposure of 1 year. Ultrasonic examination revealed that all of the steels tested suffered from HIC in saturated solution (3000 ppm H_2S), whereas only one exhibited HIC as the H_2S concentration is lowered to 1000 ppm and no cracking was observed at 100 ppm H_2S. They concluded that the critical H_2S partial pressure to induce cracking lies between 0.06 and 0.35 atmosphere. Similar findings were reported by many others but the minimum reported hydrogen sulphide concentration for cracking varied significantly. Some of these variations can be due to differences in experimental technique and conditions.

pH also influences the susceptibility of steels in hydrogen sulphide environment. Treseder and Swanson /115/ reported a remarkable increase in the cracking susceptibility of a high strength steel wire by lowering the pH from 5 to 3 (Figure 2.20). Ikeda /119/ tested pipe line steels in four different solutions with pH values (adjusted by the addition of acetic acid) ranging from 3.0 to 5.4 and they found that the corrosion rate and the hydrogen absorption increased consistently with decreasing pH. Other workers also have found similar trends and it appears that, over the pH range

from 1 to 6, HIC tends to increase with decreasing pH, although the magnitude of the effect can vary with the type of steel.

It is generally agreed that HIC in steels is most severe near room temperature with significant recovery both below and above. Townsend /120/ investigated temperature effects on the susceptibility of high strength wire to HIC in acified 3% NaCl solution saturated with H_2S and found a maximum tendency to cracking near 25°C (Figure 2.21). The cracking tendency was slightly reduced at sub-ambient temperatures (4°C), but was considerably reduced at temperatures around 80°C, and many specimens had not cracked at the end of the test period.

Onoyama et al /60/ investigated the behavior of 25% Cr-7%Ni-3%Mo duplex stainless steel, using both spring loading and slow strain rate tests, in order to clarify the effect of some of these factors. He concluded that an optimum alloy composition of 25%Cr-7%Ni-3%Mo-0.15%N-0.05%Sn provides excellent corrosion resistance in a sour environment and observed that sscc occurs most severely at a strain rate of 3.0×10^{-6}/s and a temperature of about 80°C; the susceptibility decreases at higher and lower temperatures (Figure 2.22). This he attributed to the aggressiveness of the Cl ion at lower temperatures and the decrease in H_2S solubility at the higher temperature. He also reported an increased cracking trend as the H_2S pressure increased, as might be expected. The cracking was attributed to scc via pit formation and involved dissolution of the austenite and cracking of the ferrite phase. Ordsson and Bernhardsson

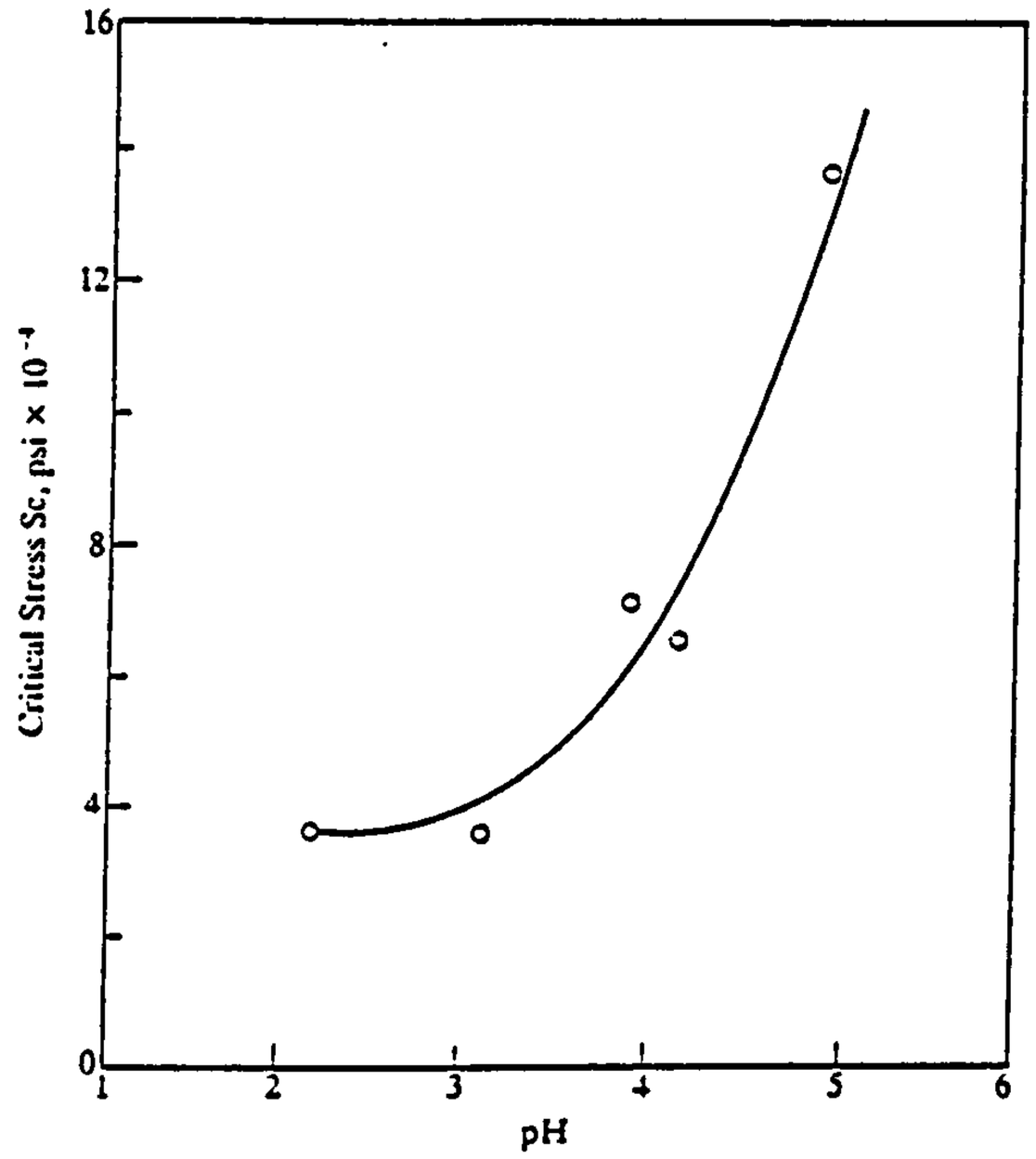

Figure 2.20 Effect of pH On sulphide stress corrosion cracking /115/.

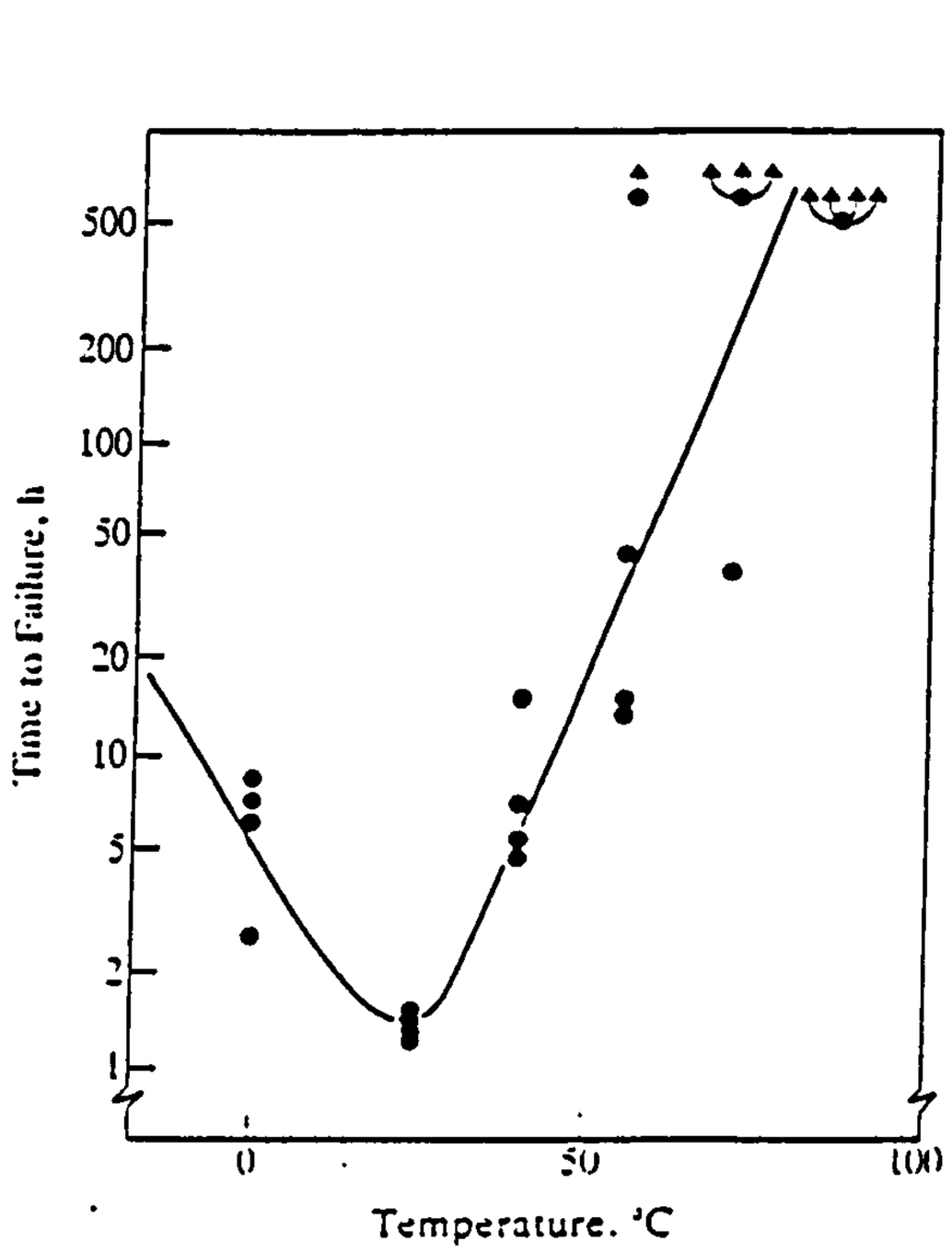

Figure 2.21 Effect of test temperature on the time to failure of bent wire freely corroding in H_2S solution /120/.

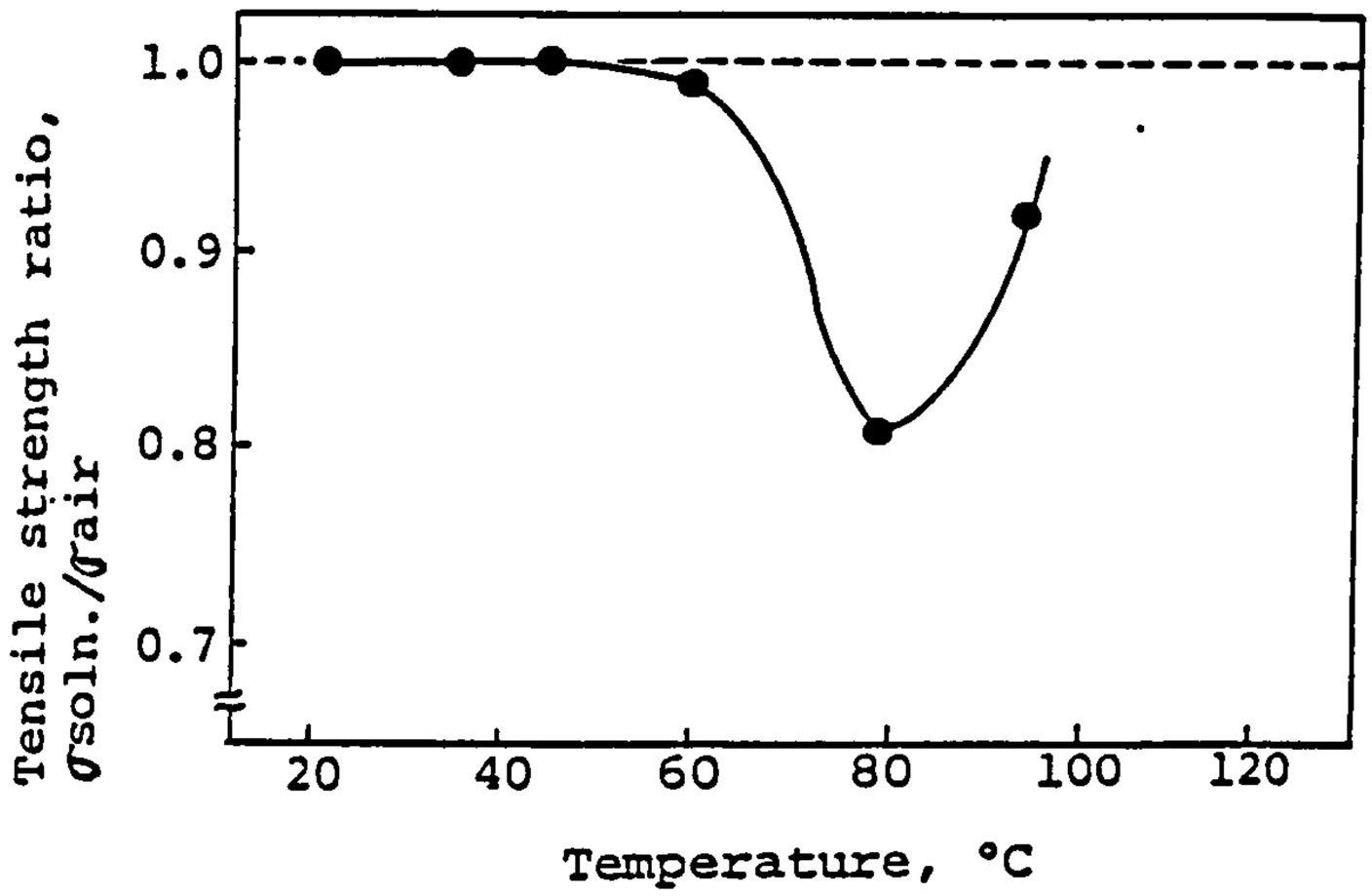

Figure 2.22 Effect of test temperature on scc susceptibility of solution treated duplex stainless steel in slow strain rate tests /60/.

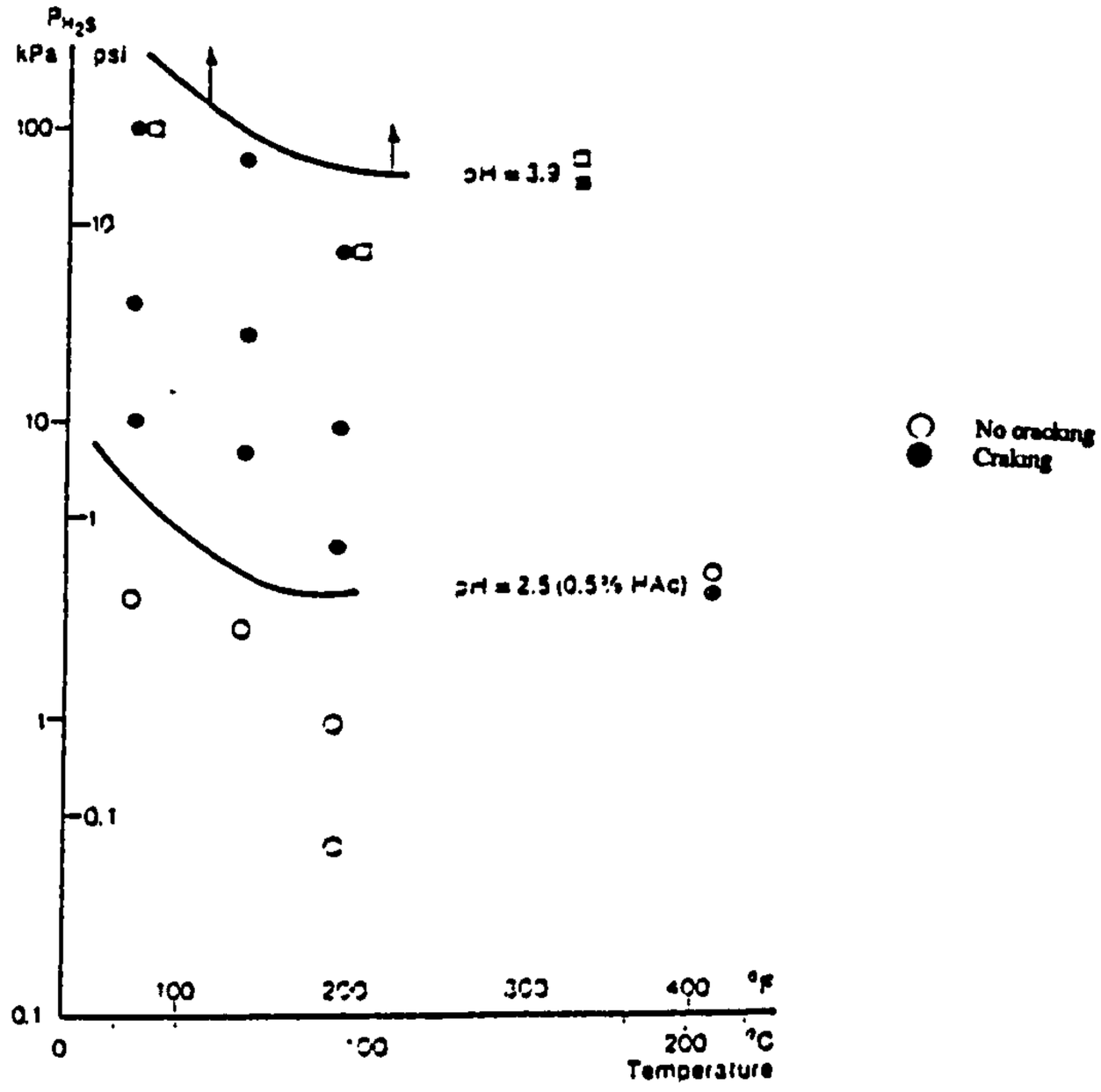

Figure 2.23 Atmospheric pressure scc tests of 17%CW tube of SAF 2205 in 5% NaCl at different pH values, H_2S partial pressure, and test temperatures up to 90°C. Stress = $R_{0.2}$ at test temperature. Testing time = 500h /121/.

/121/ investigated the 2205 duplex alloy in NACE and other $H_2S/Cl^-/CO_2$ environments at various loads and reported a decrease in the σ_{th}/σ_y ratio (where σ_{th} is the threshold and σ_y the yield stress) for cold worked specimens with a critical threshold stress at room temperature of $1.1\sigma_y$. They reported that the pH value of the solution has the strongest influence on the scc resistance, expressed in terms of the critical H_2S partial pressure (Figure 2.23). The maximum acceptable H_2S pressure increased more than 10 times with an increase of the pH from 2.5 to 3.9. They also found that a higher H_2S pressure is needed to cause embrittlement at higher temperature. This result could be an indication that hydrogen embrittlement plays a significant role in the scc process.

Kudo et al /111/ investigated 25%Cr-7%Ni-3%Mo duplex steel, in modified NACE solution (20% NaCl saturated with hydrogen sulphide), using four different loading methods (constant strain, constant load, SSRT, DCB). The maximum cracking susceptibility, was reported around 100°C and was independent of the test method. The explanation that was offered for the decrease in the scc susceptibility at the higher temperature was the formation of a protective chromium oxide film. The cracking was attributed to active dissolution rather than hydrogen embrittlement, as failure was inhibited by cathodic polarization and accelerated by anodic polarization. (Figure 2.24). In constant strain rate tests, he observed that cracks propagated through the ferrite and were arrested by the austenite phase. He also showed that a much higher applied stress is needed to cause cracking at temperatures higher than 100°C (Figure 2.25).

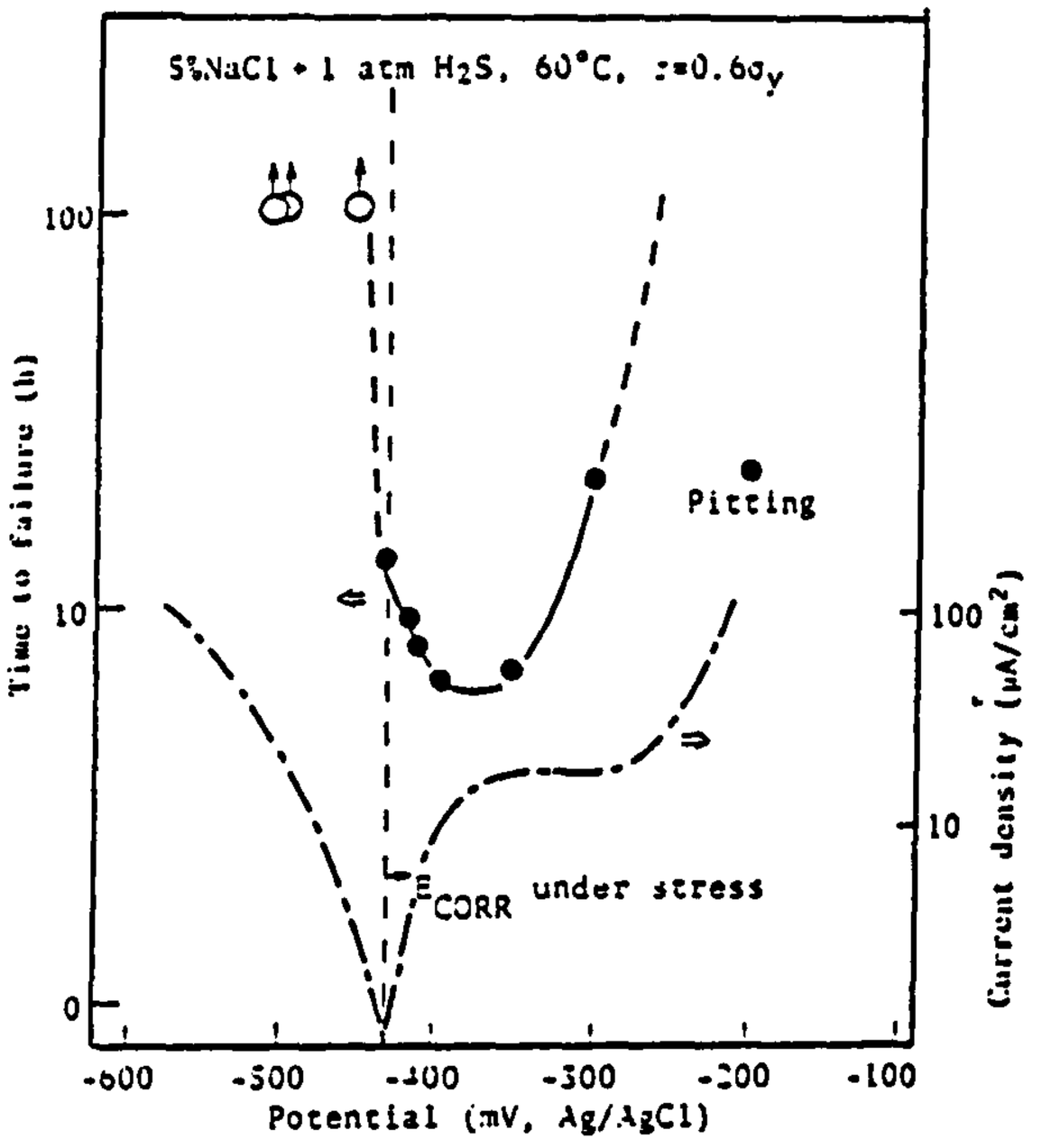

Figure 2.24 Effect of potential on time to failure of 25%Cr duplex stainless steel (30% cw) in constant load testing in 5%NaCl solution with 1 atm H_2S at 60°C /111/.

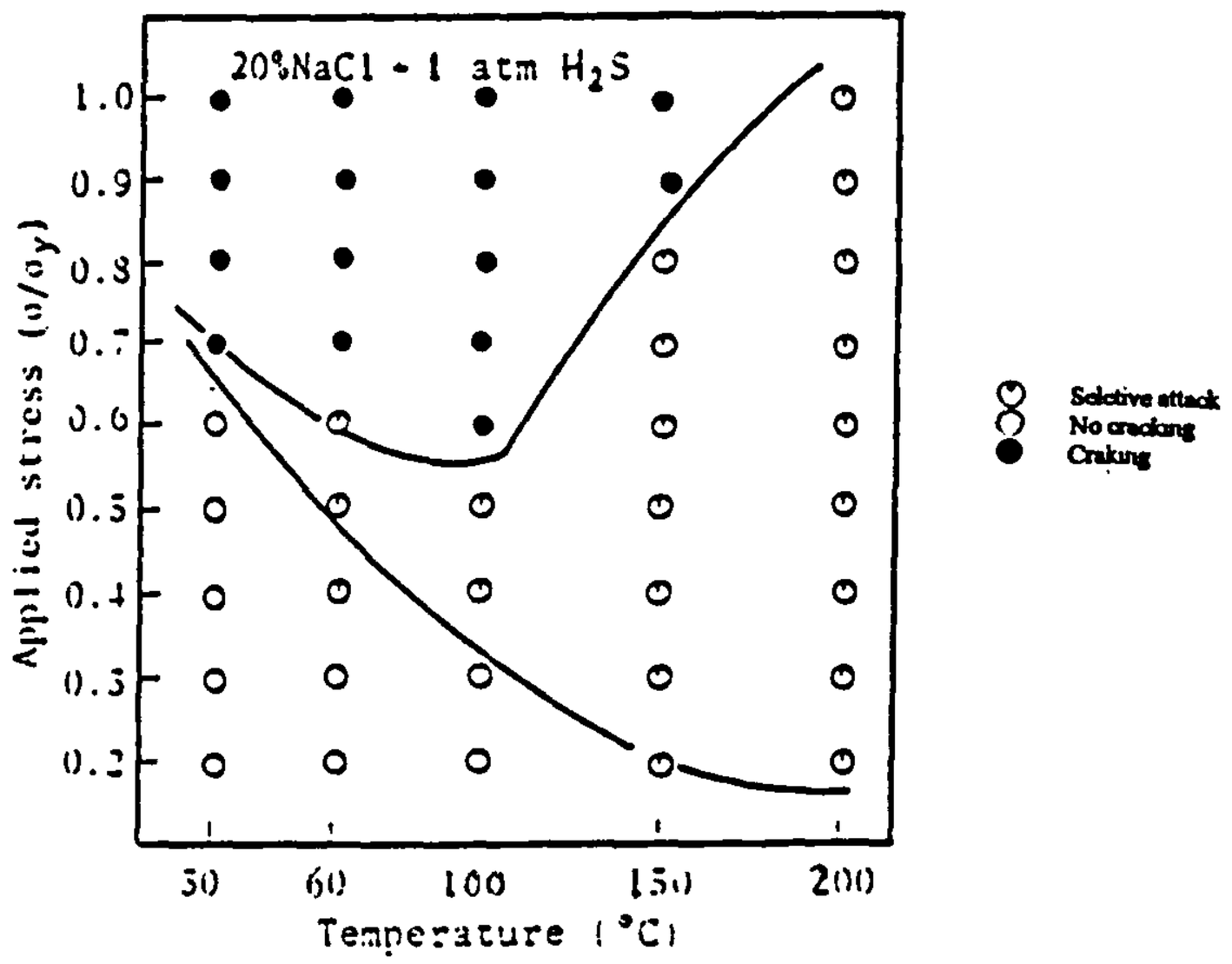

Figure 2.25 Scc test results for 25%Cr duplex stainless steel (30%cw) from four point bend tests in 20% NaCl solution saturated with 1 atm H_2S for 336 hr /111/.

This may be attributable to the softening of the alloy that occurs at higher temperatures.

2.3 Hydrogen embrittlement

2.3.1 Introduction

The damaging effect of hydrogen has long been recognised in ferrous materials and subsequently in many other metals and alloys. The classical example is the hydrogen embrittlement of high strength martensitic steel as a result of hydrogen concentration build up during production processes such as pickling, electroplating and cleaning. With time this hydrogen will form blisters and cracks at internal interphases such as grain boundaries, inclusions and second phase particles that will eventually lead to failure. This form of damage was first recognized by Johnson in 1875 /3/ when he noted the loss of ductility of iron after immersion in acids for a few minutes. Since this pioneering observation, hydrogen effects on metals have become one of the most investigated problems in the metallurgical engineering field.

Depending on the source and the location of hydrogen, hydrogen embrittlement can be classified into three different types /122/:

2.3.1.1 Internal (reversible) hydrogen embrittlement (IHE)

This type of embrittlement is caused by hydrogen located within the bulk of the alloy that has been charged with hydrogen prior to the application of the load.

Moreover, aging of the alloy at room temperature fully restores the ductility providing that the internal hydrogen has not caused microcracks nor chemically reacted with itself or with other elements within the bulk of the alloy (e.g. forming hydrogen molecules, methane gas or metal hydride).

2.3.1.2 Hydrogen environment embrittlement (HEE)

This occurs when a hydrogen-free alloy is mechanically strained in gaseous hydrogen or in hydrogen-containing environments such as corrosive environments (i.e. hydrogen sulphide). Hydrogen has to be delivered by some means (i.e. diffusion or dislocation sweeping) to a critical location within the metal for the embrittlement to occur.

2.3.1.3 Hydrogen reaction embrittlement (HRE)

Although the source of hydrogen can be either external or internal, the main difference is that once the hydrogen is absorbed into the metal it reacts chemically in three distinct ways:

a) Hydrogen atoms combine with one another to form molecular hydrogen H_2 which is frequently encountered in metal processing and welding in the form of "flaking" or "fish eye" characteristics on the fracture surface.

b) Hydrogen reacting with a foreign element in the matrix to form a gas, i.e. the reaction with carbon in low alloy steel to form methane gas (CH_4) bubbles.

c) Hydrogen reaction with the matrix atom to form a brittle hydrogen-rich phase. This form of chemical reaction occurs

when the hydrogen solubility limit is exceeded leading to the precipitation of metal hydride (i.e. zirconium and titanium hydrides).

2.3.2 The process of hydrogen embrittlement

The term hydrogen embrittlement does not describe a single process of degradation or a specific change in the behaviour of an engineering alloy. Rather, it is more generic and describes a group of related phenomena, all involving hydrogen and all resulting in some change in the mechanical behaviour of the alloy.

The exact process involved in hydrogen embrittlement of an alloy will reflect: (i) the origin or the source of hydrogen (the beginning of the process), (ii) the observed change in the behavior of the alloy (the end of the process), and (iii) the required hydrogen transport reaction and the hydrogen-metal interaction mechanisms (the path required to get from the beginning to the end of the process).

2.3.2.1 The entry of hydrogen into metals

Hydrogen, the smallest atom of all elements, can readily penetrate metals when their surfaces are in suitable conditions. Hydrogen can be introduced into metals from many environments and among these are:

(i) gaseous hydrogen atmosphere at ambient temperature,

(ii) a high pressure hydrogen atmosphere at high temperature (thermal charging),

(iii) an acidic corrosion process (i.e. hydrogen sulphide solution),

(iv) cathodic polarization in neutral and acidic aqueous solutions.

Experience has shown that hydrogen does not dissolve into metals in the form of molecules but as atoms. In all of the environments mentioned above molecular hydrogen must be adsorbed on the surface and dissociate before it can enter into the metal. In gaseous hydrogen,(i), straining is usually necessary to provide means of fast transport into the metal since lattice diffusion of hydrogen in metals at ambient temperature is relatively slow. The penetration distance during straining is usually small. On the other hand in thermal charging(ii), due to the fast hydrogen diffusion at higher temperatures, a high uniform concentration across the specimen cross section is produced without the need for simultaneous straining.

The charging pressure and temperature control the amount of hydrogen that can be dissolved into the material, and according to Sieverts /123/:

$$C_s = C_o P_H^{1/2} \exp \frac{-Hs}{RT} \qquad 2.19$$

Where C_s is the equilibrium concentration of hydrogen in the metal, C_o the solubility constant, P_H the external hydrogen pressure, H_s the heat of solution, R the gas constant, and T the absolute temperature. Therefore, at a specific charging temperature, the pressure dictates the concentration of hydrogen in the specimen (i.e. the equilibrium solubility).

During aqueous corrosion in acids, (iii), hydrogen is produced, at cathodic sites, by the cathodic partial

reaction of the corrosion process. The amount, and hence the fugacity, of the hydrogen produced depend upon the pH of the solution. The lower the pH the higher hydrogen pick up by the corroding metal providing that it does not passivate. In cathodic charging, (iv), however, the metal is made the cathode in acidic aqueous solution. Under the application of an appropriate cathodic potential, hydrogen ions are attracted to the metal surface, where they pick up electrons. Depending upon many factors, these hydrogen atoms may become adsorbed by the metals or recombine to form molecules and bubble off. The latter reaction can be suppressed by the addition of hydrogen ion recombination poison (i.e. cyanide, sulphur,...) to the electrolyte, which increases the adsorbed hydrogen atom coverage on the metal surface and hence the amount of hydrogen entering the lattice. During cathodic charging, hydrogen is available at the metal surface at very high fugacities; values of 10^8 atmosphere have been reported /124/. Cathodic charging of austenitic stainless steels produces a high concentration of hydrogen near the surface layer and a steep gradient, which is known to result in extensive surface cracking and phase transformation /93,125-128/.

Since duplex stainless steels contain equal amounts of ferrite and austenite and the ferrite matrix has high hydrogen diffusivity and low solubility while the austenite has low hydrogen diffusivity and high solubility, it is expected that the response of these materials to hydrogen would be more complicated than that of either the fully austenitic or the fully ferritic stainless steels. Rhode et al /129/ have studied the diffusivity of hydrogen in duplex stainless steel and quoted a value 0.7×10^{-14} m^2/s in the

longitudinal specimens and 1.4×10^{-14} m^2/s in the transverse specimens. Perng and Altstettter /130/ studied hydrogen diffusivity in ferritic 29/4/2 and austenitic 304 stainless steels, which have similar composition to the two phases in duplex stainless steels, and developed the following equations:

$$D\alpha = 8.45 \times 10^{-6} \exp \frac{-33.7\ (KJ/mol)}{RT}\ m^2/s \qquad T < 170\,^{\circ}C \qquad 2.20$$

$$D\alpha = 6.40 \times 10^{-9} \exp \frac{-7.0\ (KJ/mol)}{RT}\ m^2/s \qquad T > 170\,^{\circ}C \qquad 2.21$$

$$D_{\gamma} = 7.69 \times 10^{-7} \exp \frac{-53.3\ (KJ/mol)}{RT}\ m^2/s \qquad 2.22$$

They concluded that the hydrogen diffusivity in ferritic 29/4/2 stainless steel at temperatures above 170°C is 10 to 20 times lower than that for pure α-iron and this was attributed to the extensive alloying in the 29/4/2 steel.

2.3.2.2 Source of hydrogen

Hydrogen can be available either externally (in contact with the external surface) or internally within the bulk of the alloy. Externally it can exist as a molecule, dissociated molecule, or atom, or a component of a complex molecule such as hydrogen sulphide, water or methane. Internally, however, it has been established that hydrogen exists as a dissociated atom /131/. Oriani reaffirmed that the exact nature of the dissolved hydrogen is that of a "screened" proton within the electron sea of the metal lattice. This equilibrium exists in the form:

$$H \leftrightarrows H^{+} + e^{-} \qquad 2.23$$

When hydrogen is dissolved into a metal, it occupies well-defined interstitial sites that have been identified by neutron diffraction measurements. In bcc transition metals hydrogen occupies the tetrahedral sites and in fcc transition metals it occupies the octahedral sites (Figure 2.26).

The exact location of hydrogen and its form are of primary importance to the overall embrittlement process in that they establish the starting point for the transport mechanism required to deliver the hydrogen to the critical location where the degradation reaction occurs. An excellent example of the importance of the origin of hydrogen is the slow crack growth behavior observed by Nelson /132/ in high strength steel exposed to different hydrogen-containing environments, namely, i) high-purity molecular hydrogen, ii)high-purity hydrogen sulphide, and iii) dissociated or atomic hydrogen. The observed hydrogen-induced slow crack growth rates in these three environments, under identical conditions (i.e. applied stress intensity, temperature, and gas phase pressure), revealed that in both hydrogen sulphide and dissociated hydrogen environments the slow crack growth rates are several orders of magnitude higher than that observed in a molecular hydrogen environment. The difference in the observed severity of the embrittlement is the influence of the original form of hydrogen in determining the required hydrogen transport process. In other words, in both atomic hydrogen and hydrogen sulphide environments the overall rates of hydrogen transport are similar and controlled by similar transport steps while in the molecular hydrogen environment the transport process is complicated perhaps by the fact

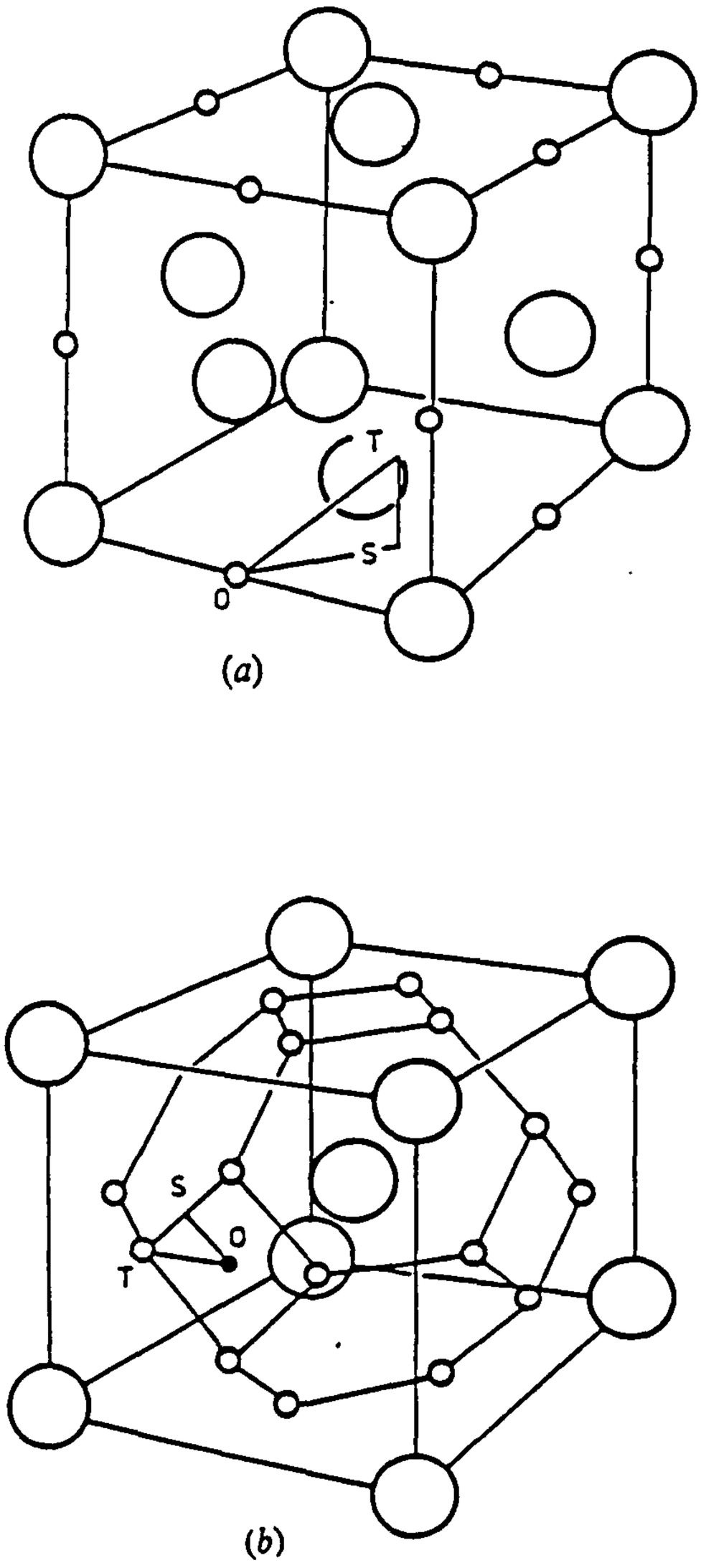

Figure 2.26 Interstitial sites occupied by hydrogen in a) fcc metals b) bcc metals /133/.

that molecular hydrogen has to dissociate to atomic hydrogen before it can enter the metal and complete the transport process to the critical site.

2.3.2.3 The transport of hydrogen

The transport of hydrogen from its source to the critical location within the bulk of the alloy where degradation can occur is probably the most complex aspect of the embritllement. It can involve a large number of reaction steps (Figure 2.27), and under certain conditions any one of these reaction steps can be rate-determining /132/. A hydrogen molecule has to be adsorbed (step a-b) then dissociated (step b-c) before it can enter the metal lattice. Once it is inside the lattice, it can move about via two different ways: i) lattice diffusion, or ii) dislocation sweeping. In the lattice diffusion, hydrogen will move as an interstitial atom or as a shielded proton. At room temperature hydrogen occupies a specific interstitial site depending upon the metal structure. The elementary step of the diffusion process is a thermally-activated jump from one interstitial site to another. These jumps can be executed by tunnelling from one site to the next or by jumping over the potential barrier. In the first case, thermal activation is necessary to bring the energy level of both sites to the same height, while in the second case a higher activation energy is necessary to overcome the potential (energy) barrier. At high temperatures, the interstitial will be mainly above the potential barrier and hydrogen diffuses as a dense gas or a liquid, and several collisions occur with the host atoms /134/.

Due to its small atomic radius, hydrogen is expected to have a much higher diffusivity in metals than all other

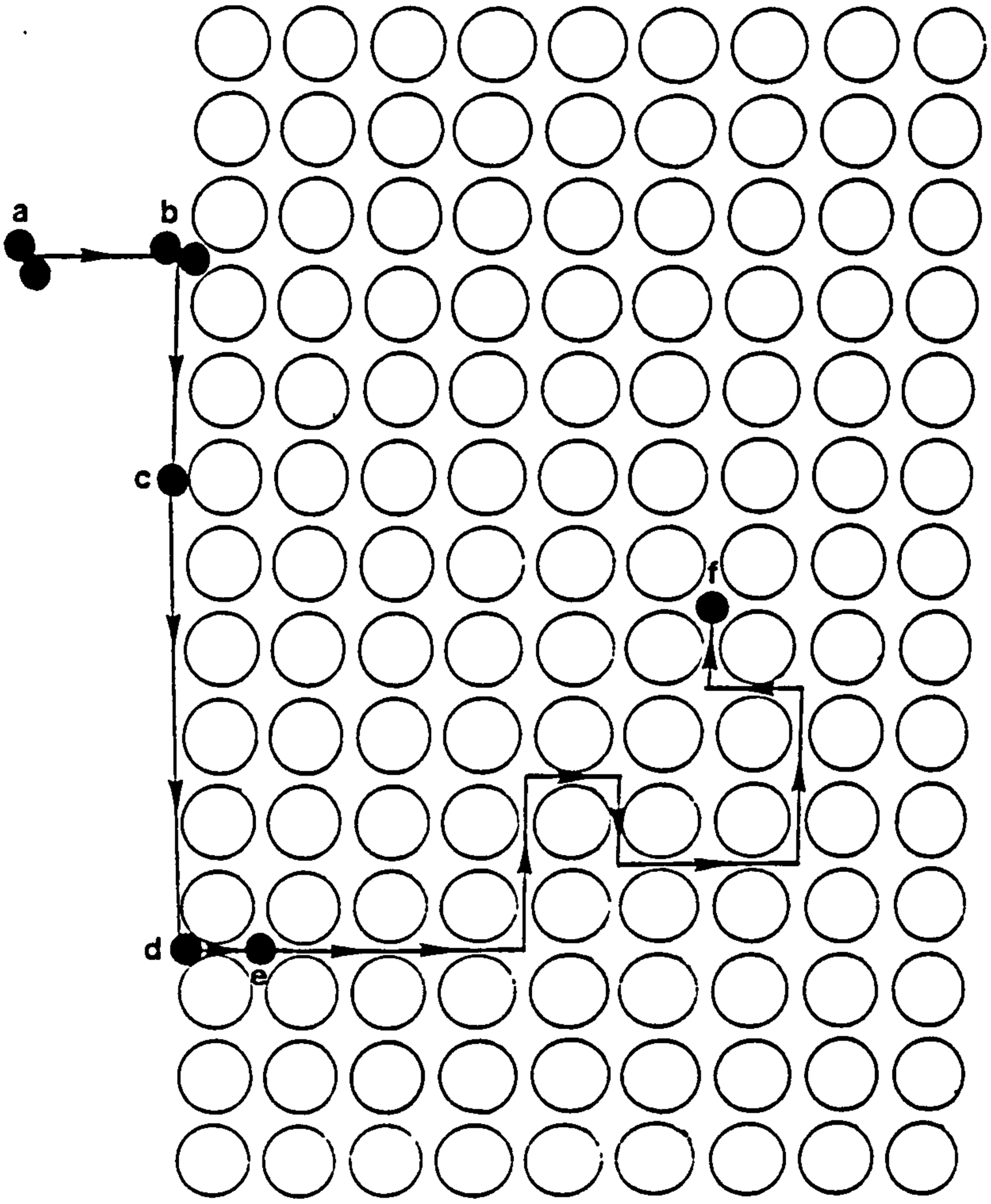

a→b gas-phase diffusion
b→c physisorption and dissociation
c→d adatom migration and chemisorption
d→e solution
e→f lattice diffusion

Figure 2.27 Schematic of possible reactions involved in the embrittlement of a structural alloy by an external molecular hydrogen environment /132/.

interstitial atoms. In fact, at room temperature its diffusivity is about 10^{12} times that of other intersitials such as carbon and nitrogen. The diffusivity of hydrogen in many metal systems has been measured experimentally over a wide temperature range /135/ and it has been established that, except at very low temperatures ≤ 50°K, the diffusion is a thermally-activated process and follows the Arrhenius law:

$$D = D_0 \exp\left(\frac{-\Delta E}{k\,T}\right) \qquad 2.24$$

For fcc transition metals, this law is obeyed with a single activation energy ΔE over the entire temperature range that has been examined (300-1000°K). In bcc transition metals, however, the diffusion is also thermally activated but there seem to be two temperature regimes: the activation energy at high temperature is typically twice that at low temperature. This suggests that in the former there is a single diffusion mechanism over the whole temperature range examined while in the second there are different mechanisms at high and low temperatures /133/. The diffusivity of hydrogen in bcc metals is much higher than that in fcc metals because of the more open lattice structure but it increase more rapidly with temperature because of the higher activation energy.

It is evident that the diffusivity of hydrogen in stainless steels is very low at room temperature /136/, and it has been suggested , in view of the embrittlement that is caused by a low pressure hydrogen atmosphere, that interstitial hydrogen may be transported by dislocations /137,138/. This concept is not new, since Cottrell /139/ proposed that interaction between interstitial carbon atoms

and dislocations can explain the appearance of yield point drops in certain steels. Cottrell's model is by no means limited to carbon atoms and there should be no convincing reason why hydrogen, the smallest of all interstitial atoms and hence the most mobile, can not also be transported by mobile dislocations. Bastien and Azou /140,141/ were the first to suggest that hydrogen transport in the form of "Cottrell atmospheres" (as a moving dislocation model) is consistent with experimental observation, particularly in the dependency of the embrittlement on strain rate and temperature. More recently, this subject has received more attention and direct evidence of hydrogen dislocation interaction has begun to emerge in many alloy systems. Kirkela and Latanision /142/ studied the permeability and diffusion of hydrogen in nickel while being plastically deformed by constant extension rate and found that the effective hydrogen diffusivity increased from 10^{-14} m^2/s in unstrained nickel to about $10^{-9}m^2/s$ during straining. Hwang et al /143/ investigated hydrogen transport by dislocations in an iron single crystal, using a permeation method, and attributed the increase in hydrogen flux, through the strained crystal, to hydrogen transport by screw dislocations. Frankel and Latanision /144,145/ studied the influence of plastic straining on the steady state flux of hydrogen in both a nickel single crystal and polycrystalline nickel using a permeation technique. They observed direct evidence for dislocation transport of hydrogen in the nickel single crystal. The hydrogen flux increased in the easy glide region of deformation even after accounting for the effect of a decrease in specimen thickness. In polycrystalline nickel they found that the hydrogen flux depends strongly on the strain rate. At fast strain rates

(1.0 x 10^{-4} /s) the hydrogen flux decreased with increasing strain. This decrease was attributed to the fact that dislocations are generated very quickly at fast strain rates and these newly-created dislocations act as traps and attract the hydrogen atoms in the lattice (dynamic traps). As these new traps are filled the lattice becomes depleted of hydrogen, causing a decrease in the hydrogen flux. At an intermediate strain rate (1.0 x 10^{-5}/s) similar observations were reported yet the decrease in the hydrogen flux was smaller than in the previous case. They explained that this was due to the decrease in the rate of creation of dislocation (dynamic traps), hence the lattice has a chance to become partially refilled with hydrogen from the charging surface. At the slowest strain rate employed (1.0 x 10^{-6} /s), however, an increase in the flux rate was reported and attributed to the fact that the rate of dynamic trap creation is slow enough that a complete refilling of the lattice with hydrogen occurs, and also to the combined effect of the increase in the input concentration of hydrogen, due to a more noble potential shift during deformation, and the decrease in the specimen thickness. They concluded that, in polycrystalline nickel, there was no evidence of dislocation transport of hydrogen /144/. However, they did observe direct evidence of dislocation transport in a nickel single crystal /145/. This discrepancy was rationalized to the fact that in thin single crystals dislocations can move throughout the entire thickness with little interaction from other dislocations, hence an increase in hydrogen flux is detected, while in polycrystalline nickel hydrogen transport by dislocations still occurs but the hydrogen is being dumped in a vast number of trap sites such as grain boundaries, voids, and second phases.

From the few previous paragraphs it is evident that hydrogen can be transported by dislocations in the form of a "Cottrell atmosphere", and when these dislocations encounter microstructural features such as grain boundaries, inclusions, microvoids, and second phases, the hydrogen is stripped off and dumped at these sites.

2.3.3 Mechanisms

Over the years, several mechanisms have been proposed to explain the embrittling effect of hydrogen, although no single universal mechanism can account for all the observed experimental results /146/. The currently popular accepted mechanisms fall into four main groups involving :

i) internal pressure generation,

ii) hydrogen/lattice-bond interaction,

*iii)*dislocation interaction, and

iv) hydride formation.

2.3.3.1 Internal pressure theory

The internal pressure theory is probably the oldest of those proposed for the hydrogen degradation of engineering alloys. It was first suggested by Zapffe and Sims /147/ to explain the embrittlement of cathodically charged steels. Subsequent modifications have been introduced by De Kazinczy /148/, Bilby and Hewitt /149/, and Tetelman and Robertson /150/. The basic idea is that the embrittlement is a result of the high pressure produced by formation of molecular hydrogen in voids or fissures. Atomic hydrogen in supersaturated solid solution is presumed to precipitate into voids, pre-existing or formed during plastic deformation, where they recombine to form molecular hydrogen and

build up a very substantial interior pressure. When the gas pressure at an internal interface reaches some critical value, i.e. the yield strength of the material, the void or crack will grow and this leads to premature failure. The value of the damaging pressure has to be maintained in order to cause further crack propagation, and since upon crack extension the pressure inside is lowered, due to the enlarged crack or void size, further propagation will cease until enough hydrogen is delivered to the crack. The restoration of the damaging pressure is achieved from the reserve of hydrogen atoms in the adjoining lattice, which exist under conditions of quasi-equilibrium:

$$C_H = K\ (p_{H_2})^{1/2} \qquad 2.25$$

where C_H is the concentration of hydrogen in the surrounding lattice, K is the solubility constant, and P_{H_2} is the pressure of hydrogen gas in the void.

If the material is subjected to external tensile stresses, both the rate of straining and the rate of hydrogen delivery to the crack are very important to explain the embrittlement of the material. If the rate of straining exceeds the rate of hydrogen pressure restoration then embrittlement will decrease. On the other hand, if the straining rate is slower than the pressure restoration rate the brittle crack will grow and the material is embrittled.

Temperature would be expected to have a similar effect on the embrittlement, since the rate of hydrogen delivery to the void or crack will increase substantially with increasing temperature and thus the rate of pressurisation increases and this should lead to much more severe

embrittlement. However, many investigations /140,141,151-157/ concerned with the effect of temperature have shown that, for given charging conditions and strain rate, as the temperature is raised the embrittlement first increases and then decreases with ductility passing through a minimum (Figure 2.28). While the low temperature portion of the curve lies within the scope of the internal pressure theory, the second portion, involving an increase of the ductility with temperature, is difficult to explain.

The greatest weakness of the internal pressure theory is its failure to explain the embrittlement observed in a low pressure gaseous hydrogen atmosphere, conditions under which the occurrence of significant internal hydrogen pressure would not be expected. However, Bastien and Azou /140,141/ have shown that hydrogen transported by dislocations and deposited (pumped) into traps can lead to significant pressurisation. Moreover, based on theoretical calculations, Tien /138/ claimed that voids can be pressurized to high pressures, even when the external hydrogen fugacity is low, if hydrogen is transported to dislocations faster than it escapes from them, but Hirth /158/ found that Tien had overestimated the arrival rate and underestimated the departure rate of hydrogen, which gives a gross overestimate of the amount of pressurisation. Substituting more realistic values, he concluded that large hydrogen fugacities at the surface (i.e. cathodic charging) lead to internal pressurisation but low external fugacities (i.e. hydrogen gas atmosphere) can not produce a large internal pressure in voids, and thus the internal pressure theory can not explain the observations.

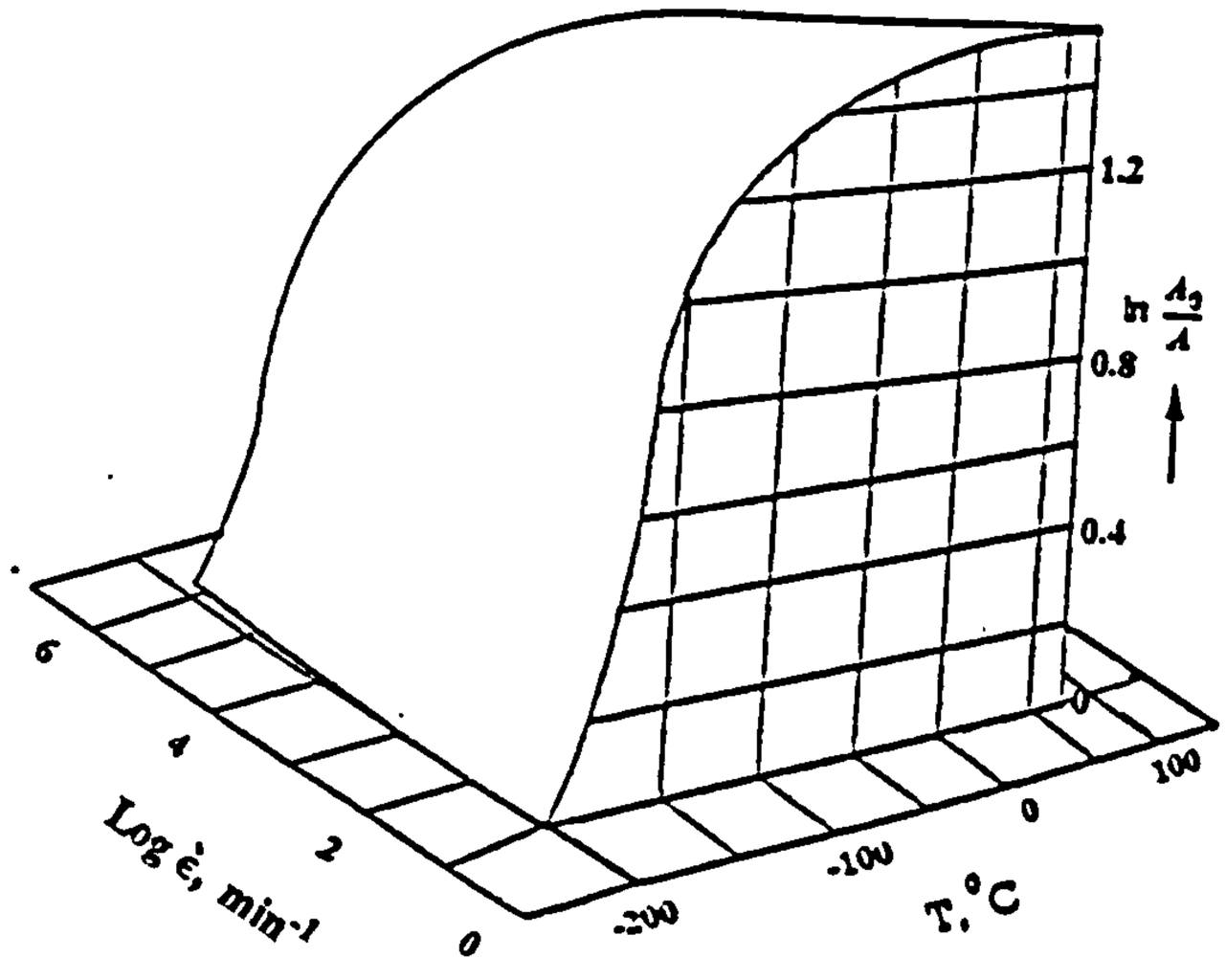

Not Charged

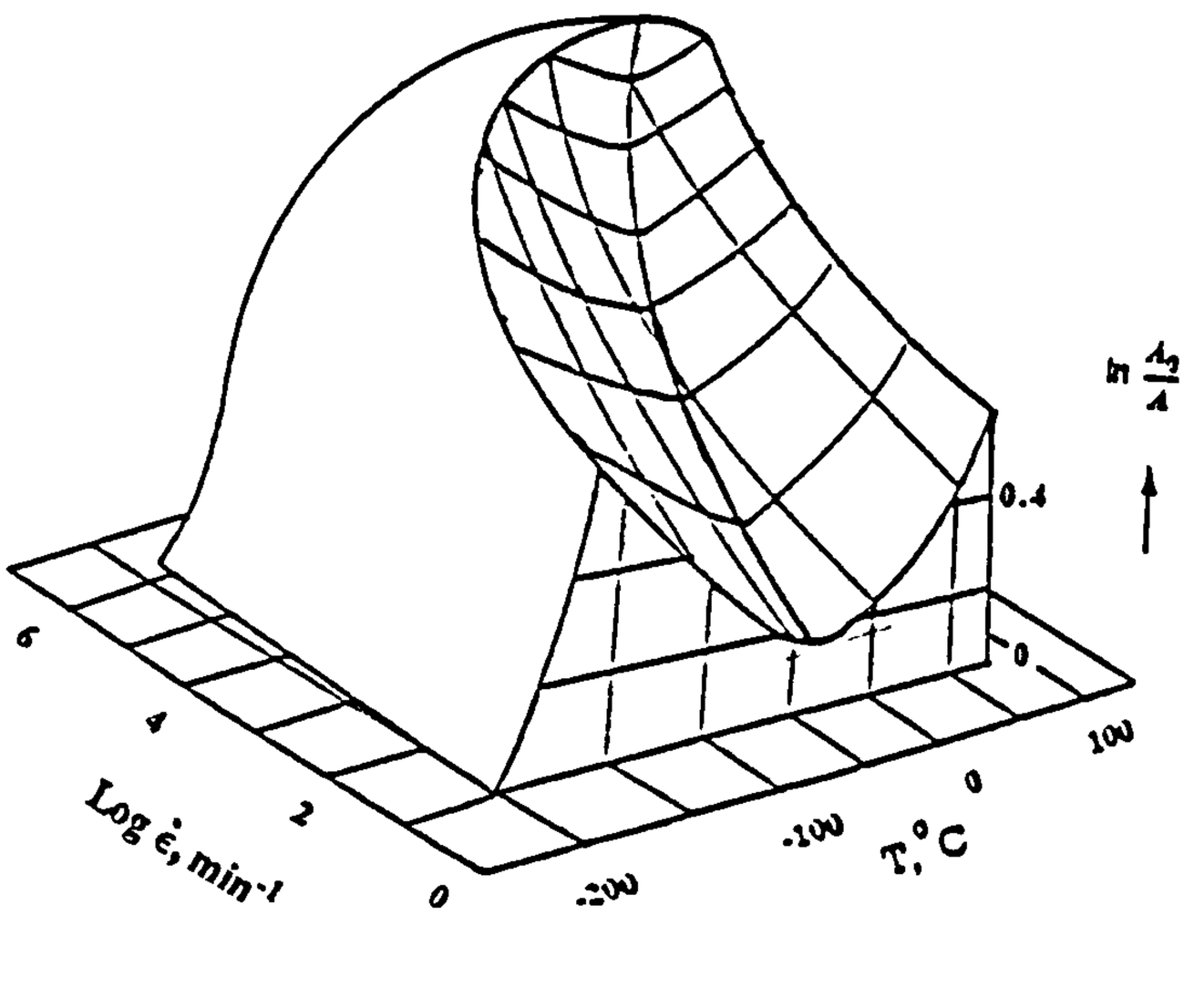

Charged

Figure 2.28 The effect of strain rate and temperature on the susceptibility of mild steel to hydrogen embrittlement /153/

2.3.3.2 Hydrogen / lattice bond interaction

The basic idea that hydrogen can influence the bond strength of a metal lattice was originally proposed by Petch and Stables /79,80/, who suggested that the adsorption of hydrogen to the metal surface lowers the surface energy of the crack, with a resultant lowering of the applied stress required for brittle crack propagation (Equation 2.12). This was dealt with in the embrittlement mechanism of stress corrosion (section 2.2.2.3)

There are at least two criticisms of this model. Firstly, in all but ideally brittle solids (glasses) significant amounts of plastic deformation occur, at least in the crack tip region of a growing crack, and the energy required to produce plastic deformation forms a significant proportion of the total energy in forming a crack. Therefore, any reduction in the surface energy would not produce significant reduction in the overall energy required to cause fracture. Secondly, this mechanism could not possibly explain the fact that oxygen, which has much greater heat of adsorption, fails to promote cracking; on the contrary, the pressure of oxygen has been shown to actually retard embrittlement by hydrogen, possibly by blocking hydrogen from the crack tip region. This was dealt with in the embrittlement mechanism of stress corrosion (section 2.2.2.3)

Troiano and his coworkers /84,159-162/ proposed embrittlement by another type of hydrogen/lattice-bond interaction, wherein hydrogen diffuses, under the influence of the stress gradient, to a region of high triaxial stress ahead of the crack tip (Figure 2.16-b), where it accumulates to a concentration much higher than the equilibrium concentra-

tion and weakens the cohesive strength of the lattice.

Oriani /85-87,131,163/ adopted these ideas to explain the embrittlement in gaseous hydrogen. He proposed that lowering of the chemical potential ahead of the crack tip, by the higher localized stresses together with accumulation of dissolved hydrogen, is sufficient to produce hydrogen concentrations (C_H) much larger than the equilibrium value, and acts to lower the maximum cohesive force, F, between the atoms. This reduces the maximum local tensile stress perpendicular to the plane of the crack σ_i needed to cause crack propagation:

$$\sigma_i = n F_m (C_H) \qquad 2.26$$

Where n is the number of atoms per unit area of the crystallographic plane, F_m maximum cohesive force and C_H is the local hydrogen concentration in terms of atoms/iron atom.

The observed discontinuous nature of the crack propagation in steels was attributed to an incubation period required for the arrival of a sufficient quantity of hydrogen to the region of triaxial stress in order to produce a further increment of crack growth.

The surface energy model and the decohesive model are very similar in the sense that both depict some sort of reduction in the stress or force needed to split the material along some crystallographic plane. Troiano /161/ postulated that, for transition metals, hydrogen atoms tend to loose their electrons upon dissolution into the metal and these electrons are thought to be taken up by the 3d electron band of the metal atom, so increasing the repulsive

forces between these atoms and lowering the work needed to split them apart.

2.3.3.3 Dislocation interaction theory

This mechanism is based on the idea that the association of hydrogen with a dislocation can change the mobility of the dislocation, which in turn will determine the extent and character of plasticity in the structural alloy and thus its fracture behavior. Observation of the influence of hydrogen on dislocations seems to support both hardening and softening effects, depending on the alloy system and experimental conditions /164/.

The idea that hydrogen will associate itself with a dislocation was first proposed by Bastien and Azou /140,141/, who suggested that hydrogen may be transported in the form of a "Cottrell atmosphere" on a moving dislocation. Many investigations since then have supported this transport phenomenon. Frank /165/ showed that hydrogen evolution from iron was enhanced by deformation. Donovan /166/ indicated that deformation enhances the release rate of tritium from charged Armco iron by a factor of about 4 and correlated the tritium release rate, for 304L stainless steel, with the position on the stress-strain curve (Figure 2.29) and in turn with the mobile dislocation density, providing strong confirmation of the Bastien-Azou suggestion. The large release of tritium at fracture can be attributed to the release of tritium from irreversible traps.

The concentration of hydrogen around the core of the dislocation, C_L can be estimated from the mean concentration of hydrogen in the lattice, C_H by the Boltzman equation:

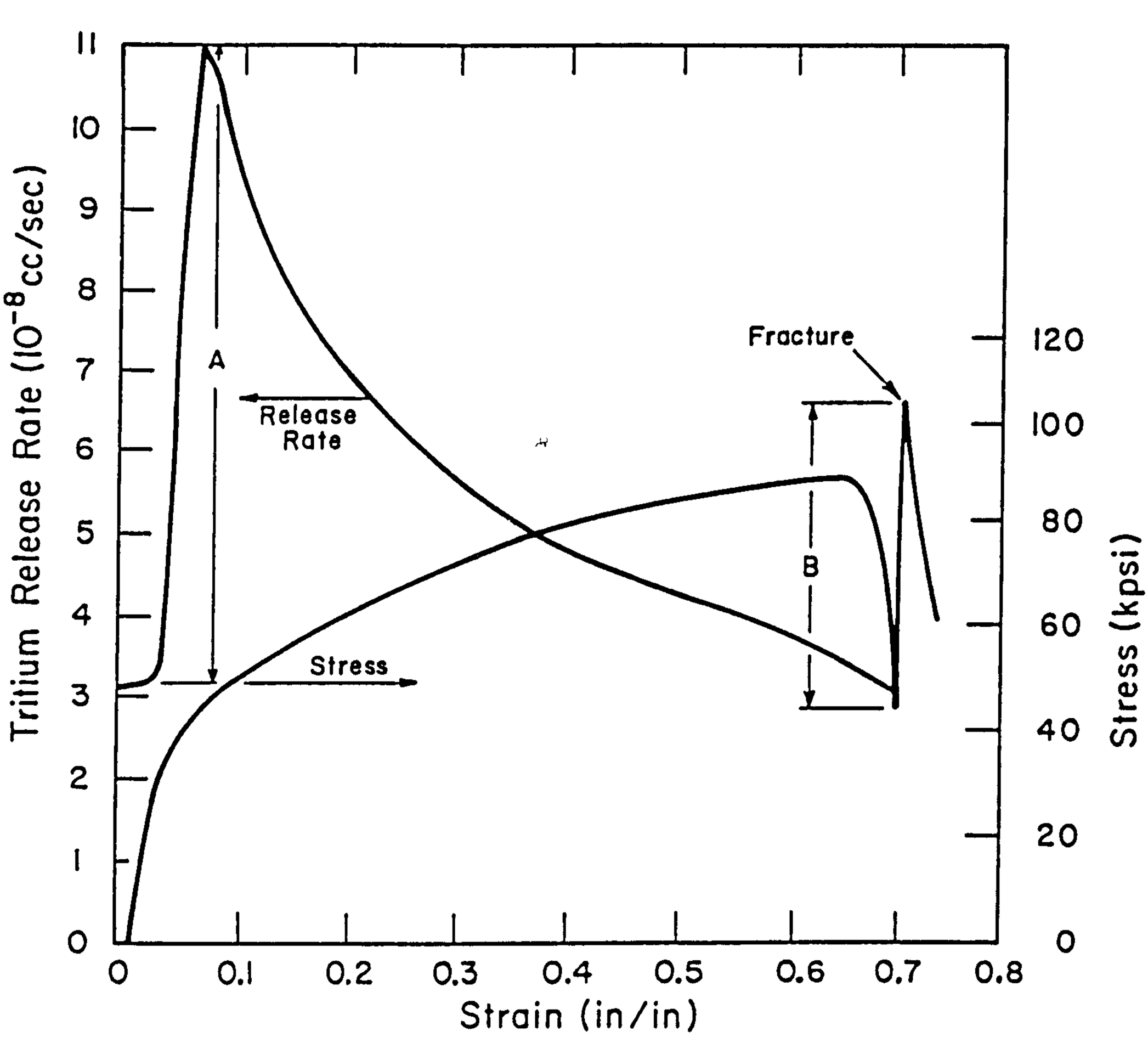

Figure 2.29 Stress·strain curve and tritium release rate as a function of stain in 304L stainless steel /166/.

$$C_{\perp} = C_{H} \exp\left(\frac{-E_b}{RT}\right) \qquad 2.27$$

Where:

E_b = the binding energy of hydrogen to the dislocation.

Louthan /167/ and Tien /138/ have shown through mathematical calculation that the concentration of hydrogen at the dislocation core, at room temperature, is quite large even when the lattice concentration is quite low. The velocity of dislocations also plays an important role in the transport process for hydrogen. Tien and coworkers /168/ have suggested that whenever the velocity of dislocations is less than a certain critical value, V_c , hydrogen will be transported by moving dislocations :

$$V_c = \frac{D_H E}{K T \ 30 \ b} \qquad 2.28$$

Where:

D_H = Is the diffusivity of hydrogen in the metal lattice,

$30b$ = The estimated effective trapping radius of the dislocation with Burgers vector b.

If the velocity of a dislocation exceeds this value, V_c, the dislocation will break away from the hydrogen and the transport mechanism will stop.

Although this mechanism provides a means by which hydrogen is transported to a particular critical location, it does not explain the resultant embrittlement.

2.3.3.4 Hydride formation

The embrittlement of structural alloys involving the precipitation of a hydride was first proposed by Westlake /169/. It is based on the hypothesis that, when a metal charged with hydrogen at a high temperature is cooled to a lower temperature, supersaturation is produced, which results in the precipitation of a hydrogen-rich phase or "metallic hydride". In general, these hydrides are less dense than the host metallic lattice and are very brittle. Hydride formation only occurs under equilibrium conditions in exothermic hydrogen occluders like zirconium and titanium and when such metals are strained, the metal matrix is essentially free from hydrogen and can deform plastically. The brittle fracture, if it should occur, will take place either through the hydride or along the brittle hydride/matrix interface. It is also proposed that the morphology and dispersion of the hydride is dependent on the rate of cooling and the stress state of the metal. Fine particles do not result in cracking but larger precipitation resulting from slow cooling can cause embrittlement. Since iron alloys are endothermic occluders of hydrogen that do not form hydrides, no further discussion of the hydride embrittlement is considered necessary.

2.3.4 Trapping of hydrogen in metals

Metals and engineering alloys are polycrystalline materials and contain a large variety of inhomogeneities, such as inclusions, second phases, grain boundaries and cracks or flaw. In addition, each crystal may contain many defects such as dislocations, vacancies, stacking faults and twin boundaries. Consequently, the stress situation throughout the matrix is not uniform, which may provide the driving

force to the movement and the accumulation of hydrogen at these sites. Therefore, all the defects mentioned above can serve as trapping sites for hydrogen. Trapping of hydrogen in this way can be divided into two categories depending upon their nature and characteristics, i.e. reversible or irreversible /170/ (Figure 2.30).

The trapping energies of these sites may differ, ranging from 0.1 - 1.34eV /171/, and therefore many of these traps can be reversible. That is to say, they will give up hydrogen to other traps that possess higher trapping energies, thereby acting as hydrogen sources. Among these, in α-iron are titanium atoms, dislocations, and low angle grain boundaries. On the other hand, other traps will be so strong that they will not release hydrogen, at the test conditions, i.e. temperature and stress. These are called irreversible traps or hydrogen sinks. Among these are high angle boundaries and titanium carbonitride particles.

The role of traps in hydrogen embrittlement mechanism can be demonstrated by the fact that embrittlement will occur only after a certain critical concentration of hydrogen is reached at the crack initiation site. Some of these traps can be a site of crack initiation, depending upon its capacity and the quantity of hydrogen delivered to it during the test. When this quantity reaches a critical concentration a crack may nucleate. Others, however, may not act as crack initiation sites and, on the contrary, may prevent hydrogen from reaching a potential flaw in sufficient amounts, especially when the hydrogen supply is restricted (i.e. external hydrogen atmosphere), thus preventing crack initiation Figure 2.30 (i). If hydrogen is available in substantial amounts within the material, i.e. precharged

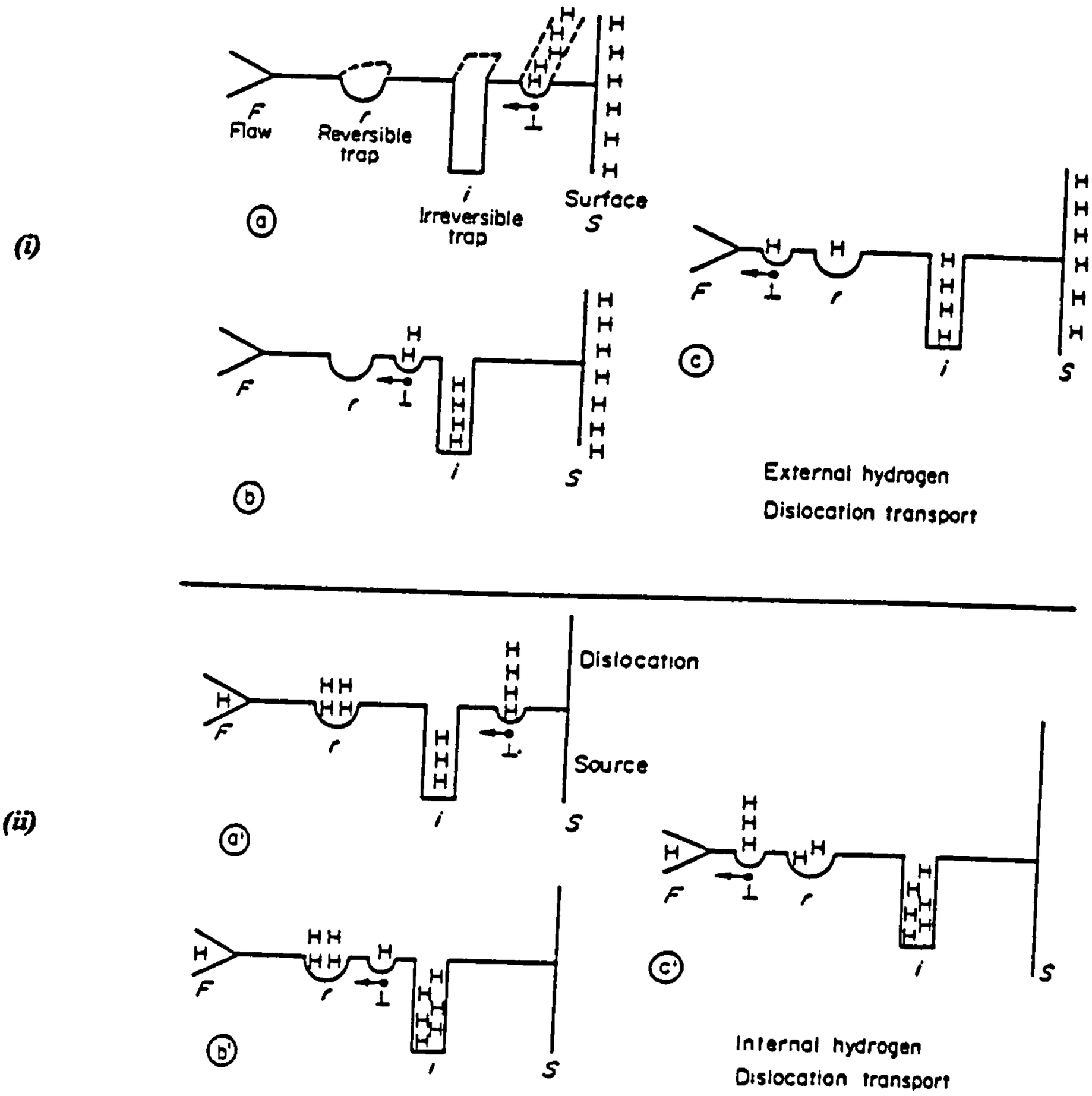

(i) External hydrogen atmosphere:
(a) Dislocation just nucleated at the surface has picked up hydrogen and moved toward a flaw. (b) On passing over an irreversible, trap, some hydrogen is lost by the dislocation. (c) Some more hydrogen is lost to the reversible trap , r. The flaw thus sees little hydrogen coming in.

(ii) Internal hydrogen (precharged material):
(a') Hydrogen is distributed on all trap sites when the dislocation begins to move. (b') Some hydrogen is lost on the irreversible trap. (c') Because of the preceding loss, the dislocation recharges itself at the reversible trap r. The flaw will see more hydrogen coming in than if there had been no reversible trap.

Figure 2.30 Schematic diagrams of the delivery and trapping of hydrogen in metals /170/.

material, a moving dislocation with its saturated hydrogen atmosphere will encounter both irreversible and reversible traps in its path. When it meets an irreversible trap, some of the hydrogen will be stripped off, but when it meets a reversible trap it will be recharged with hydrogen, hence a sufficient amount will be delivered to the flaw (Figure 2.30(ii)).

2.3.5 Distinction between SCC and hydrogen embrittlement

Over the years, many criteria have been proposed to distinguish between scc and hydrogen embrittlement. The susceptibility of an alloy to cracking under an anodic potential was considered characteristic of a material sensitive to scc. Conversely, the cracking of an alloy under cathodic potential was attributed to hydrogen embrittlement. Investigation of the effect of electrochemical polarization on the cracking of high strength steels in aqueous chloride solution has led to the proposal that two mechanisms may operate, namely active path corrosion APC (Figure 2.31 A), where the cathodic partial process (H^+ reduction) serves only as a means to consume the electrons generated by the anodic process, and hydrogen embrittlement (Figure 2.31 B), where the atomic hydrogen produced by the cathodic reaction is absorbed into the metal and causes embrittlement /172/. These viewpoints derived from the applied current densities/time to failure (T_f) characteristics, which are summarized in Figure 2.32. When application of anodic polarization decreases T_f and cathodic increases it the mechanism is said to be due to APC (Figure 2.32 C). If however the T_f is decreased by an applied cathodic current the mechanism is hydrogen embrittlement (Figure 2.32 B). Figures 2.32 A and 2.32 D are combination of both processes

in which cracking at the steady state corrosion potential (E_{corr}) is said to be APC and HE respectively.

Although Bhatt et al./173/ reported behaviour such as that shown in Figure 2.32 A in 13%Cr-martensitic steel in sodium chloride solution and attributed it to a dual mechanism, Truman /174/ and later Wilde /172/ convincingly demonstrated that HE is the operative mechanism in both potential regimes. The fractographic evidence showed that crack morphology at both potentials are similar. This should not be surprising since the potential and the pH at the crack tip vary significantly from that of the easily measured bulk conditions, where Brown et al. /76/ have shown that the pH of the crack tip in aqueous NaCl was 3.8 regardless of bulk pH. Hence even though hydrogen production should not occur at bulk solution conditions it may occur at the crack tip.

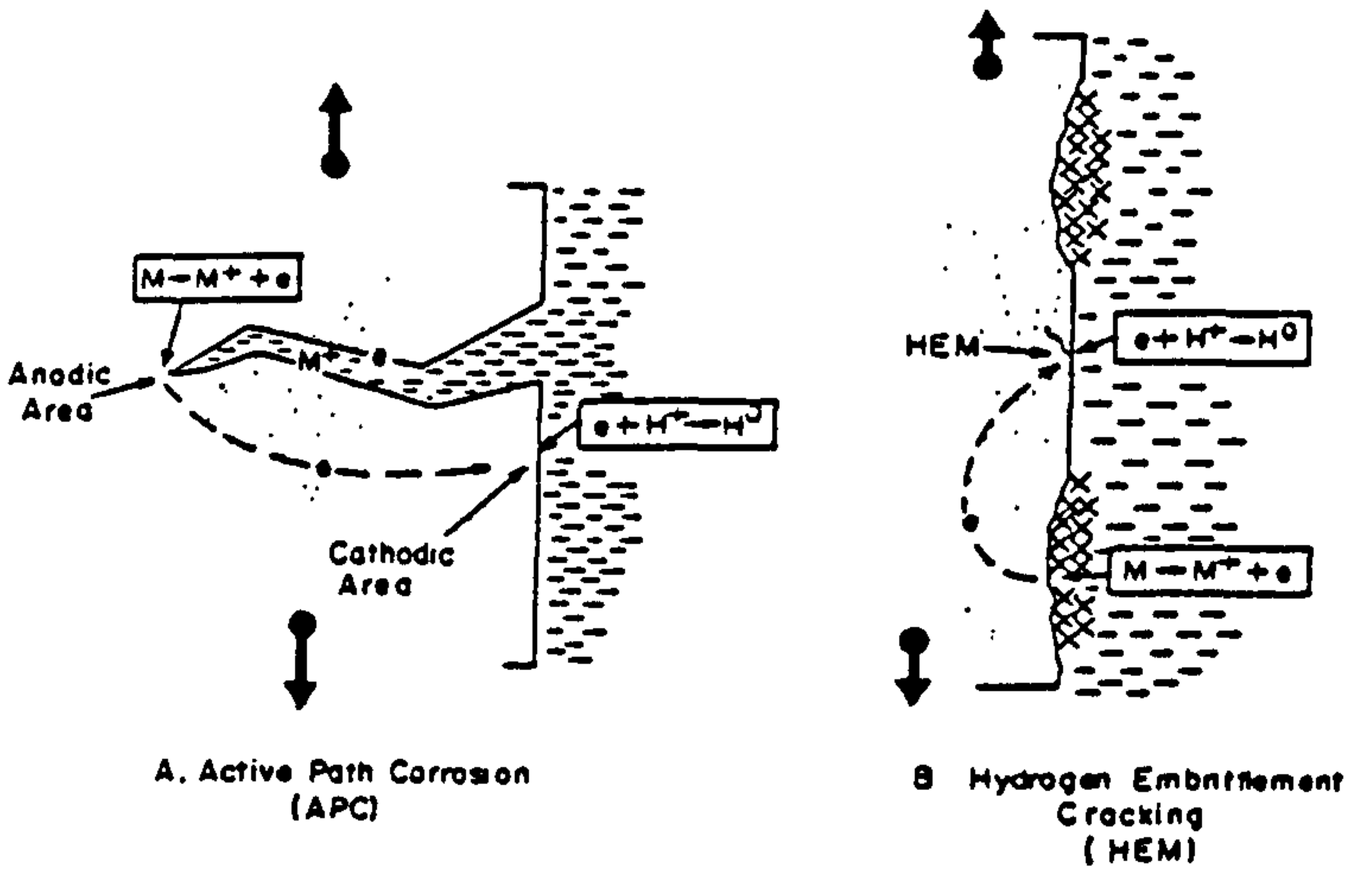

Figure 2.31 Schematic of cracking by active path corrosion (APC)and hydrogen embrittlement (HE) mechanisms /172/.

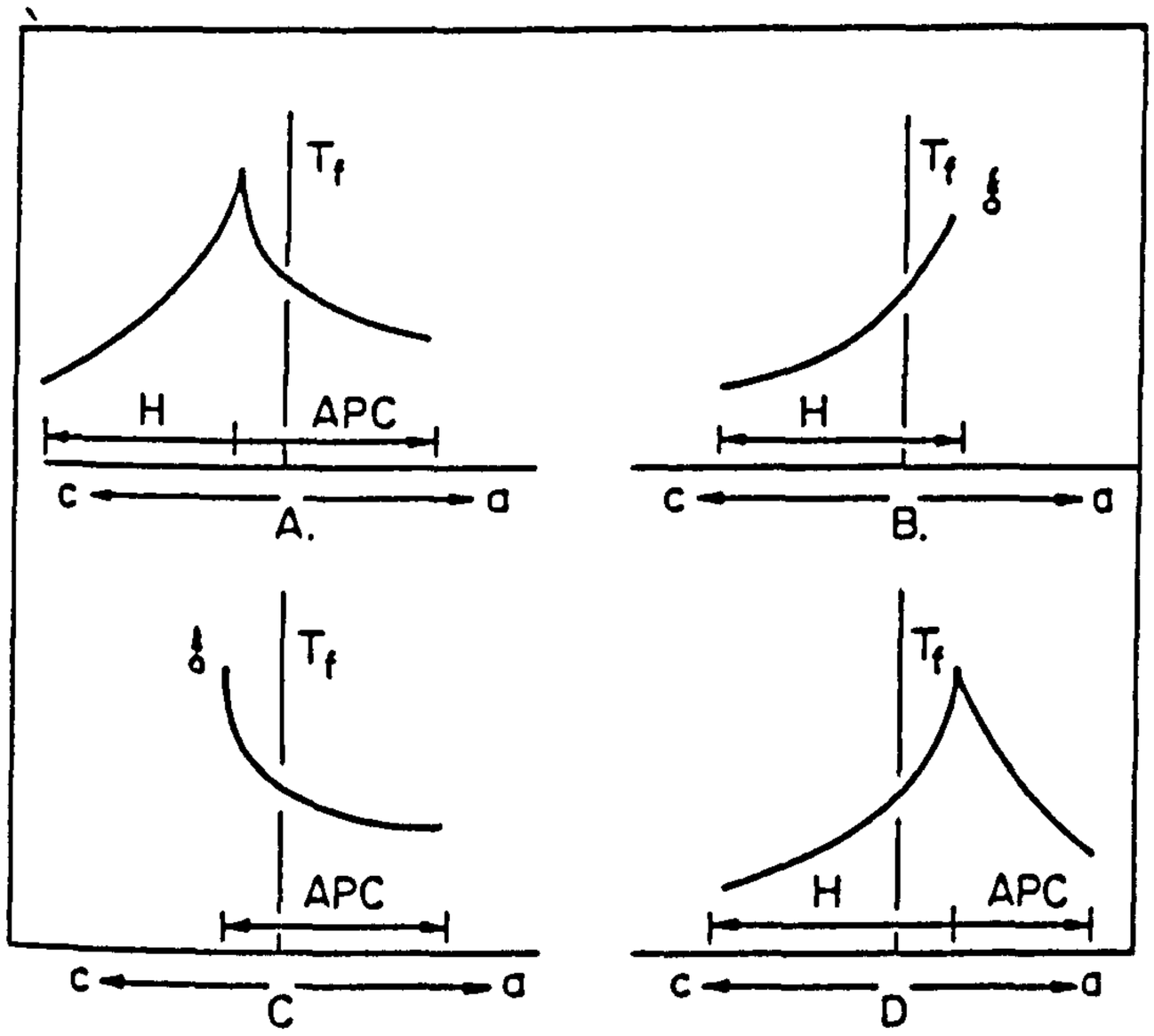

Figure 2.32 Influence of anodic and cathodic polarization on cracking susceptibility /172/.

Chapter 3

Experimental procedure

3.1 Material composition and microstructure

The four different commercial duplex stainless steels that were used in this investigation were supplied from two different sources. Material A and B, came from one source in the form of pipes and ready machined specimens respectively, while materials C and D were from another in the form of tubes. The dimensions and manufacturing routes of these materials are given in Table 3.1

The chemical composition and the chromium and nickel equivalents, estimated using equations 2.3 and 2.4, of the materials used are given in Table 3.2. Small coupons 10mm x 10mm perpendicular to the 3-principal directions were cut from each of the four materials and prepared for metallographic examination by wet grinding successively on 220, 400, 600, and 1200 silicon carbide grit papers, after which they were polished on 6μm and 1μm diamond-based cloth wetted with paraffin. Several etching solutions were tried to differentiate between the two phases of the material. The most successful was *80% H_2O + 20% HCl + 3g $K_2S_2O_5$, for 20 second,* which attacks the ferrite phase (becomes the dark phase) and leaves the austenite unattacked (white phase). Each time this etch was used it needed the addition of a few grains of the active agent: the potassium metabisulphate ($K_2S_2O_5$). The microstructure of the four materials so revealed consists of elongated islands of austenite (light phase) in a continuous ferritic matrix (dark phase) (Figure 3.1). The proportions of ferrite and austenite in the structures of the materials were assessed using three different methods and the results were averaged (Table 3.3).

Table 3.1 Dimensions and manufacturing routes of the four duplex stainless steels.

Material Designation	Outside diameter inches (mm)	Wall Thickness inches (mm)	Manufacturing routes
A	6 (152)	0.2 (5.1)	Seamless
B	Ready made Tensile specimens.		
C	12 (305)	0.4 (10.2)	Seamless
D	28 (711)	0.5 (12.7)	Welded

Table 3.2 Chemical composition of the duplex steels used in the investigation.

Element	Composition wt.% wt.%			
	A	B	C	D
Chromium	22.25	25.30	23.00	22.90
Nickel	5.74	6.70	5.00	5.20
Molybdenum	2.90	3.83	2.99	3.12
Manganese	1.62	0.29	0.98	0.99
Nitrogen	0.15	0.29	0.14	0.12
Silicon	0.35	0.24	0.48	0.50
Cobalt	0.046	0.15	0.02	0.07
Copper	0.064	0.10	0.03	0.03
Tungsten	n.d	0.06	n.d	n.d
Vanadium	0.06	0.04	0.05	0.04
Niobium+Thallium	n.d	0.03	<0.01	<0.01
Carbon	0.027	0.024	0.015	0.016
Phosphorus	0.021	0.015	0.016	0.019
Titanium	nd	0.003	<0.01	<0.01
Sulphur	< 0.002	0.002	0.001	0.002
Iron	balance	balance	balance	balance
Chromium equivalent	26.20	30.0	27.57	27.6
Nickel equivalent	7.12	10.68	7.41	7.41

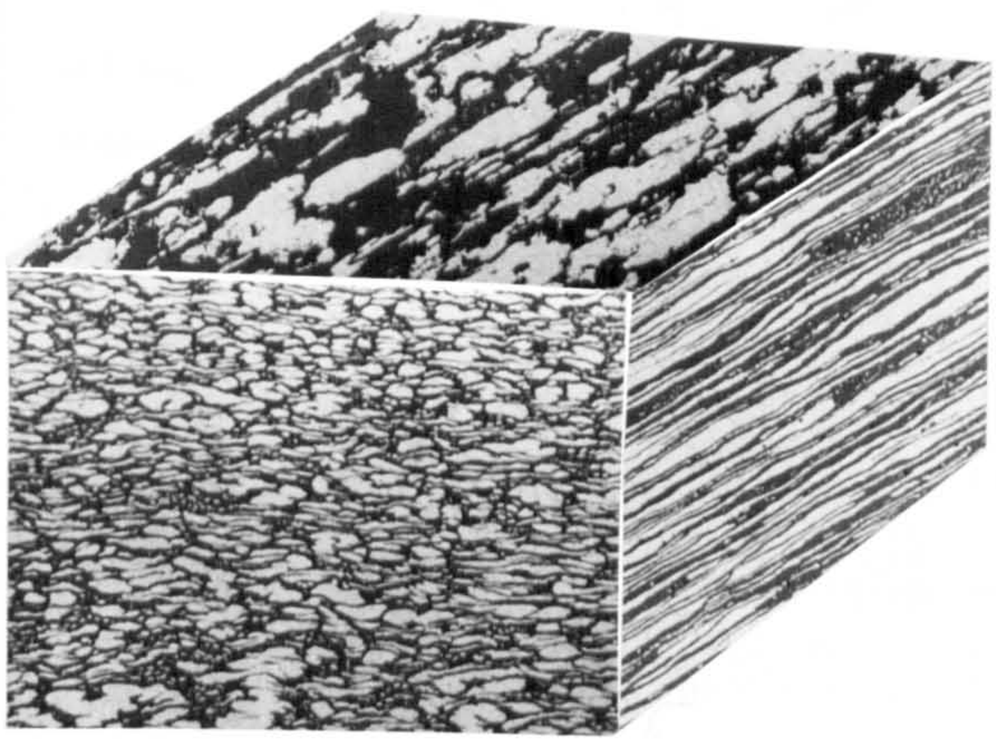

Material A

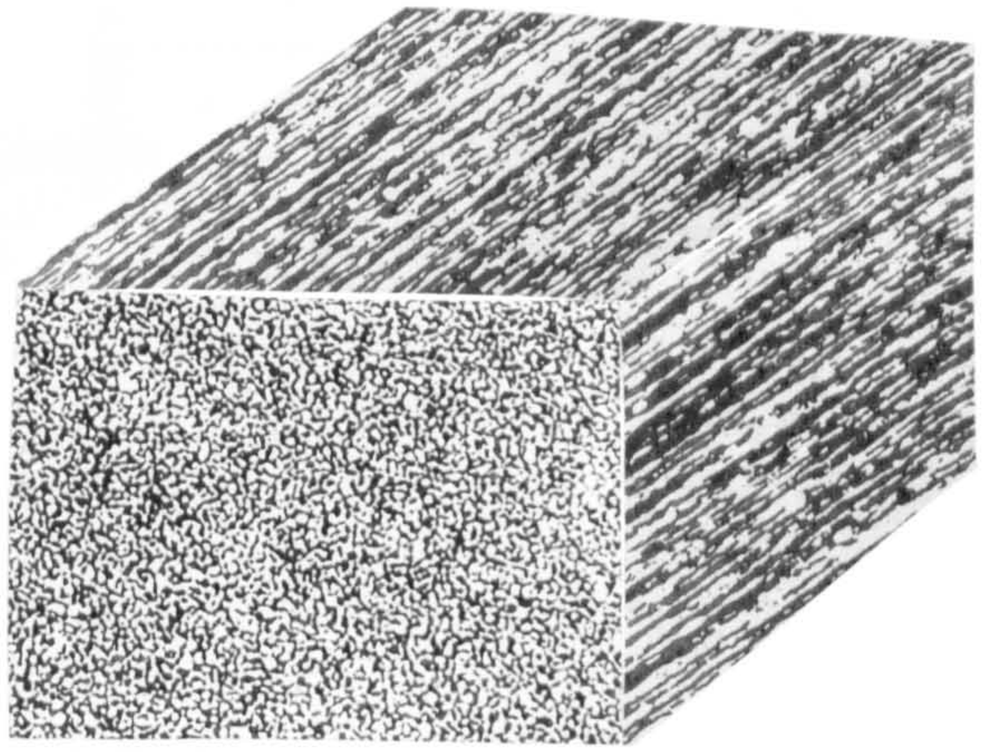

Material B

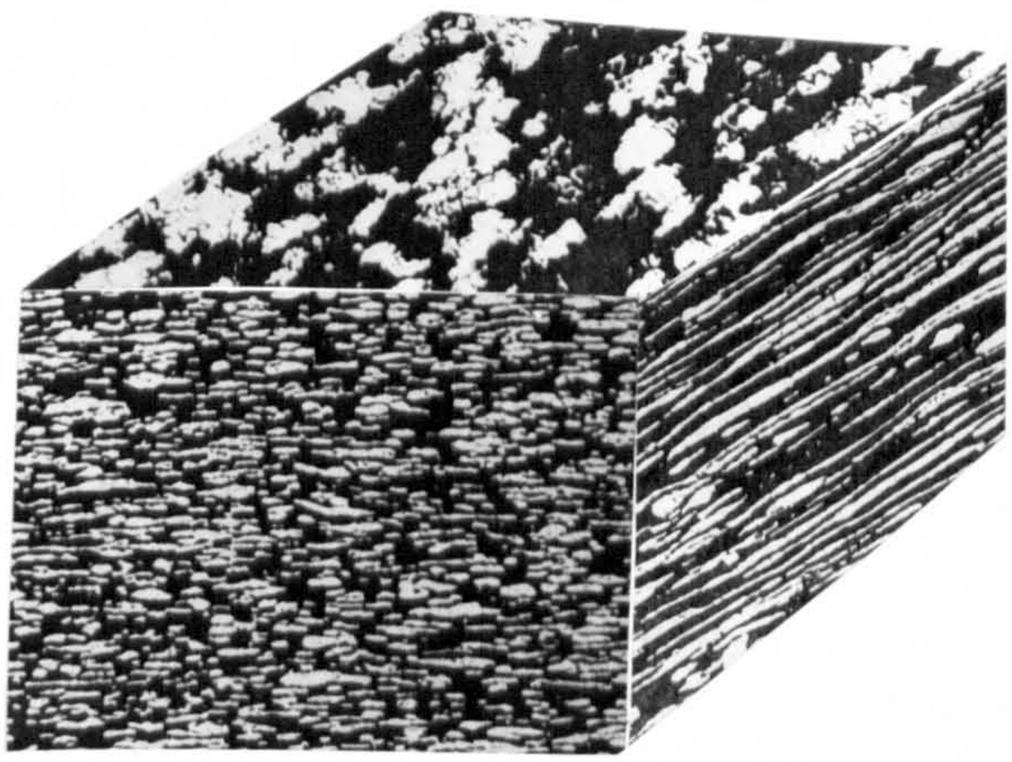

Material C

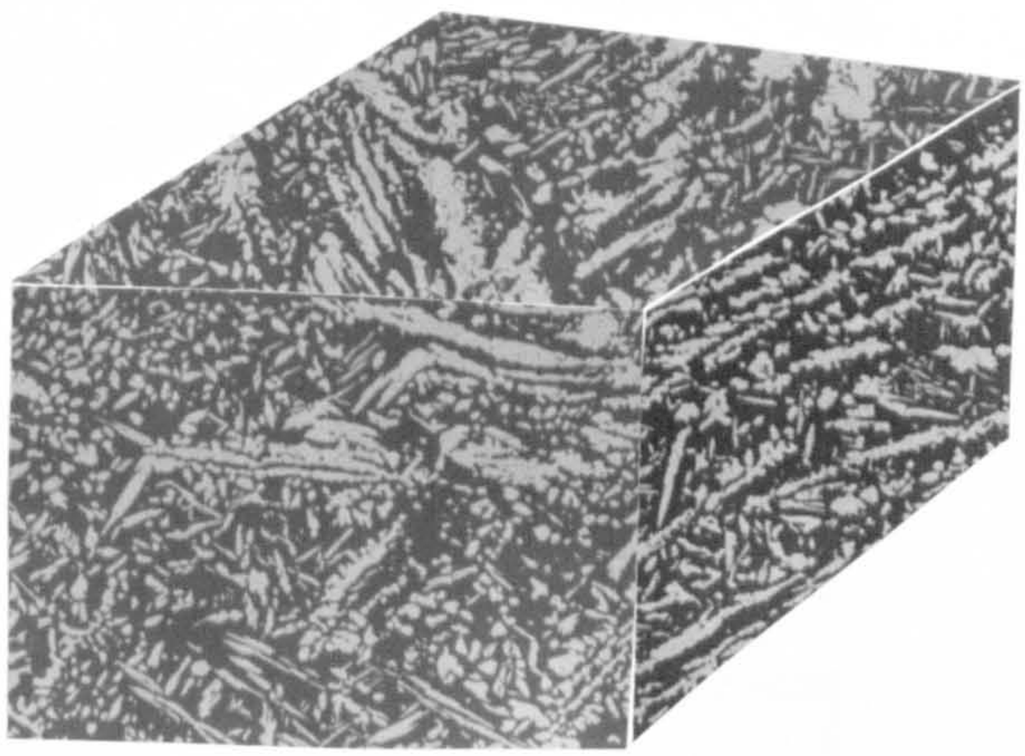

Material D

Figure 3.1 Three dimensional representation of the as received materials.

Table 3.3 Summary of the results of phase assessment of the materials.

Method	A		B		C		D	
	α	γ	α	γ	α	γ	α	γ
Ferrometer	n.d*	n.d*	n.d*	n.d*	64.7	35.3	63.5	36.5
X-ray	61.6	38.4	49.2	50.8	65.4	34.6	62.4	37.6
Image-analyzer	60.8	39.2	50.4	49.6	63.4	36.6	60.7	39.3
Average	61.2	38.8	49.8	50.2	64.5	35.5	62.2	37.8

(*) Not determined because the dimension of the as received material is too small to make a standard ferrometer specimens.

Table 3.4 The solute partitioning between the austenite and the ferrite phases as indicated by the EDX analysis.

Materia	Phase	Cr	Ni	Mo	Mn	Fe	Si
A	α	24.6	4.6	5.2	1.4	62.7	0.5
	γ	22.0	7.0	2.8	1.5	66.4	0.4
B	α	27.7	5.3	5.6	0	61.0	0.4
	γ	24.5	8.1	3.2	0	63.7	0.3
C	α	24.5	4.2	5.2	0.9	64.4	0.6
	γ	21.9	7.1	2.6	1.0	67.0	0.4
D	α	24.7	4.7	5.0	0.8	63.4	0.6
	γ	22.2	6.7	2.5	1.0	67.1	0.5

Back reflection X-ray analysis on a Phillips diffractometer, using copper-K_α monochromatic radiation ($\lambda = 1.54051$ Å) was performed on thin plates (measuring 10.0mm x 10.0mm whenever possible) perpendicular to the three principal directions of the tubes. The specimen were polished to 1µm finish and placed in the rotating holder of the diffractometer. The preferred orientation nature of the microstructure of the materials necessitated the calculation of integrated intensities for the first five major peaks of both phases: (111), (200), (220), (311), and (222) for the austenite and (110), (200), (211), (320), (310) for the ferrite (Figure 3.2a, Figure 3.2b) and hence, the specimens were scanned from $2\theta = 35°$ to $2\theta = 140°$. The identification of the diffraction lines was made by comparing the calculated d-spacing, obtained from:

$$d = \frac{\lambda}{2 \sin\theta} \qquad 3.1$$

with the standard tabulated powder diffraction data /175/ for both phases.

The volume fractions of the ferritic and austenitic phases were calculated from :

$$\frac{V(\gamma)}{V(\alpha)} = \frac{I_{hkl}(\gamma)}{I_{hkl}(\alpha)} \cdot \frac{R_{hkl}(\alpha)}{R_{hkl}(\gamma)} \qquad 3.2$$

Where:-

$V(\alpha)$ is the volume fraction of the ferritic phase.

$V(\gamma)$ is the volume fraction of the austenitic phase.

$I_{hkl}(\alpha)$ is the integrated intensity of the hkl reflection for ferrite.

$I_{hkl}(\gamma)$ is the integrated intensity of the hkl reflection for austenite.

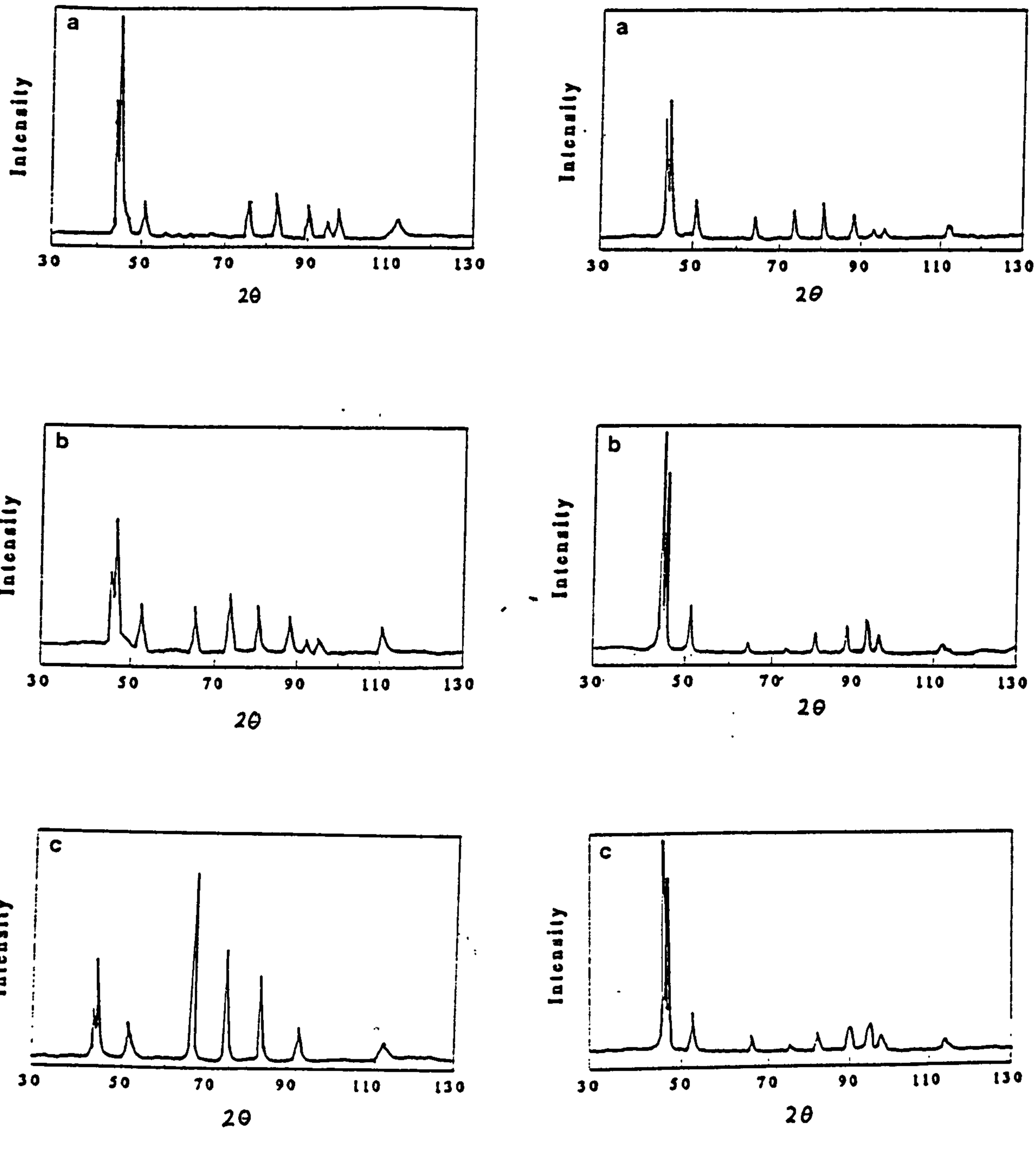

Figure 3.2a X-ray diffraction spectra of the four different as received material; a) radial, b) tangential, and c) longitudinal planes.

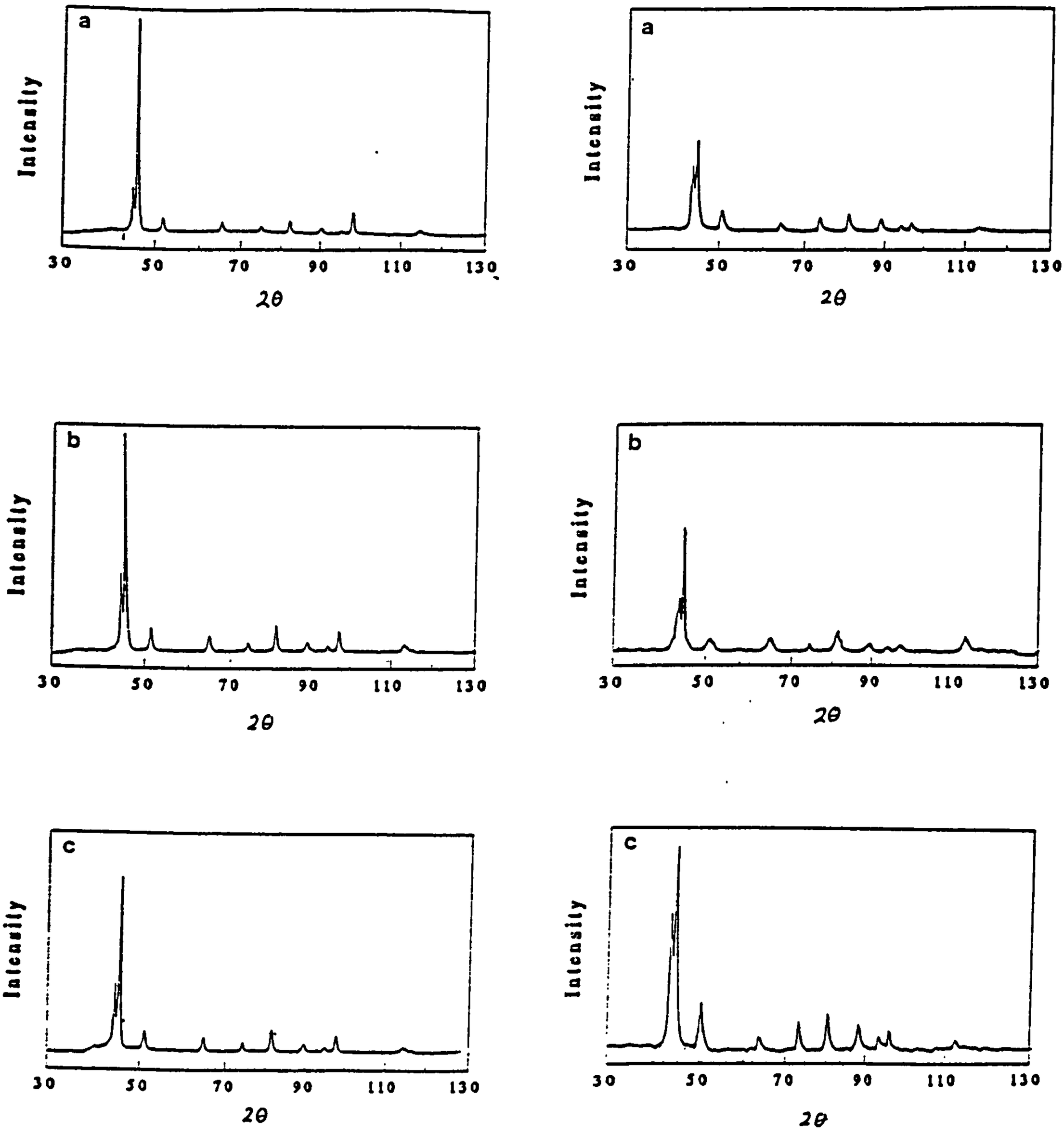

Material C **Material D**

Figure 3.2b X-ray diffraction spectra of the four different as received material; a) radial, b) tangential, and c) longitudinal planes.

$R_{hkl(\alpha)}$ is the calculated intensity for a specific hkl reflection from 100% ferrite with random orientation.

$R_{hkl(\gamma)}$ is the calculated intensity for specific hkl reflection from 100% austenite with random orientation.

The amount of each phase was also assessed using (Delco) image analyser at a magnification of 200x. Five areas were analysed for each of the three principal planes of each material and the results then averaged.

The percent magnetic material (Ferrite) was assessed using a previously calibrated ferrometer. Standard ferrometer specimens, 10 mm high and 12.7 mm diameter, were machined with their principal longitudinal axis along the longitudinal and radial direction of the tubes, wherever possible. The ferrometer consists of three separate coils wound around a common soft iron core (Figure 3.3) and arranged in such a way that a current is generated if a magnetic material is placed in the specimen cavity, due to the change in the magnetic field. The two secondary coils are balanced in the absence of specimen and the ammeter reading the resultant current then indicates zero. Introduction of a specimen centrally to the top cavity causes a change in the magnetic field and the resultant imbalance current depends upon the ferromagnetic content of the specimen. Calibration by using standard compacted specimens containing various proportions of iron and copper (Figure 3.4) allows the current generated to be converted to a ferrite content.

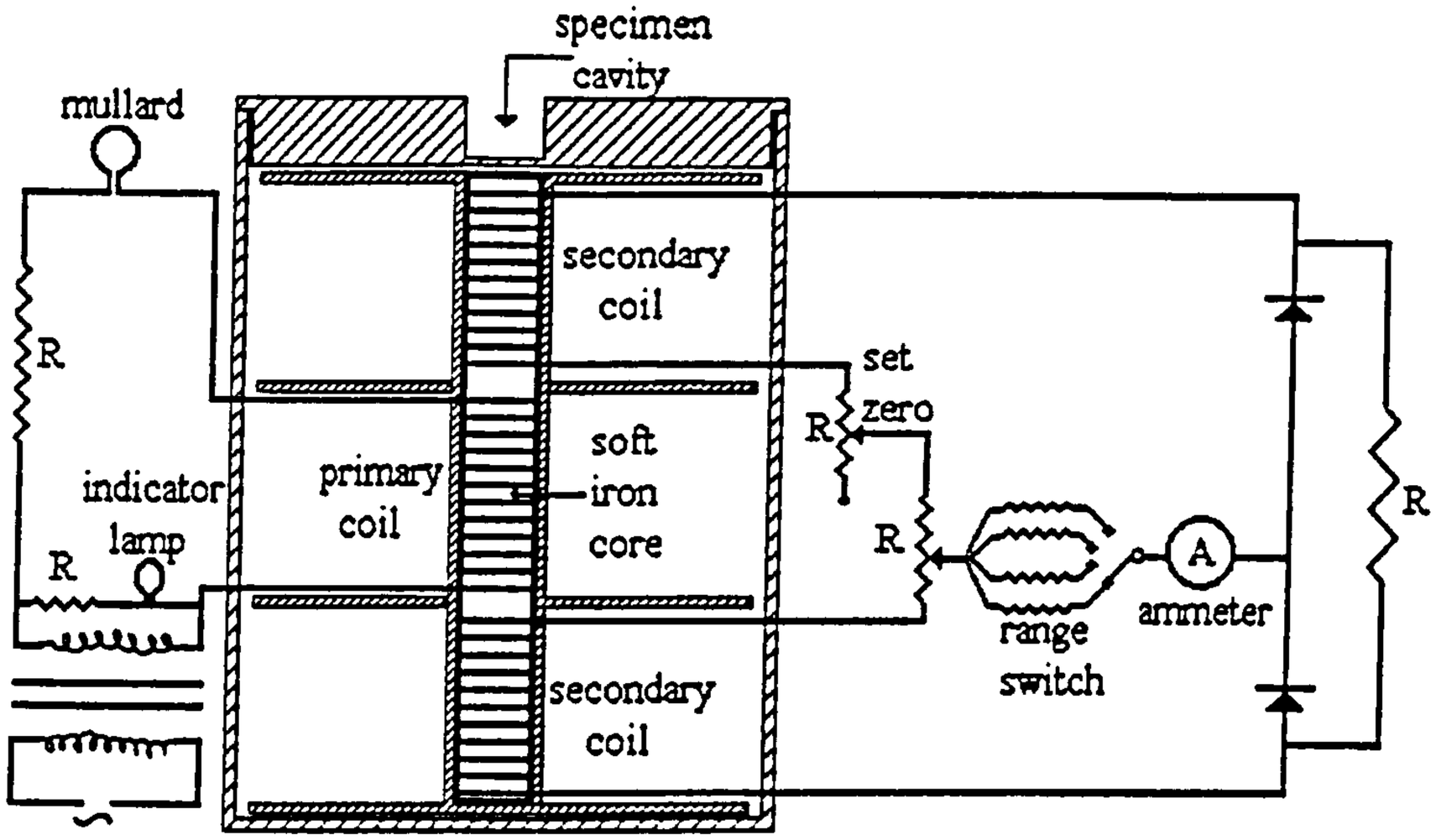

Figure 3.3 Schematic diagram of the ferrometer arrangement.

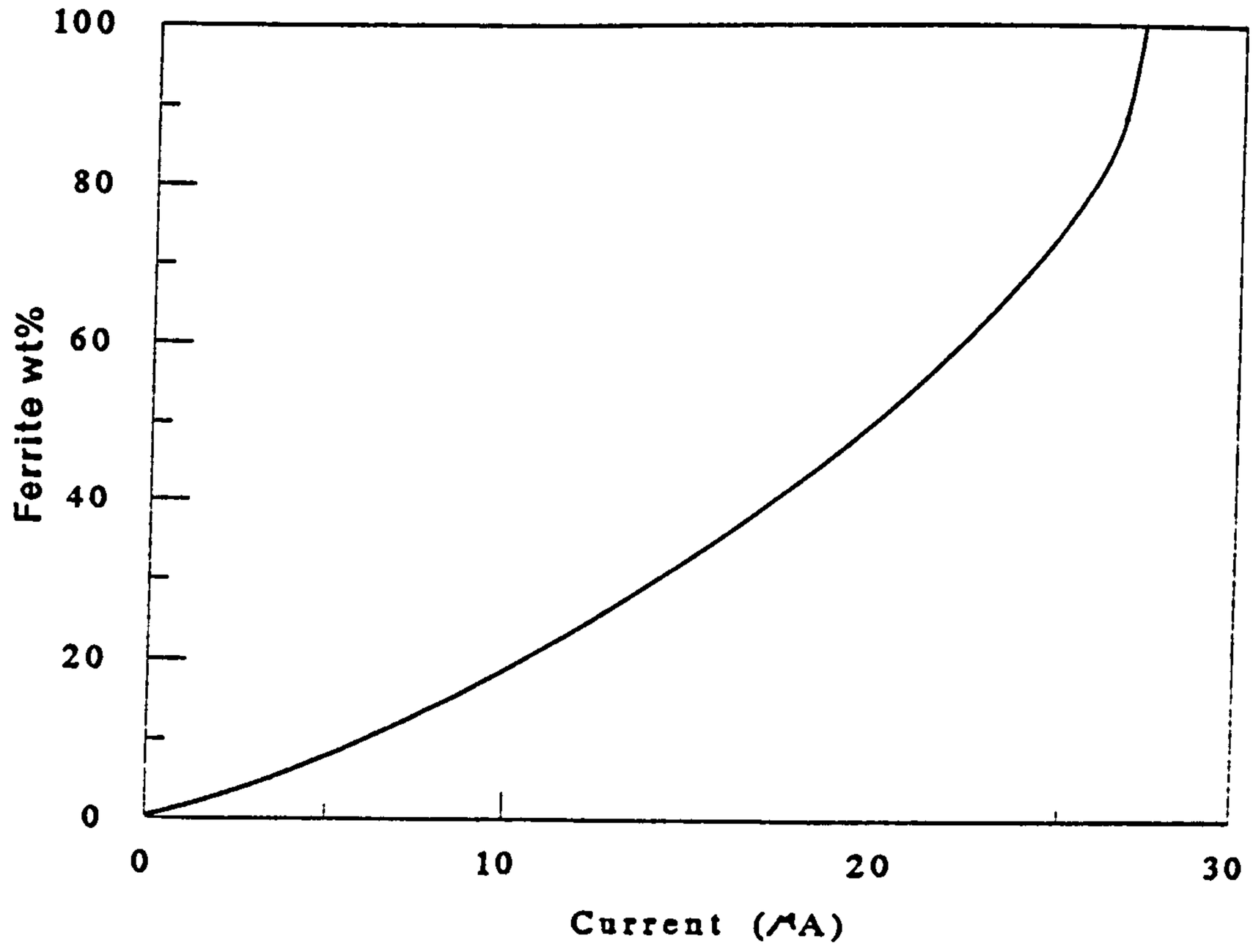

Figure 3.4 The calibration curve for the ferrometer used in the phase assessment.

Energy dispersive spectroscopy (EDS) was performed on ground, polished, and etched specimens of the four materials employing a Joel JSM-35 scanning electron microscope equipped with a microscan probe at an excitation voltage of 20kV. This showed (Table 3.4) that ferrite stabilizing elements (Cr, Mo, and Ni) tend to segregate into the ferrite phase, while austenite stabilizing elements (Ni and Mo) segregate to the austenite phase. Although, nitrogen segregation behavior was not obtained due to low energy resolution (low atomic number element), most of it would be expected to go into the austenite phase, since Hertzman /54/ and Bernhardsson /64/ reported a partitioning coefficient, (N_2wt% in γ)/(N_2wt% in α), of 7.0. The partitioning coefficients in the various materials were calculated from Table 3.4 (Table 3.5).

Hardness measurements were performed on the as received material, using a Vickers pyramid hardness testing machine with 10 kg load. The samples were polished to 1µm finish before testing. The indentations always cover both phases at this load, but microhardness measurements were also carried out with a 5g load to establish the relative hardness of the ferrite and the austenite phases. However, these results showed a large scatter, perhaps due to two reasons: (i) the fact that even at this low load the diamond indenter sometimes penetrates through both phases and (ii) there is a difference in the work hardening behavior of the two phases. The hardness and the microhardness measurements were calculated as a mean of about 20 results (Table 3.6).

Table 3.5 Partitioning coefficient for the major alloying elements in the various duplex stainless steels.

Material A

Austenite	Ferrite
Ni (1.50)	Cr (0.89)
Mn (1.10)	Mo (0.80)
	Si (0.80)

Material B

Austenite	Ferrite
Ni (1.52)	Cr (0.88)
Mn (0.0)	Mo (0.57)
	Si (0.75)

Material C

Austenite	Ferrite
Ni (1.69)	Cr (0.89)
Mn (1.10)	Mo (0.50)
	Si (0.67)

Material D

Austenite	Ferrite
Ni (1.52)	Cr (0.89)
Mn (1.2)	Mo (0.41)
	Si (0.75)

Table 3.6 Vickers hardness values for the as received materials.

Material	**A**		**B**		**C**		**D**	
Vickers (10 Kg)	262 ± 3		256 ± 2		268 ± 3		254 ± 3	
Phase	α	γ	α	γ	α	γ	α	γ
Micro-hardness	258± 12	231± 9	256± 11	231± 14	249± 10	228± 11	243± 8	215± 13

The errors were calculated as the standard deviation with population n:

$$\sigma_x = \sqrt{\frac{\Sigma x^2 - n\bar{x}^2}{n}}$$

3.2 Specimen design and preparation

Four different designs of smooth tensile specimen were used in this investigation, all of which have gauge lengths of 11.35 mm (Figure 3.5). The Hounsfield No.11 specimens with gauge diameters of 3.20 mm were used for straining in the hydrogen atmosphere and for straining hydrogen-charged specimens, but the longer threaded-end specimens with gauge diameters of 2.50 mm were designed to fit into a glass cell containing the aqueous environments. The subsized threaded-end specimens with a gauge diameter of 3.20 mm, were machined out of the shoulders of specimens from material designated B since only a limited number of ready-machined specimen was supplied by the second source. Specimens (except the subsized) were machined (whenever possible) with their axes parallel to the longitudinal axis and the tangential direction of the pipes. In addition, some specimens were machined from material C in such away that their gauge lengths included the weld and the Heat Affected Zone (HAZ)(Figure 3.6). The gauge lengths of the specimens were always polished to 5/0 emery in order to remove any machining marks that might initiate premature failure, after which they were degreased with acetone prior to tensile straining or thermal charging with hydrogen.

3.3 Heat treatment of specimens

The purpose of the heat treatment programme was to vary the proportions of the austenite and ferrite in order to study their effect on the hydrogen embrittlement of the material. The class of duplex stainless steels under study solidify completely in the ferrite phase field, and it is only during cooling of the solid that part of the ferrite transforms to austenite. This transformation is reversible,

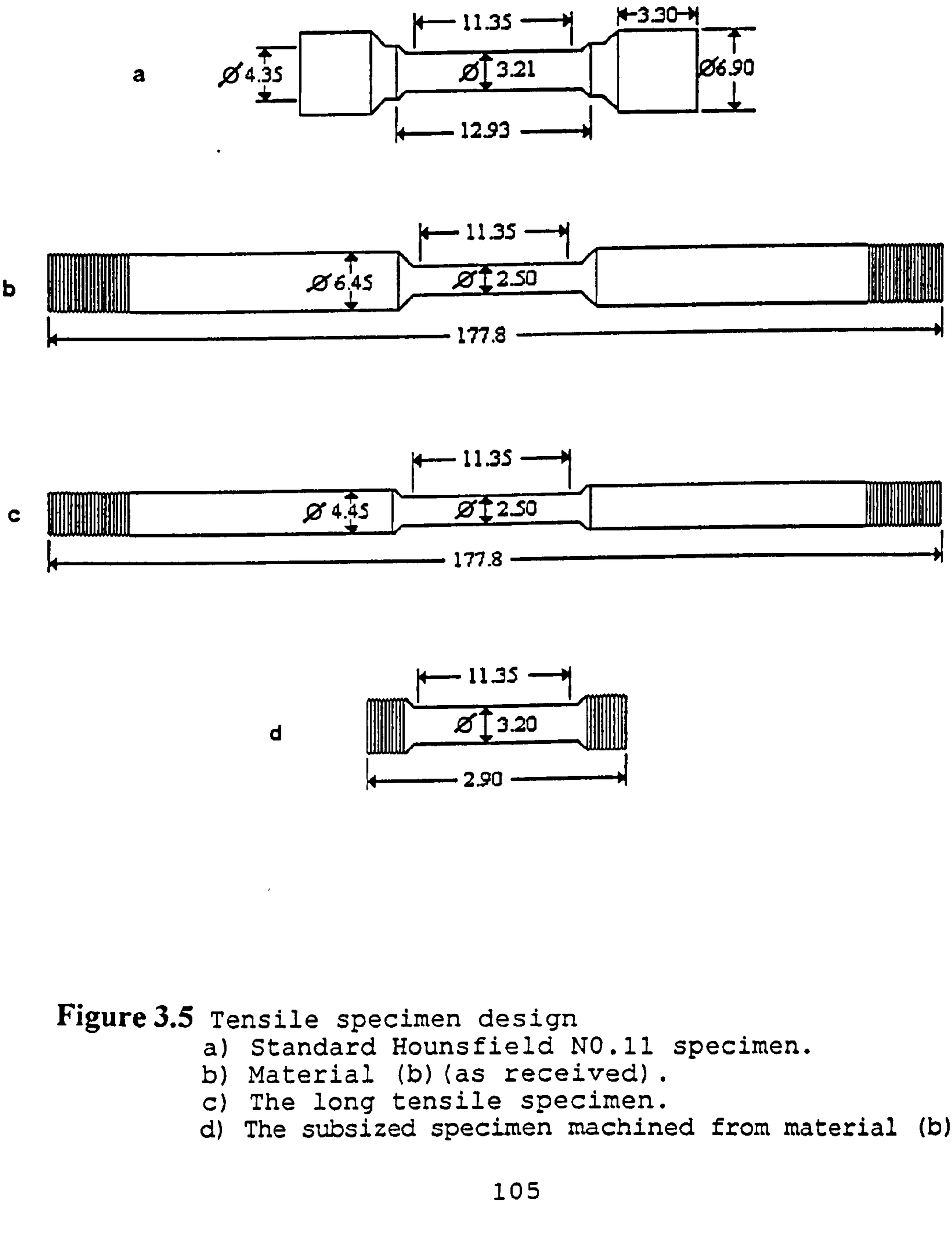

Figure 3.5 Tensile specimen design
a) Standard Hounsfield NO.11 specimen.
b) Material (b)(as received).
c) The long tensile specimen.
d) The subsized specimen machined from material (b).

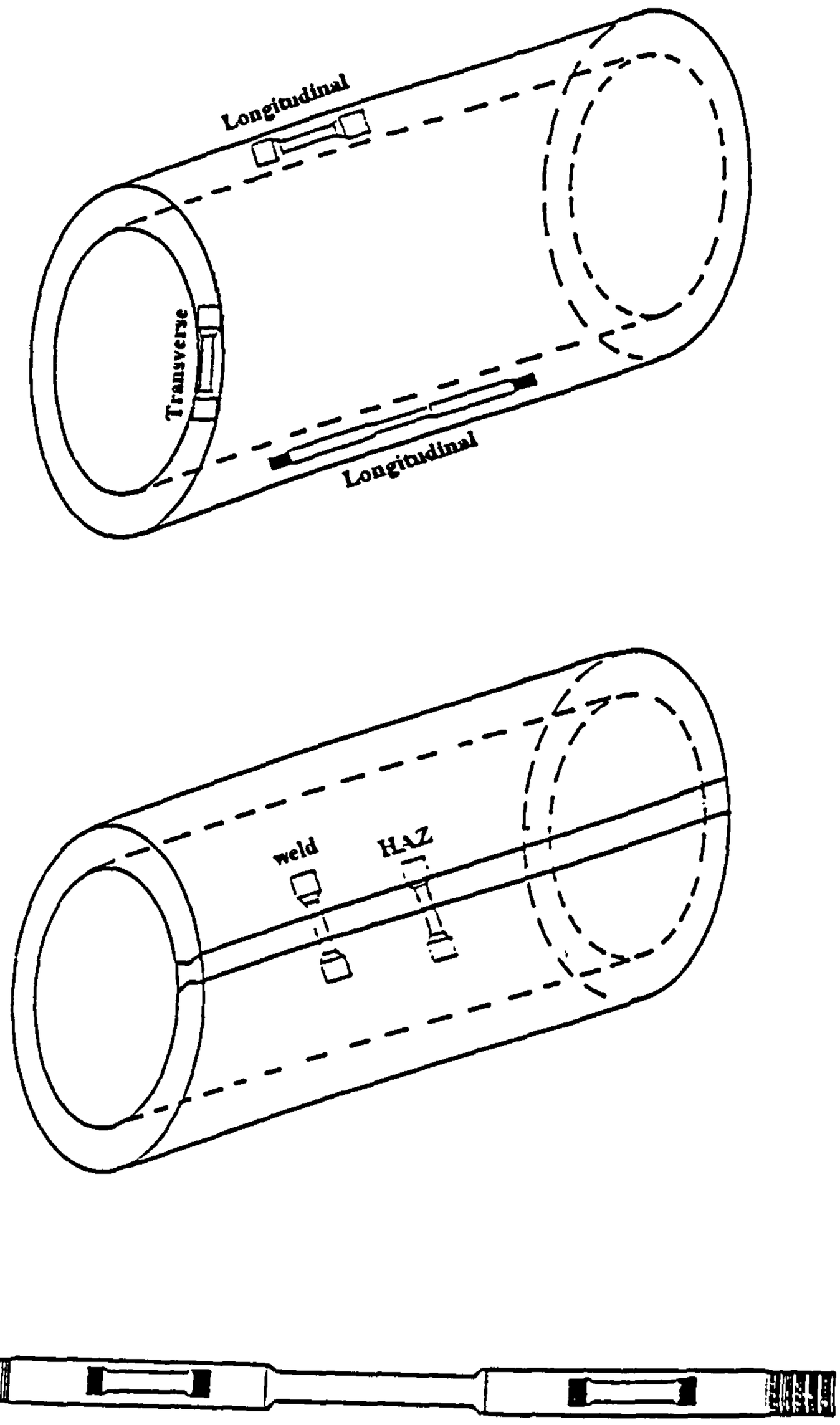

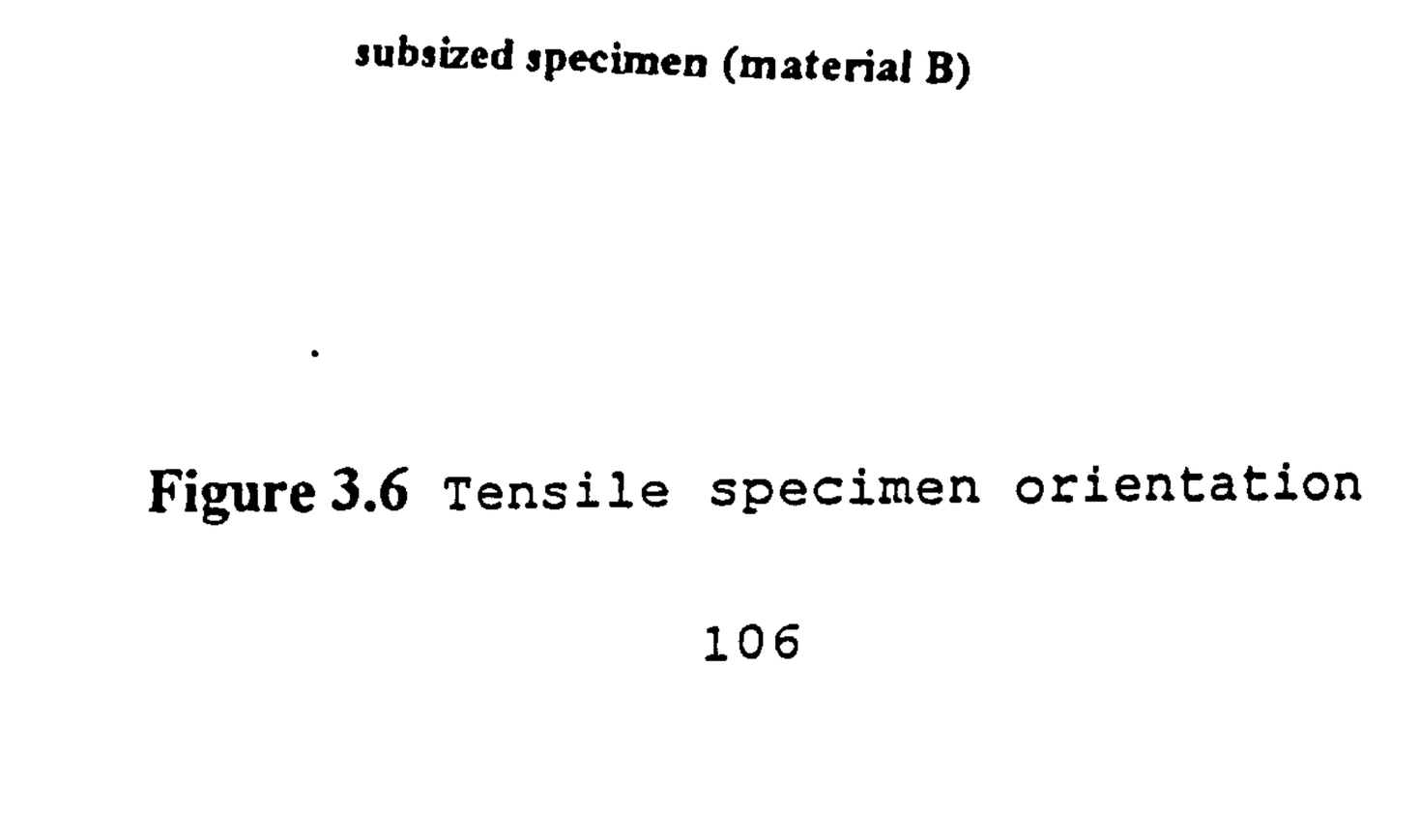

subsized specimen (material B)

Figure 3.6 Tensile specimen orientation

i.e. heating from 1000 to 1300°C leads to re-dissolution of austenite in the ferrite (Figure 3.7). Thus, any large increase in temperature, in the range mentioned above, will result in significant change in the volume fraction and the chemical composition of the two phases. Caution was exercised to avoid the formation of any detrimental phases, hence, any cooling below 1000°C was performed at such a fast rate as to avoid spending any significant time in a particular phase field (Figure 3.8). An attempt was made to avoid formation of any significant oxide film on the specimen surfaces during heat treatments. At first, a few specimens were encapsulated in silica glass before heating in a muffle furnace, but unfortunately, the silica glass did not break completely upon quenching and the water leaked slowly into the glass, so that the resultant microstructure of the specimens varied significantly. Subsequently, the heat treatment procedures had to be revised and were carried out on 10mm x 10mm x 120mm slabs from which tensile specimens were subsequently machined. Heat treatment was conducted in a 3 inch diameter tube furnace equipped with a programmable controller and capable of temperatures up to 2000°C. Prior to the heat treatment, the furnace was calibrated using a nickel-chromium thermocouple and a voltmeter. The size of the furnace tube limited the number of slabs to be heat treated in any one run to three. The slabs were degreased with acetone, placed on alumina boats and pushed into the centre (hot zone) of the furnace tube using a steel rod. The two ends of the tube were then sealed with rubber stoppers having stainless steel pipes passing through them to facilitate argon passage through the tube to keep air out during the entire time of the heat treatment. The inlet side was connected via a regulator to an argon cylinder while the outlet passed into a glass cell

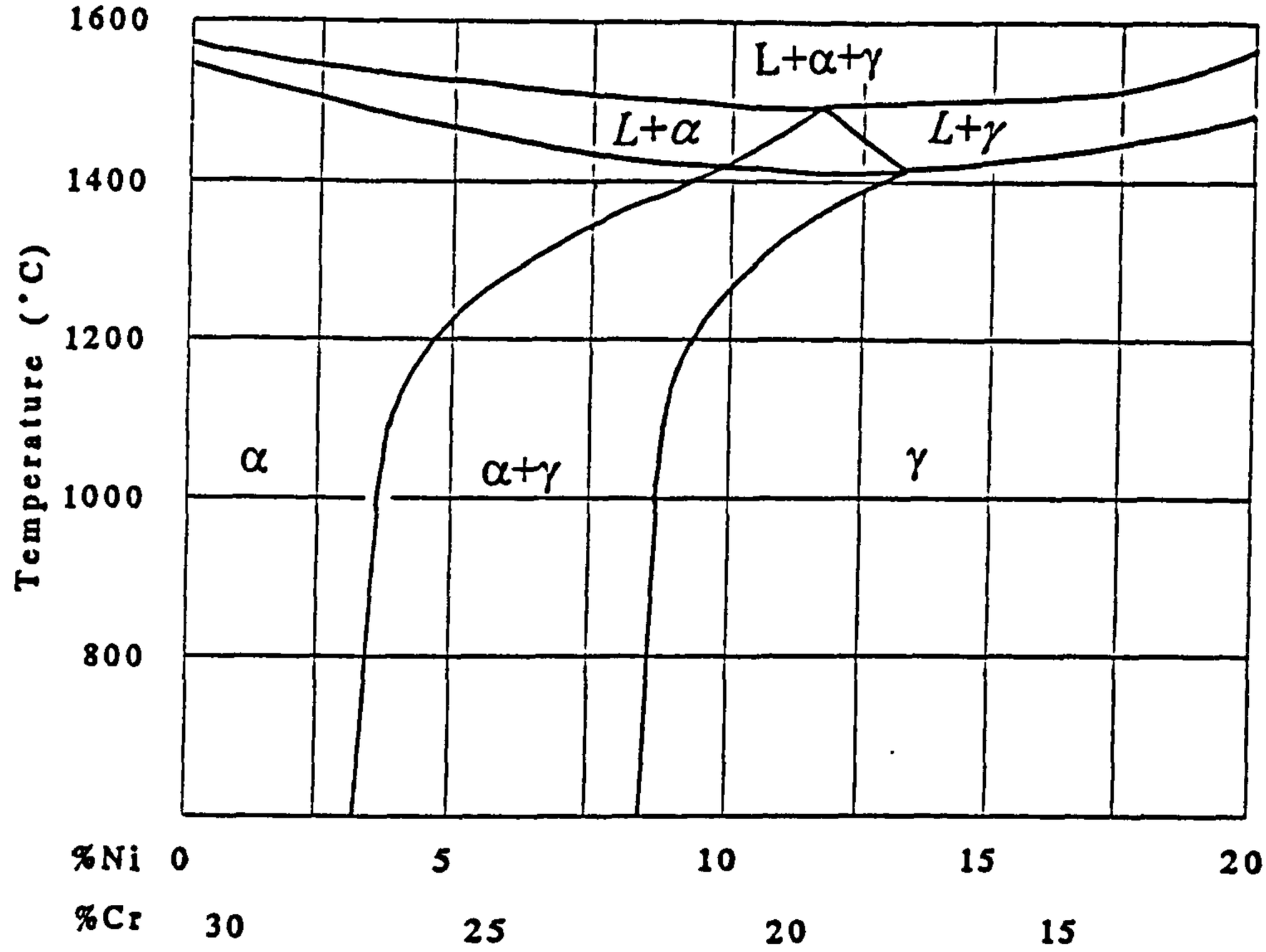

Figure 3.7 Pseudo binary diagram for 68% Fe-Cr-Ni.

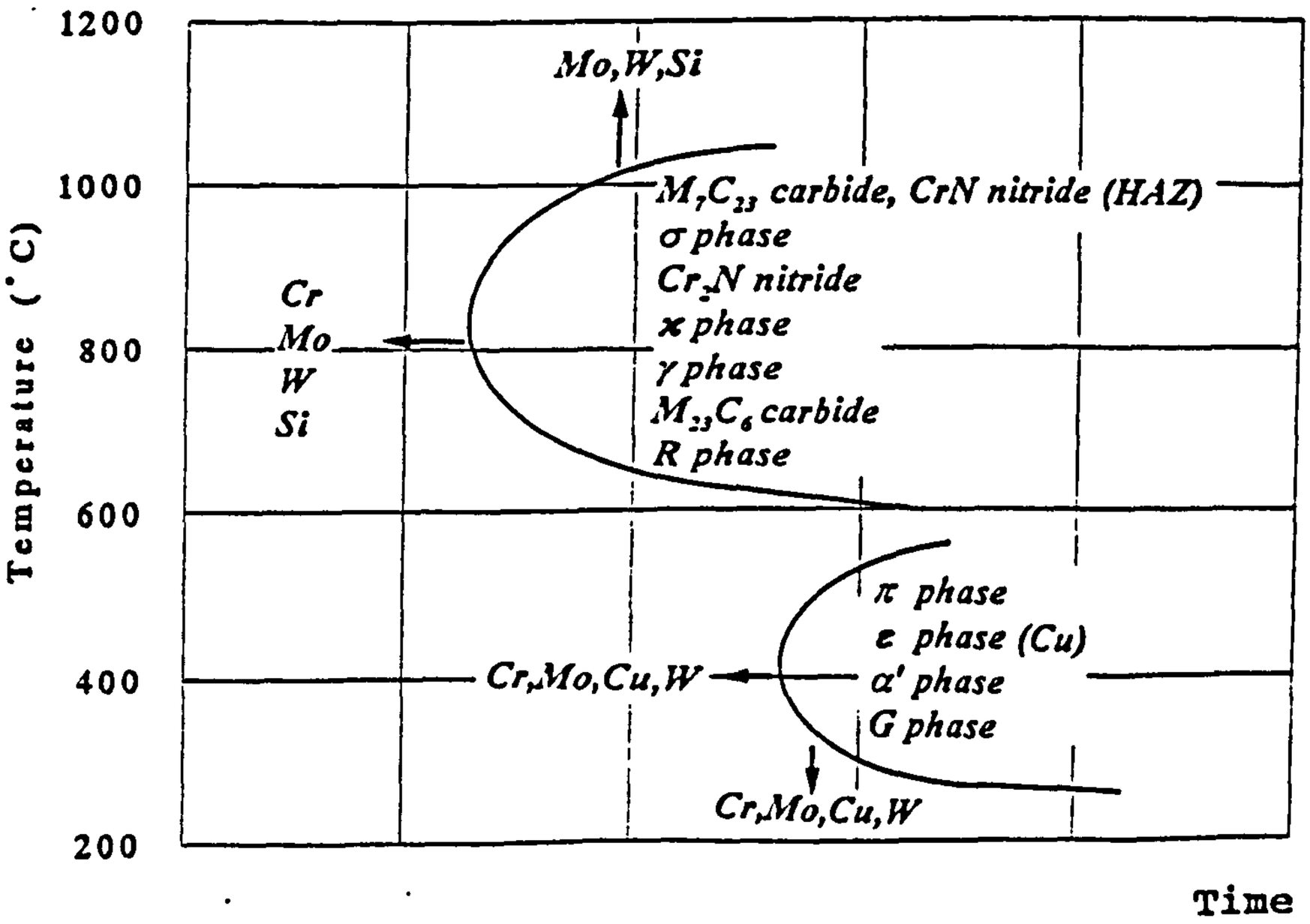

Figure 3.8 Possible precipitation in duplex stainless steels.

partially filled with oil to allow exit of the argon but stop any air from entering the system (Figure 3.9). Before turning the furnace on, argon was passed through at a relatively high flow rate for several minutes to flush out the air from the system. The argon flow rate was then lowered and the furnace was switched on.

In order to achieve a suitable volume fraction of the two phases, three temperatures were chosen: 1200, 1250, and 1300°C all of which were achieved using the same rate of heat input of 30°C per minute. Certain specimens were cooled in the furnace to 1000°C at a rate of 5°C/min to allow the α-γ transformation to take place. After the heat treatment cycle was completed, the slabs were removed from the furnace and immediately quenched in a 15 litre ice water container, in order to retain the high temperature structure. Each slab was then machined to provide four Hounsfield No. 11 tensile specimens .

3-4 Thermal charging with hydrogen

The thermal charging of specimens with hydrogen was conducted in a high pressure stainless steel autoclave capable of withstanding up to 320 bar at 350°C (Figure 3.10). The polished and degreased specimens were placed in batches into the autoclave and left to evacuate over night to < 10^{-5} torr. The vacuum system is then isolated and the autoclave is slowly charged with hydrogen (from a 150 bar cylinder), at ambient temperature, to a pressure sufficient to produce the required pressure at 350°C. The autoclave is then isolated from the hydrogen cylinder and the excess pressure in the pipes is released via a vent , before it is removed to be placed in a specially designed furnace to be heated

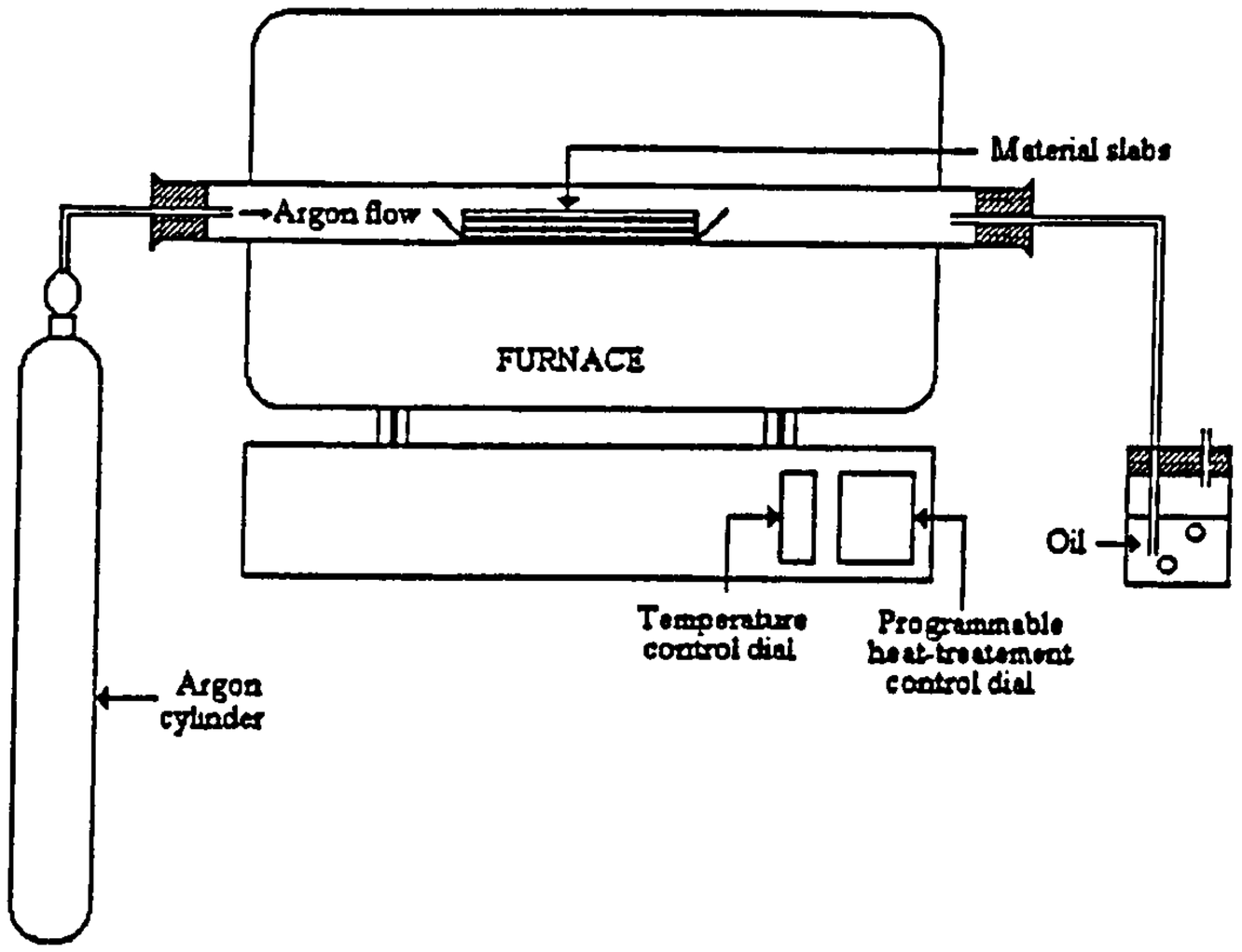

Figure 3.9 Schematic representation of the tube furnace arrangement used in the heat treatment of the specimens.

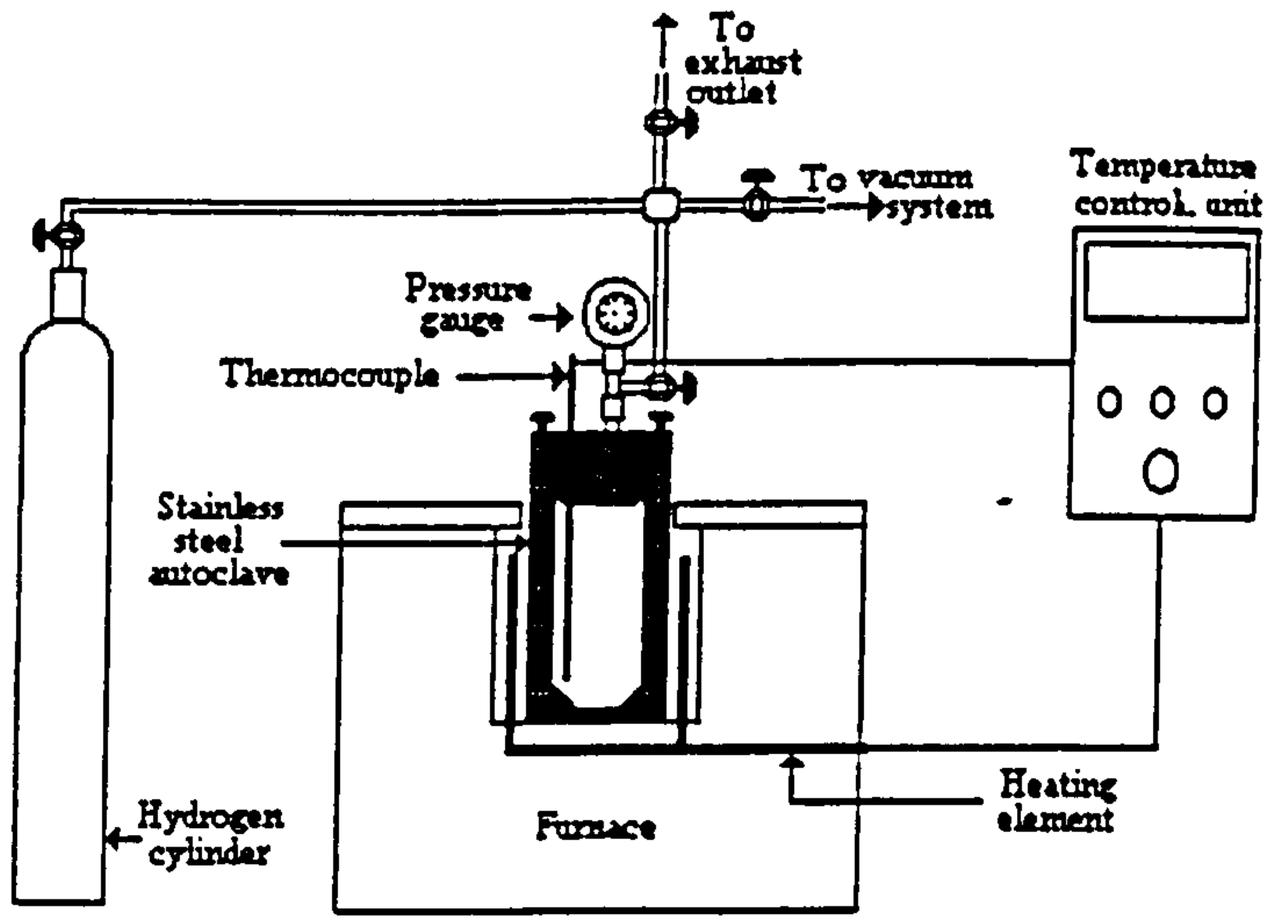

Figure 3.10 The high pressure autoclave arrangement used for hydrogen thermal charging.

to a temperature of 350°C. Since it was noted that when hydrogen pressurisation is conducted rapidly the temperature of the gas in the autoclave is raised significantly, it was left at room temperature for one hour before commencing with the heat treatment in order to record a correct initial pressure reading and to check for leakage. Upon heating the pressure increases and the observed pressure was recorded at different temperatures to produce a calibration curve (Figure 3.11) that can be used to estimate the initial pressure at room temperature that will produce a specific pressure at a higher temperature. The autoclave was left in the furnace for the required charging time (48 hours) to produce a uniform hydrogen concentration in 3.20mm diameter specimens. After the time was elapsed, the autoclave was removed from the furnace, allowed to cool to room temperature, which took about 6 hours (Figure 3.12), and then reconnected to the vacuum system and the hydrogen released to the atmosphere via a vent.

As might be expected, due to the high pressure involved, the system was found to behave non-ideally (Figure 3.11) and obey the Van der Waals equation for real gases:

$$\left(p + \frac{an^2}{V^2}\right)(V - nb) = nRT \qquad 3.3$$

where:
- P *is the gas pressure.*
- V *is the volume occupied by the gas.*
- T *is the absolute temperature.*
- $\frac{an^2}{V^2}$ *is a correction factor to account for the intermolecular attraction among n moles of atoms.*
- nb *is a correction for the volume of gas occupied by n moles of gas.*
- a *is a constant = 0.2444 l^2 atm/mol^2 for hydrogen.*
- b *is a constant = 0.02661 l/mol for hydrogen.*

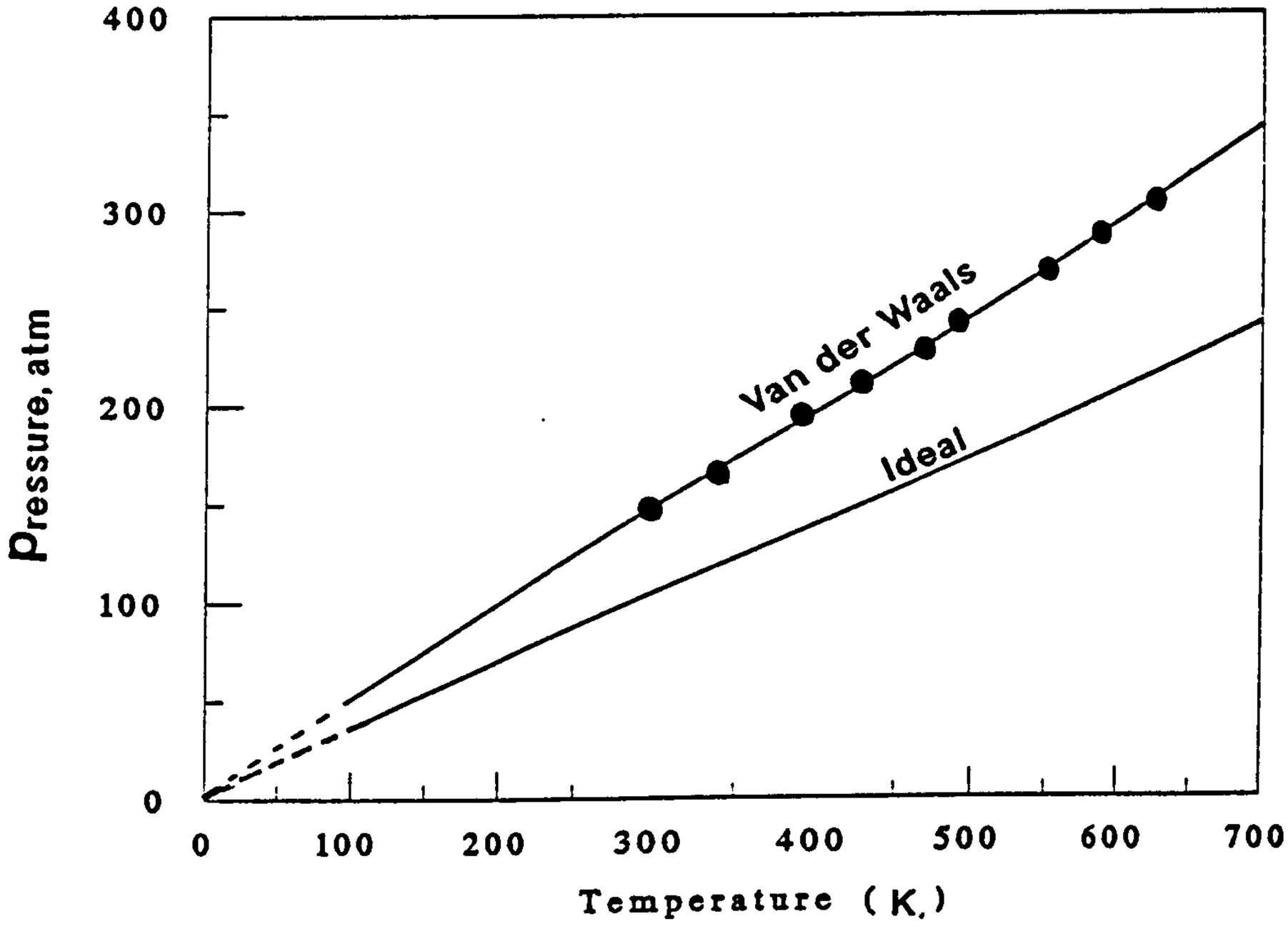

Figure 3.11 Calibration curve for the autoclave.

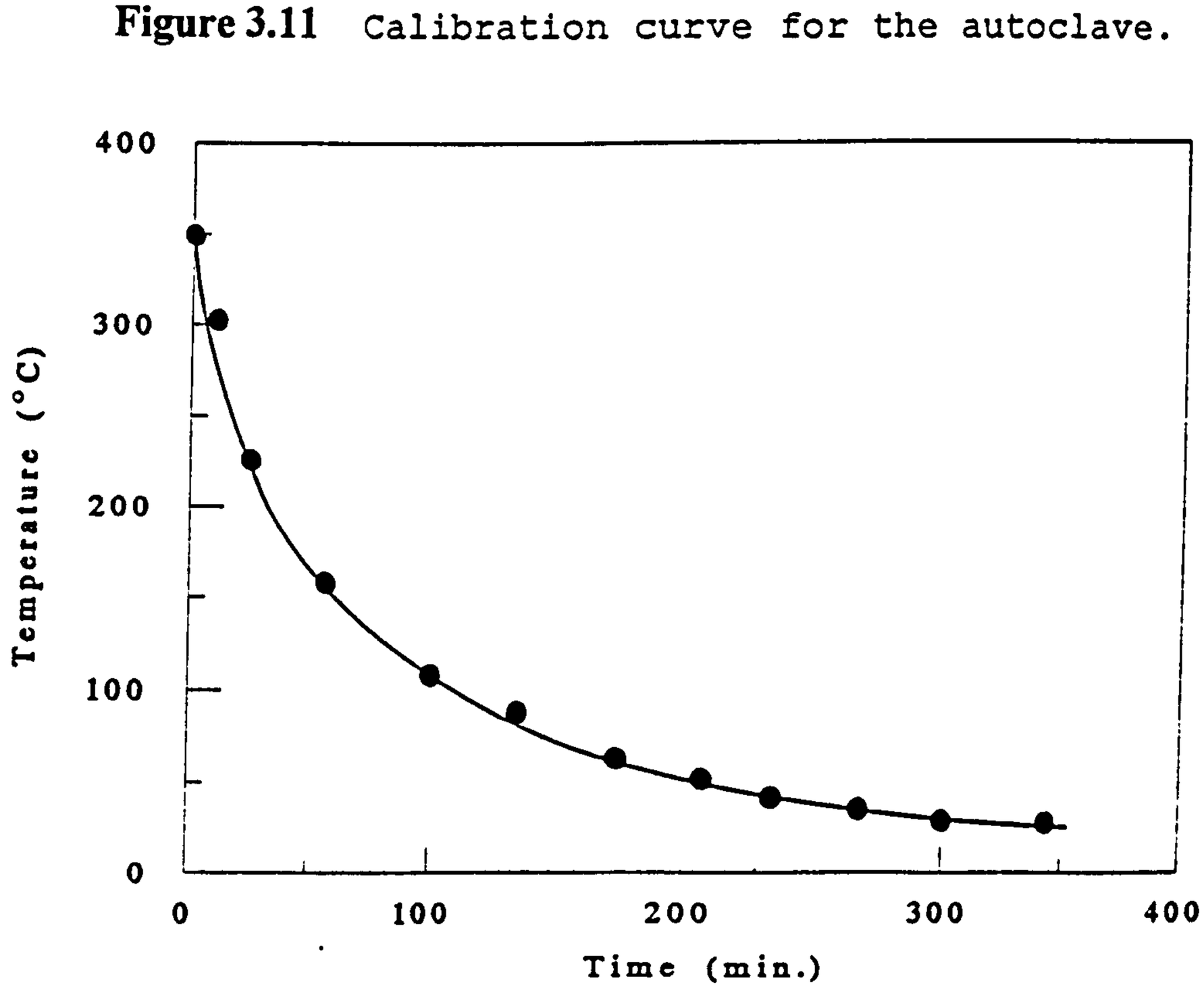

Figure 3.12 The cooling curve for the high pressure autoclave.

3.5 Slow strain rate testing

3.5.1 Straining uncharged and charged specimens in air

The tensile straining of all the specimens, whether in air or in a gaseous hydrogen atmosphere, was carried out in a relatively-hard vertically mounted tensile machine equipped with a calibrated 5000-lb load cell (519 N/mV) and a calibrated transducer (3.98 x 10^{-3}mm/mV) for measuring the extension (Figure 3.13). The outputs from the load cell and the transducer were fed into an X-Y recorder and load vs extension curves were thus obtained. The strain rates provided by this machine cover the range 10^{-7} to 1.9 x 10^{-2}/s, as referred to the original gauge length of the specimen (11.35mm).

The mechanical properties were assessed in terms of the following parameters: 0.2% flow stress and the ultimate tensile strength (UTS) were calculated by dividing the load to produce 0.2 plastic strain and the maximum load respectively, by the original cross section area of the specimen (A_o), and the true fracture stress was obtained by dividing the breaking load by the final fracture area (A_f). The elongation to fracture (EL) was calculated as a percentage of the original gauge length. The degree of embrittlement was assessed by using either one of three expressions:

$$\%RA = \frac{A_0 - A_f}{A_0} \times 100 \qquad 3.4$$

$$(Embrittlement\ Index)\ EI = \frac{RA_{air} - RA_{hydrogen}}{RA_{air}} \times 100 \qquad 3.5$$

$$\%EL = \frac{L_{final} - L_{initial}}{L_{initial}} \times 100 \qquad 3.6$$

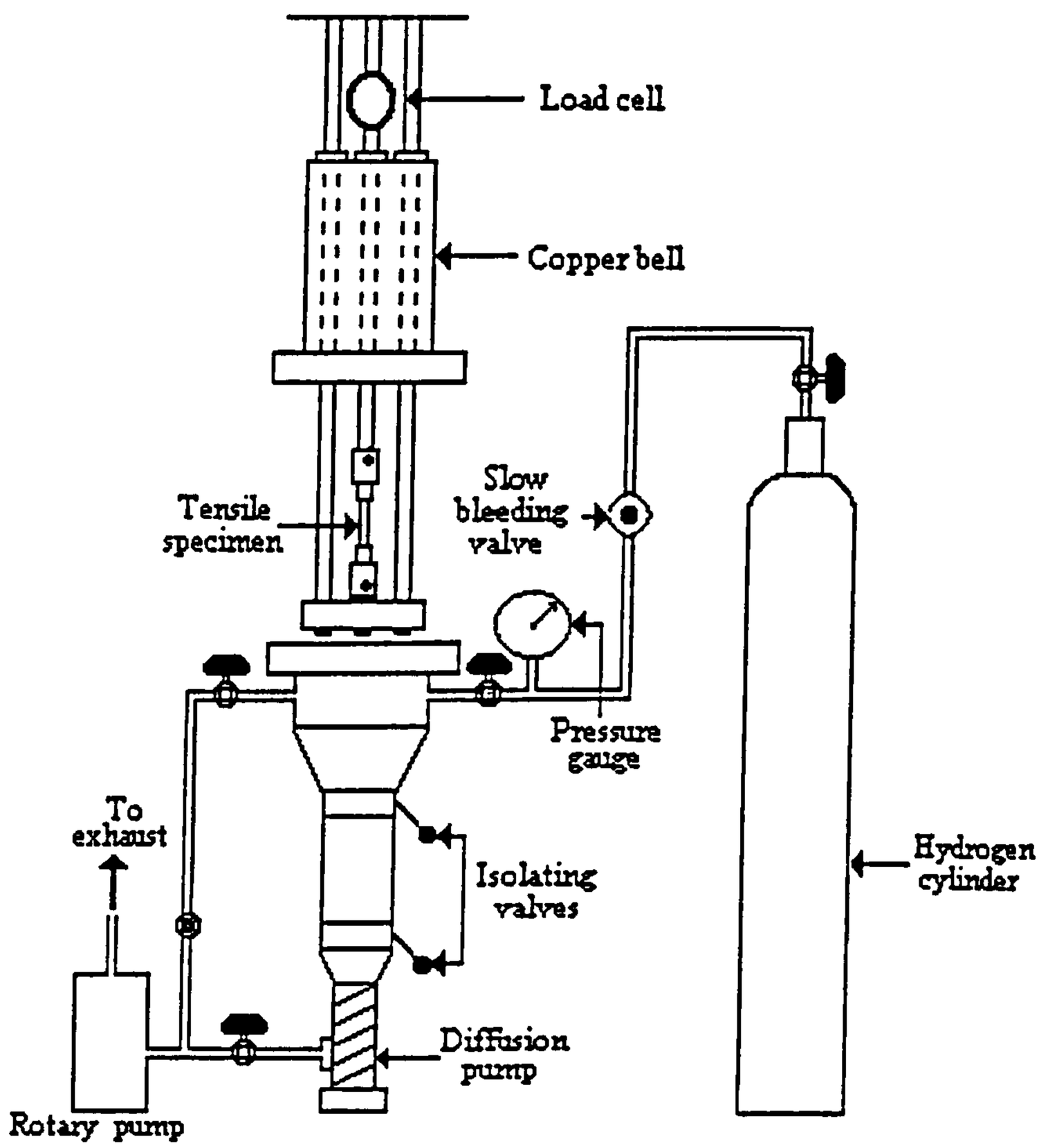

Figure 3.13 The semi-hard straining machine.

The mean diameter of the final area was measured from a profile image of the two halves of the broken specimens fitted together using travelling microscope. The % reduction in area (%RA) was obtained by comparing this with the original.

3.5.2 Straining in gaseous hydrogen atmosphere

For straining in a gaseous hydrogen atmosphere, the specimen is mounted in the relatively-hard tensile machine and then surrounded by a 150 mm diameter copper bell which can be sealed onto a flange leading to rotary and diffusion pumps that can produce a vacuum of < 2.0 x 10^{-5} torr, (Figure 3.14). After achieving a good vacuum, the bell is sealed off from the vacuum system and hydrogen gas in introduced, through a slow bleeding valve, to the desired testing pressures (0.5, 1.0, or 2.0 bar). The specimens were then strained to failure at the desired rate.

3.5.3 Straining cathodically polarized specimens in aqueous environments

Potentiostatic control was implemented in testing specimens in various, aqueous solutions at different temperatures. The straining was carried out in a hard tensile machine (Figure 3.14) with a calibrated 5000 lb load cell (1200 N/mv), at a strain rate of 2.0 x 10^{-6}/s as referred to the original gauge length of the specimen. The potentiostatic technique maintained the electrode potential of the tensile specimen constant with respect to a saturated calomel electrode (sce) throughout the test period. The specimen was fixed in the centre of a 150 ml cylindrical glass cell, which was surrounded by a heating coil for high temperature testing. The cell contained a platinum counter electrode, a thermometer, and a control thermocouple and

was connected to a saturated calomel electrode (sce) via string bridge. The potentiostat was used to control the potential of the tensile specimen from -300 to -1200 mV (sce) at the desired temperatures. The output of the load cell was fed into a recorder, and load vs time curves were obtained for subsequent analysis.

3.6 Hydrogen sulphide testing

To establish the effect of hydrogen generated in a hydrogen-sulphide-bearing environment on the material under investigation, specimens were strained in a glass cell similar to that used in the cathodic polarization tests. However, large scatter in the results, particularly at room temperature (Table 3.7), led to the belief that the cell was not completely sealed and air may have leaked in. Therefore, a special PTFE cell, cylindrical in shape with a screw-in top lid which can be sealed to the main body of the cell via an O-ring, was designed. It incorporates a thermometer, a control thermocouple, a saturated calomel reference electrode, a platinum counter electrode for testing under controlled potential conditions, and glass inlet and outlet tubes to allow continuous bubbling of the hydrogen sulphide gas into the solution during the entire period of the test (Figure 3.15). After fitting in all the components needed, the cell was filled with the testing solution and mounted into a hard tensile machine, similar to that used in the cathodically polarized experiment, but situated in a fume cupboard. A mini hydrogen sulphide gas cylinder is then connected to the inlet tube of the cell via a slow bleeding valve and stainless steel tube. The outlet from the cell is connected to a 2.0 litre container of 1M NaOH solution, via a 1.0 litre plastic container to prevent backflow of the caustic solution into

Table 3.7 The results obtained when using the glass cell showing a large scatter in the %RA.

Test environment	Temperature(°C)	pH_0	pH_f	Pot.(sce) mV	%RA
3.5% NaCl + H_2S	27	6.50	4.23	-420	36.8
3.5% NaCl + H_2S	22	6.62	4.34	-432	72.1
3.5% NaCl + H_2S	25	6.56	4.26	-419	68.7
3.5% NaCl + H_2S	25	6.60	4.25	-428	34.6
3.5% NaCl + H_2S	20	6.55	4.31	-437	74.3

Where: pH_0 is the pH at the start of the test (before H_2S saturation)
pH_f is the pH after saturation with H_2S.

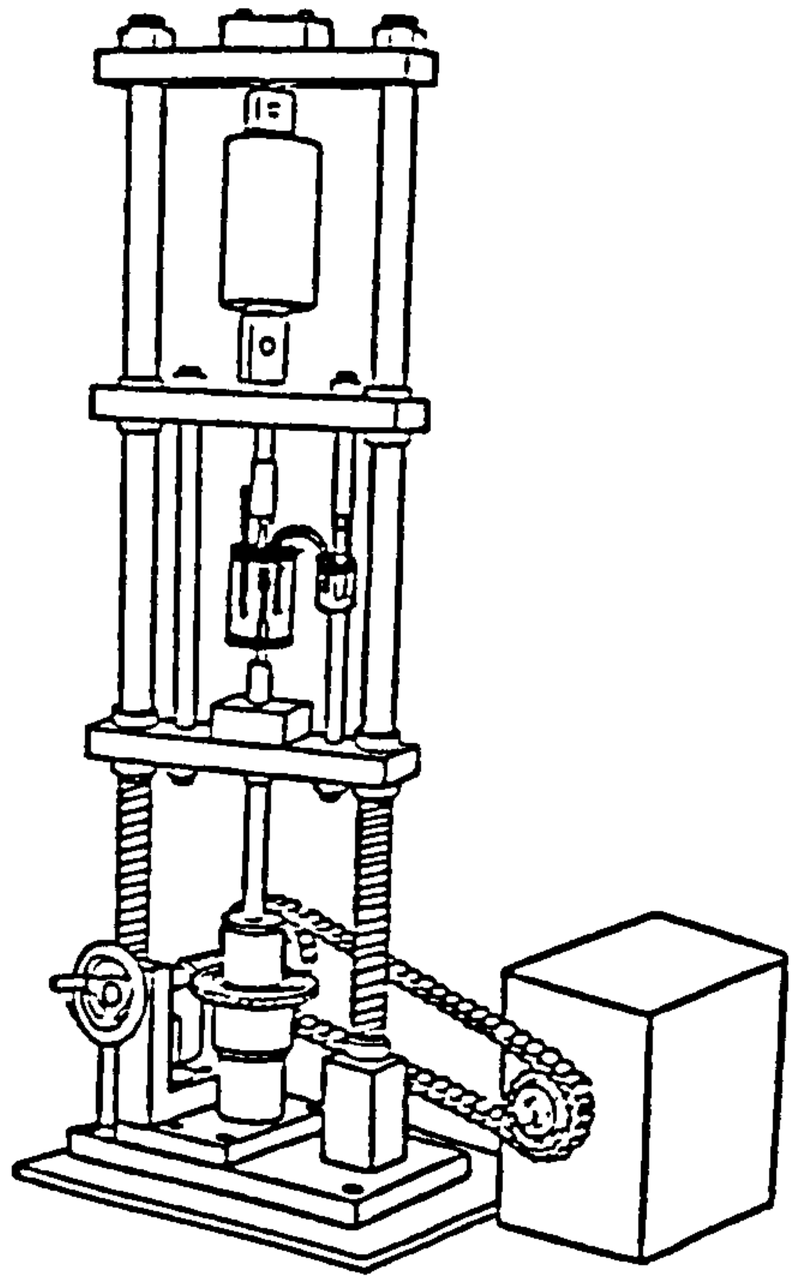

Figure 3.14 The hard tensile straining machine.

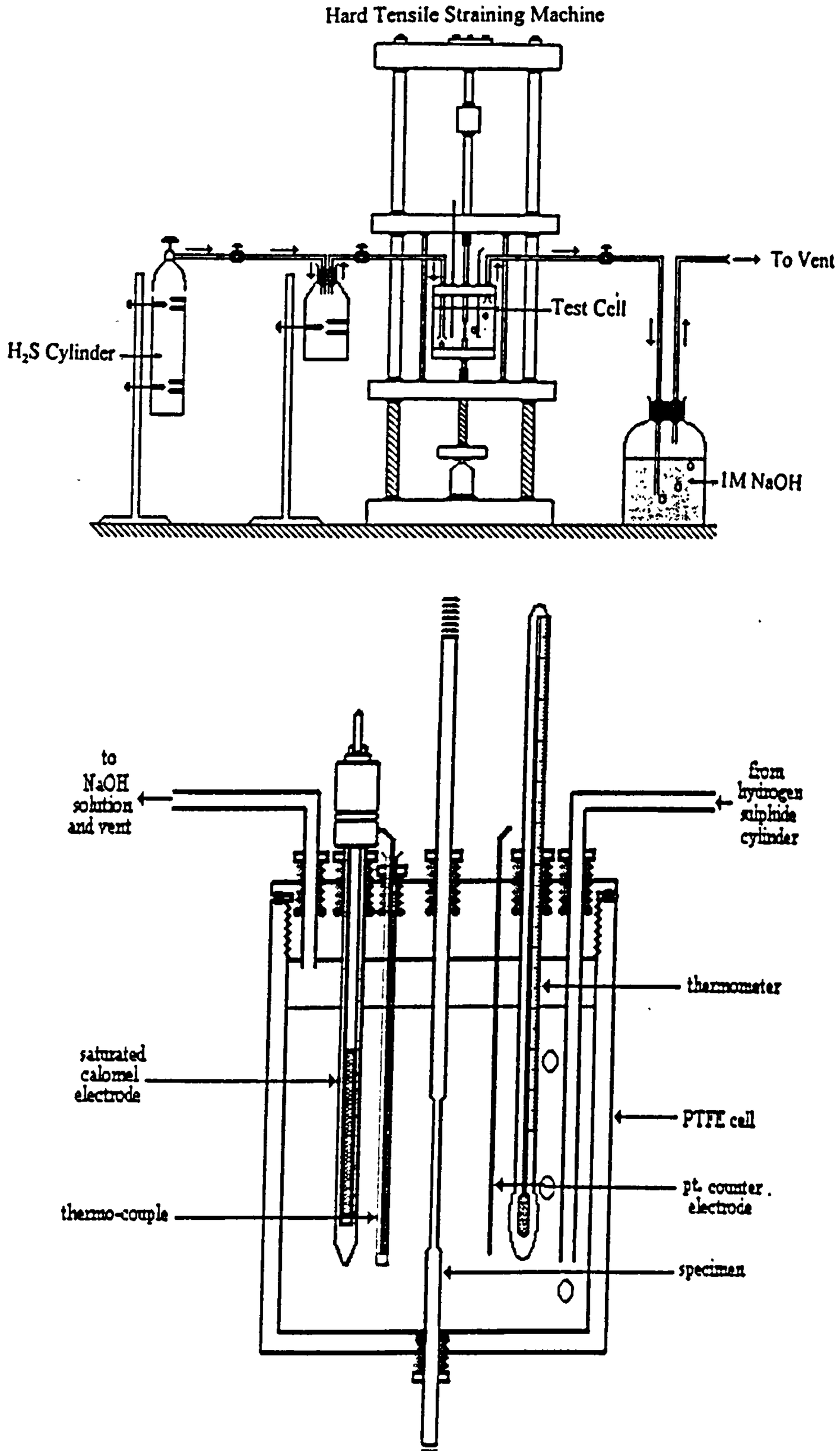

Figure 3.15 The arrangement of the apparatus used in hydrogen sulphide testing.

the test cell, in order to absorb hydrogen sulphide waste before venting it to atmosphere. The sodium hydroxide solution was replaced periodically to insure the complete absorption of the hydrogen sulphide. The bubbling rate of the H_2S into the test solution was started at rate of 300 ml/min for about 3 hours, at which the open circuit potential plot stabilized at about -550 mV (sce), (which was taken as a criteria for hydrogen sulphide saturation). The rate was then lowered to 100 ml/min, which proved to be sufficient to maintain saturation during the entire period of the tests. When the testing temperatures (0 to 95°C) and H_2S saturation were stabilized (about 3 hours), the tensile machine was switched on, and a constant strain rate applied until the final failure of the specimen. The open circuit corrosion potential was monitored continuously during testing.

Sub-ambient temperatures were achieved by using an immersion cooler . A copper block, into which the cooling coil was inserted, was fastened next to the testing cell and the whole arrangement was wrapped with glass wool for insulation. The arrangement was then left for 6 hours to cool and stabilize at the desired lower temperature before the solution was saturated with hydrogen sulphide. The lowest temperature used was 2°C in order to prevent any partial solidification of the solution. After the completion of the test the cell was drained into a hydrogen sulphide waste container, dismantled, and cleaned for the next test. The fractured specimens were washed in distilled water, dried in acetone and stored in a desiccator for analysis.

Test solutions:

All test solutions used in this work were prepared from reagent grade chemicals and distilled water(pH ≈ 7.00). Three solutions were used in these tests:

a) Deionized water + varying amounts of sodium chloride , from 0 to 600 wppm Cl^- pH ≈ 6.5

b) 3.5% sodium chloride solution pH ≈ 6.5

c) NACE standard solution (TM-01-73) (50g sodium chloride solution + 5g glacial acetic acid + 945ml deionized water, pH ≈ 2.7).

It has to be mentioned that in the first few tests conducted in low chloride solution saturated with hydrogen sulphide, a saturated calomel electrode was used not realising that Cl^- ion would leak into solution. Therefore, subsequent correction to account for the increase of the Cl^- ion in solution was made by measuring the increase of the conductivity of exactly the same volume of deionized water after leaving the saturated calomel electrode in it at the same temperature and for exactly the same time duration as the specific test. A plot relating the conductivity of solution to the amount of Cl^- present (in the form of KCl) was available and the actual concentration of the Cl^- ion was thus obtained. Two additional tests were conducted in 50 and 600 wppm Cl^- solutions using a sulphate electrode to check the integrity of the results.

3.7 Pitting tests

Long term pitting tests were conducted on 10mm x 10mm specimens cut from materials B and C. Specimens were polished to 1μm finish, after which they were slightly etched in order to investigate the sites of pit initiation. The

specimens were carefully washed with acetone, to prevent crevices that might be caused by dirt or oil spots, before being immersed in the test solution (50g NaCl + 5g glacial acetic acid + 945g deionized water pH ≈ 2.7). Tests were conducted at different temperatures from 25°C to 90°C in glass flasks. At the end of an exposure period of 96 hours (4 days) specimens were removed, washed successively with distilled water and alcohol and studied by optical microscope.

Some long term pitting tests, of both materials, were also conducted in the same solution saturated with hydrogen sulphide at 25°C and 90°C for 720 hours.

3.8 Polarization curves

Potentiodynamic polarization measurements were conducted, on 2.0 cm^2 specimens made out of material B and C using a Wenking PGS-81 potentio-galvano-scan coupled with a logarithmic output current sink (Model MLS-81). The specimens were dry polished to 600 grit paper followed by wet polish. The test cell (Figure 3.16) was filled with the test solution and heated to the desired temperature. Prior to immersion into the cell the specimen were degreased with acetone and dried in air. A negative potential of -1000 mV (sce) was applied to the specimen immediately and kept there for a constant time period in all of the tests (1 hour) before starting the potential scan, to ensure compatibility of the results. It was observed that varying the holding time at the negative potential could affect the surface of the specimen and the pH of the solution, which in turn may influence the free

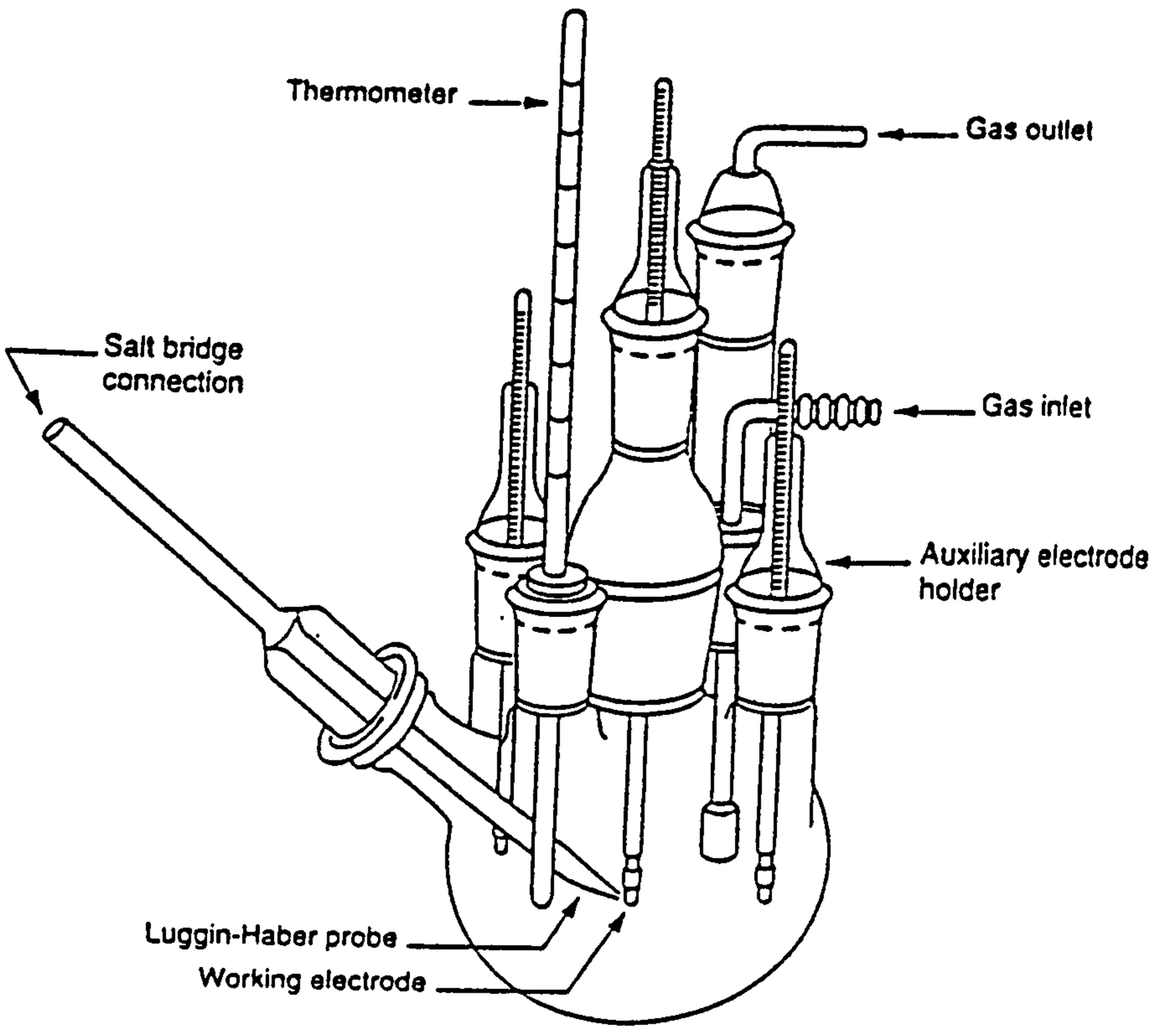

Figure 3.16 The apparatus arrangement used in the potentiodynamic polarization measurements.

corrosion potential of the specimen (Figure 3.17). The potential scanning rate also seems to have an effect on the position of the free corrosion potential (Figure 3.18) and therefore it was kept constant at 10 mV/s for all tests. For polarisation curve measurements in solutions saturated with hydrogen sulphide the apparatus was moved into a fume cupboard and the solution was purged with hydrogen sulphide for 10 minutes. The bubbling rate was lowered to 100ml/min for about 2 hour (until the open circuit potential of the specimen stabilized which was the criteria adapted for hydrogen sulphide saturation) before commencing with the potential scan. Some polarization tests were conducted in solution purged with nitrogen for 1 hour before saturating with hydrogen sulphide in order to study the effect of exclusion of oxygen from the environment, yet the obtained curves were identical to those done without nitrogen purging, which indicates that adequate saturation with hydrogen sulphide would be as effective in expulsion of oxygen from the test solution.

3.10 Microstructural and fractographic examinations

Selected samples from the specimen were mounted in bakelite and wet ground on 220,400 and 600 grit before polishing to 1μm diamond finish, prior to etching with 20 ml HCl + 80 ml H_2O + 3g $K_2S_2O_5$, which colours the ferrite(brown

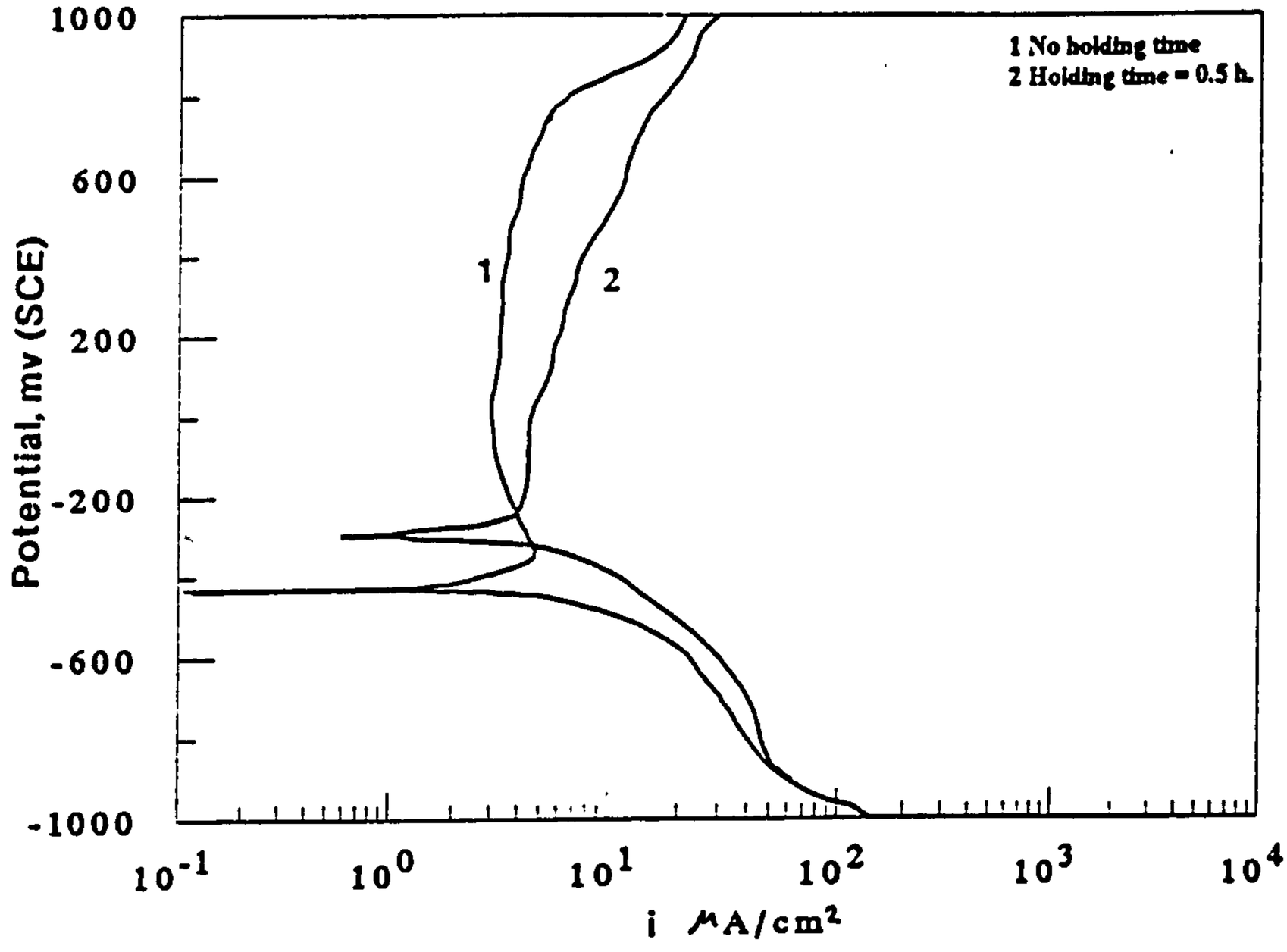

Figure 3.17 The influence of holding time at low potential on the polarization curve at 10mV/s.

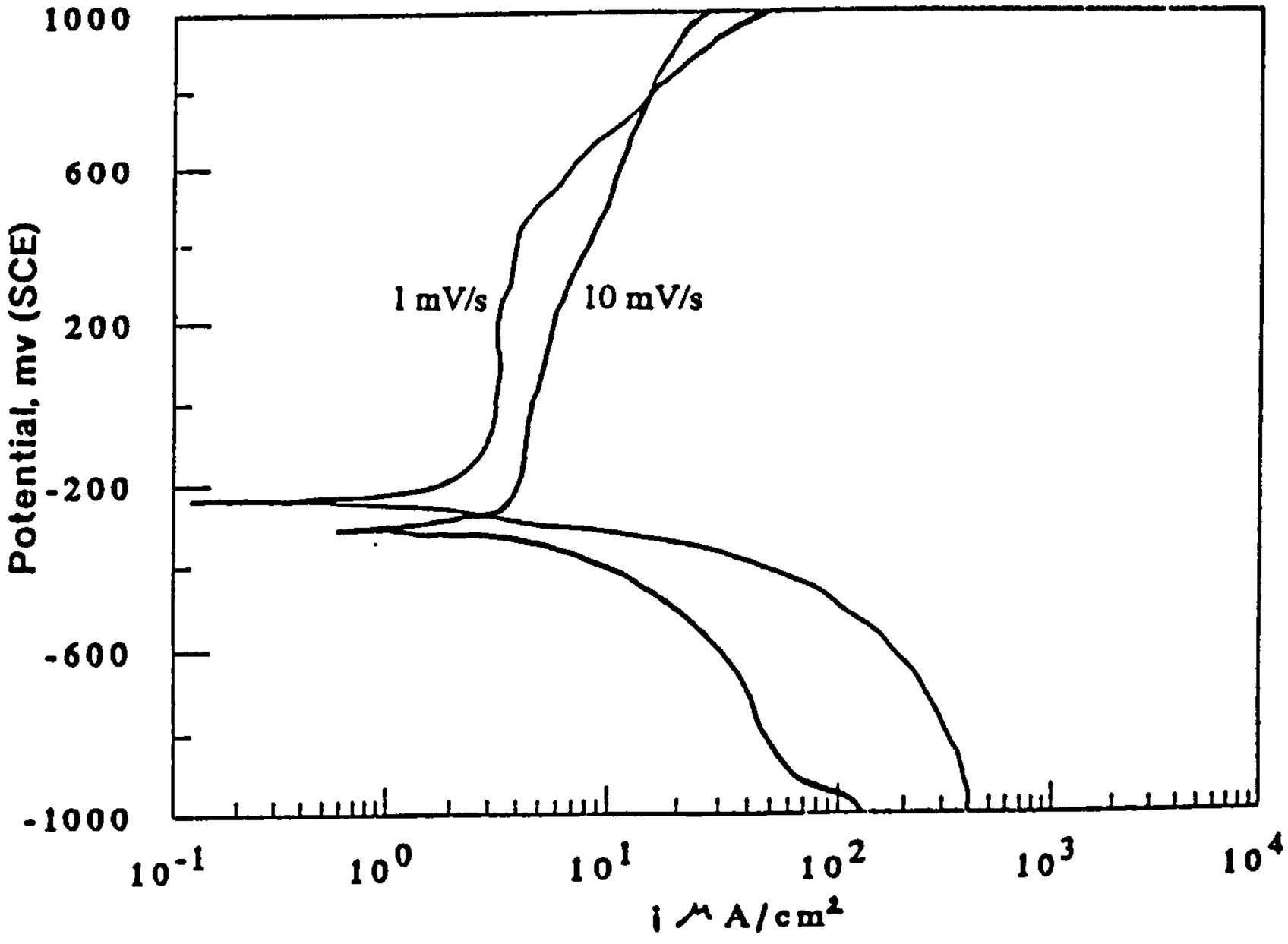

Figure 3.18 The influence of scanning rate on the polarization curve for a holding time of ½h.

or blue depending on the immersion time) and leaves the austenite unattacked. The formation of martensite in the austenite islands was identified using 100ml of the above etch with the addition of 1 g $NH_4F.HF$. Beraha and Shpigler /176/ found that this etch colours the martensite blue and the austenite yellow in 301 austenitic stainless steel. They also indicated that if delta ferrite is present, as in 17-4 PH stainless steel, it would be coloured brown. In the duplex steels, however, it was found after numerous trials that both martensite and ferrite will attain the same colour, brown or blue depending on the etching time. Metallographic specimens were then examined on an Olympus BHSM optical microscope.

Fractured tensile specimen were ultrasonically cleaned with acetone before being examined in an Hitachi S2400 electron microscope. When corrosion product was present on the fractured specimens, e.g. in the hydrogen sulphide tests, they were cleaned, for a few minutes, by cathodic polarization in alkaline sodium cyanide solution with simultaneous ultrasonic cleaning, which produced very clean fracture surface.

Chapter 4

Results and discussion

4.1 The effect of strain rate on mechanical behaviour

4.1.1 Uncharged material strained to failure in air

The mechanical properties of all the uncharged materials (A, B, C, and D) showed no significant dependence on the variation of strain rate, in the range 2.1×10^{-6}/s - 6.4×10^{-3}/s (Figure 4.1a and 4.1b), and a characteristic ductile fracture consisting of micro-void coalescence was universally observed (Figure 4.2). The cross sections of the fracture were circular for materials B and D, whereas for materials A and C they were elliptical, reflecting microstructural anisotropy (Figure 4.3a and 4.3b).

Optical microscopy of a longitudinal specimen of material C revealed that the larger axis of the ellipse (a) corresponds to the tangential direction of the original pipe, and the short axis (b) corresponds to the radial direction (Figure 4.4). The average values obtained for the various mechanical properties for the four materials (listed in Table 4.1) were employed subsequently to calculate the embrittlement index (EI) for uncharged specimens strained to failure in hydrogen environments and for thermally charged specimens strained to failure in air.

4.1.2 Uncharged specimens strained to failure in hydrogen gas

When uncharged longitudinal specimens (material C) were strained to failure in gaseous hydrogen, at various pressures up to 2.0 bar, there was no detectable change in the 0.2% flow stress or in the ultimate tensile strength.

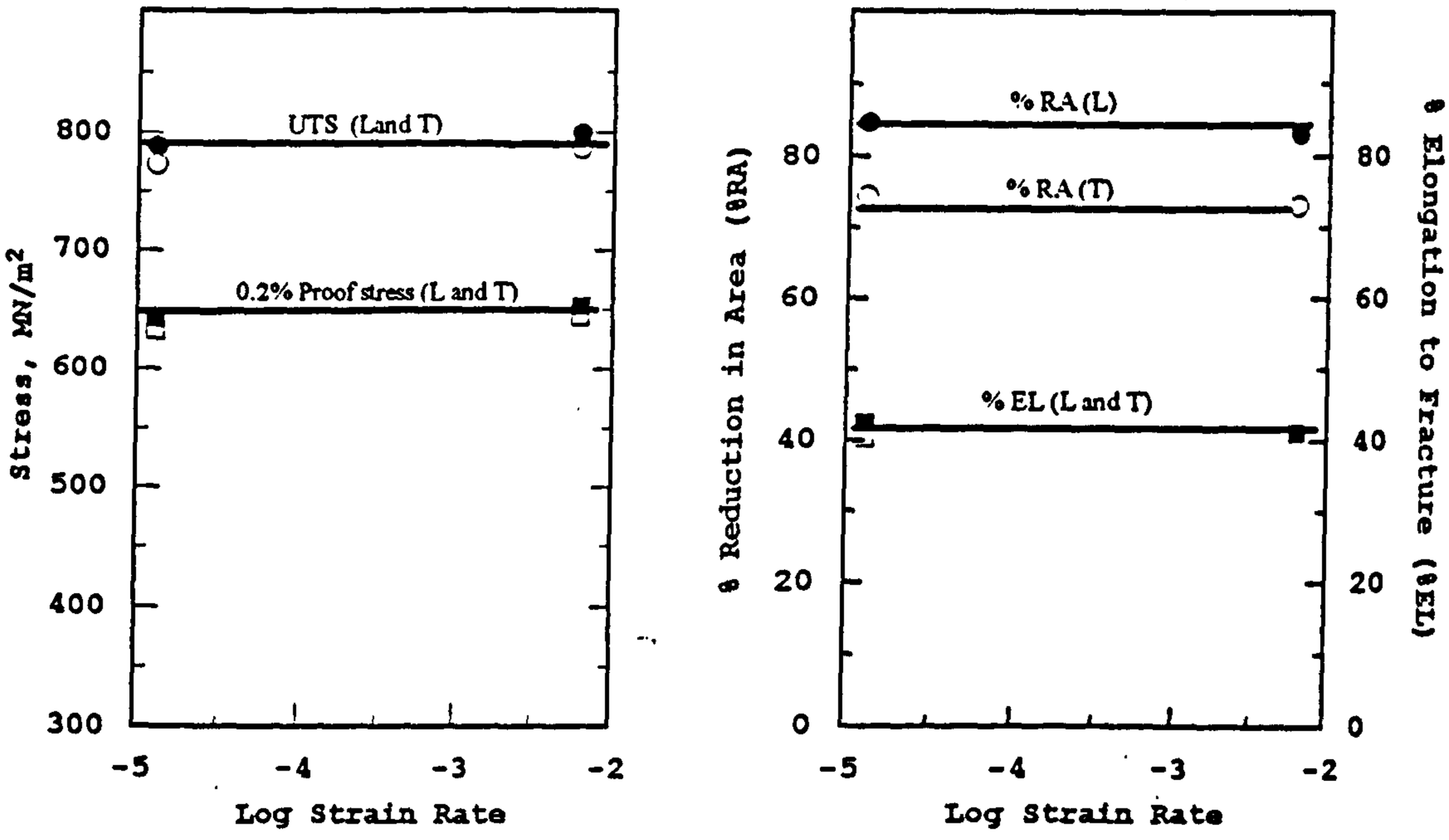

Material A

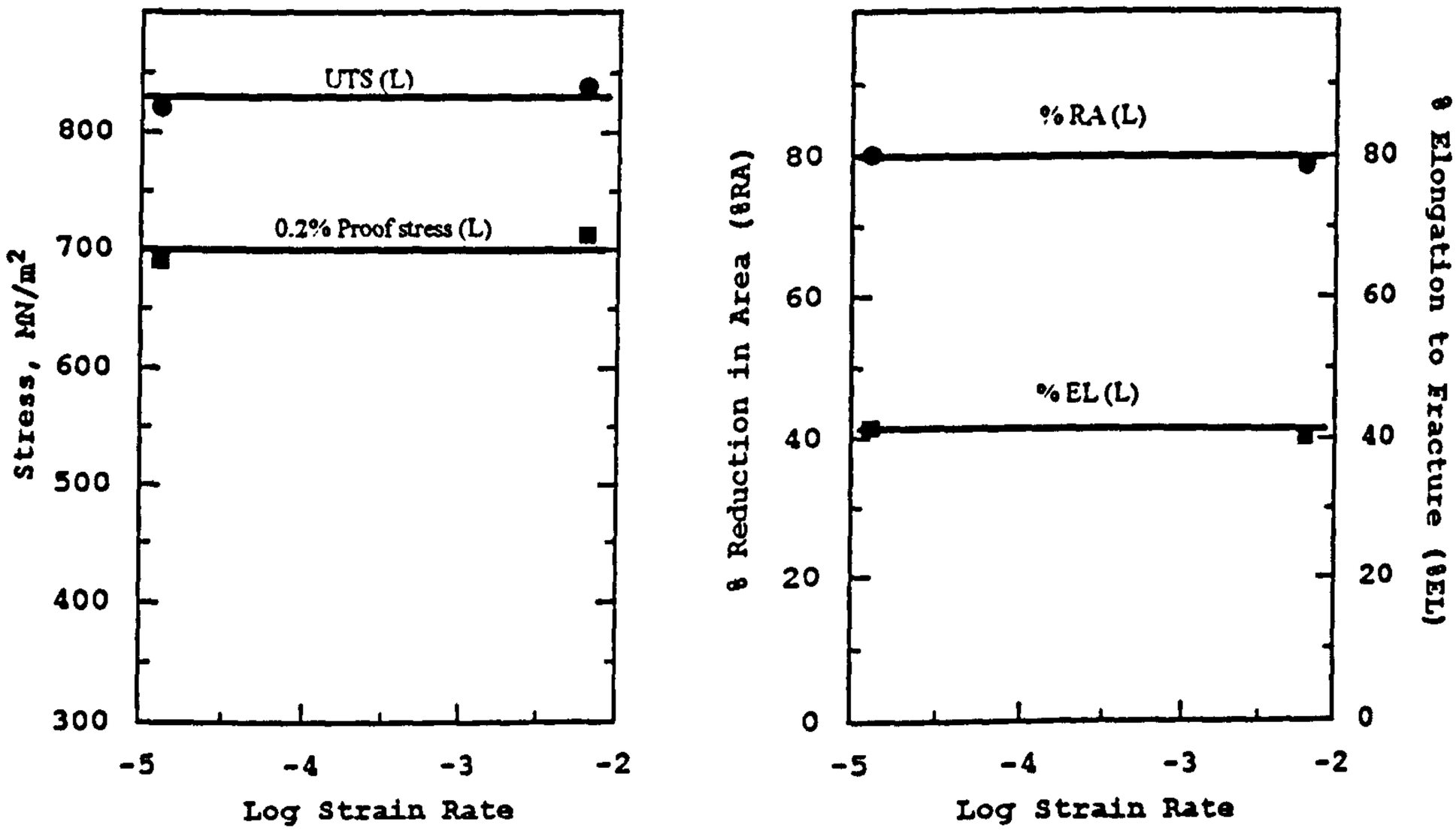

Material B

Figure 4.1a The mechanical properties of the duplex steels, strained to failure in air, as a function of strain rate.

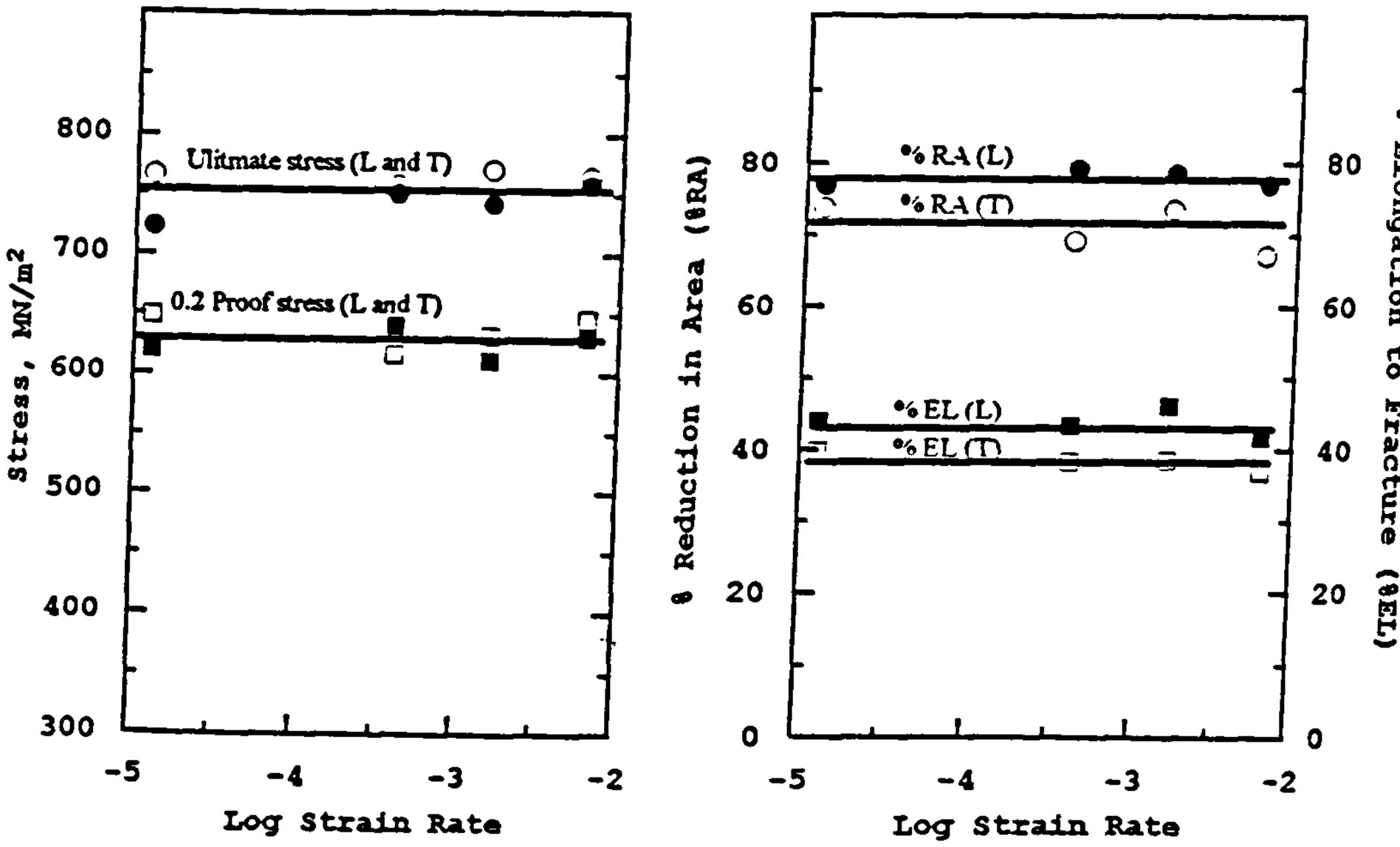

Material C

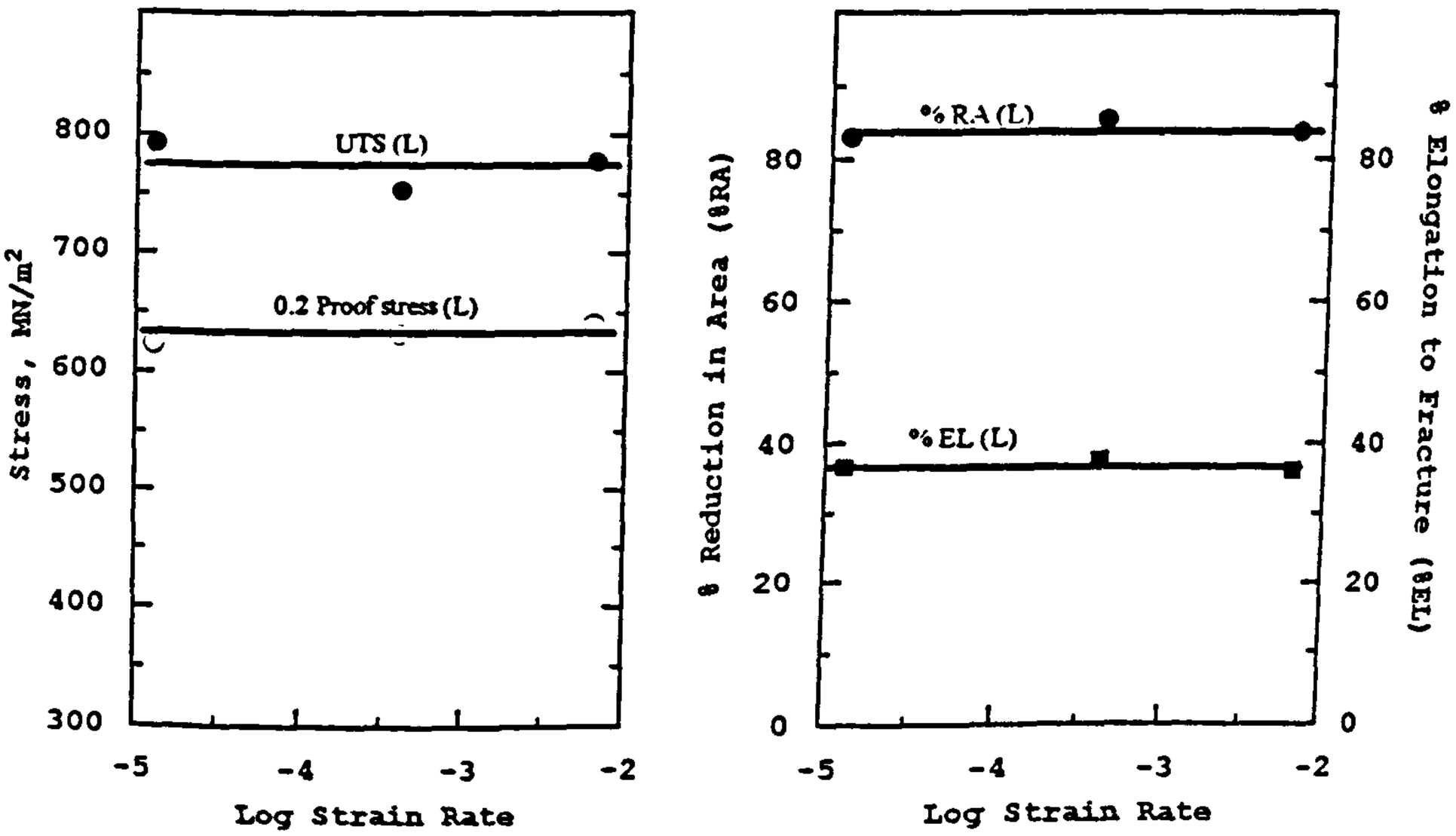

Material D

Figure 4.1b The mechanical properties of the duplex steels, strained to failure in air, as a function of strain rate.

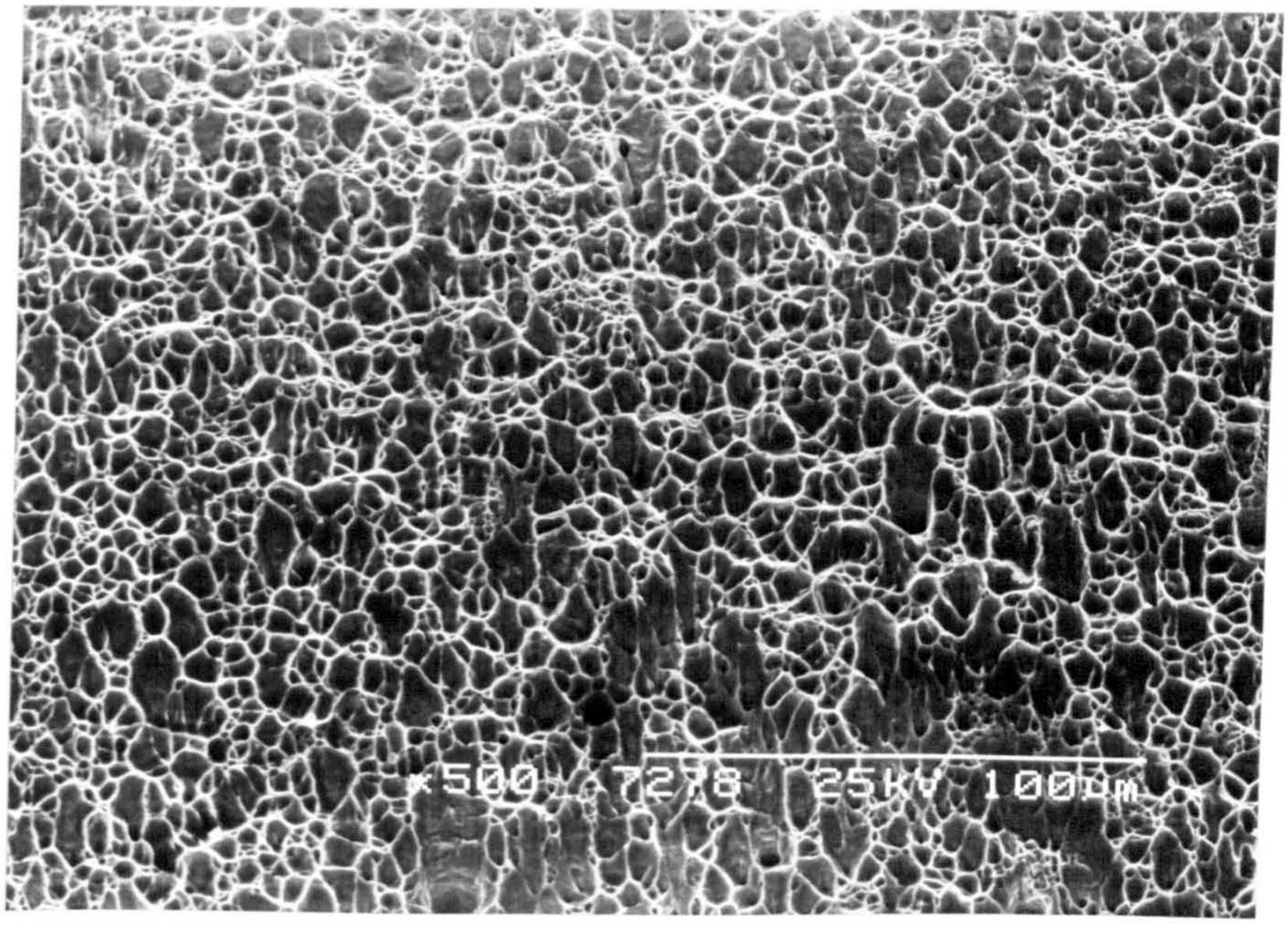

(a)

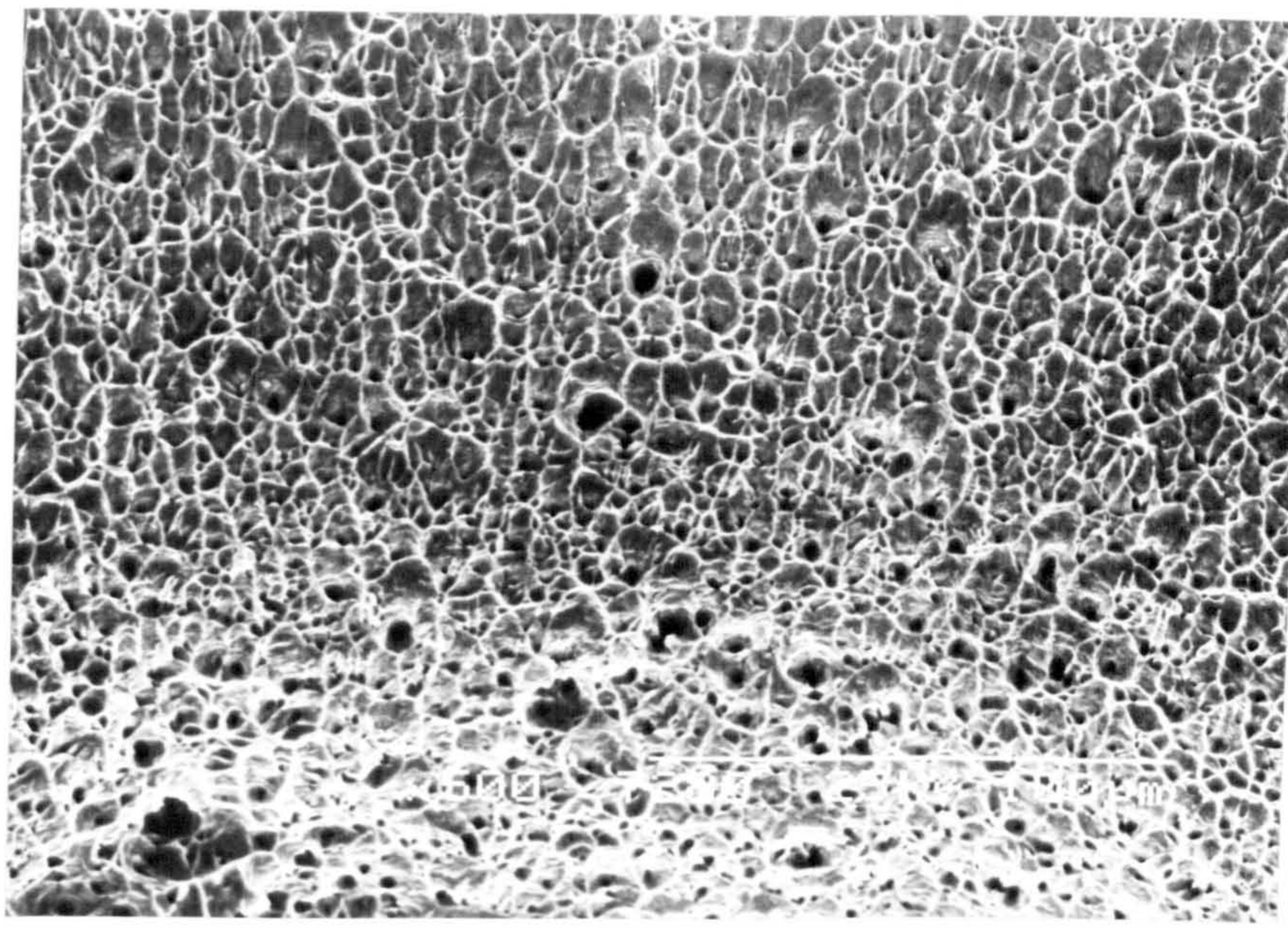

(b)

Figure 4.2 Fracture surfaces of uncharged duplex stainless steel strained to failure in air at a strain rate of 1.2×10^{-5}/s; a) material C, b) material D. Both exhibit micro-void coalescence.

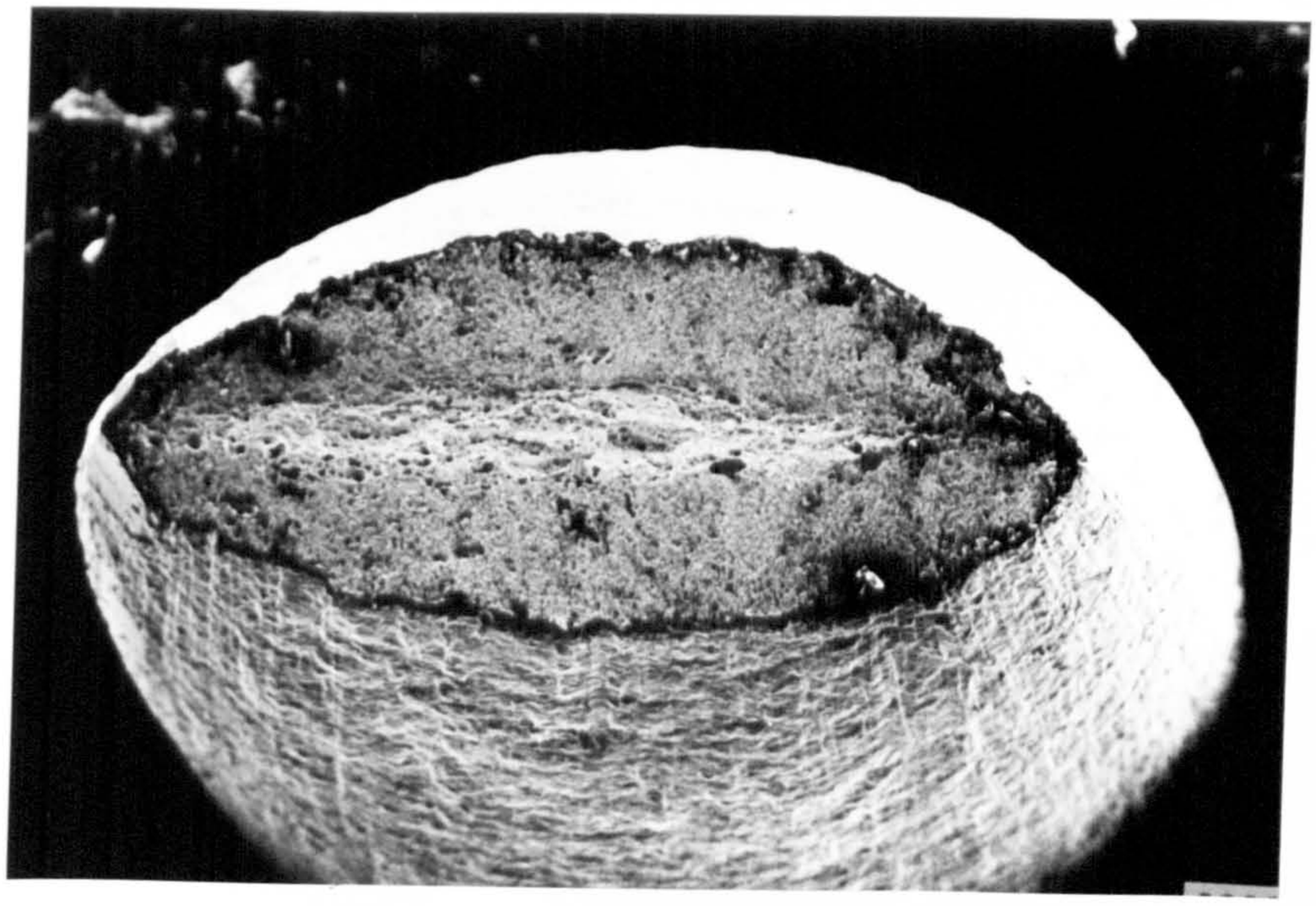

Material A

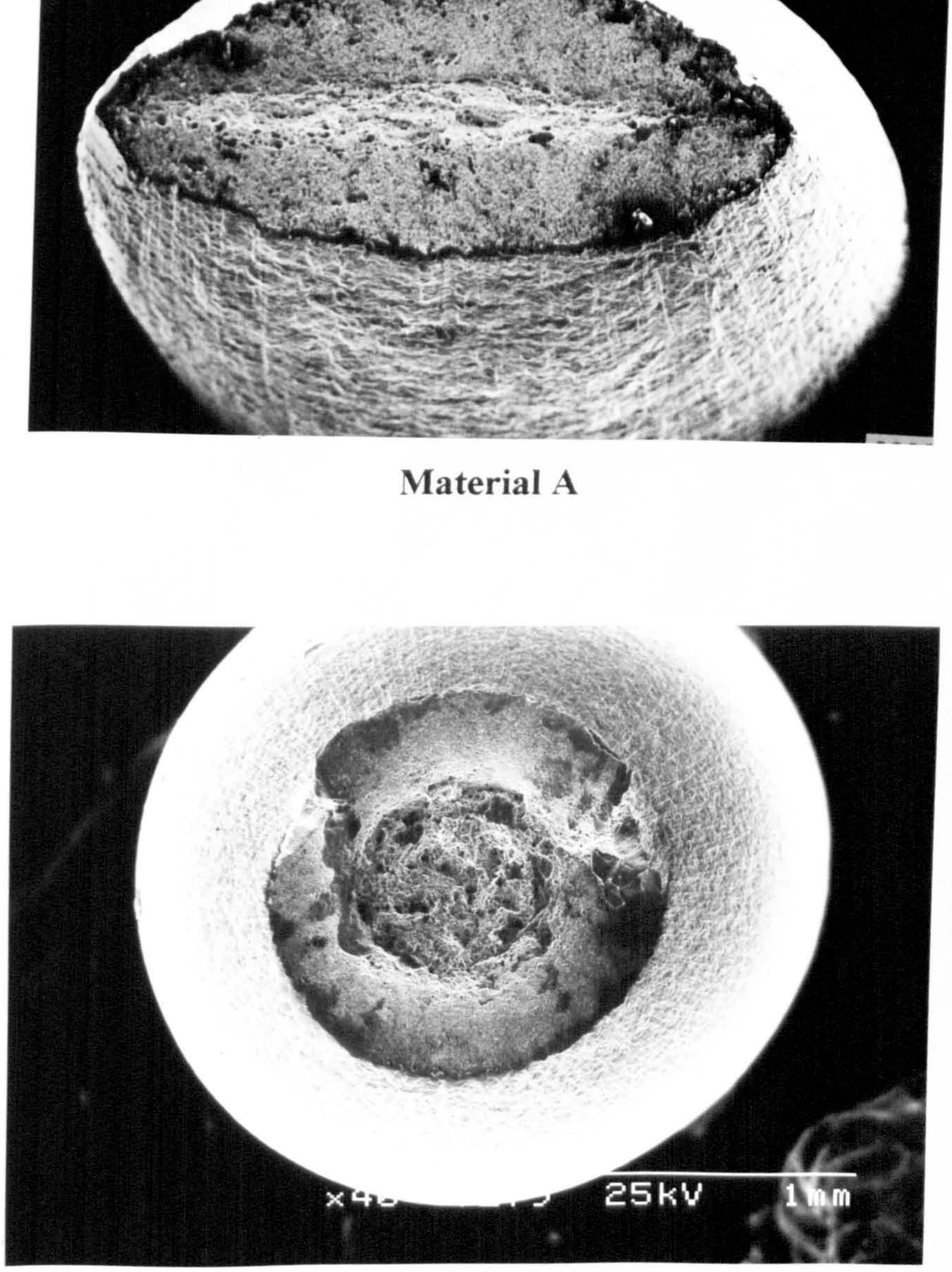

Material B

Figure 4.3a Fracture surface of tensile specimens of as received material strained to failure in air at 1.3×10^{-5} /s.

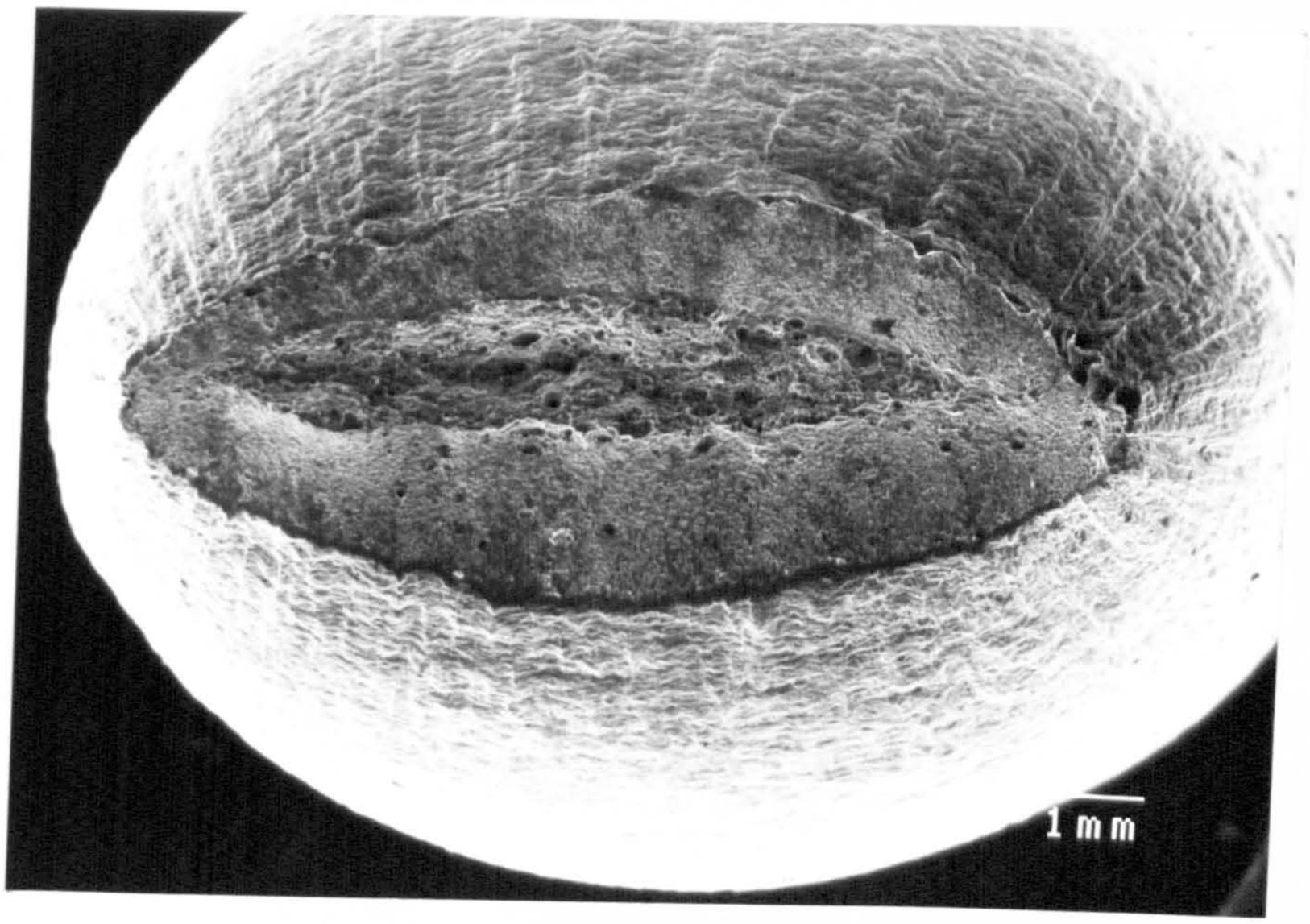

Material C

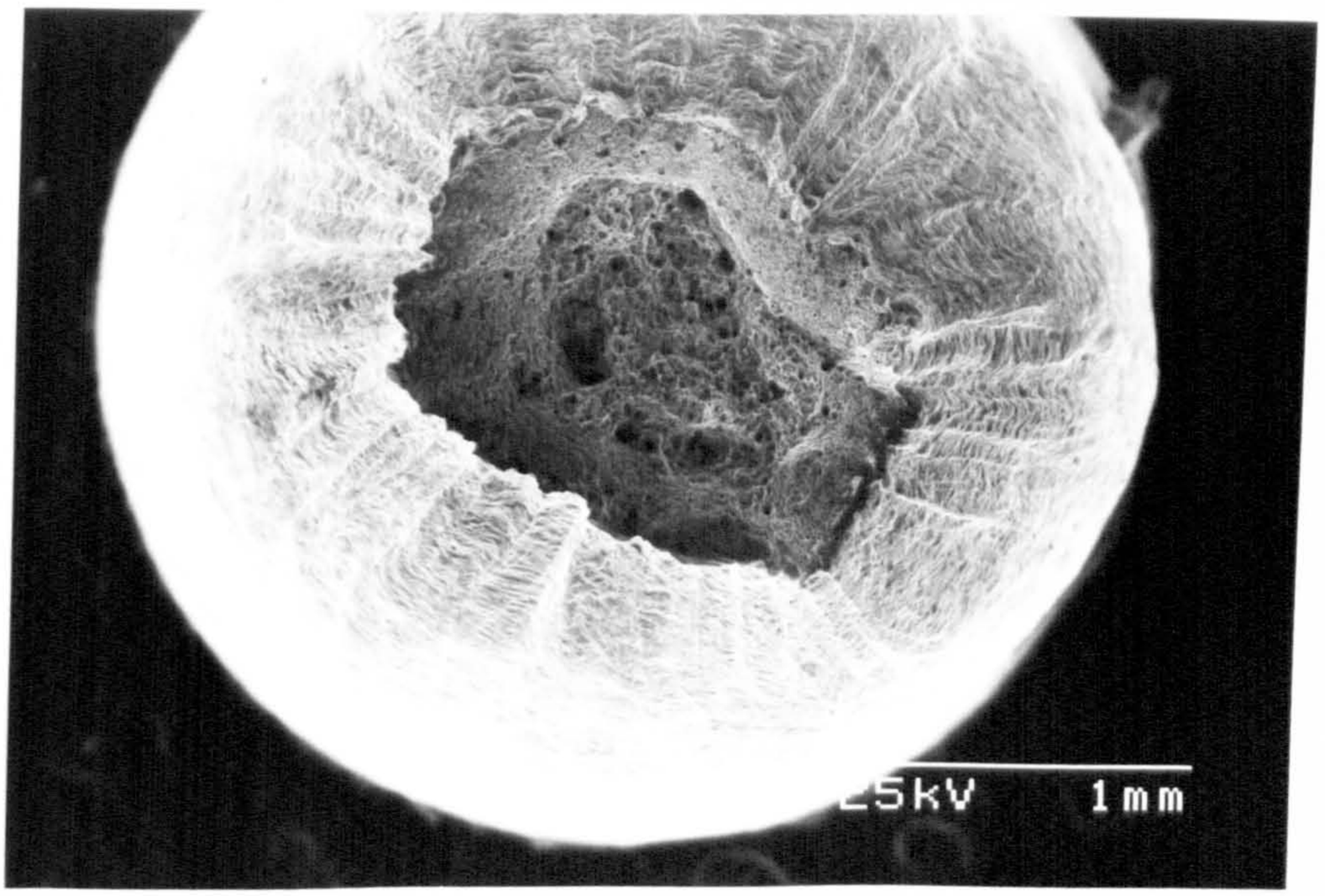

Material D

Figure 4.3b Fracture surface of tensile specimens of as received material strained to failure in air at 1.3×10^{-5} /s.

Table 4.1 Mechanical properties of duplex stainless steels in the as received condition.

Material	Orientation	% Reduction in area	% Elongation	0.2% Proof stress MN/m²	Ultimate tensile strength MN/m²
A	Longitudinal	83	42	650	794
	Transverse	74	41	638	779
B	Longitudinal	80	41	701	830
	Transverse	-	-	-	-
C	Longitudinal	78	44	623	744
	Transverse	71	38	636	771
D	Longitudinal	84	37	632	774
	Transverse	-	-	-	-

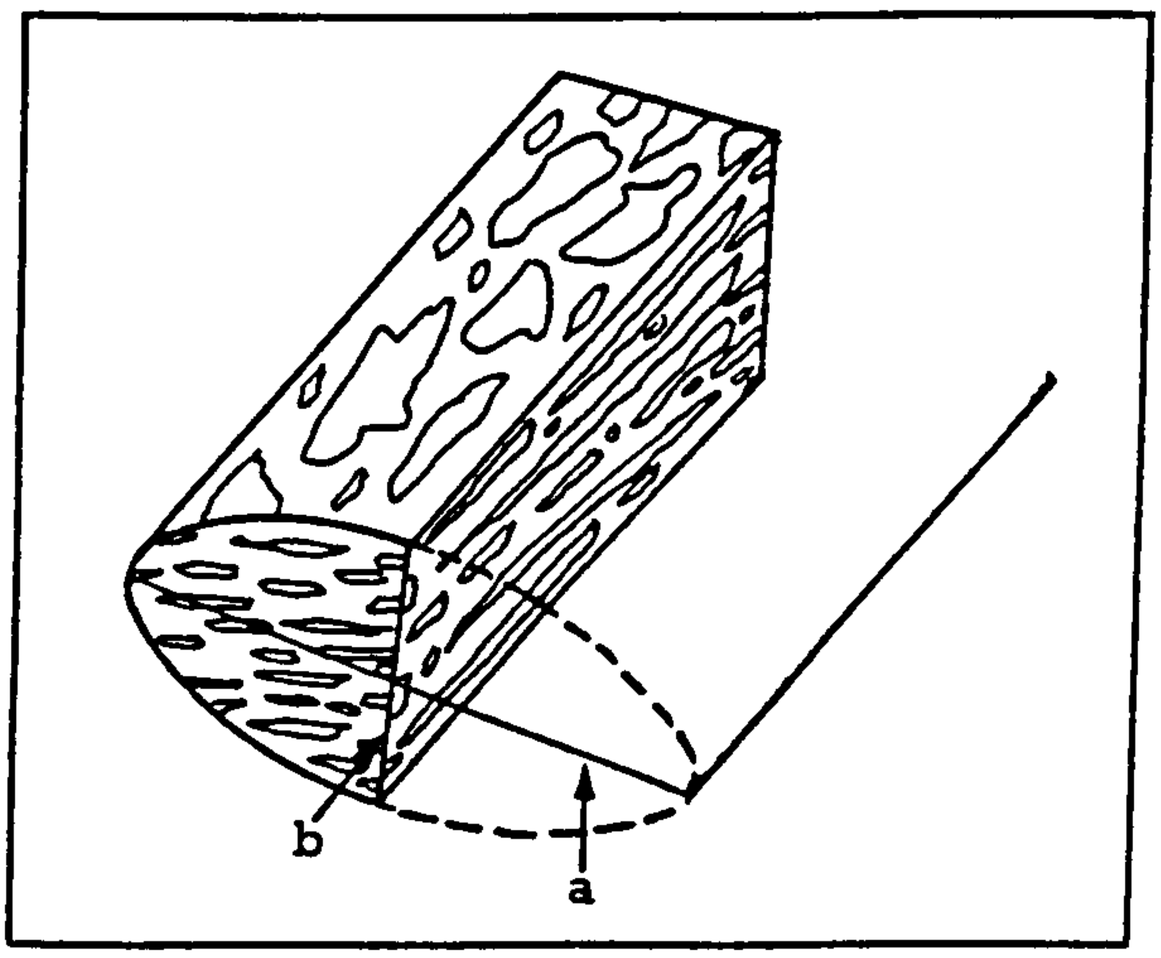

Figure 4.4 Schematic representation of the microstructure of an uncharged longitudinal specimen (material A and C) strained to failure in air.

However, the % reduction in area, % plastic elongation were significantly reduced. As the hydrogen pressure increased, the embrittlement also increased. The induced embrittlement, expressed as % reduction in area, especially at the higher hydrogen pressures, showed definite dependency on the strain rate. The % reduction in area, in 2.0 bar hydrogen atmosphere, decreased from about 68% at a strain rate of $6.4x10^{-3}$/s to about 40% at a strain rate of $1.3x10^{-5}$/s (Figure 4.5). On the other hand, even though the % elongation to fracture showed a dependence on the strain rate, this only involved a drop from 38% to 30% over the same range of strain rate, and this dependence was less clear due to large scatter, especially in the longitudinal directions (Figure 4.6). This phenomenon is attributable to the fact that the austenite is less susceptible to embrittlement (at least from straining in hydrogen where the anticipated hydrogen concentration is much less than when specimens are thermally charged) and a few of the long austenite islands (fibre-like) may hold the specimen together until a very late stage of the stress strain curve. As a result, the measured elongation and the drop in fracture stress are not highly affected by the hydrogen. Therefore, a decision was made to adopt the % reduction in area as the main parameter for assessing embrittlement. The overall embrittlement or drop in ductility observed is only evident very late in the straining process and variations in the shape of the load extension curve only become apparent after necking occurs (Figure 4.7 and Table 4.2), and all of the fractures showed different degrees of necking. Scanning electron microscopy of the gauge length after fracture revealed multiple secondary cracking. This was generally confined to the necked region, especially at the higher strain rate, but at the slower strain rate of $1.3x10^{-5}$/s cracks were

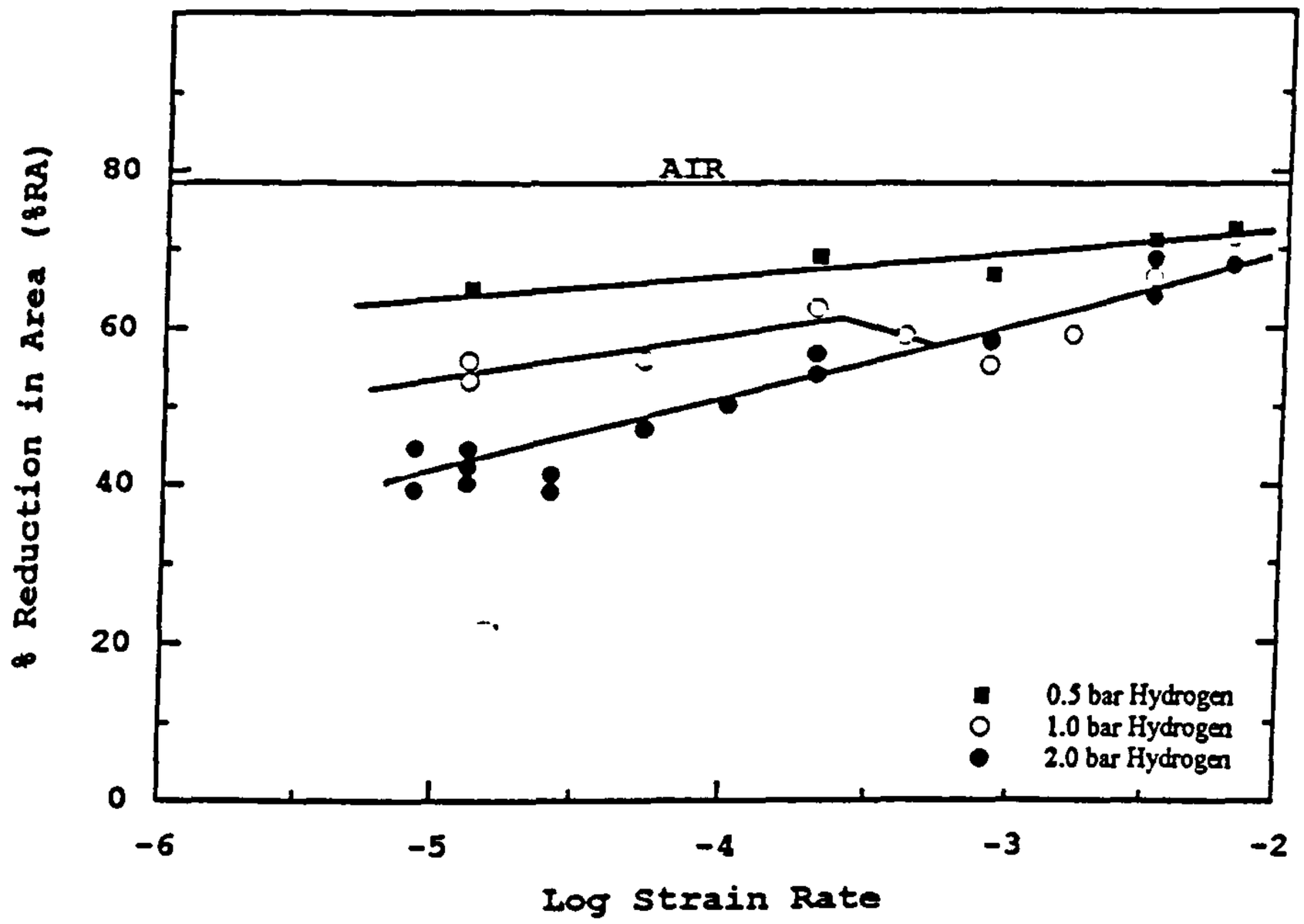

Figure 4.5 Variation of % reduction in area with strain rate for longitudinal specimens of duplex stainless steel (material C) strained to failure in different hydrogen pressures.

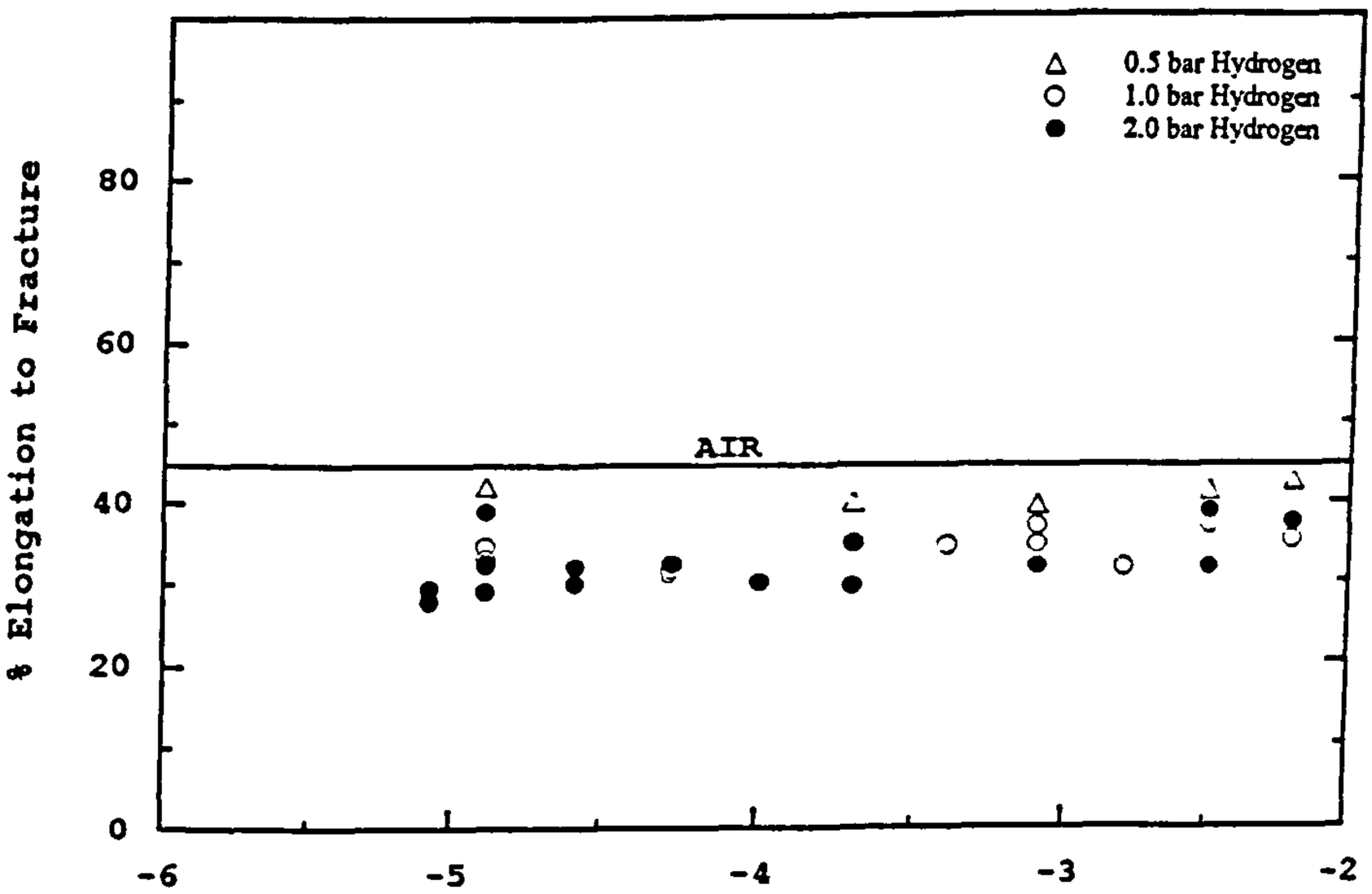

Figure 4.6 Variation of % elongation to fracture with strain rate for longitudinal specimens of duplex stainless steel (material C) strained to failure in different hydrogen pressures.

Table 4.2 Mechanical parameters of longitudinal specimens of duplex steel (material C) strained to failure in hydrogen gas.

Environment	Strain rate/s	% Reduction in area	% Uniform elongation	% Elongation to fracture	0.2% Proof stress, MN/m^2	Ultimate tensile strength, MN/m^2
0.5 bar hydrogen	1.3×10^{-5}	65.0	18.6	42.2	585	697
	2.0×10^{-4}	69.1	17.5	40.1	597	694
	8.0×10^{-4}	67.0	17.9	39.7	579	726
	3.2×10^{-3}	71.3	17.3	41.6	633	746
	6.3×10^{-3}	72.2	17.3	42.7	637	741
1.0 bar hydrogen	1.3×10^{-5}	54.6	17.1	33.8	598	710
	5.3×10^{-5}	56.0	18.2	31.5	632	708
	2.0×10^{-4}	62.6	17.6	35.0	626	726
	4.0×10^{-4}	59.0	17.4	34.5	607	607
	8.0×10^{-4}	55.3	17.8	35.9	638	643
	1.6×10^{-3}	56.3	17.4	31.7	655	656
	3.2×10^{-3}	66.5	18.6	37.2	668	594
	6.4×10^{-3}	71.6	17.9	35.3	649	593
2.0 bar hydrogen	8.4×10^{-4}	42.1	19.6	28.7	587	722
	1.3×10^{-5}	42.3	18.3	33.4	584	708
	2.6×10^{-5}	40.2	17.3	30.9	601	712
	5.3×10^{-5}	47.2	17.9	32.3	587	707
	1.0×10^{-4}	50.2	17.7	29.9	596	716
	2.0×10^{-4}	55.4	18.4	32.2	604	729
	8.0×10^{-4}	58.2	17.1	31.9	611	731
	3.2×10^{-3}	66.5	17.1	35.4	627	728
	6.4×10^{-3}	68.0	17.7	37.6	651	746

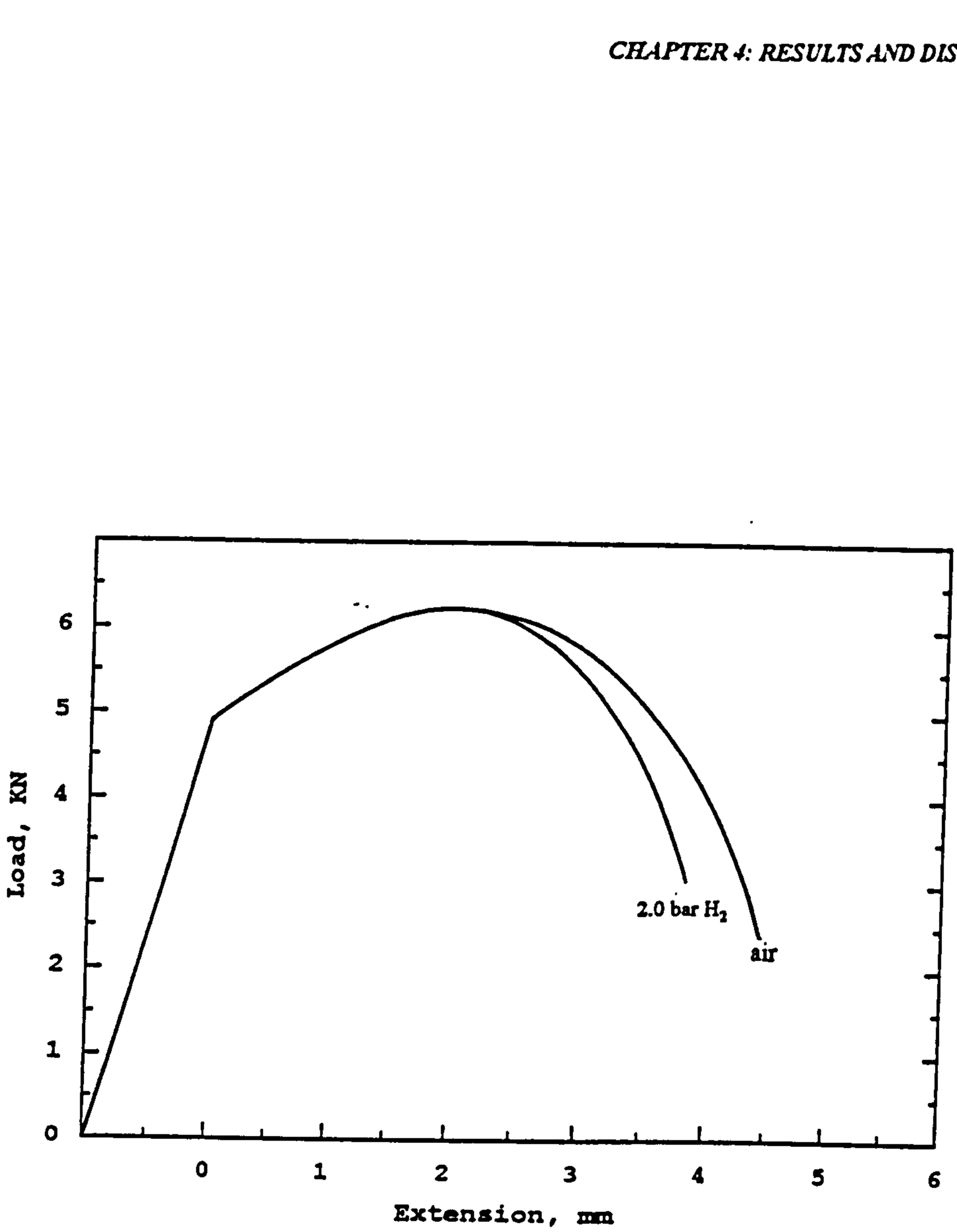

Figure 4.7 Load extension curve for longitudinal specimens of duplex steel (material C) strained to failure in air and in 2.0 bar hydrogen gas at a strain rate of 1.3×10^{-5}/s.

observed at greater distances from the main fracture, sometimes even in the uniform part of the gauge length. Secondary cracks naturally contribute to the erratic behaviour of the ductility loss assessed from % elongation to fracture (i.e. multiple secondary cracking and subsequent opening of the larger cracks give rise to a spurious ductility) and hence such measurements were not used to assess embrittlement. The ductility loss at the higher pressure of 2.0 bar increased linearly with the log of strain rate but, at the lower pressures of 0.5 and 1.0 bar, although the linear dependence is still generally apparent an enhanced loss in ductility is observed over a narrow range of strain rate between $2.0x10^{-4}$ and $1.6x10^{-3}$/s (Figure 4.5). This suggests that perhaps a multiple embrittlement mechanism is operative within this range. At lower strain rates the delivery of hydrogen to the critical sites, via dislocation sweeping, is increased thus delivering enough hydrogen to cause significant loss in ductility. On the other hand, at faster strain rates, the hydrogen delivery rate may be reduced because dislocations tend to break away from hydrogen /138,168/ and therefore hydrogen needs to be transported by some other means. The formation of martensite, α'(bcc) or ϵ (hcp), will undoubtably increase the delivery rate of hydrogen to the critical sites due to the higher diffusivity of hydrogen in these structures. Zheng and Hardie /178/ encountered a similar effect in their study of a similar duplex stainless steel, which they attributed to the formation of the hexagonal closed-packed ε martensite, identified by means of X-ray diffraction from the surface of a flat specimen. However, several attempts made to confirm whether austenite preferentially transforms to martensite within such a narrow range of strain rate (again using X-ray diffraction) have failed. This may

however be due to the confinement of any transformation to a very small region near the fracture which makes detection by X-rays difficult. Calculation of the austenite stability using the criterion proposed by Angel /44/(equation 2.9) gives a value of Md_{30} = -89°C, for material C, which indicates that the austenite is very stable and should not undergo transformation to martensite upon deformation at room temperature. However, as will be seen later, formation of martensite was observed in all specimens (material A, C and D), whether strained to failure in air (charged or uncharged), in hydrogen gas, with cathodic polarization, or in hydrogen sulphide environments.

When specimens of material D were strained to failure in 2.0 bar hydrogen, the results were similar to those obtained for material C, but there was a higher degree of embrittlement (Figures 4.8). This can be related to the difference in the austenite distribution in the two materials. In material D the austenite is more randomly distributed, which may facilitate a faster crack propagation through the ferrite (the phase that is more susceptible to hydrogen embrittlement) (Figure 3.1). Furthermore, specimens machined from material C with their axes parallel to the transverse direction of the pipe showed rather more embrittlement than longitudinal specimens, especially when the hydrogen supply is limited (i.e. at 1 bar), than those oriented along the length of the pipe (Figures 4.9). Such behaviour is understandable when comparing the microstructures of the two orientations. A crack propagating in a plane perpendicular to the transverse direction is less likely to meet an austenite barrier than one propagating in a radial plane, perpendicular to the longitudinal direction (Figure 4.10).

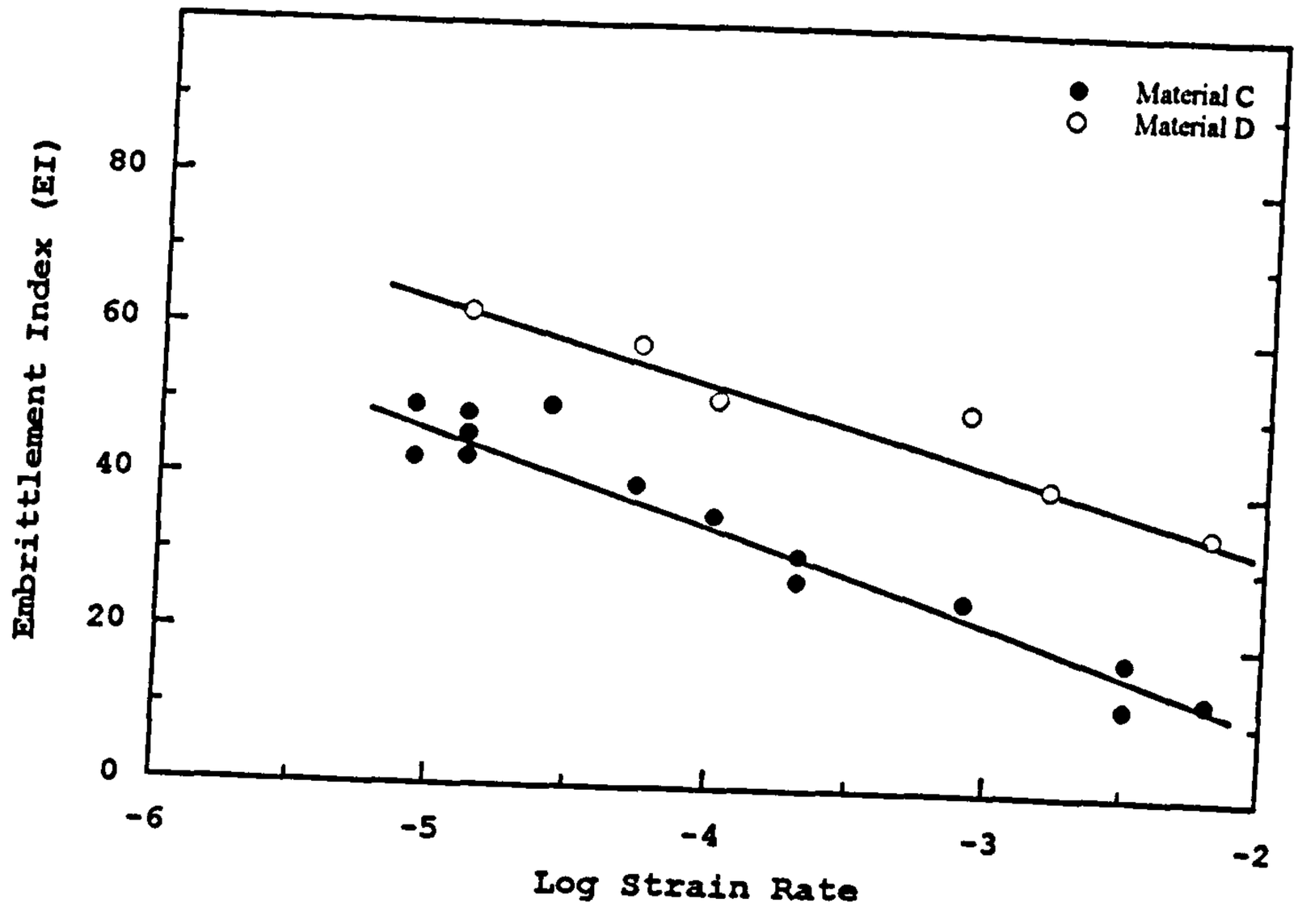

Figure 4.8 The dependence of the embrittlement index on the strain rate for materials C and D strained to failure in 2.0 bar hydrogen gas.

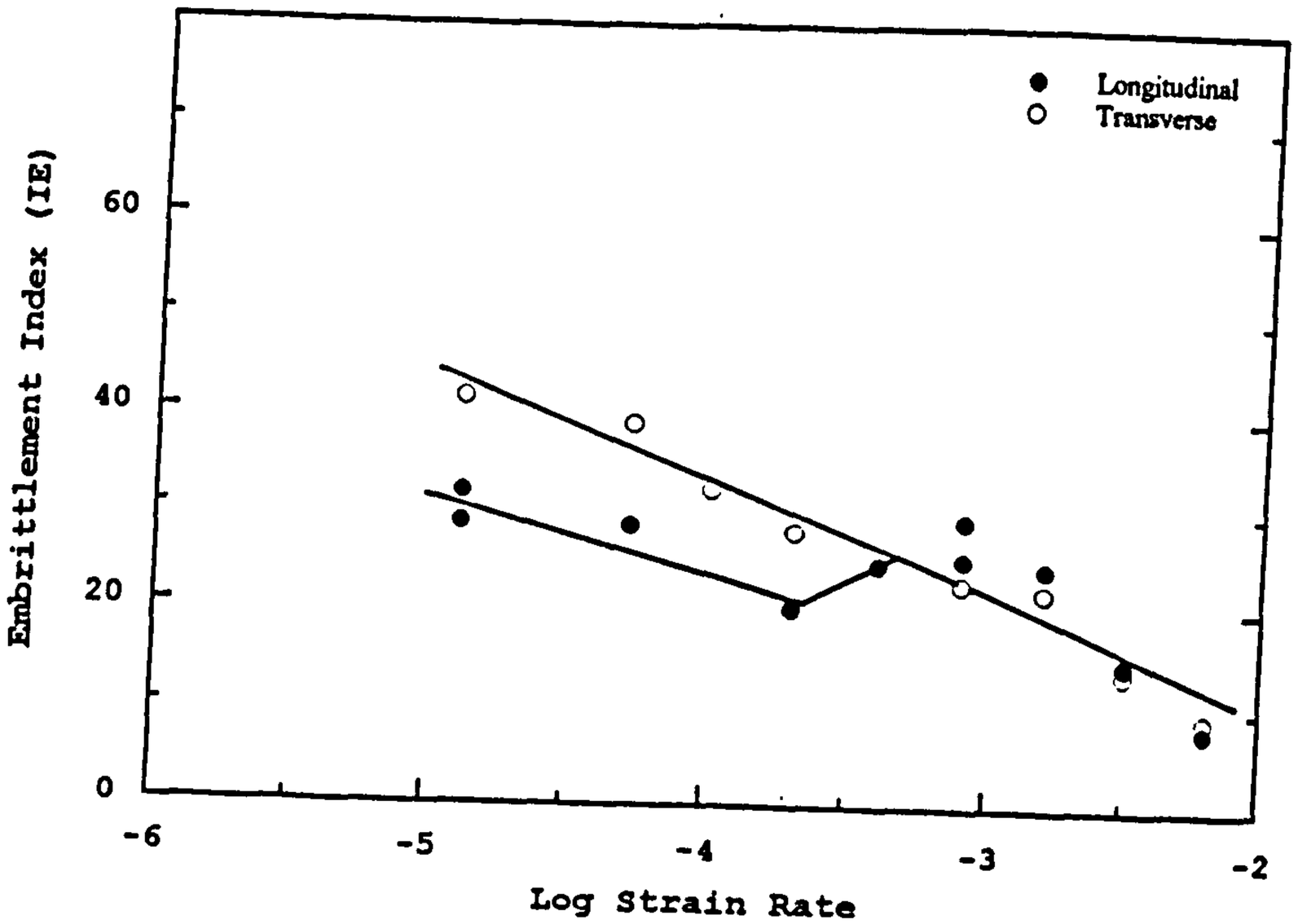

Figure 4.9 Effect of strain rate and specimen orientation on the embrittlement index for duplex stainless steel C strained to failure in 1.0 bar hydrogen gas.

Straining material B in 1 and 2 bar hydrogen produced no measurable loss of ductility and this can be attributed to three factors. Firstly, the very fine fibrous structure (Figure 3.1) hinders crack intiation and propagation. Secondly, the microstructure contains a greater proportion of the less affected phase (austenite) than the other materials (50%α-50%γ). Thirdly, the austenite in this material appears to be more stable, possibly due to the higher nickel and, more importantly, nitrogen contents (Md_{30}= -217). No martensite transformation was observed in this material under any circumstances, as compared to materials A, C, and D where martensite invariably formed.

Metallographic examination of the gauge lengths of the broken specimens revealed many secondary cracks initiated at the surface in the ferrite phase and running perpendicular to the tensile axis, as might be expected (Figure 4.11). For the two materialS, A and C, that exhibit microstructural anisotropy the cracks initiate on the tangential plane and this may be attributed to the fact that this plane contains larger ferrite areas where cracks may initiate readily. In addition, the strain perpendicular to this plane is greater than in the other directions, which may make a significant difference in the hydrogen transport via dislocations. Many of these cracks terminate at an austenite island; the phase that requires a much higher hydrogen concentration if it is to be embrittled. Some of the cracks deviate, when they meet a long austenite island, and follow the austenite/ ferrite boundary (Figure 4.12). The fracture surfaces (Figure 4.13) show that there is transgranular cleavage fracture radiating from one or more sites in the brittle region (Figure 4.14) until the load-bearing cross section is sufficiently reduced for ductile failure to occur that produces

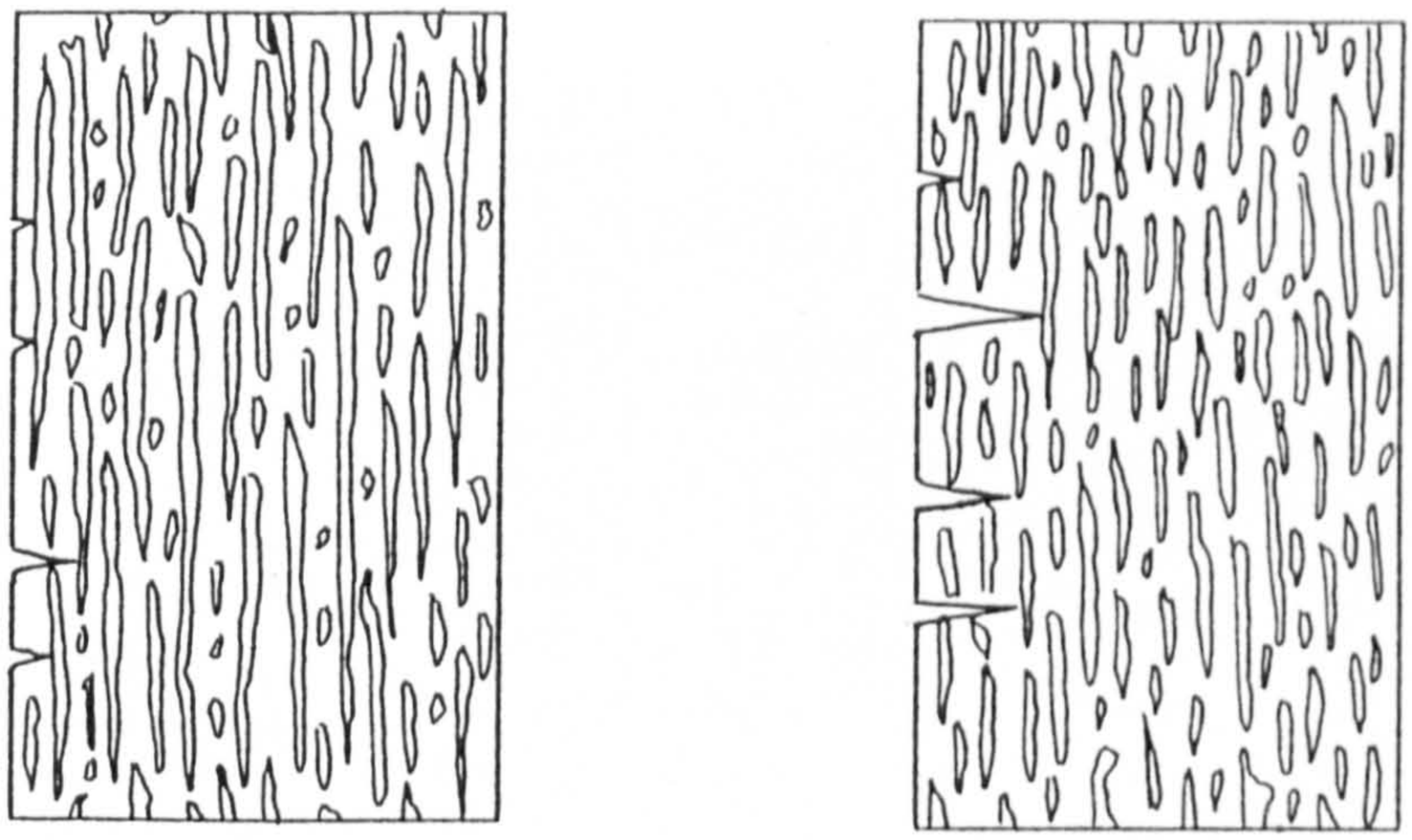

(a) **(b)**

Figure 4.10 Schematic representation of crack propagation in duplex stainless steel (material C). a) crack propagation on a radial plane. b) crack propagation in a plane perpendicular to the transverse direction.

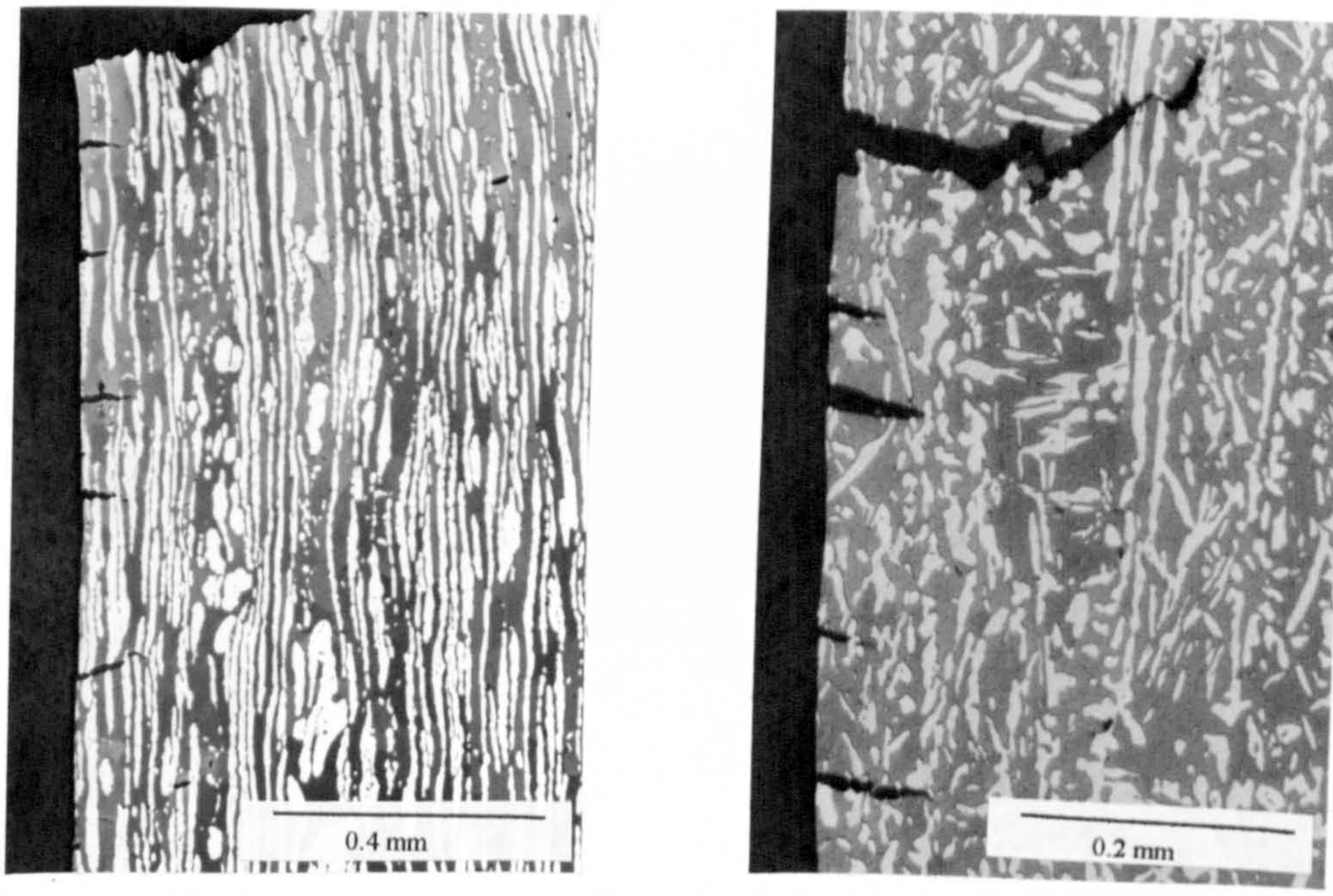

(a) **(b)**

Figure 4.11 Polished section from the gauge length of a duplex stainless steels specimen strained to failure at 1.3×10^{-5}/s in 2.0 bar hydrogen. a) Material C, b) Material D.

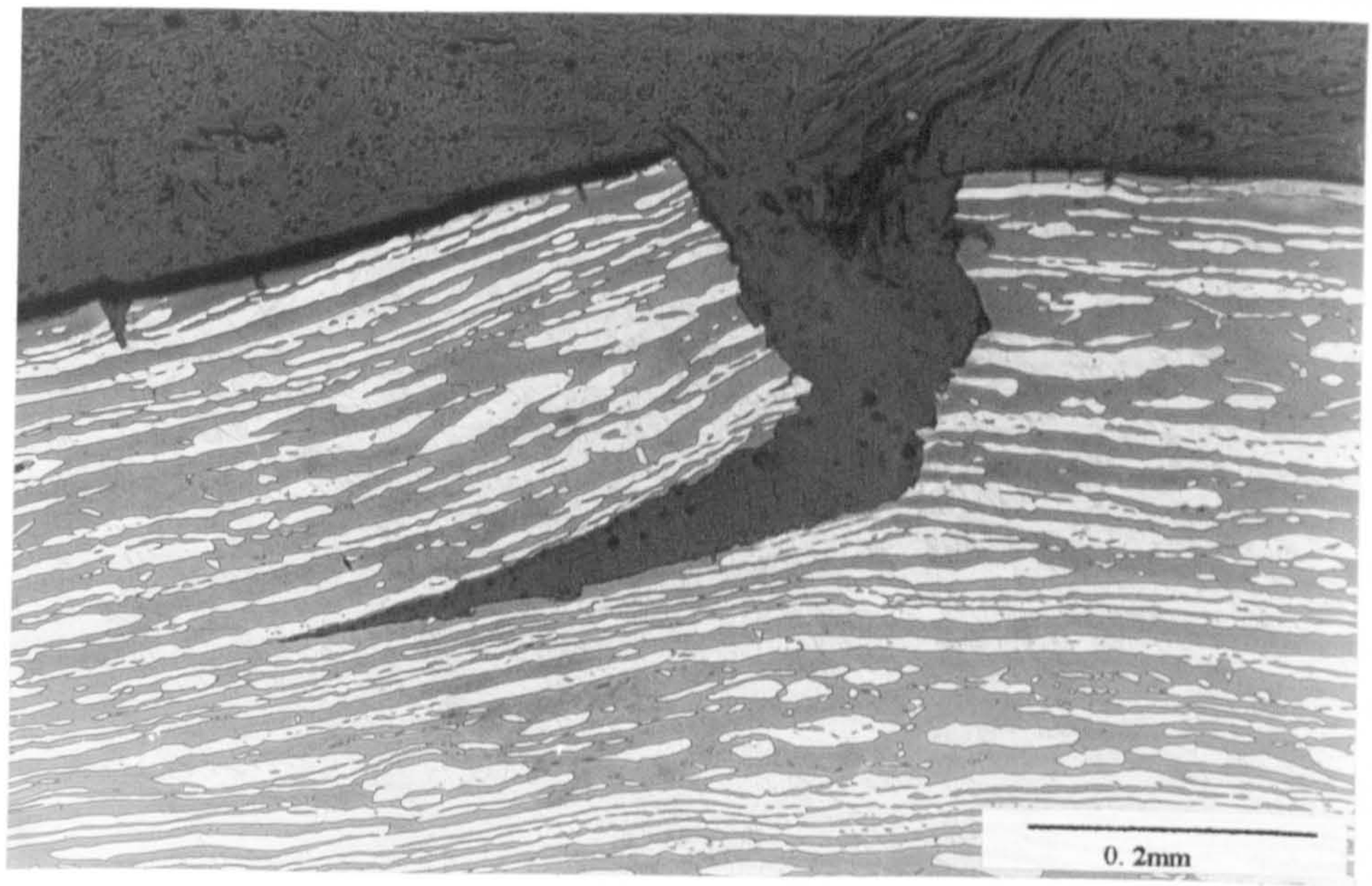

Figure 4.12 Polished section from the gauge length of a duplex stainless steel material C specimen strained to failure at 2.6×10^{-5}/s in 2.0 bar hydrogen.

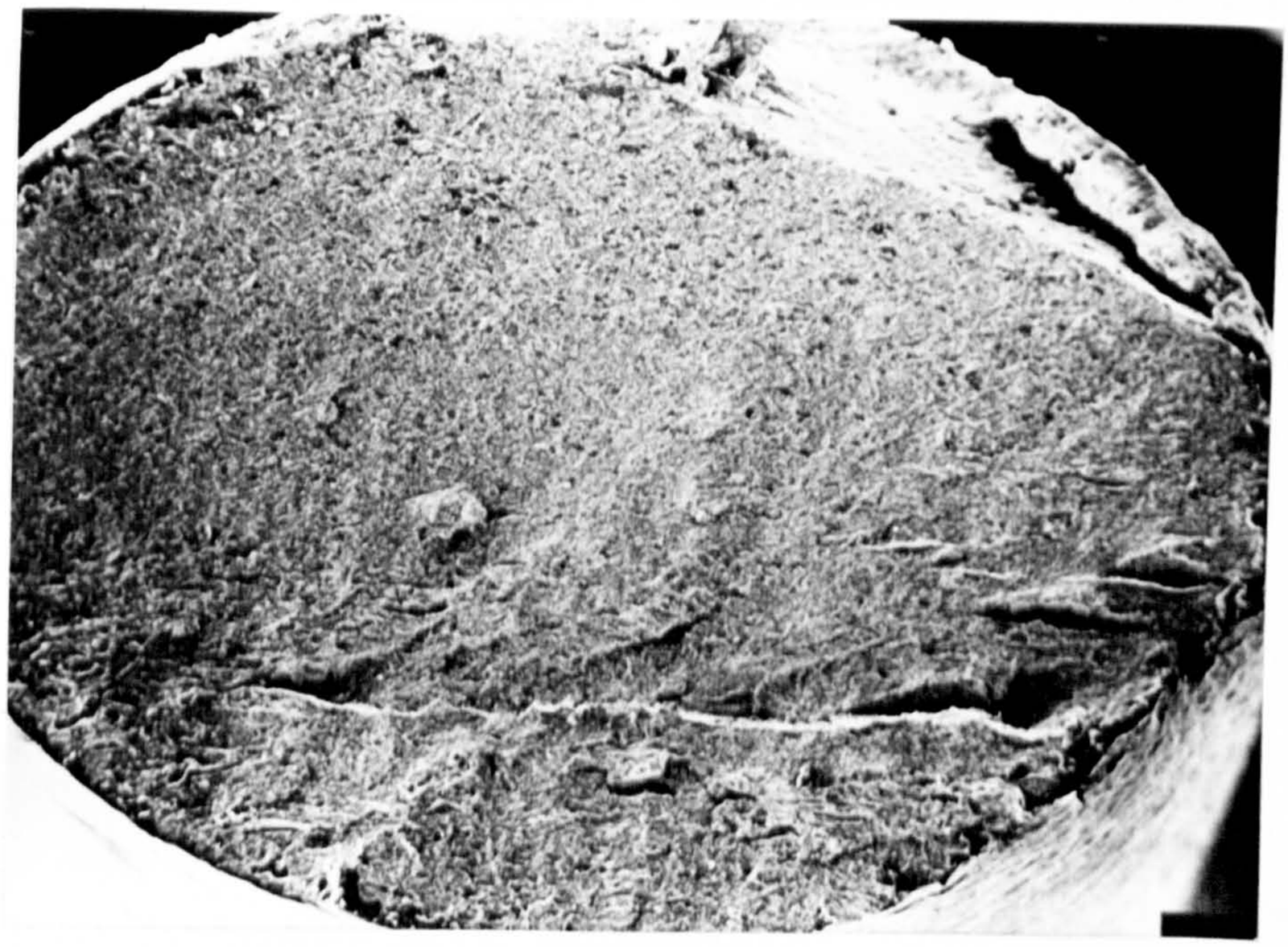

Figure 4.13 Fracture surface of tensile specimen of duplex stainless steel (material C) strained to failure at 5.2×10^{-5}/s in 2 bar hydrogen, showing brittle initiation.

a dimpled fracture surface. Moreover, when the fracture surfaces were lightly polished , to produce a flat surface, and then etched, it was revealed that martensite transformation had occurred near the fracture surface in all specimens of materials A, C and D, whether strained to failure in air or in hydrogen.

The positive identification of the formation of martensite was facilitated by using an etch (20ml HCl + 80ml H_2O + 0.5-1g potassium metabisulphite + 2g ammonium bifluoride) that colours the martensite blue (the same as the ferrite) whilst the untransformed austenite remains relatively unattacked (light yellow) (Figures 4.15 and 4.16). Although Beraha and Shpigler /176/ demonstrated that this etchant colours the martensite in an austenitic stainless steel blue, the situation is more complex in duplex stainless steels because they contain ferrite. Here the etch colours the martensite and the ferrite the same depending on etching time. If the etch time is short (5-8 sec.) the colour will be brown but a longer time (15 sec) will result in both phases, ferrite and martensite, appearing blue. It was found , however, that there exists a very narrow range of etching time where the martensite attains a bluish shade while the ferrite is still brown, but this was extremely difficult to achieve, though noticed a few times.

4.1.3 Thermally charged specimens (strained to failure in air)

High pressure thermal charging with hydrogen is intended to produce a uniform hydrogen concentration throughout the gauge length. The charging pressure controls the amount of hydrogen that can be dissolved into the material at a given

Figure 4.14 Fracture surface of tensile specimen of duplex stainless steel (material C) strained to failure at 5.2 x 10^{-5}/s in 2 bar hydrogen, showing transgranular cleavage areas in the brittle region of Figure 4.13.

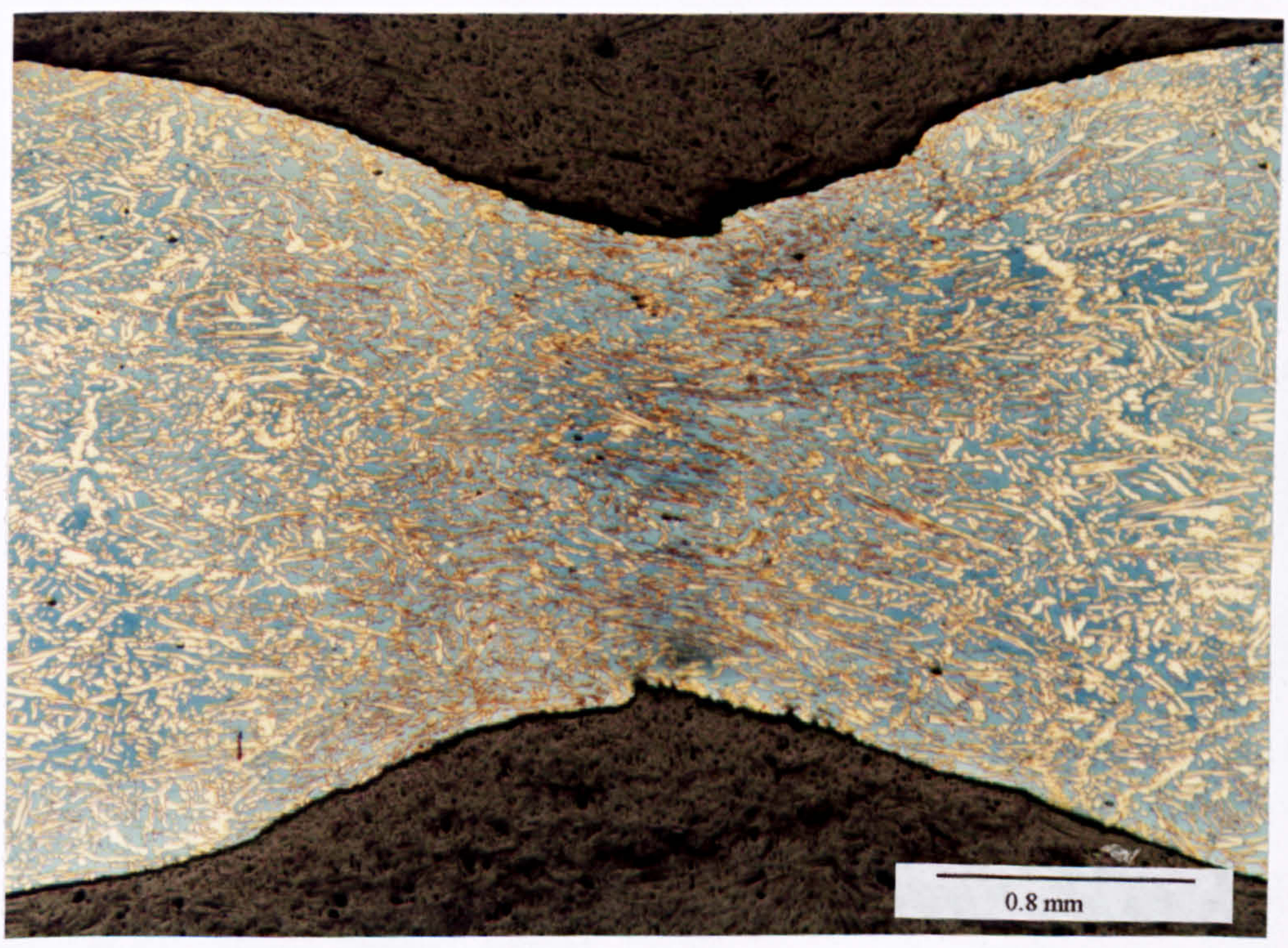

Figure 4.15 Martensite formed in material D in austenite islands (in the necked region) after straining uncharged specimens in air.

Table 4.3 Fractional saturation of cylindrical specimens with hydrogen.

Dt/L^2	Fractional Saturation
0.005	0.157
0.01	0.216
0.02	0.302
0.03	0.360
0.04	0.412
0.05	0.452
0.06	0.488
0.08	0.550
0.10	0.606
0.15	0.708
0.20	0.781
0.25	0.832
0.30	0.878
0.40	0.9316
0.50	0.9616
0.60	0.9785
0.70	0.9879
0.80	0.9932
0.90	0.9960
1.00	0.9979
1.50	0.9999

$$\text{Fractional Saturation} = \frac{C_m - C_0}{C_s - C_0}$$

Where C_m = mean concentration at time t
C_0 = uniform initial concentration
C_s = constant surface concentration

L = radius of the cylindrical specimen
D = diffusivity

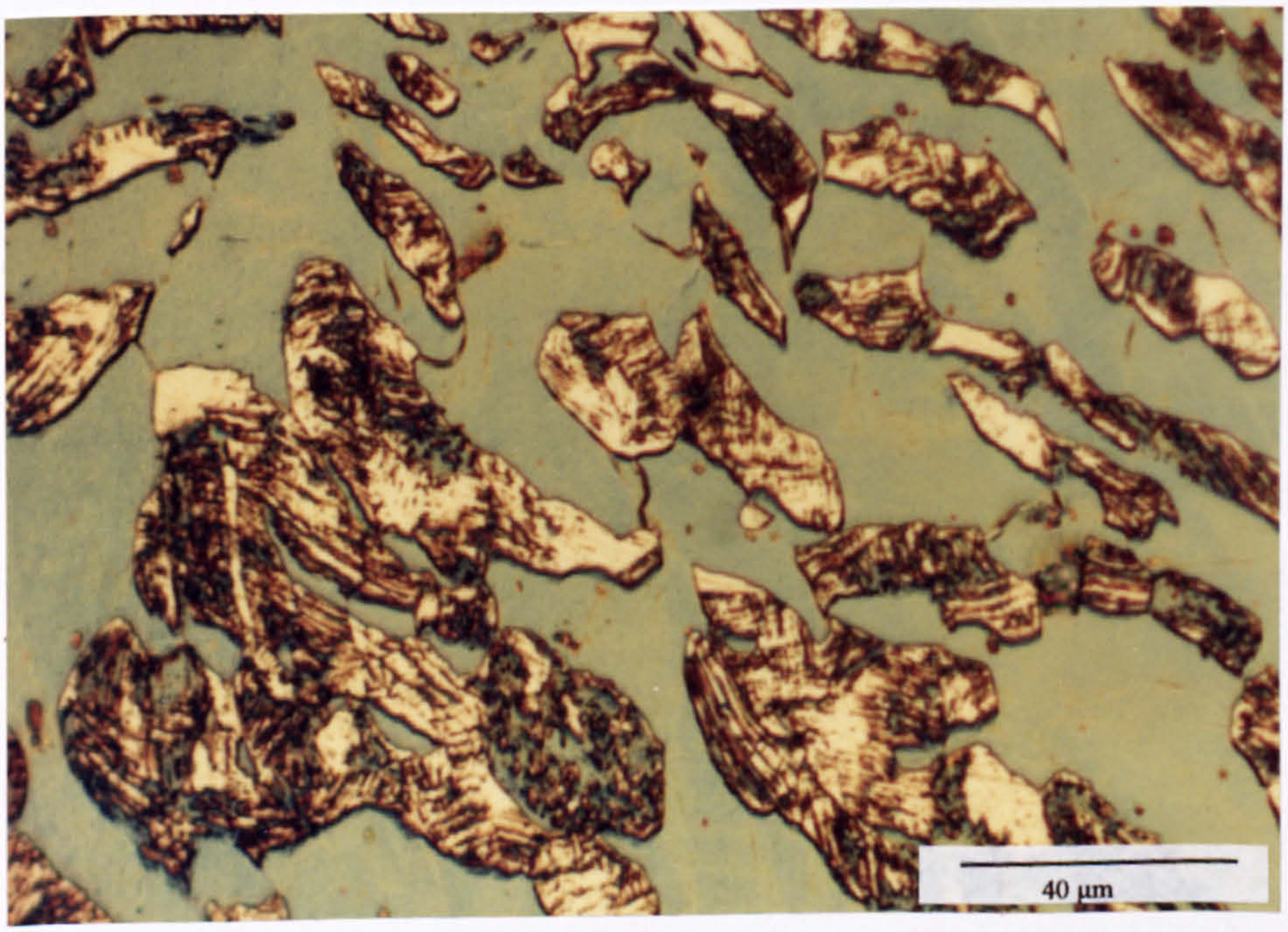

Figure 4.16: Slightly polished fracture surface for uncharged specimens (material C) strained to failure in 2 bar hydrogen showing martensite formed in austenite islands.

charging temperature (Equation 2.19). Therefore, in thermal charging, the pressure and the charging temperature dictate the concentration of hydrogen in the specimen (i.e. the equilibrium solubility). Since the duplex stainless steel contains roughly equal proportions of austenite and ferrite, the diffusivity of hydrogen in the ferrite is much higher than that in the austenite /136,179/. Therefore, saturation of specimens with hydrogen is controlled by the diffusivity through both phases which can be calculated using equations (2.20-2.22) and the fractional saturation function for cylindrical shape specimens provided by Darken and Gurry /180/ (Table 4.3). At a charging temperature of 350°C, D_γ = 2.61×10^{-11} m^2/s and hence, to achieve uniform saturation in specimens having a diameter of 3.20mm, Dt/L^2 must be ≈ 1.50 (Table 4.3). This yields a time of 40.8 hours considering only the austenite phase. In contrast, a time of 38.6 minutes was calculated to achieve uniform hydrogen saturation if the ferrite diffusivity value, $D\alpha = 1.66 \times 10^{-9}$ m^2/s (Equation 2.21) is used. Specimens charged at 350°C and 250 bar hydrogen for varying times ranging from 3-200 hours, have revealed that the minimum time to achieve the maximum loss of ductility is about 30 hours (Figure 4.17), which is considerably lower than the time required to achieve uniform hydrogen distribution in fully austenitic stainless steels (40.8h), but much higher than the time required to achieve saturation for fully ferritic stainless steels (38.6min), which may be due to the fact that hydrogen diffuses through the ferrite and around the austenite islands which will reduce the time for saturation. The effect of increasing the charging pressure, at 350°C for 48h, on the loss of ductility was also investigated (Figure 4.18) and this indicated that a pressure above ≈ 200 bar is necessary to produce maximum embrittlement. Thus, a pressure

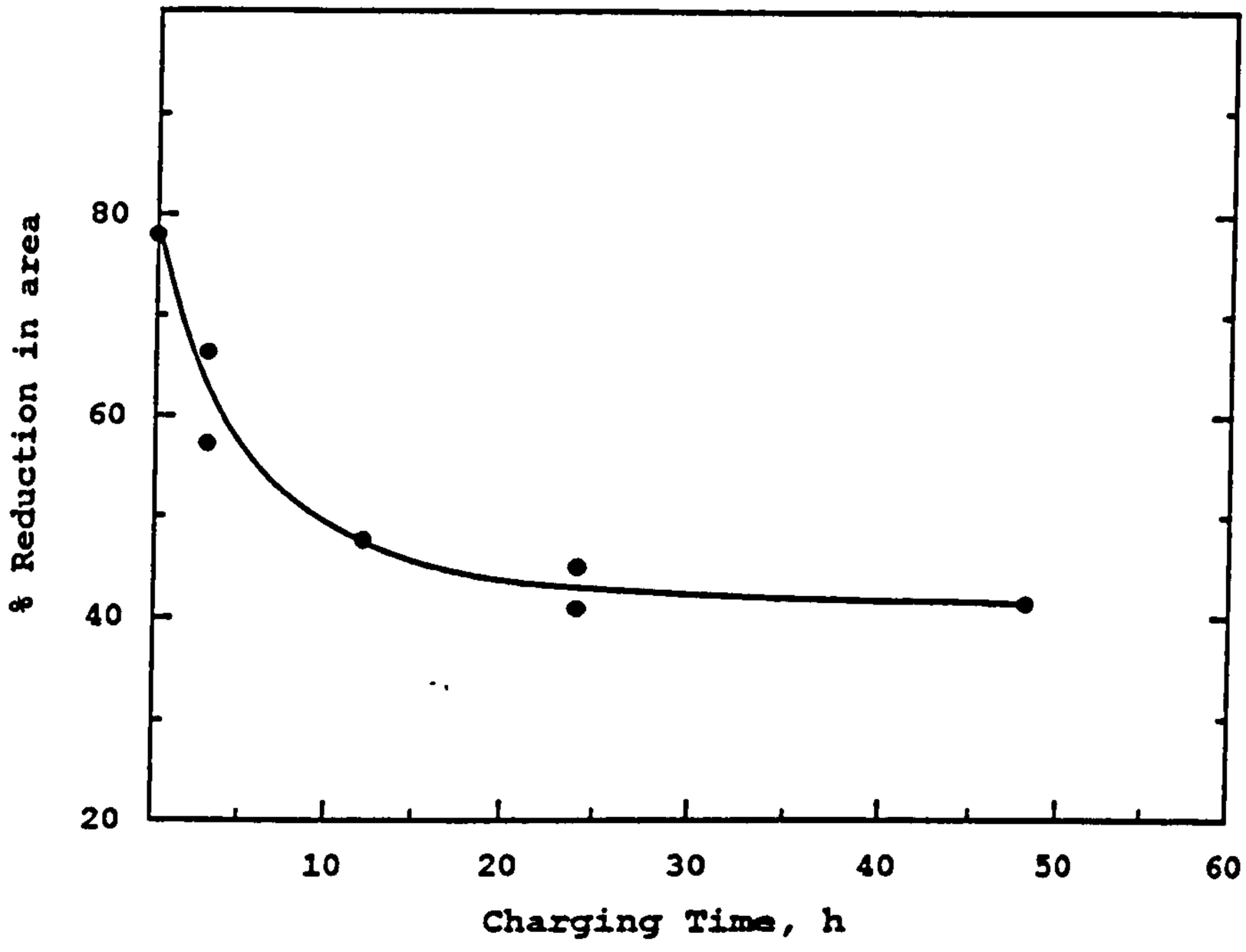

Figure 4.17 Charging time vs %RA for longitudinal specimens of duplex stainless steel material C charged at 250 bar hydrogen and 350°C and strained to failure at 2.0 x 10^{-4}/s in air.

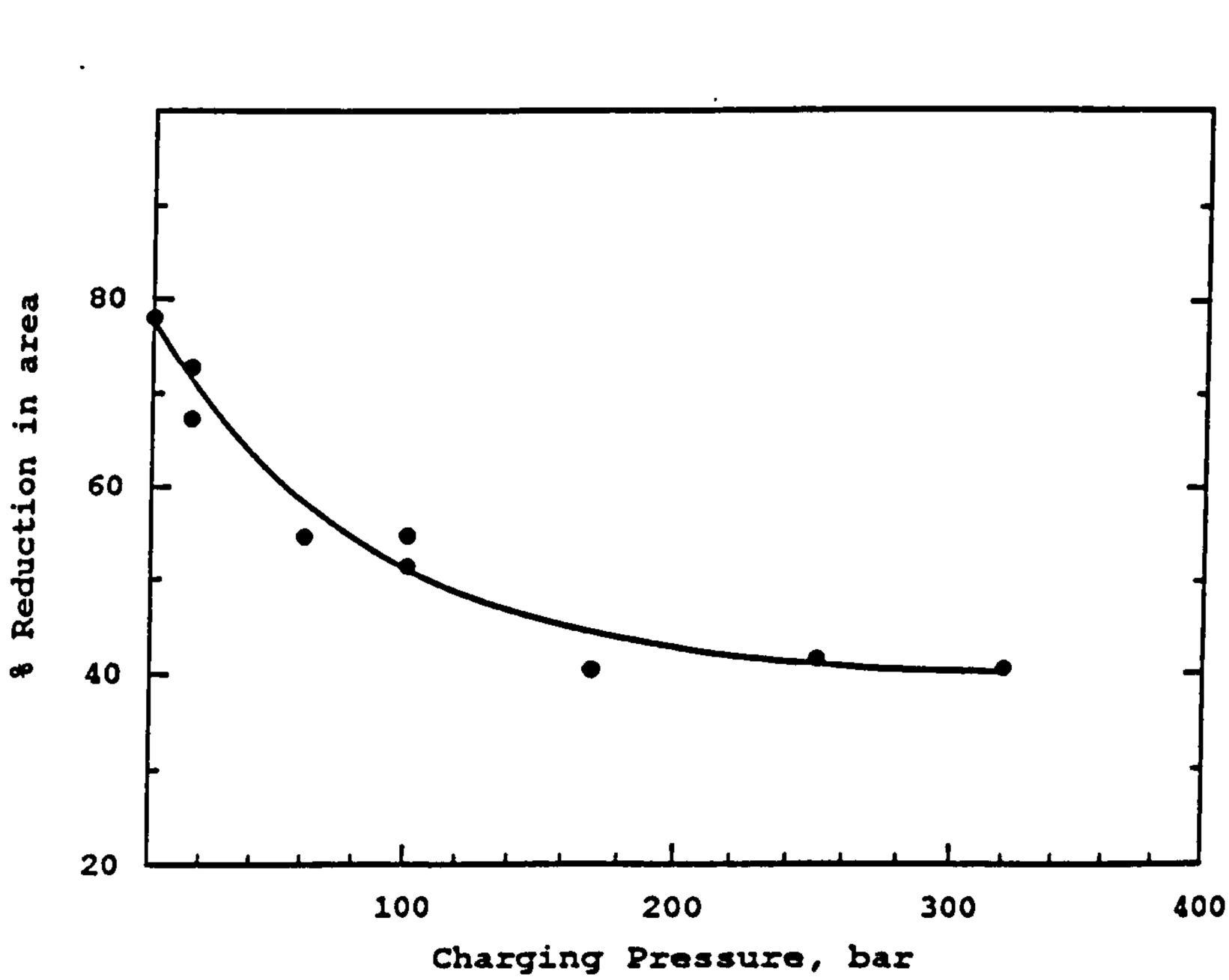

Figure 4.18 Charging pressure vs %RA for longitudinal specimens of duplex stainless steel material C, charged at 350°C for 48h and strained to failure at 2.0 x 10^{-4}/s in air.

above 200 bar and a charging time of at least 48 hours, at 350℃, was generally employed for comparing the embrittlement of different materials structures. Two Hounsfield specimens (material C) that had been charged in 250 bar hydrogen at 350°C for 48 hours were analysed for hydrogen content, by inert gas extraction, and were found to contain 20 wppm. The actual hydrogen concentration for other charging pressures may be estimated from these analysed results using the proportional relationship embodied in equation 2.19:

$$\frac{C_1}{C_2} = \frac{P_1^{1/2}}{P_2^{1/2}} \qquad 4.1$$

Where C_1 and C_2 are the amounts of hydrogen dissolved into the metal when it is exposed to pressures of P_1 and P_2 respectively. These results are listed in Table 4.4 along with the theoretical value calculated from the diffusivity and permeability data provided by Perng and Altstettler /130/ for austenitic and ferritic steels, and by Xiukui et al /181/ for austenitic steels. In both cases allowance was made for the fact that the duplex stainless steel C contains only 37.8% austenite. It seems that most of the hydrogen is dissolved in the austenite, the ferrite hardly retaining any hydrogen, and therefore, it seems quite reasonable to consider only the austenite in calculating the hydrogen content of duplex steels.

When the concentration of hydrogen dissolved at 170 bar is calculated in this way (using equation 4.1) there is good agreement with the analysed value obtained by Zheng and Hardie for similar duplex steel (15 wppm) /182/. Buckley /183/ analysed a number of 304 austenitic stainless steel specimens that had been charged in the same autoclave at different hydrogen pressures and his results, when

plotted as $P^{½}$ vs hydrogen content, revealed a good fit (Figure 4.19) that indicates that the actual hydrogen concentration [H] follows the relation $[H]=3.165\ P^{½}$. In other words, the actual hydrogen concentration is proportional to the square root of the charging pressure, which indicates that the calculation using equation 4.1 is valid. In fact, the result obtained fits very well with both the actual analyed data and the data provided by Xiukui et al /181/.

Increasing the hydrogen content of the tensile specimens by increasing the charging pressure resulted in a slight increase in the 0.2% proof stress, from ≈ 623 N/mm^2 for the uncharged specimen (material C) strained to failure in air to ≈ 647 N/mm^2 for specimens charged to the maximum pressure of 320 bar (23 wppm hydrogen). The ultimate tensile stress is also increased from ≈734 N/mm^{-2} to 764 N/mm^2 for the same charging conditions. Increasing the charging pressure has a detrimental effect on the ductility of duplex stainless steels (Figure 4.20) and the degree of embrittlement is dependent upon strain rate. The loss in ductility increases as the charging pressure increases up to ≈ 200 bar, which corresponds to a hydrogen content of ≈ 18 wppm, but any increase above this limit has no effect on the ductility as might be expected. The degree of embrittlement varied with strain rate in a similar manner to that of uncharged specimens strained in hydrogen and the reduction in area varied between ≈ 30 % at the slowest strain rate employed ($1.3 \times 10^{-5}/s$) and ≈ 54% at a strain rate of $6.4 \times 10^{-3}/s$.

When transverse tensile specimens of the same material (material C) were strained to failure in air after thermal

Table 4.4 Comparison of the hydrogen concentration in duplex stainless steel (material C) charged at various pressures at 350°C for 48h, using various formlae.(In all cases the calculated hydrogen concentration was based on a fraction of 37.8% austenite in the structure).

Hydrogen pressure (bar)	Hydrogen content (wppm)			
	Perng and Altstetter /130/	Xiukui et al /181/	Actual inert gas extraction	calculated from equation 4.1
15	7	5	n.d.	5
60	15	11	n.d.	10
100	19	14	n.d.	13
170	25	18	15 *	17
250	30	21	20	basis of calculation
320	34	24	n.d.	23

* For similar duplex stainless steel /182/.

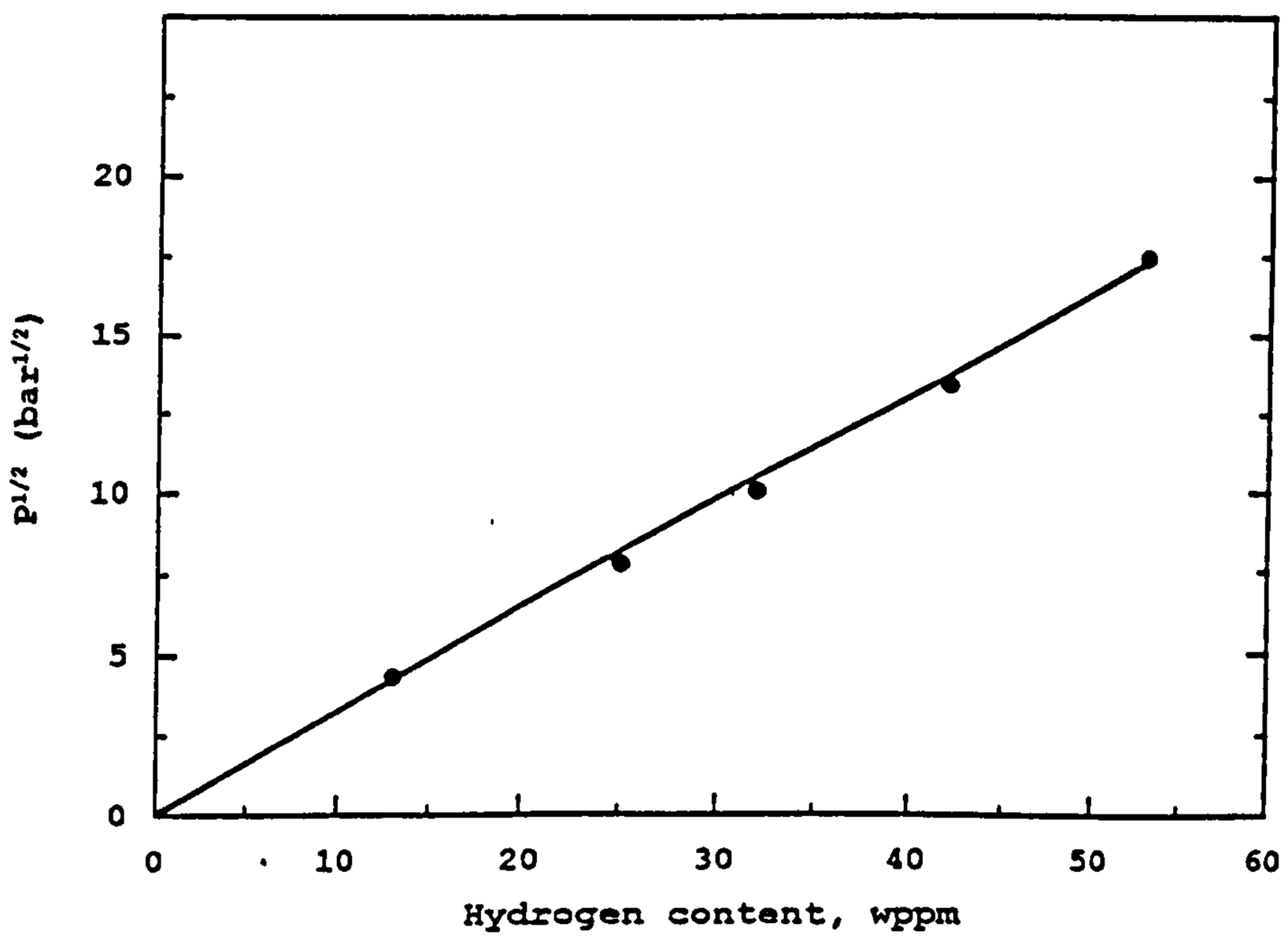

Figure 4.19 Variation of the actual hydrogen concentration, analysed by inert gas extraction, with the charging pressure /183/.

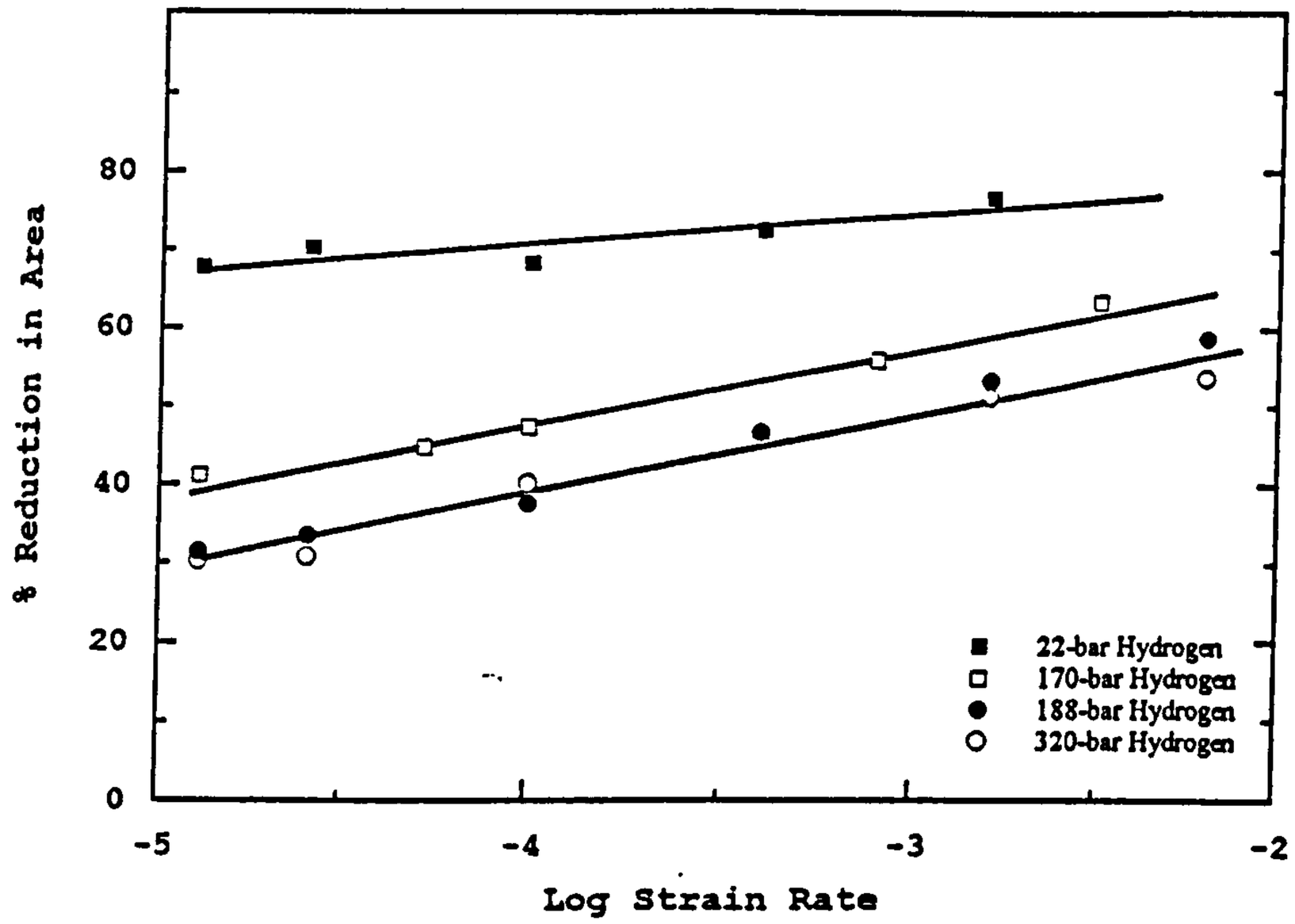

Figure 4.20 The effect of charging pressure and strain rate on the ductility of longitudinal specimens of duplex stainless steel (material C) charged at 350°C for 48h.

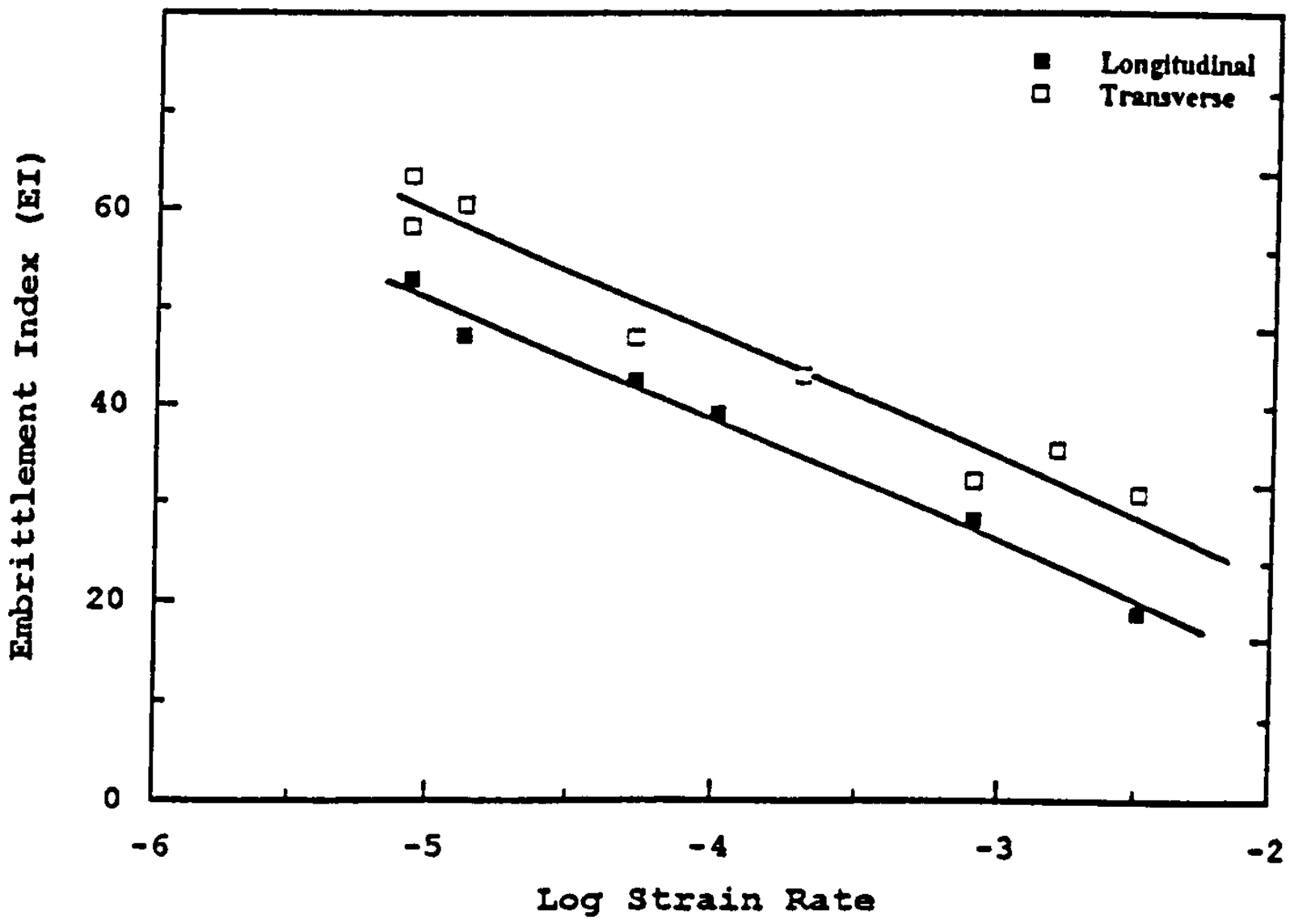

Figure 4.21 The effect of strain rate and specimen orientation on the embrittlement index at fracture for duplex stainless steel (material C) thermally charged in 170 bar hydrogen.

charging with hydrogen they also suffered a loss in ductility, but the embrittlement was more severe (Figure 4.21) which is believed to be due to the greater likelihood of an austenite-free path for crack propagation. The recorded stress strain curves for transverse specimens strained to failure after thermal charging with hydrogen revealed the existence of a distinct yield point (Figure 4.22), which was not present when straining to failure in hydrogen, nor in straining any of the charged longitudinal specimens in air (Figure 4.23). The appearance of the distinct yield point in the transverse specimens must be attributed to some form of dislocation pinning in the austenite, perhaps caused by the much higher hydrogen content compared to the specimens strained in hydrogen. The absence of this from longitudinal specimens strained under the same conditions is difficult to explain, but may be associated with the significantly different distribution of the austenite in the cross sections of longitudinal and transverse specimens, where in the former the cross section contains smaller austenite island cross sections while the latter contains much larger.

In contrast to what was found for the specimens strained to failure in hydrogen, the elongation to fracture of all thermally charged specimens provided a good measure of the loss in ductility. The elongation to fracture was reduced from 33% at a strain rate of 1.6×10^{-3}/s to 21% at a strain rate of 1.3×10^{-5}/s. These results indicate that at certain hydrogen concentrations (above about 20 wppm in the duplex material C, which is equivalent to 53 wppm in the austenite phase) the austenite suffers considerable embrittlement and the % elongation to fracture is significantly reduced. It is also noticeable that the

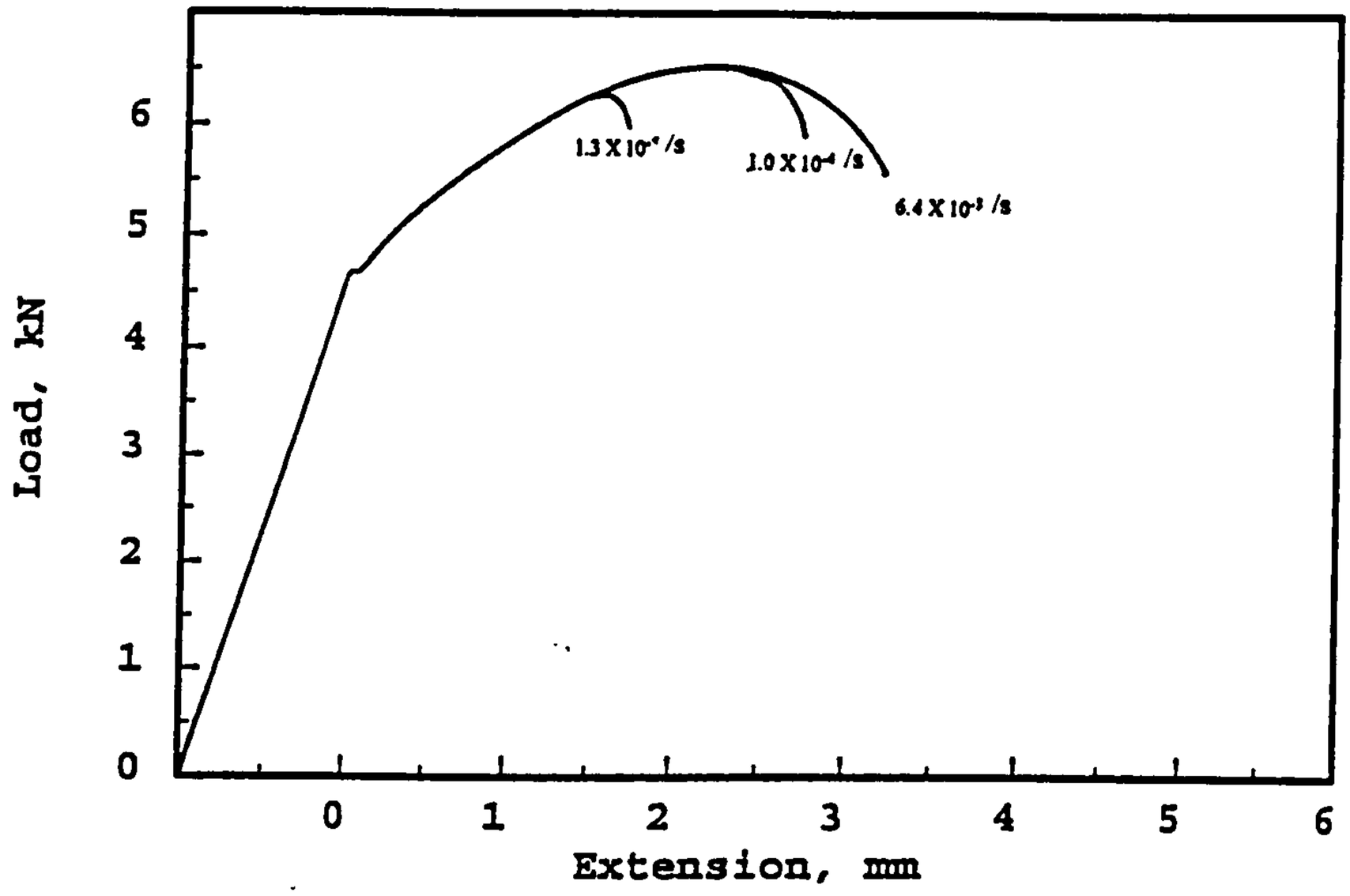

Figure 4.22 The load extension curve for transverse specimens of material C charged to 290 bar hydrogen.

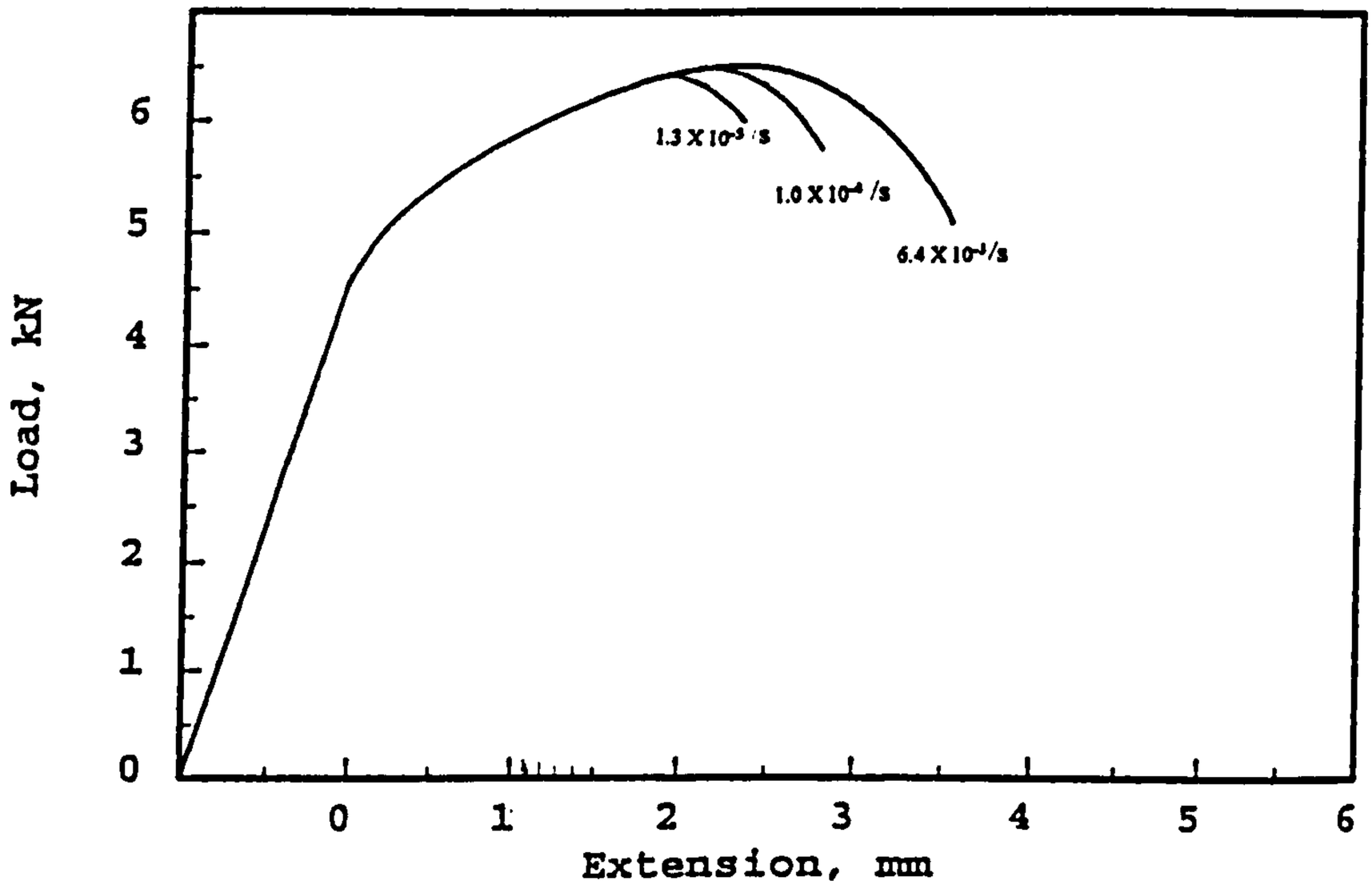

Figure 4.23 The load extension curve for longitudinal specimens of material C charged to 320 bar hydrogen.

greater scatter in results is for the longitudinal specimens specimens (Figure 4.24).

Straining of thermally charged material A revealed a very similar degree of embrittlement in both orientations, transverse and longitudinal, to that obtained for material C, which has a similar composition and microstructure (Figure 4.25). The stability of the austenite in A is also similar to that of material C, where austenite transformation to martensite was observed in all fracture surfaces. This made further investigation of this material unnecessary.

Material B, however, suffered only slight embrittlement even at the highest charging pressure of 320 bar and only at the lowest strain rate employed, 1.3 x 10^{-5}/s. The reduction in area at the higher strain rate of 1.6 x 10^{-3}/s was 80% and reduced to 73% at 1.3 x 10^{-5}/s. The gauge length of the tensile specimens of this material showed no visible secondary cracks, which indicates that crack initiation is also reduced, perhaps due to the very narrow ferrite bands on both tangential and longitudinal planes as compared to material C, where the great majority of the cracks initiated in the much larger ferrite on the tangential plane (see Figure 3.1 b and c). Moreover, the microstructure with very elongated austenite (fibrous structure) would be expected to play an even more significant role in stopping propagating cracks than in any of the other structures. Also, this alloy contains more austenite (the phase least affected by hydrogen) than any of the other alloys and on the basis of the chemical analysis the austenite should be much more stable than in the other materials (Md_{30} ≈ -217°C equation 2.9). This was confirmed by the fact that martensite has never been observed after straining this material, whatever

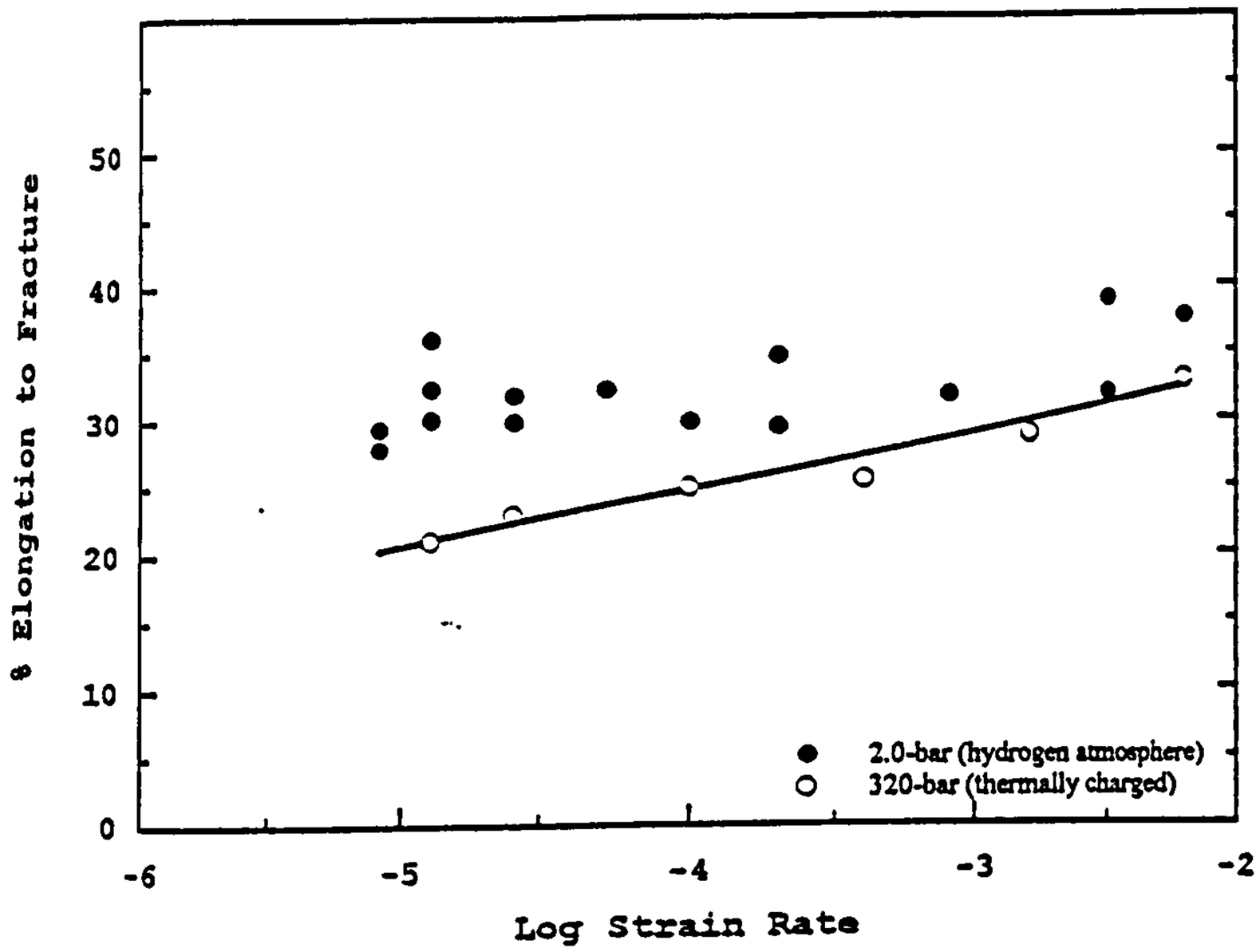

Figure 4.24 The dependence of % elongation to fracture on the strain rate for thermally charged longitudinal specimens of material C specimen strained to failure in hydrogen.

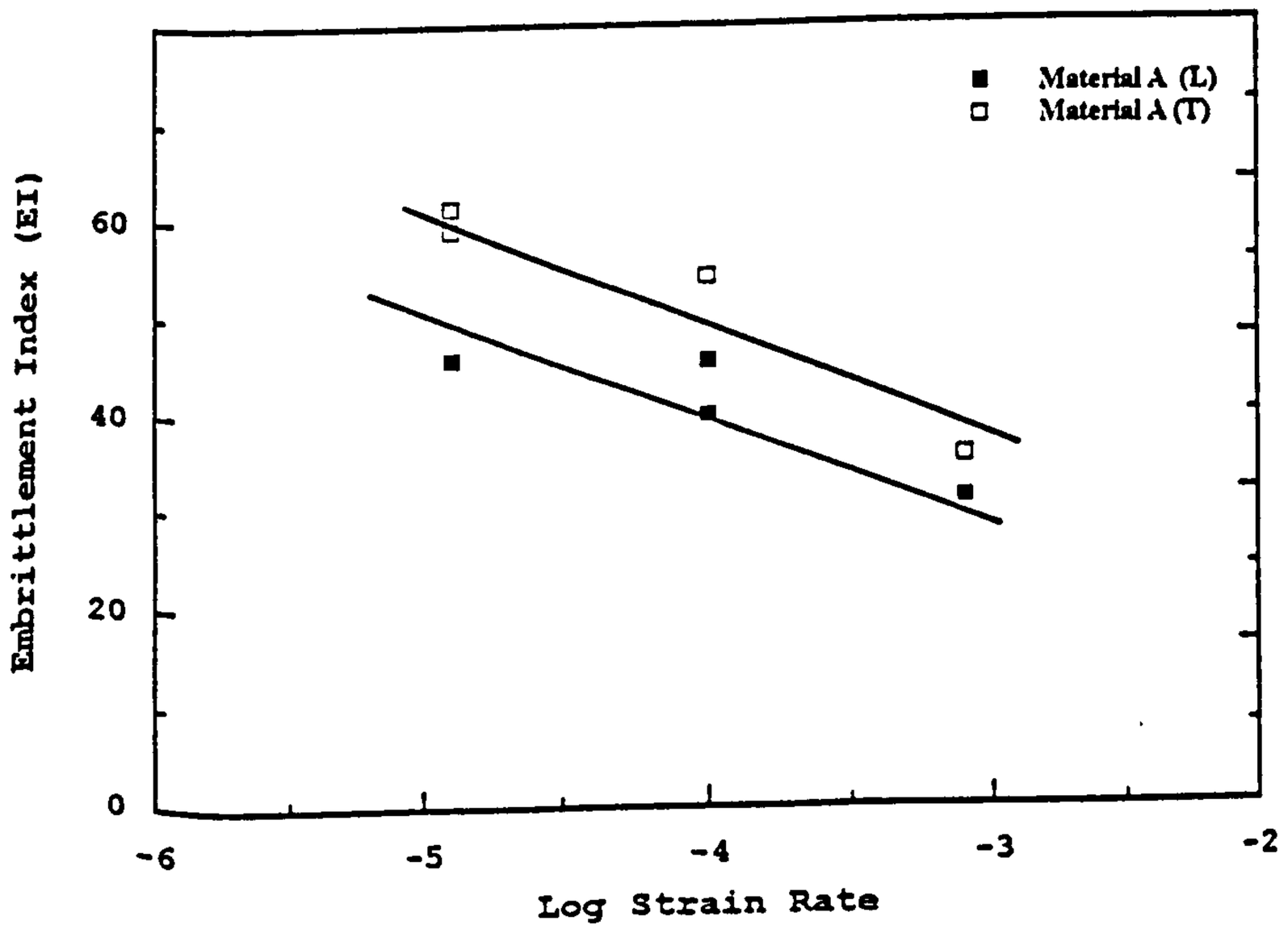

Figure 4.25 The effect of strain rate and specimen orientation on the reduction in area for duplex stainless steel (material A) thermally charged in 250 bar hydrogen.

conditions were used. It has to be said here that the use of equation 2.9 is only to demonstrate the large difference expected in the austenite stability in these materials, which correlate well with the microscopical observation of martensite in materials A, C, and D but not in material B. The actual Md_{30} values, -89 and -217°C, obtained for material C and B respectively have no absolute significance since, in deriving this equation, Angel used 18/8 type stainless steels which have different chemical composition from the austenite phase of the duplex stainless steels, especially with respect to nitrogen which, along with carbon, exerts the greatest influence on the Md_{30}.

Electron microscopical examination of the fractures revealed multiple crack initiation within the cross section (Figure 4.26). The principal fracture surface shows very brittle fracture, by cleavage, of the ferrite phase, and the austenite still exhibits some ductility, but much less than in a specimen strained to failure in hydrogen or after charging at lower pressures (lower than 200 bar). Many cracks are also visible on the fracture surfaces of charged specimens, running parallel to the tensile axis (Figure 4.27), which was not observed when straining specimens in hydrogen. This is thought to be due to the high concentration of hydrogen in the bulk of the material so that when the specimens are plastically deformed very high concentrations of hydrogen develop at the ferrite/austenite interface which then provides a favourable path for crack propagation. Microscopical examination of the gauge length also revealed a few cracks running perpendicular to the tensile axis but noticeably fewer than developed in the gauge length of specimens strained to failure in a hydrogen atmosphere or after cathodic polarization.

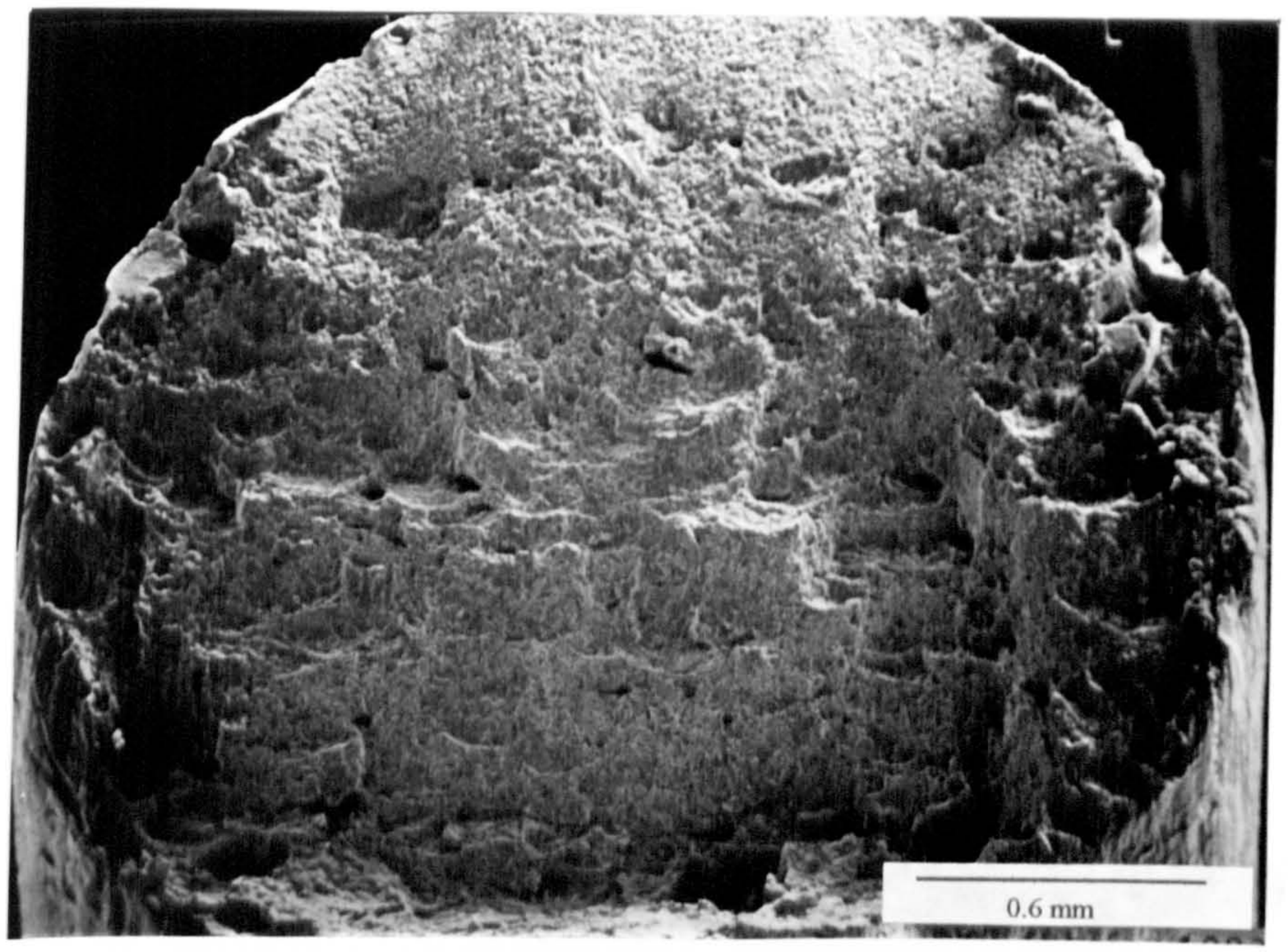

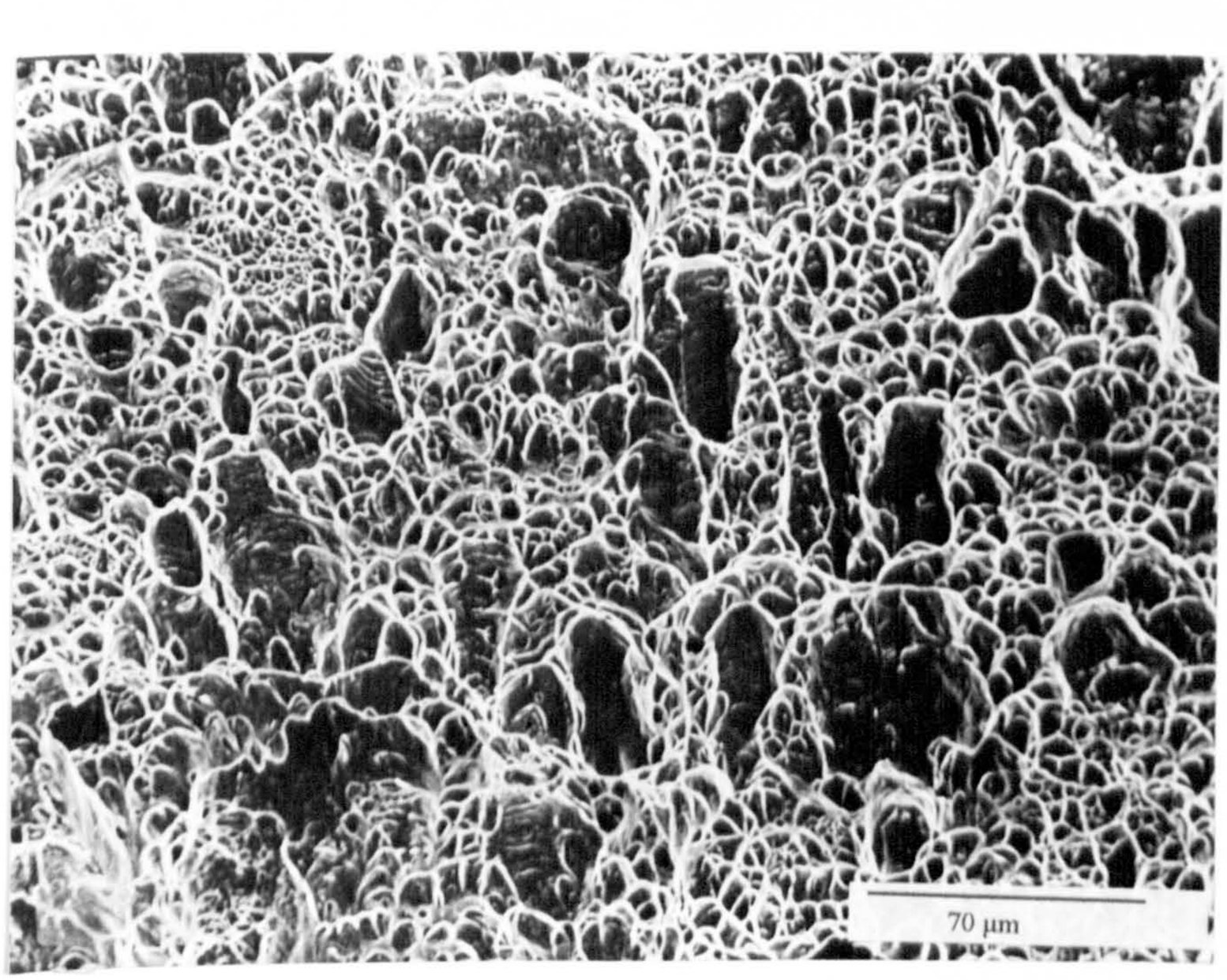

Figure 4.26 Fracture surface of duplex stainless steel (material C) strained to failure in air at 1.2 x 10^{-5}/s after charging at 350°C in 320 bar hydrogen.

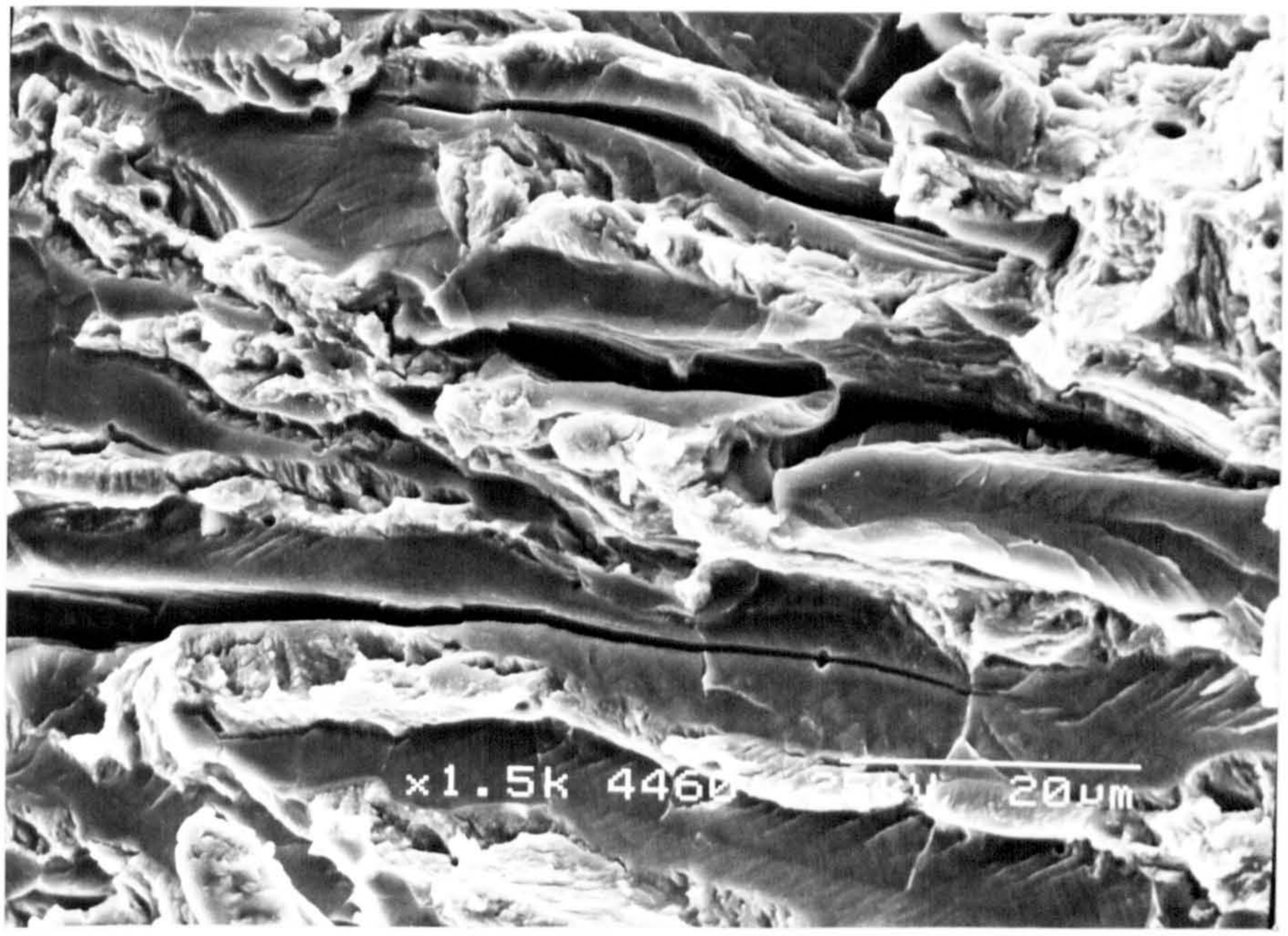

Figure 4.27 Fracture surface of duplex stainless steel specimen (material C) strained to failure in air after charging at 350°C in 320 bar hydrogen, showing cracks running along the straining axis.

4.2 Hydrogen sulphide

4.2.1 The effect of temperature

The variation in % reduction in area with straining temperature (Figure 4.28) reveals that the embrittlement first increases with temperature up to a certain intermediate temperature and then decreases at higher temperatures. Maximum embrittlement occurs at 60-70°C in NACE-01-77 solution but at 30-40°C in non-acidified sodium chloride solution. Many investigators have found similar results for both high strength steels and duplex steels /60,120,184-189/ using different loading methods. The significance of this relationship, however, is not so much the particular temperature at which maximum loss in ductility occurs, but rather the fact that the increasing amount of embrittlement as temperature increases is curtailed by recovery of ductility at a higher temperature, which suggests that two competing processes are involved. One possibility would involve hydrogen embrittlement at lower temperatures and increasing corrosion at higher temperatures. Such an idea receives some support from the fact that the gauge lengths of the tensile specimens exhibit very few secondary cracks at the lower temperatures. The decrease in the susceptibility at lower temperatures can be attributed to a decrease in the rate of hydrogen arrival at the critical site within the bulk of the specimen due to the decrease of the thermally activated hydrogen diffusion process and the prevention of hydrogen entry by the formation of some kind of protective film (such as sulphide). On the other hand , it is feasible to assume that the recovery of ductility at the higher temperatures is due to increased dissolution, which is also thermally

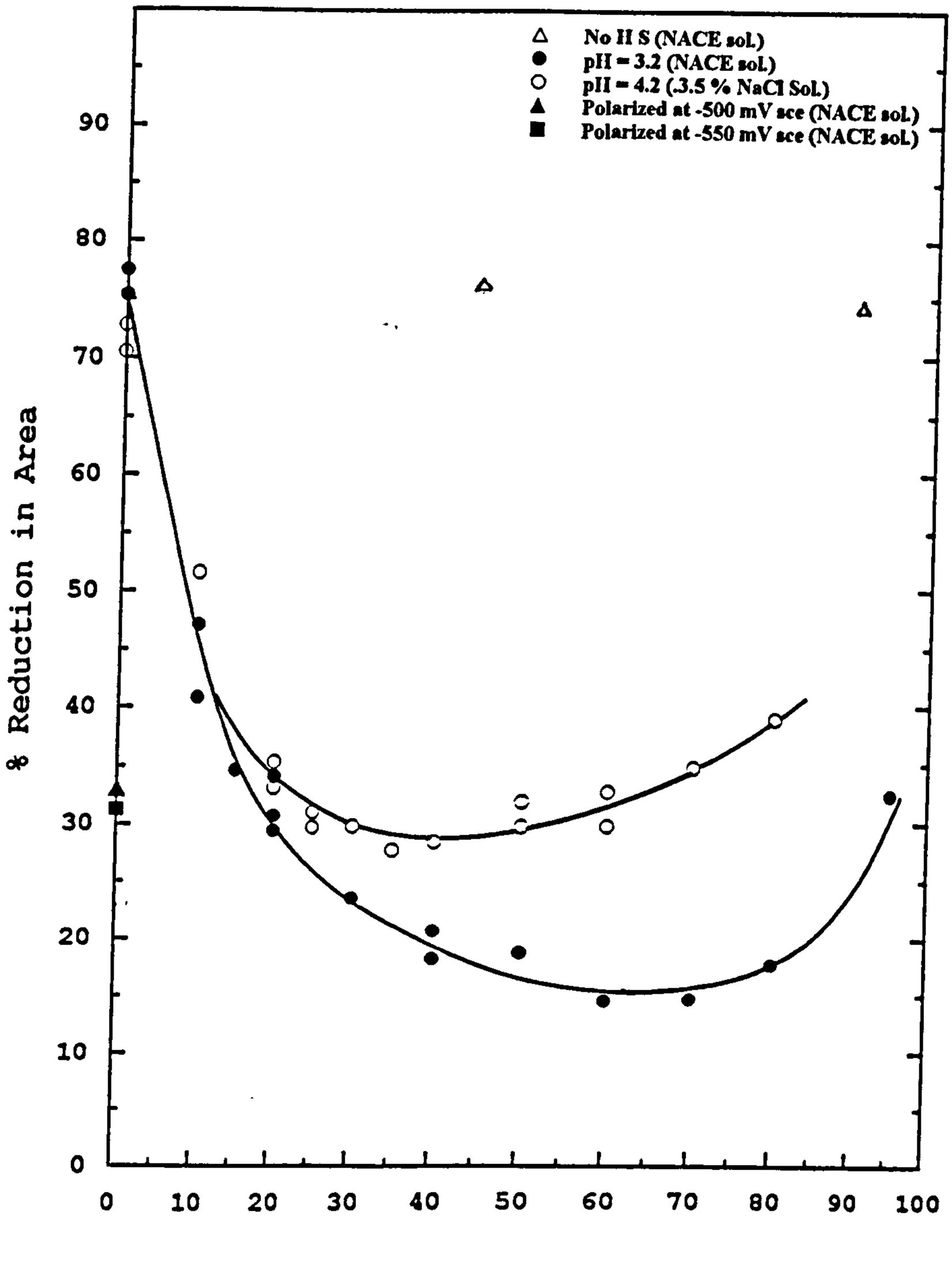

Figure 4.28 The effect of test temperature on ductility of duplex stainless steel (material C), strained in various solutions saturated with hydrogen sulphide at a strain rate of $2x10^{-6}$/s.

activated, that causes blunting of the formed cracks and hinders the entry of hydrogen, by the corrosion product.

Secondary cracks were confined to a very small necked region in specimens tested in the range 10-20°C, but as the temperature increased the number increases dramatically, especially above about 60°C (Figure 4.29). An attempt was made to count the number of secondary cracks in the gauge length of the tensile specimens and combine the results with those from the pitting tests to provide an insight into the effect of temperature on both cracking and pitting (Figure 4.30). As temperature increases, both the density of pit formation on polished specimens immersed in NACE solution for 48h, and the number of secondary cracks in the gauge length of specimens strained in NACE-01-77 solution increased only slightly up to 60°C but then showed a dramatic increase. This agrees well with the reported pitting temperature of 60°C for C material (2205 PRE_n = 35) /189/. In all cases, all pits initiate at ferrite-austenite interfaces and grow into the austenite phase (Figure 4.31). However, at temperatures in the range 20-50°C fracture frequently seems to initiate at an inclusion (Figure 4.32) and such inclusions were analysed using EDX to be rich in aluminum and calcium (Figure 4.33). On some of the tensile specimens strained to failure at 15-20°C, a thick black film formed that was analysed using an X-ray diffractometer (CuK_α radiation λ=1.54051); the scan speed was set at 0.15 deg./min to insure good trace resolution (i.e. it took about 11 h to scan the specimens 100 degree). The film was found to consist of multiple layers of iron sulphides; FeS and FeS_2 among others (Figure 4.34). When polished specimens of the steel were immersed in NACE-01-77 solution, for 720h at 30° and 90°C they showed (in both cases) that the austenite

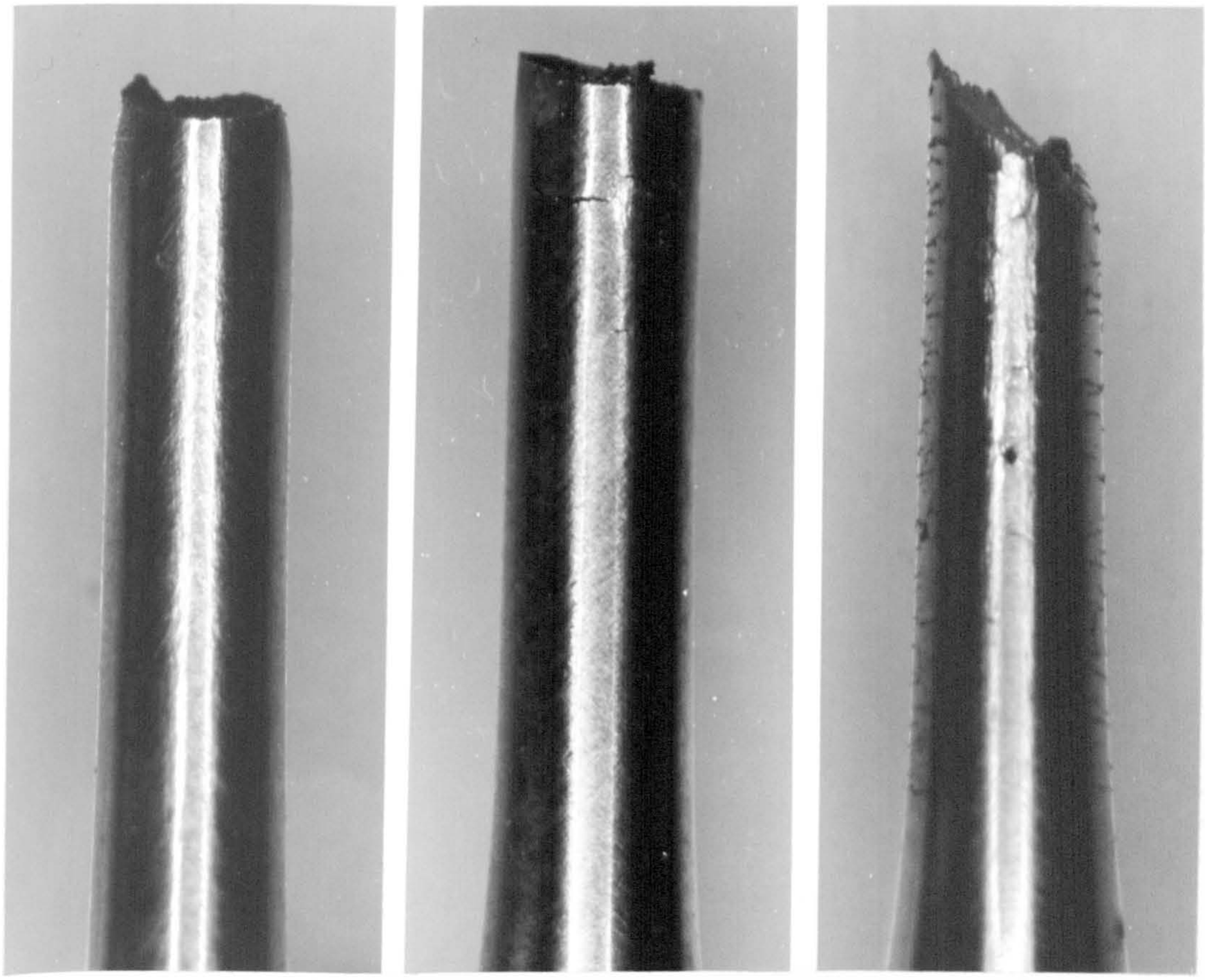

20° C **60° C** **70° C**

Figure 4.29 Duplex stainless steel (material C) tensile specimens strained to failure at different temperatures in NACE 01-77solutions, $\dot{\epsilon} = 2 \times 10^{-6}/s$.

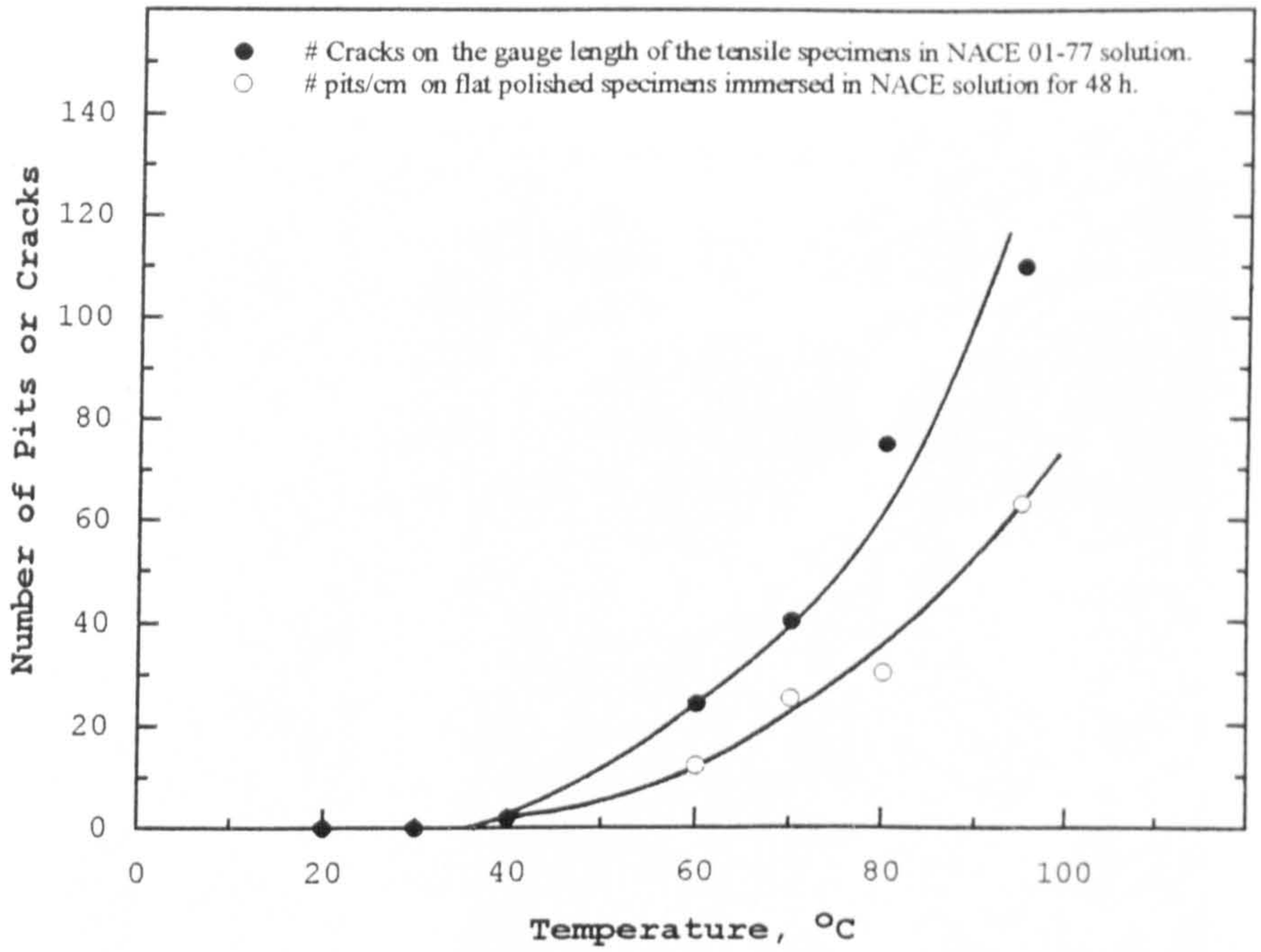

Figure 4.30 The effect of temperature on the density of intiation sites (pits or cracks). Results indicate the number of pits in an area of 1cm^2 after immersion in NACE solution and the number of cracks in the specimen gauge length after failure in NACE 01-77 solution.

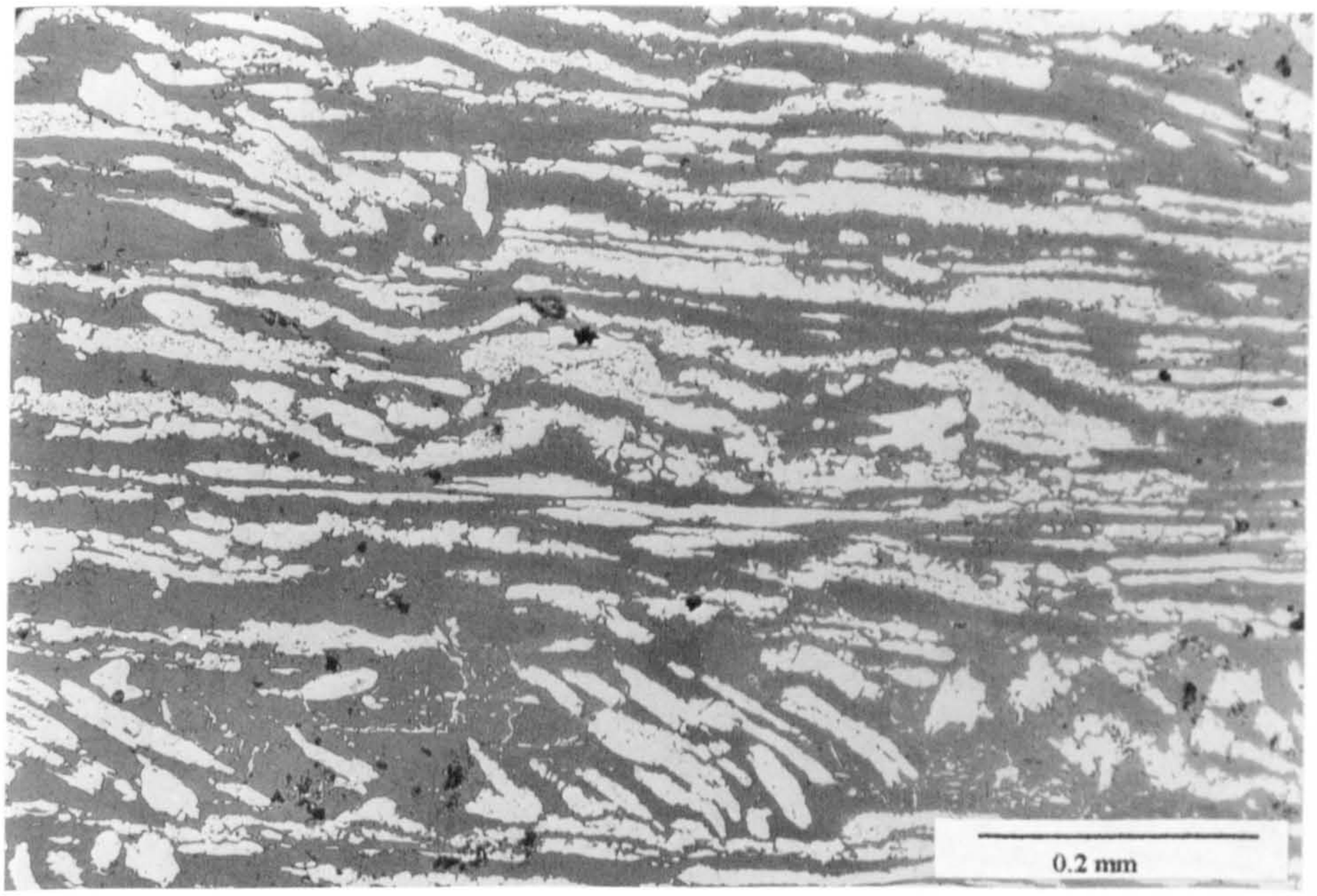

Figure 4.31 Specimen of material C immersed in NACE solution pH = 2.7 at 95° for 48h. Pits initiate at the α-γ interface and grow into the austenite.

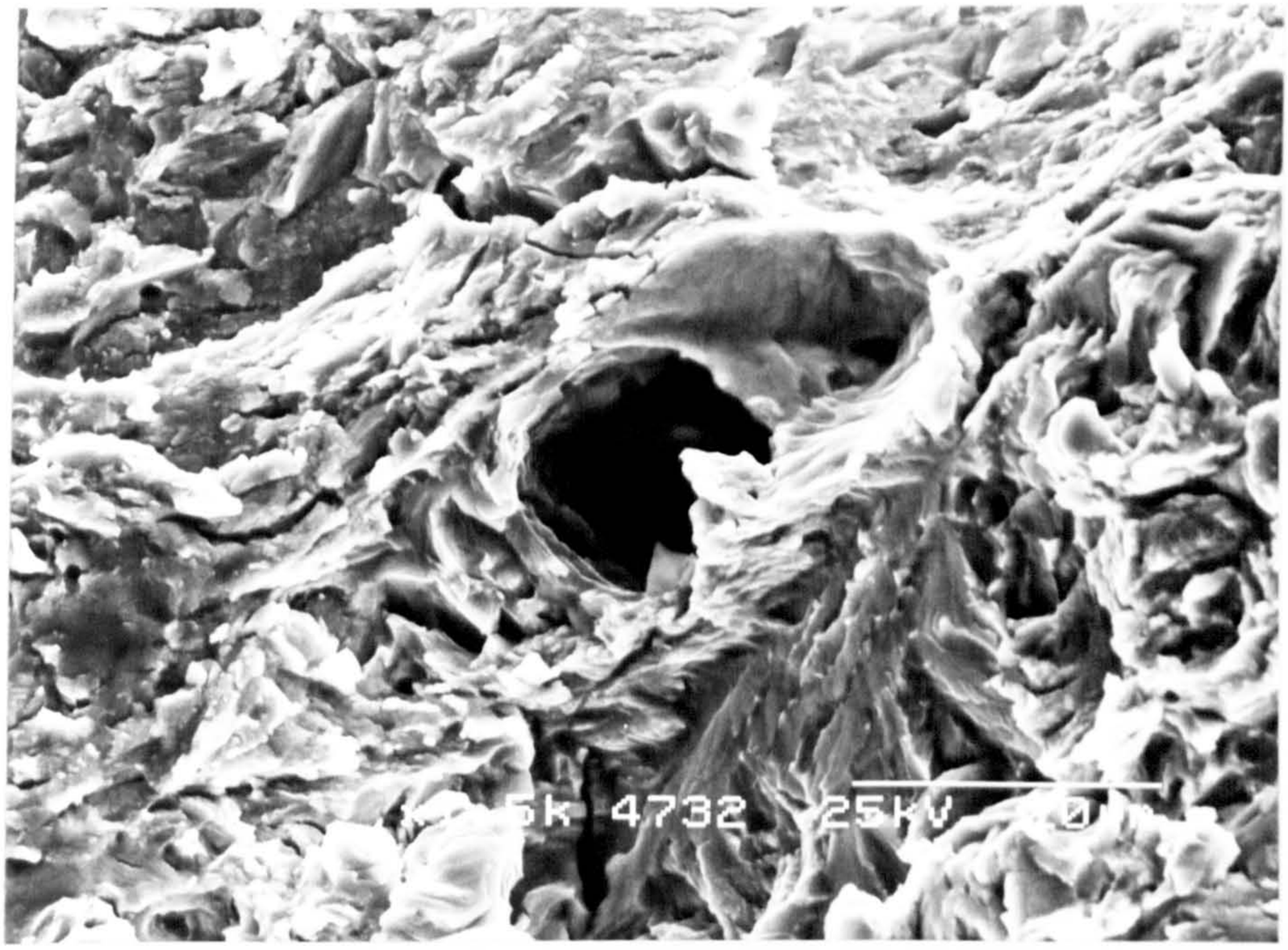

Figure 4.32 Fracture surface of duplex stainless steel showing an inclusion. (NACE-01-77 solution 40°C).

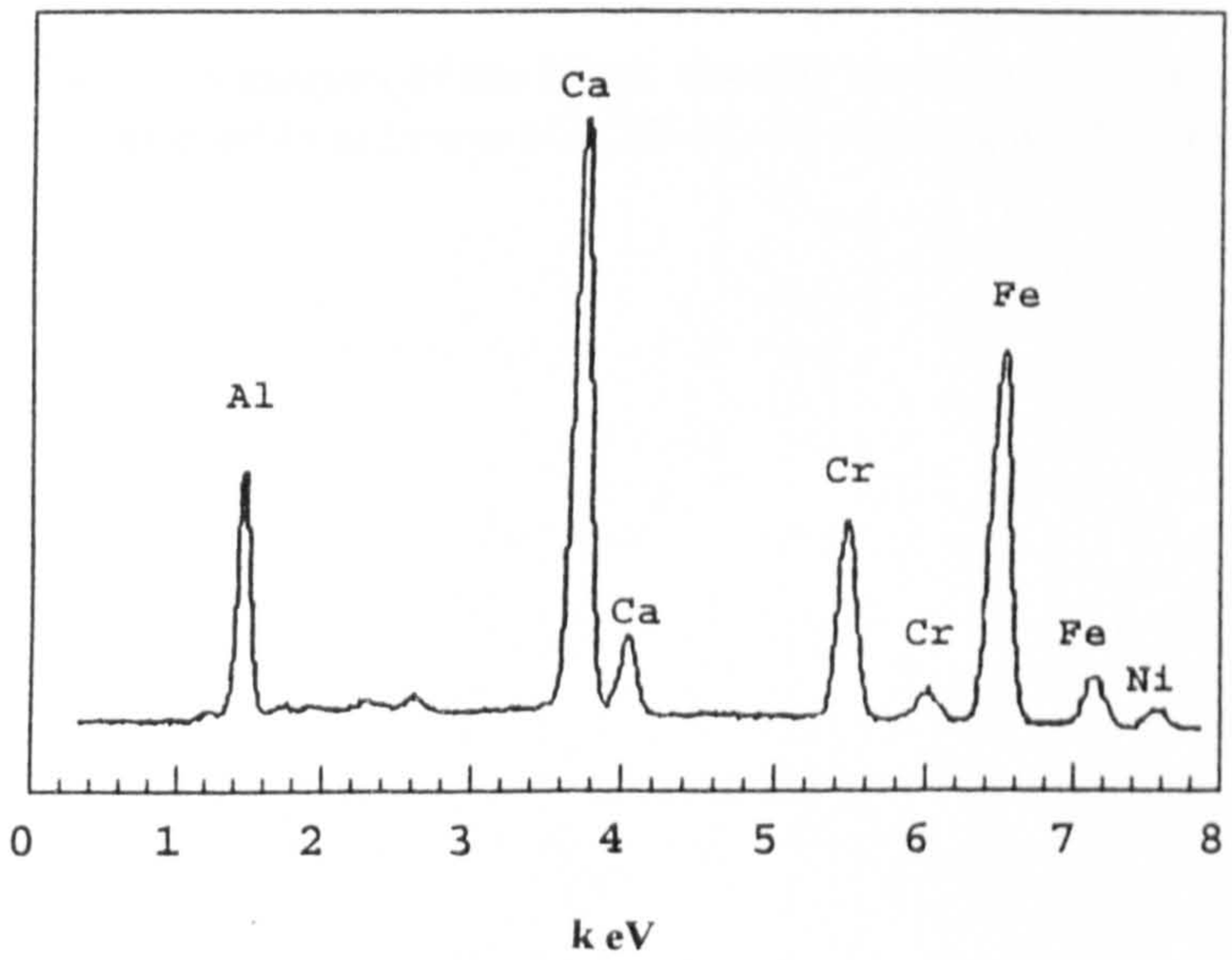

Figure 4.33 EDX analyses obtained for the inclusions at which fracture initiated.

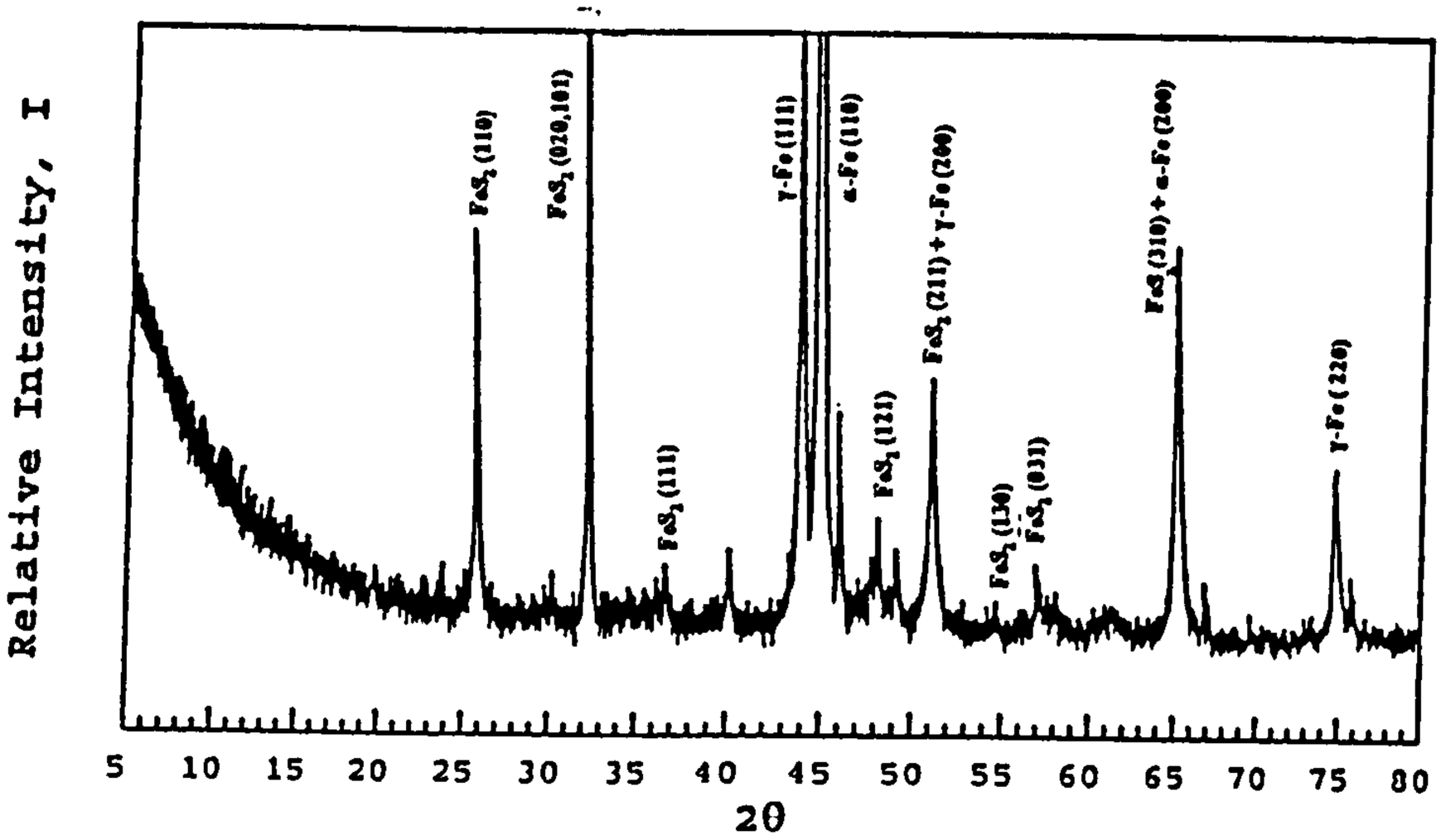

Figure 4.34 X-ray analysis of the black deposit on the surface of a tensile specimen strained to failure in NACE-01-77 solution at 15°C $\dot{\epsilon} = 2 \times 10^{-6}$/s.

was attacked preferentially. The corrosion rate, at 30°C, calculated for the dissolution of austenite (from the depth of penetration) was 0.47mm/yr.

At 30°C, the austenite was uniformly attacked (Figure 4.35) and, when this specimen was subjected to X-rays for film analysis, the austenite peaks had disappeared due to the fact that the austenite was below the general level of the surface, and hence the ferrite. The X-ray analysis of the film also revealed the presence of elemental sulphur, (Figure 4.36) which could be removed (dissolved) by immersion in carbon disulphide for a few seconds. When subsequent X-ray examination was carried out the sulphur lines had disappeared, leaving behind an indication of multi-layers of iron sulphide ($FeS+FeS_2$ among others) (Figure 4.37). At the higher temperature (90°C), however, the austenite in the duplex structure was not uniformly attacked; once initiated, dissolution appeared to be confined to certain preferential sites where it accelerated. When straining is carried out at low temperatures (20-60° C), the secondary cracks are very small and confined to the small necked region, with no evidence of any dissolution in either of the phases (Figure 4.38). The cracks initiate in the ferrite and generally propagate perpendicular to the applied stress, although crack branching at about 45°C is frequently noted.

Cracking along the ferrite-austenite interface is also observed (Figure 4.39), but cracks generally propagate through the ferrite phase and avoid the austenite i.e. many cracks are arrested by the austenite phase. This is all very similar to the cracking that occurs when straining in

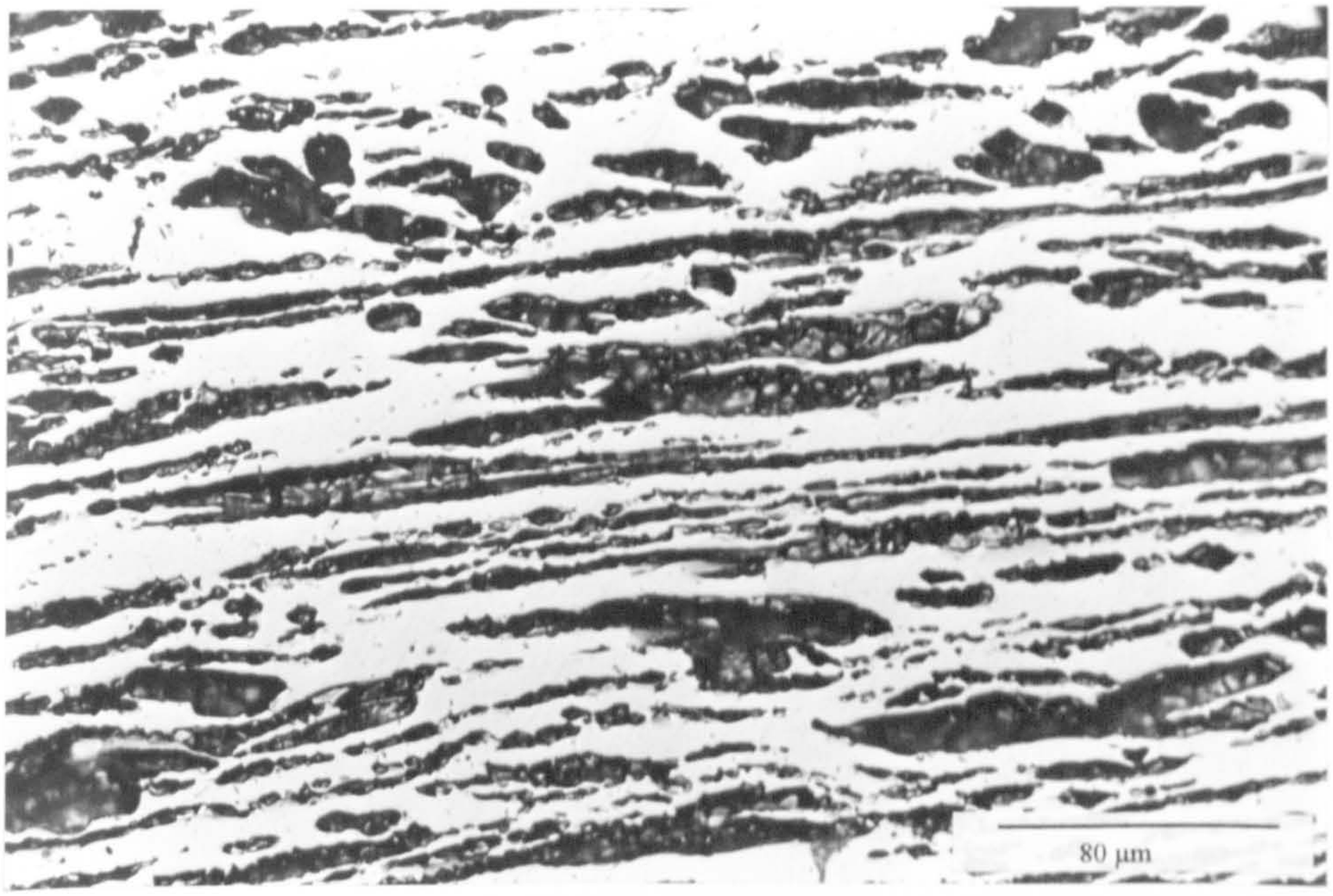

(a)

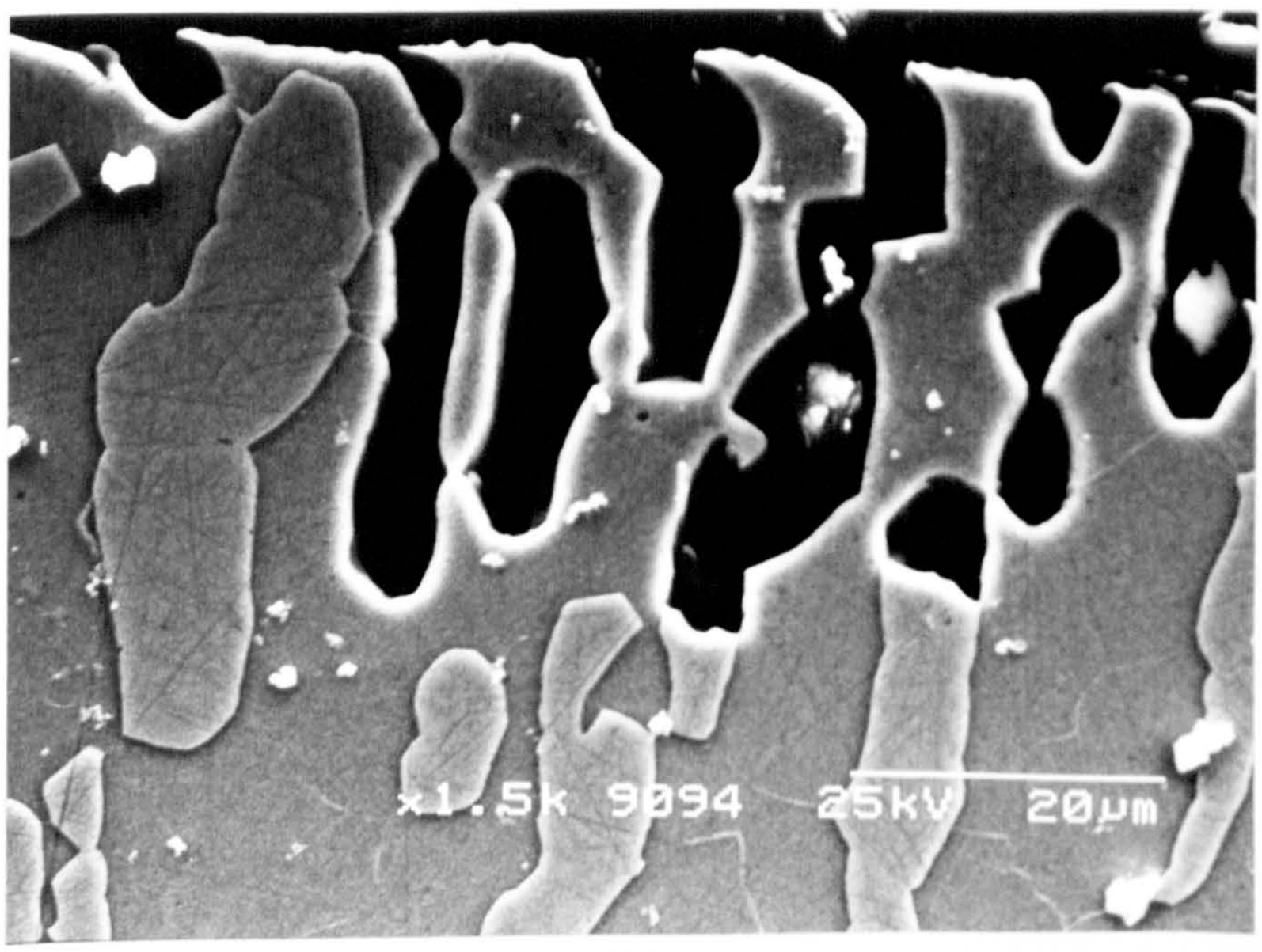

(b)

Figure 4.35 Specimen immersed in NACE-01-77 solution at 30°C for 720 h.
a)- Surface exposed to the test solution.
b)- Surface perpendicular to a).

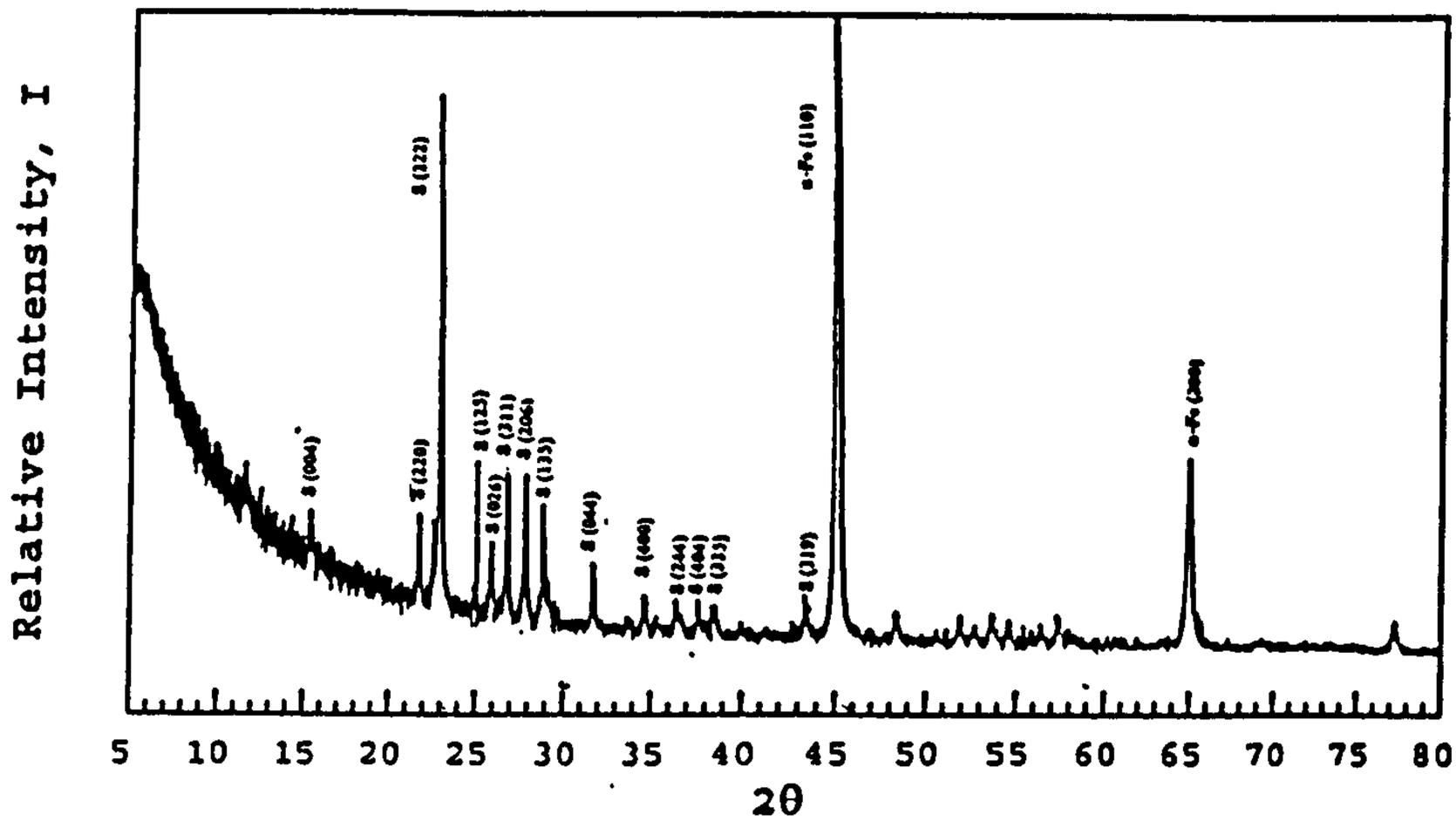

Figure 4.36 X-ray analysis of the film formed on a polished specimen of duplex stainless steel immersed in NACE-01-77 solution at 30°C for 720h. Note the absence of the Fe_{α} lines.

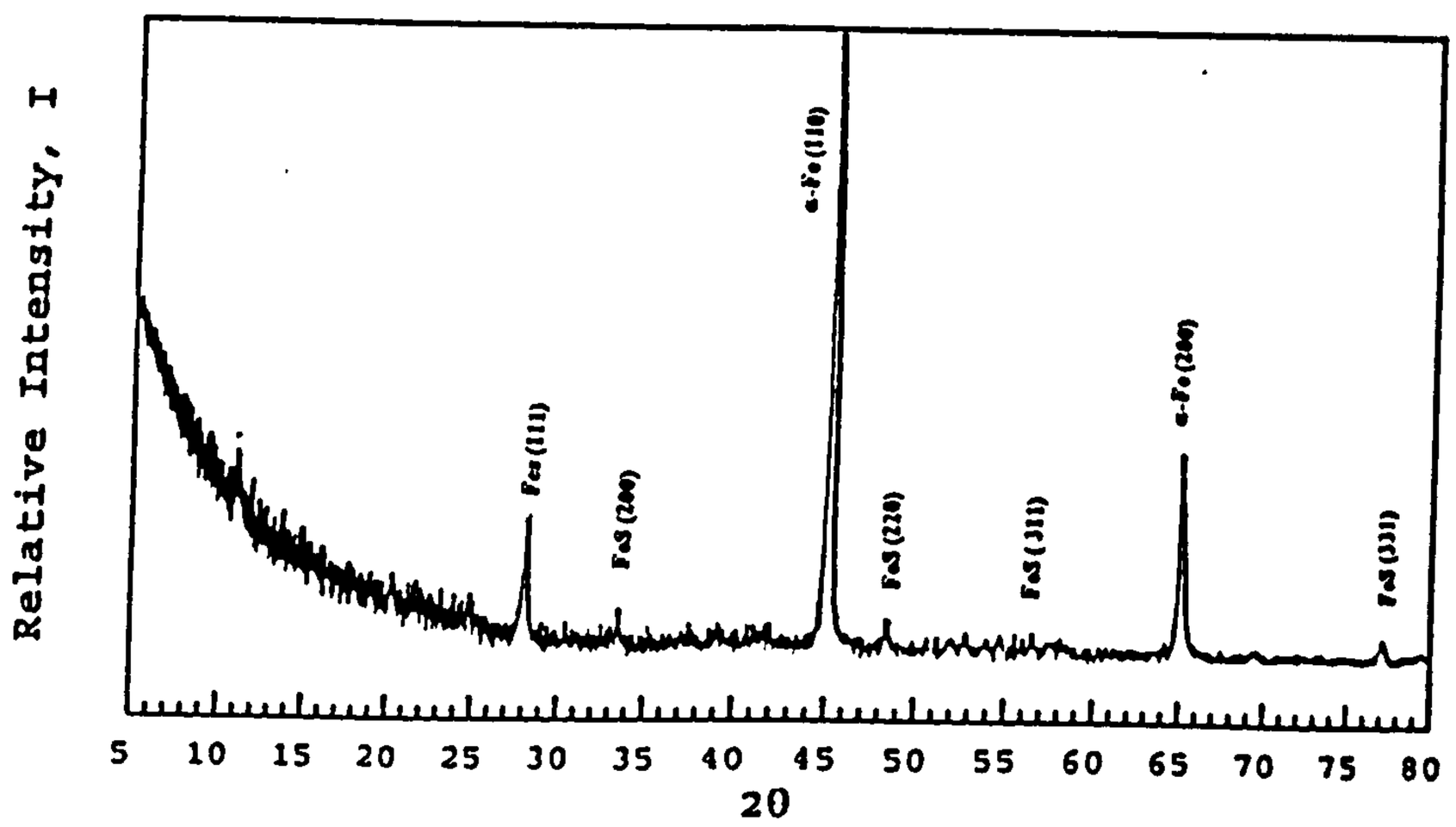

. **Figure 4.37** X-ray analysis of the film formed on a polished specimen of duplex stainless steel immersed in NACE-01-77 solution at 30°C after dissolving the elemental sulphur layer in carbon disulphide.

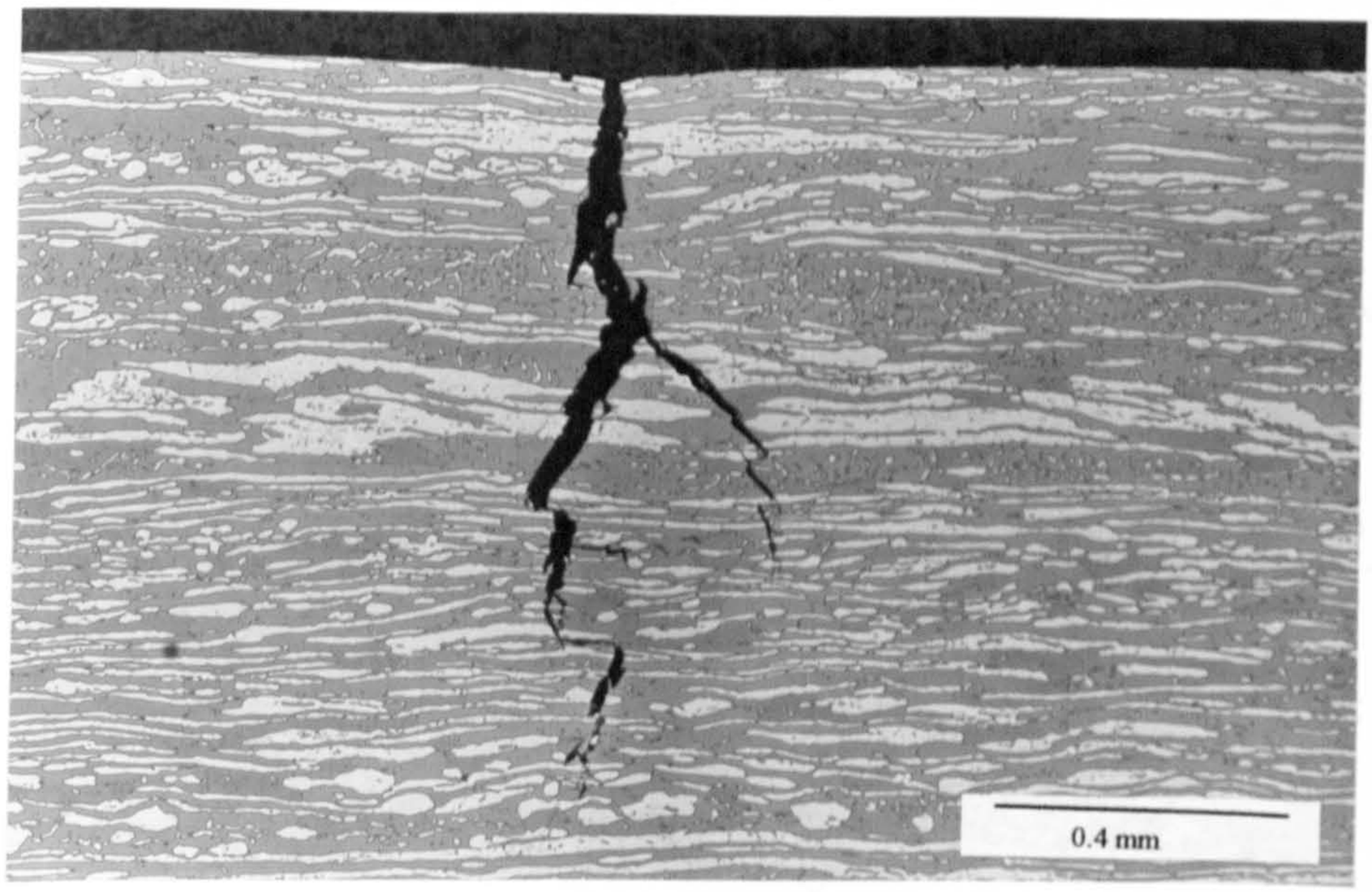

Figure 4.38 Cracking of a duplex stainless steel specimen strained to failure in NACE-01-77 solution at 20°C.

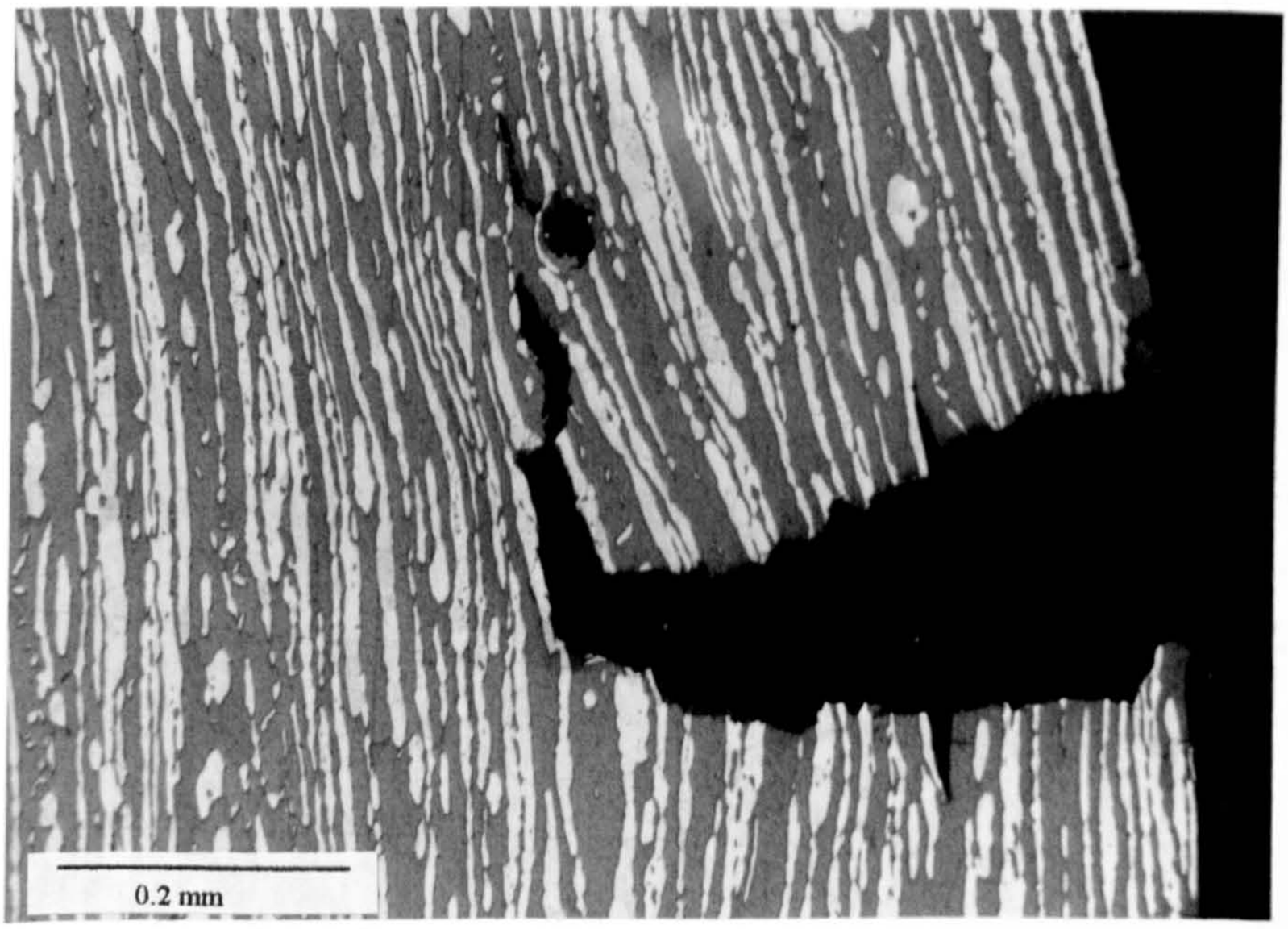

Figure 4.39 A characteristic secondary crack formed in a specimen strained to failure in NACE-01-77 solution at 20°C.

a hydrogen atmosphere and suggests that hydrogen is the embrittling species in the H_2S-bearing environment. Supporting evidence was obtained by careful scrutiny of the two mating fracture surfaces of specimens strained to failure at 30°C, which revealed complete matching of the fracture features (Figure 4.40), except where some dissolution occurs after fracture especially at higher temperatures, i.e. 60°C, (Figure 4.41). The dramatic recovery of the ductility when the temperature is reduced below 20°C could conceivably be attributed to some thermally activated process, such as hydrogen pick-up (including diffusion through any surface film) in the metal. Potentio-dynamic polarization curves were conducted over the whole temperature range in an attempt to shed light on this behaviour (Figure 4.42,4.43).

As might be expected, the polarization curves demonstrate that a decrease in temperature promotes a dramatic decrease in corrosion rate, as indicated by the current density. No passive region occurs on the polarization curve at 85°C, but as temperature is lowered, the metal tries to passivate. When the temperature reaches 2°C, some form of protective film, believed to be a type of iron sulphide, occurs over a substantial range of potential between -400 and -200 mV (sce). The measured open circuit potential during tensile straining tests performed in NACE-01-77 solution and non-acified sodium chloride solution saturated with H_2S at 0°C, was ≈-400 mV sce and this appears to correlate well with the region of passivation. This protective film may hinder the entry of atomic hydrogen into the metal and so prevent embrittlement.

Two specimens strained to failure in the NACE-01-77

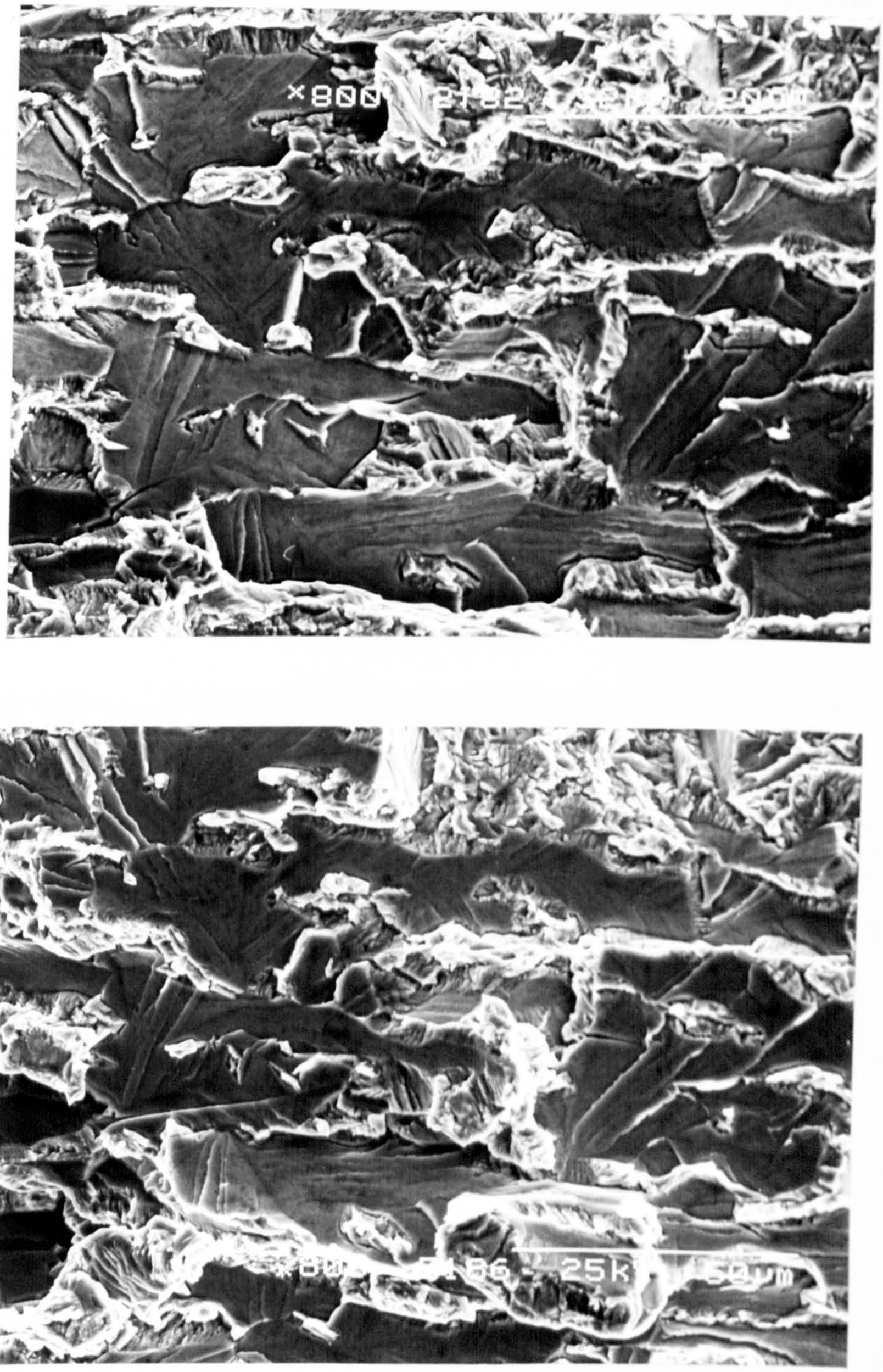

Figure 4.40 The two matching faces of the fracture surface of a specimen (material C) strained to failure in NACE-01-77 solution at 30°C.

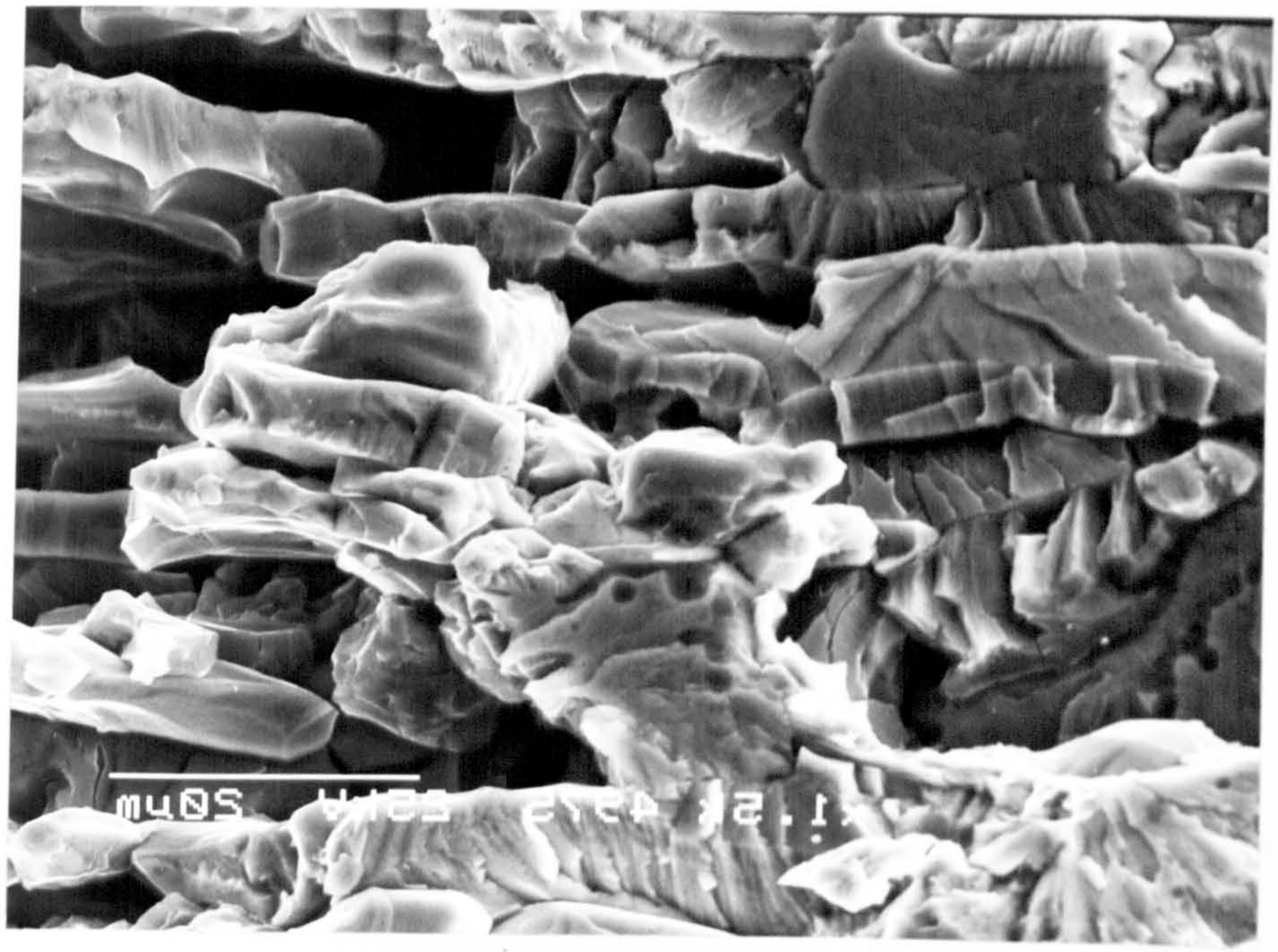

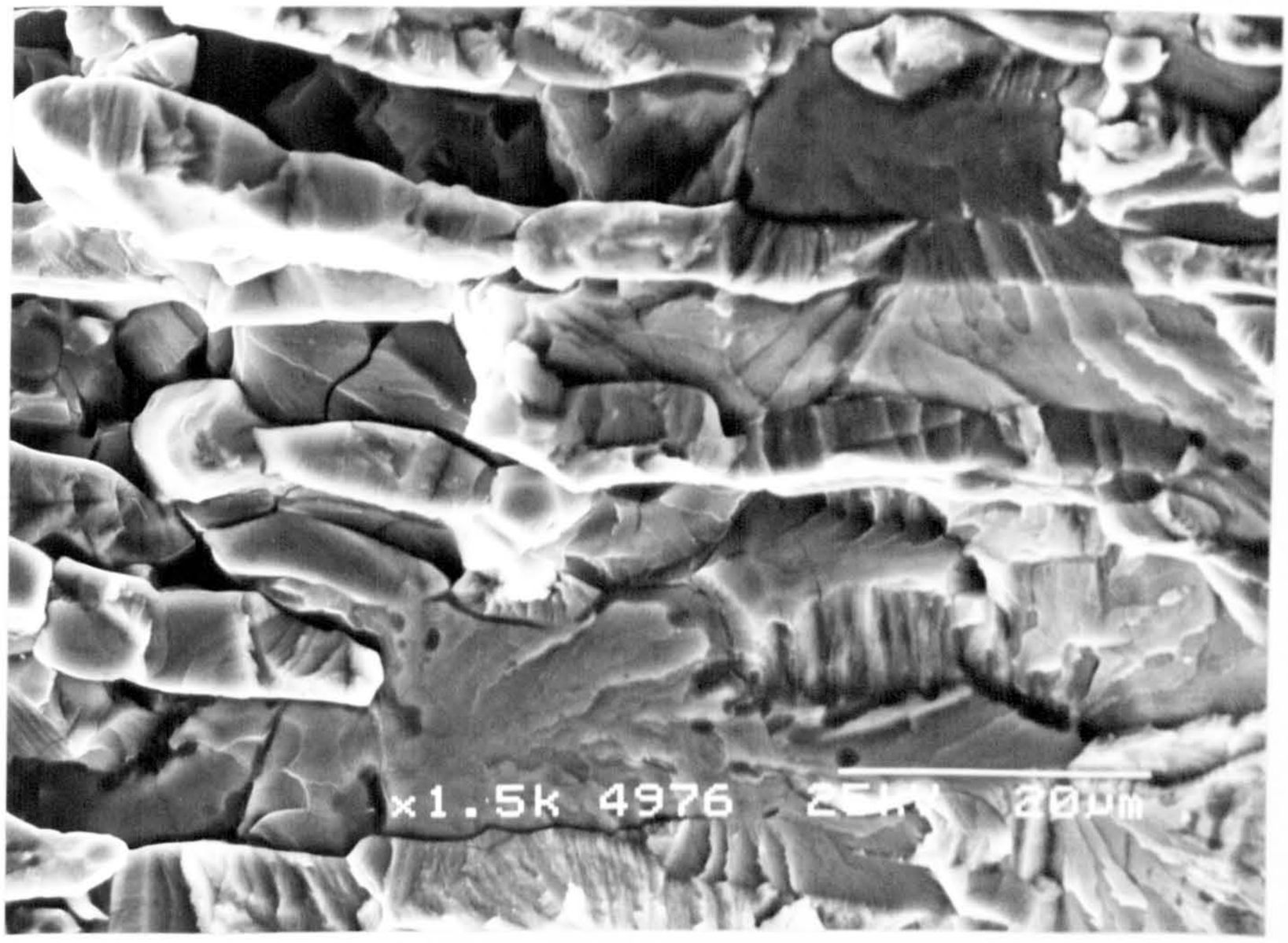

Figure 4.41 The two matching faces of the fracture surface of a specimen strained to failure in NACE-01-77 solution at 60°C.

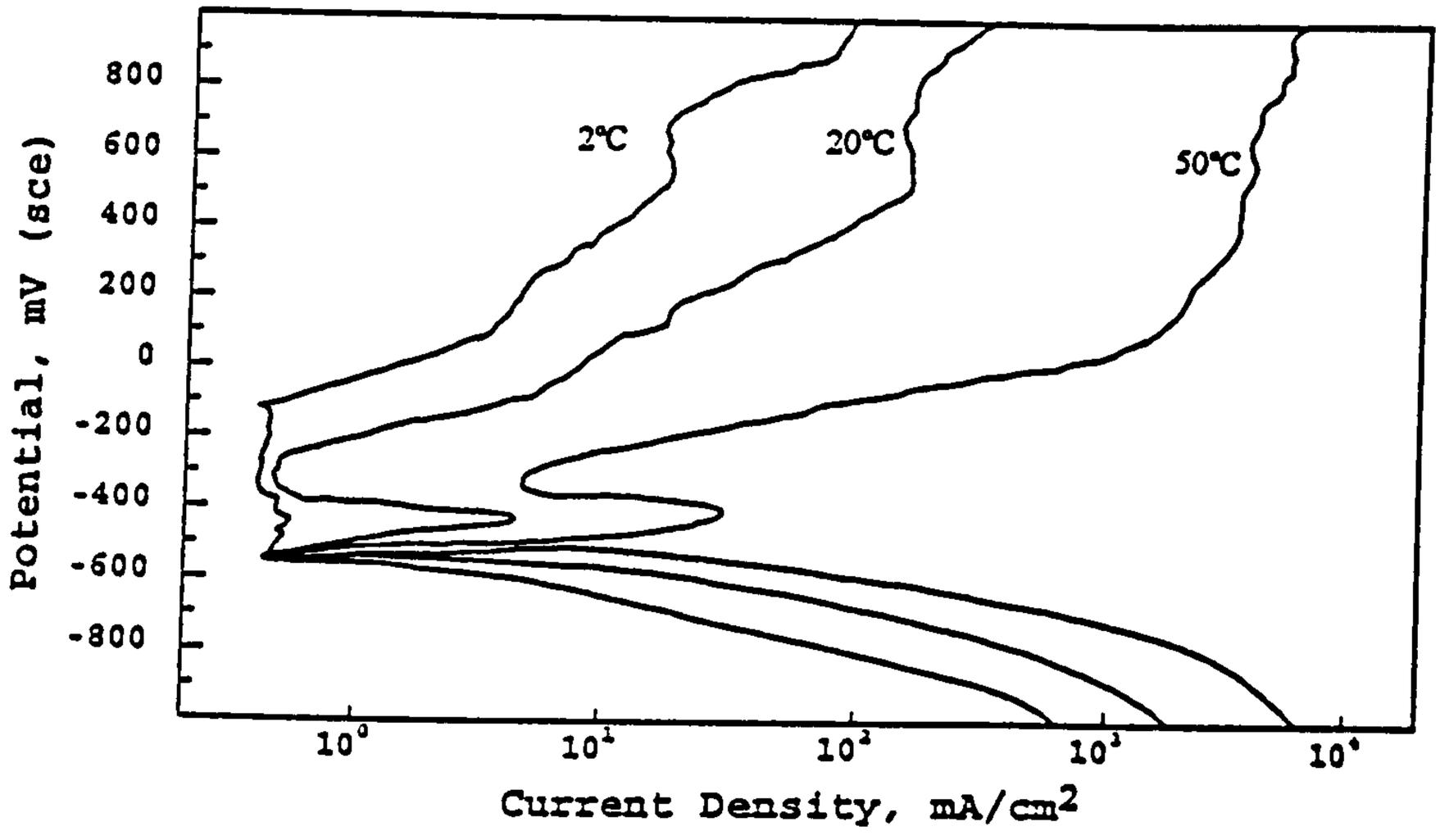

Figure 4.42 Dynamic polarization curves for duplex steel C in 3.5% NaCl solution saturated with H_2S at various temperatures. Sweep rate = 10 mV/s.

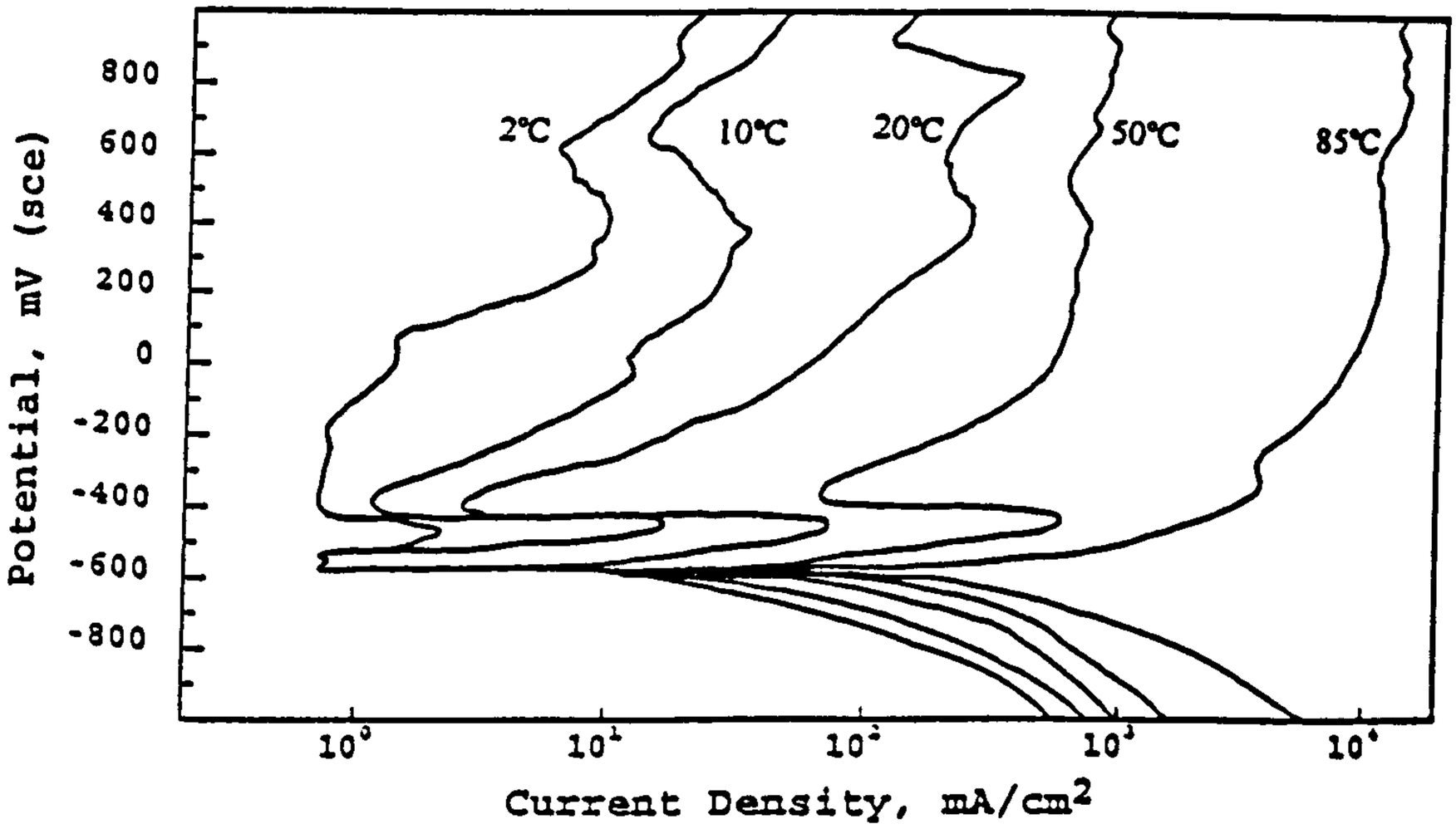

Figure 4.43 Dynamic polarization curves for duplex steel C in NACE-01-77 environment. Sweep rate = 10mV/s.

solution (at 0°C) whilst polarized to a slightly more negative potential than the open circuit i.e. -500 and -550 mV(sce) both failed in a brittle manner with %RA of 31 and 33 respectively (Figure 4.28). It would appear that the applied potential shifts the metal from the passive region (-200 to -400 mV(sce)) to a more active potential where the film does not form and this facilitates the entry of atomic hydrogen into the metal.

At temperatures above 70°C, in both solutions, numerous secondary cracks appear along the gauge length and microscopical examination of the gauge length indicates that these initiate at pits (Figure 4.44) in marked contrast to the initiation of cracks at lower temperatures (Figure 4.45). After pitting occurs, small cracks tend to initiate and propagate by cracking of the ferrite and simultaneous dissolution of the austenite (Figure 4.46). The cracks tend to become blunted by the accelerated corrosion reaction and this produces a recovery in the measured ductility. When the temperature reaches 95°C the dissolution of the austenite is very extensive and leads to the greatly enhanced ductility (Figure 4.47).

Two specimens, however, were strained to failure at 80°C in NACE-01-77 solution (near the temperature of maximum embrittlement) whilst polarized to -350 and -400 mV(sce) i.e. 150 and 100 mV more noble than the measured open circuit potential at 80°C (-500 mV sce) respectively. In these, extensive pitting was visible and the straining was stopped before final failure (separation) i.e. the tests were stopped after about 18h (Figure 4.48). It is obvious that the imposed potential caused the metal to be in the active state and hence pitting occurred. Thus, a small shift

Figure 4.44 Cracks initiated at pits in a specimen strained to failure in NACE-01-77 solution at 80°C.

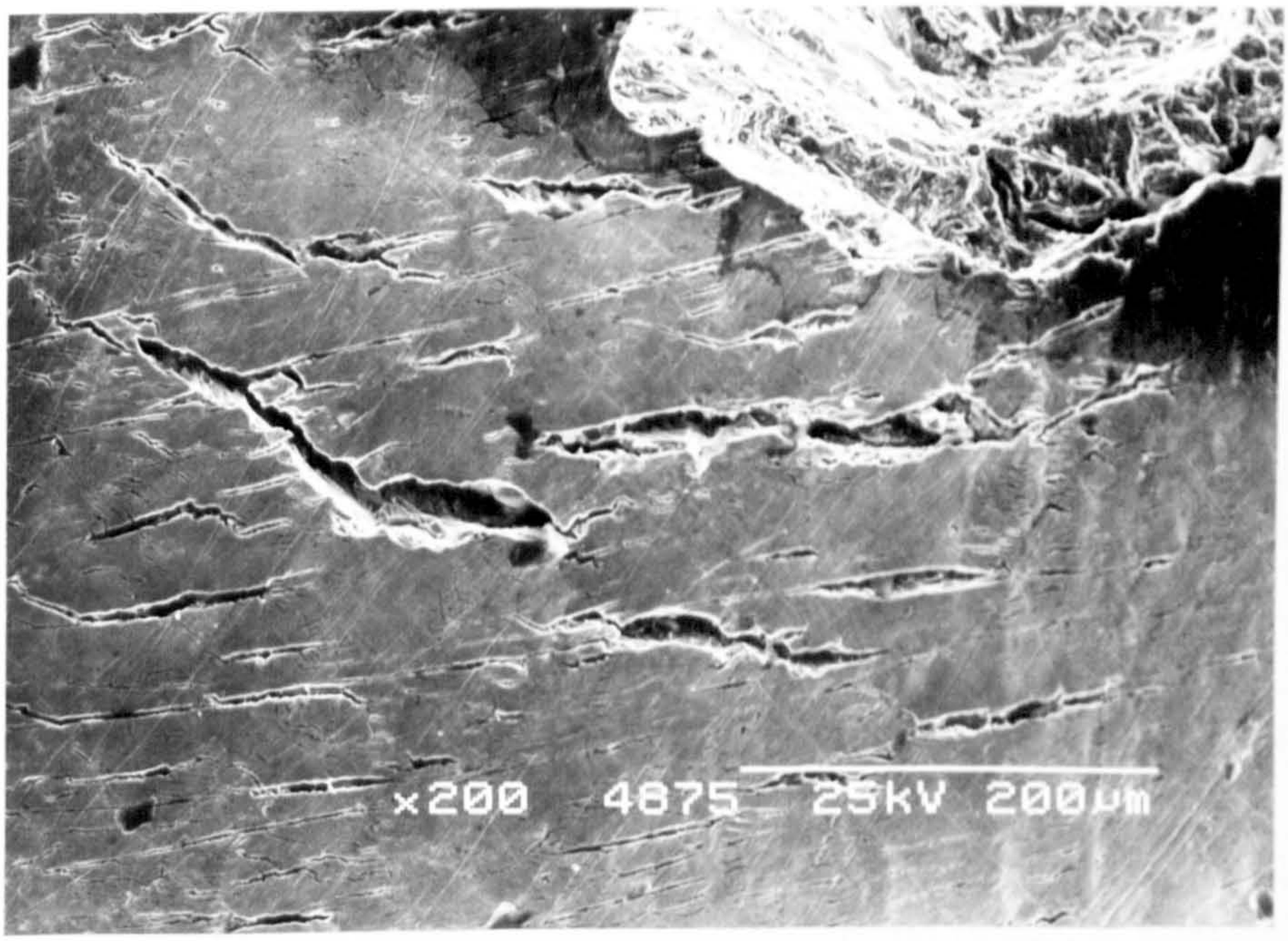

Figure 4.45 Secondary cracking in a specimen strained to failure in NACE-01-77 solution at 60°C.

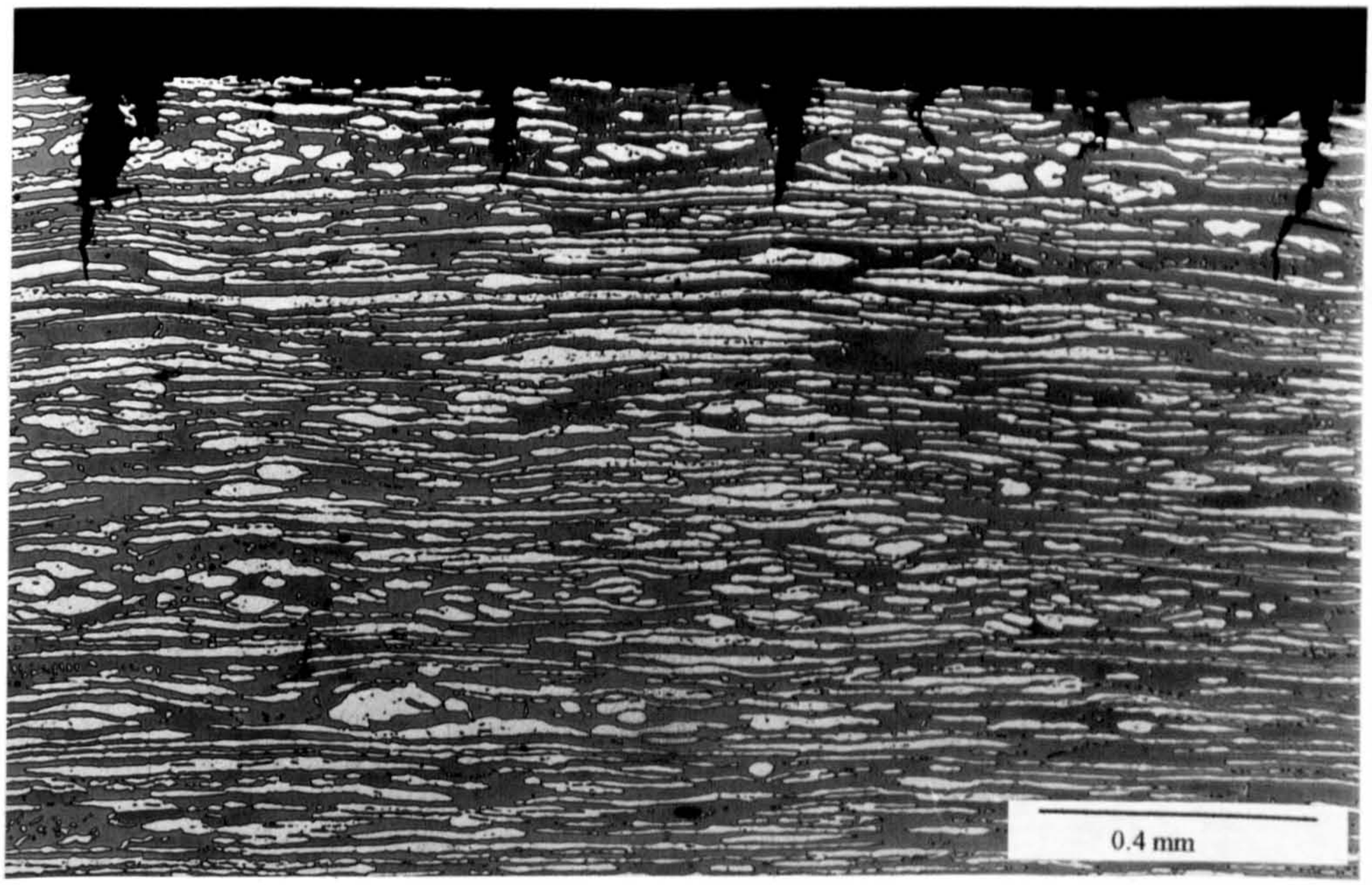

Figure 4.46 Secondary cracking of duplex material C strained to failure in NACE-01-77 at 60°C

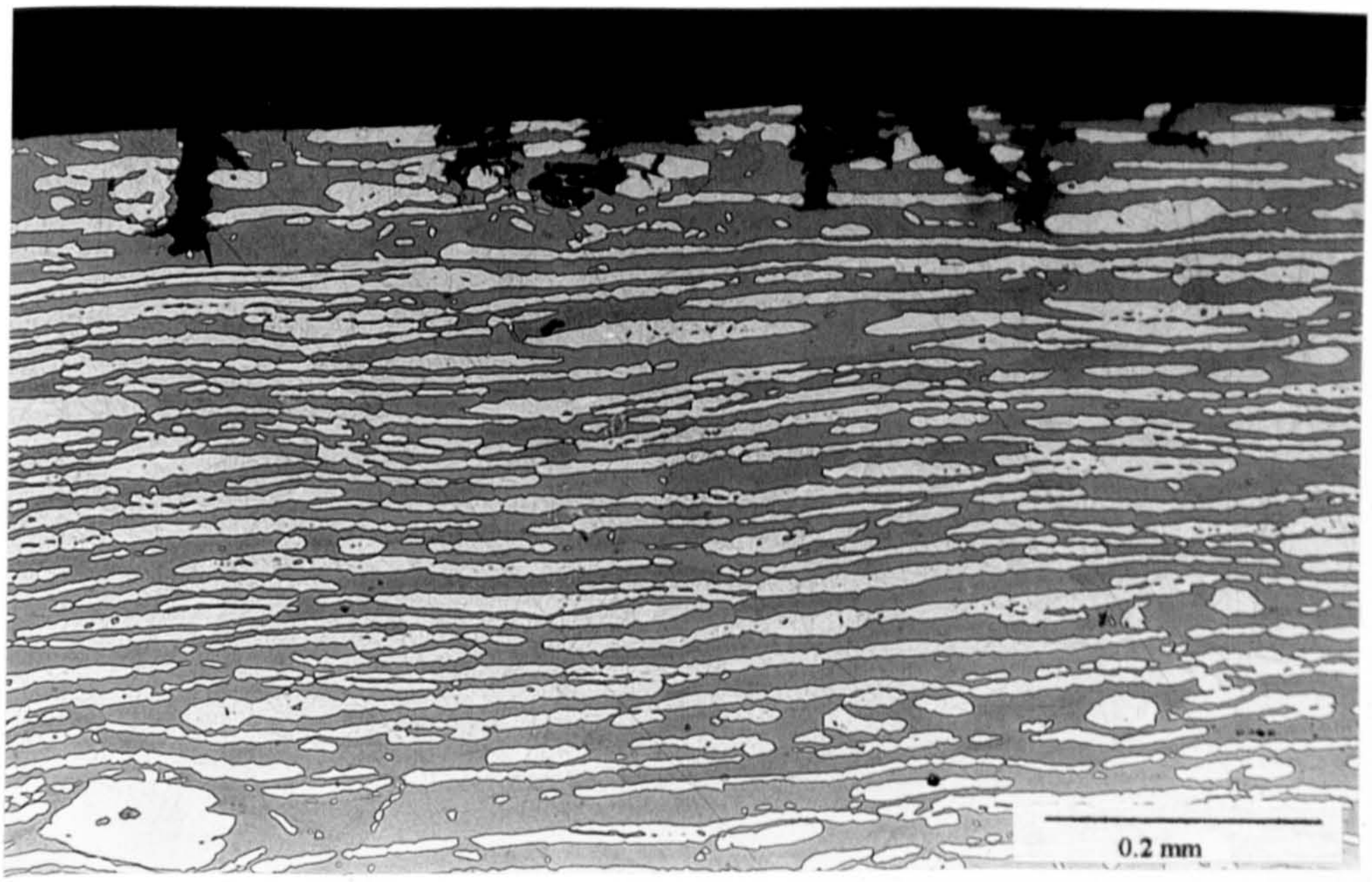

Figure 4.47 Secondary cracking of duplex material C strained to failure in NACE-01-77 solution at 95°C

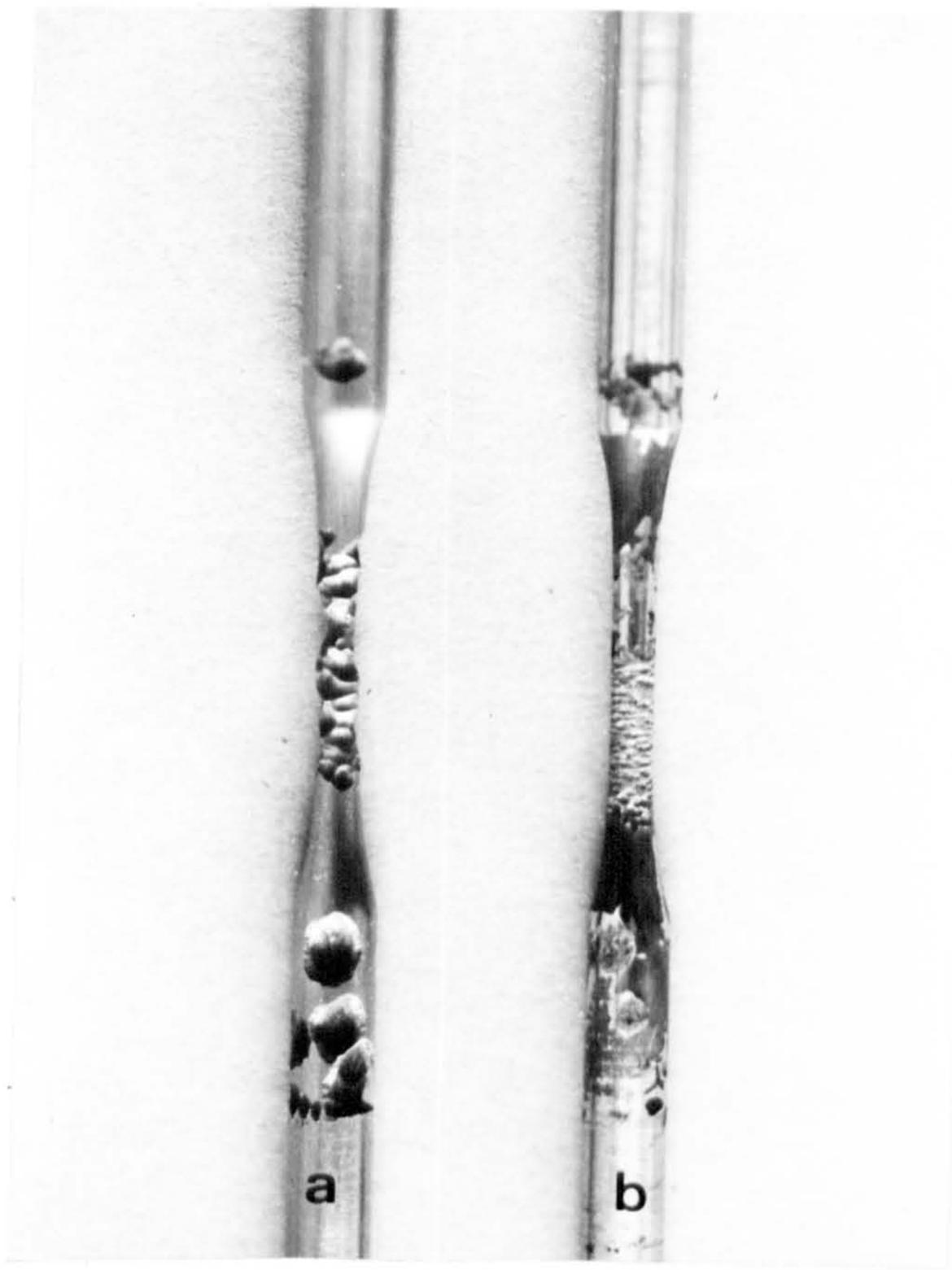

Figure 4.48 Tensile specimens strained in NACE-01-77 solution at 80°C whilst polarized at (a) -350 mV sce and (b) -400 mV sce.

in potential at a temperature where hydrogen embrittlement might be expected to dominate the failure may introduce excessive dissolution instead.

SEM examination of fractured surfaces has indicated that the ferrite always fractures in the cleavage mode and revealed river markings. The cleavage surfaces are invariably clean and free from any corrosion product. On the other hand, although the austenite phase showed some ductility at temperatures up to 30°C (Figure 4.49), the austenite islands near the crack initiation site were severely corroded above this temperature (i.e. 40°C) and there were deposits of corrosion product (Figure 4.50). When the corrosion product was analysed using EDX, it was found to be rich in sulphur (Figure 4.51), indicating that some form of iron sulphide is present. Removal of these corrosion products by means of ultrasonic cleaning during cathodic polarization in a sodium cyanide bath produced remarkable results. The new cleaned surface (Figure 4.52) showed distinct crevicing of various orientations, within the austenite islands. The fractured surface was subsequently polished slightly to produce a smooth mirror-like finish, and viewed under a microscope to confirm that all crevices marks had disappeared. When this surface was etched with 20% HCl 80%H_2O +0.5g $K_2S_2O_5$ the structure revealed transformation of the austenite near the fracture surface to martensite (Figure 4.53). The crevicing that was present before polishing was the result of corrosive attack of martensite plates by the environment. The martensite was distinguished by its brown-blue appearance, the same colour as the ferrite, depending on the etching time. This is consistent with the formation of martensite in all other specimens.

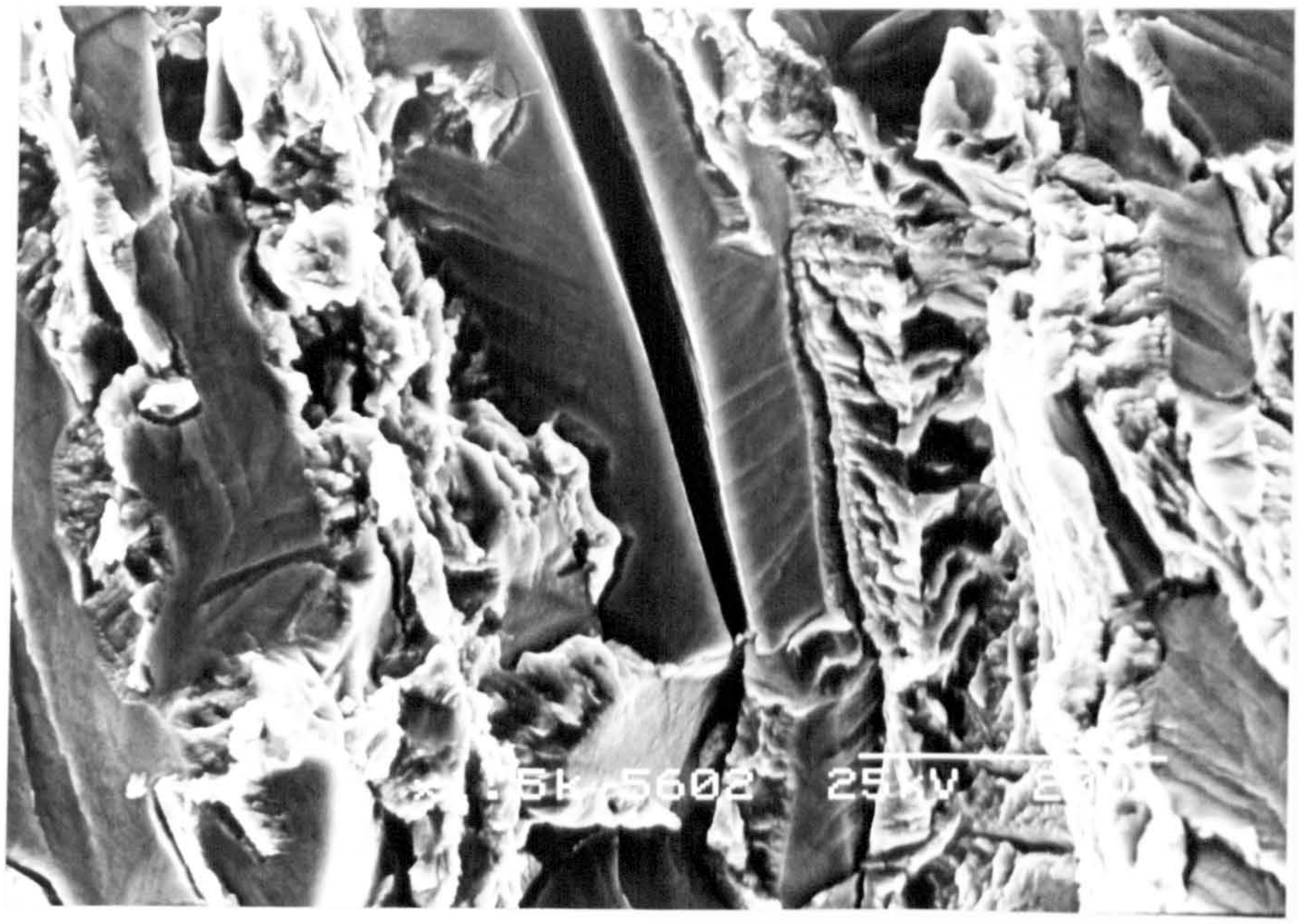

Figure 4.49 Fracture surface of duplex steel specimen strained to failure in NACE-01-77 solution at 30°C.

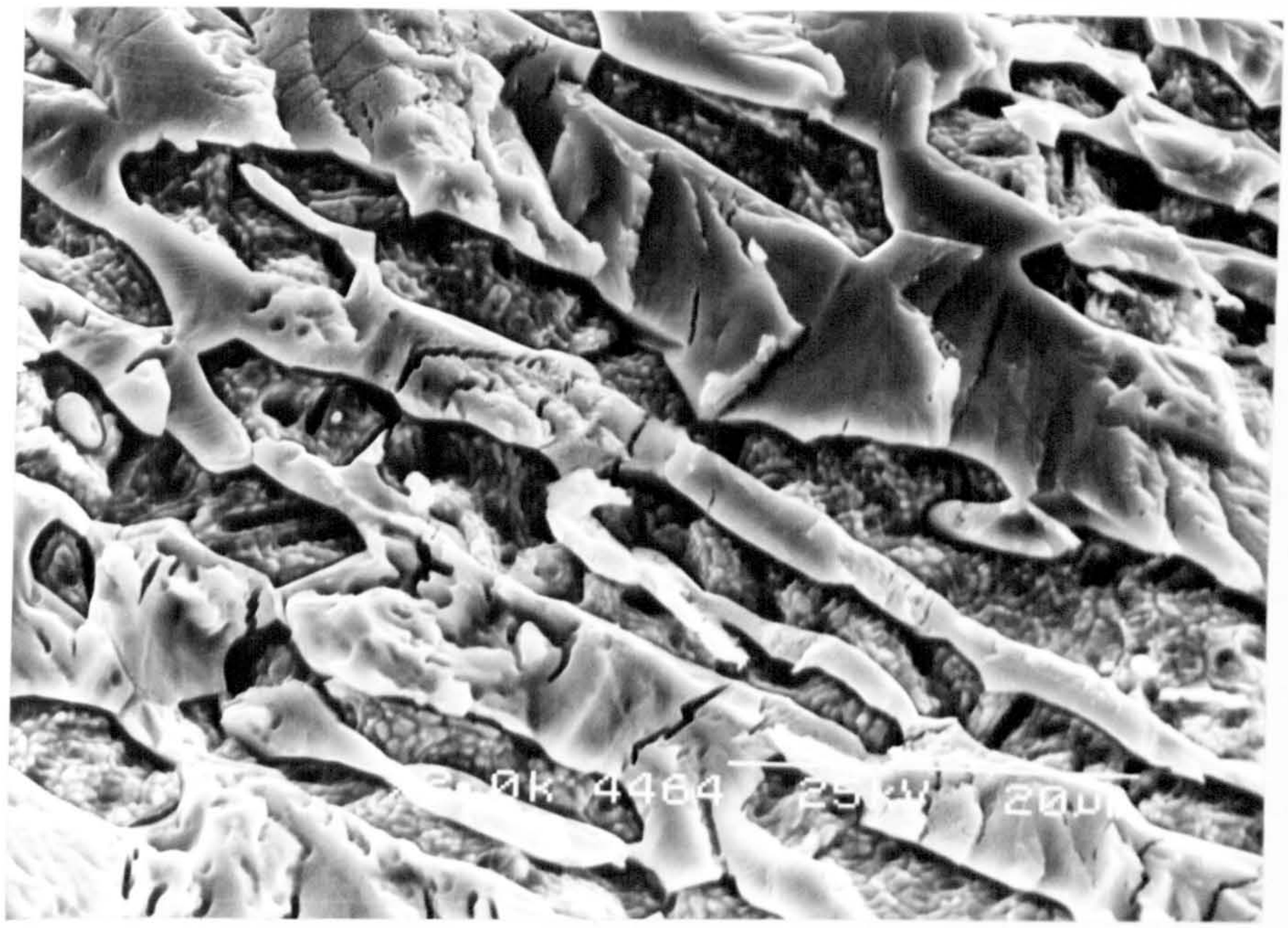

Figure 4.50 Fracture surface of duplex steel specimen strained to failure in NACE-01-77 solution at 40°C .

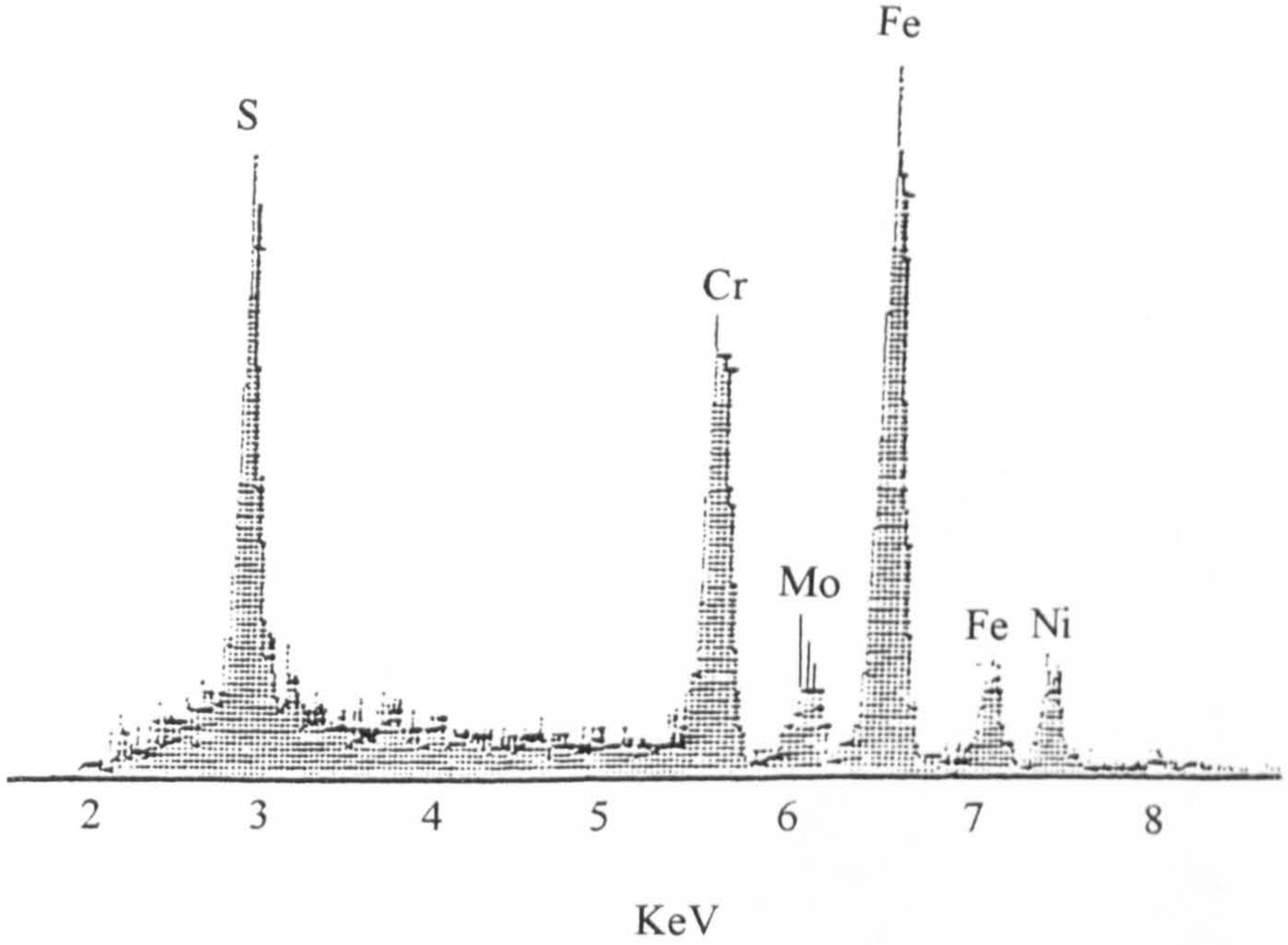

Figure 4.51 EDX analysis of the corrosion product formed on austenite islands in a duplex steel specimen strained to failure in NACE 01-77 solution at 40°C.

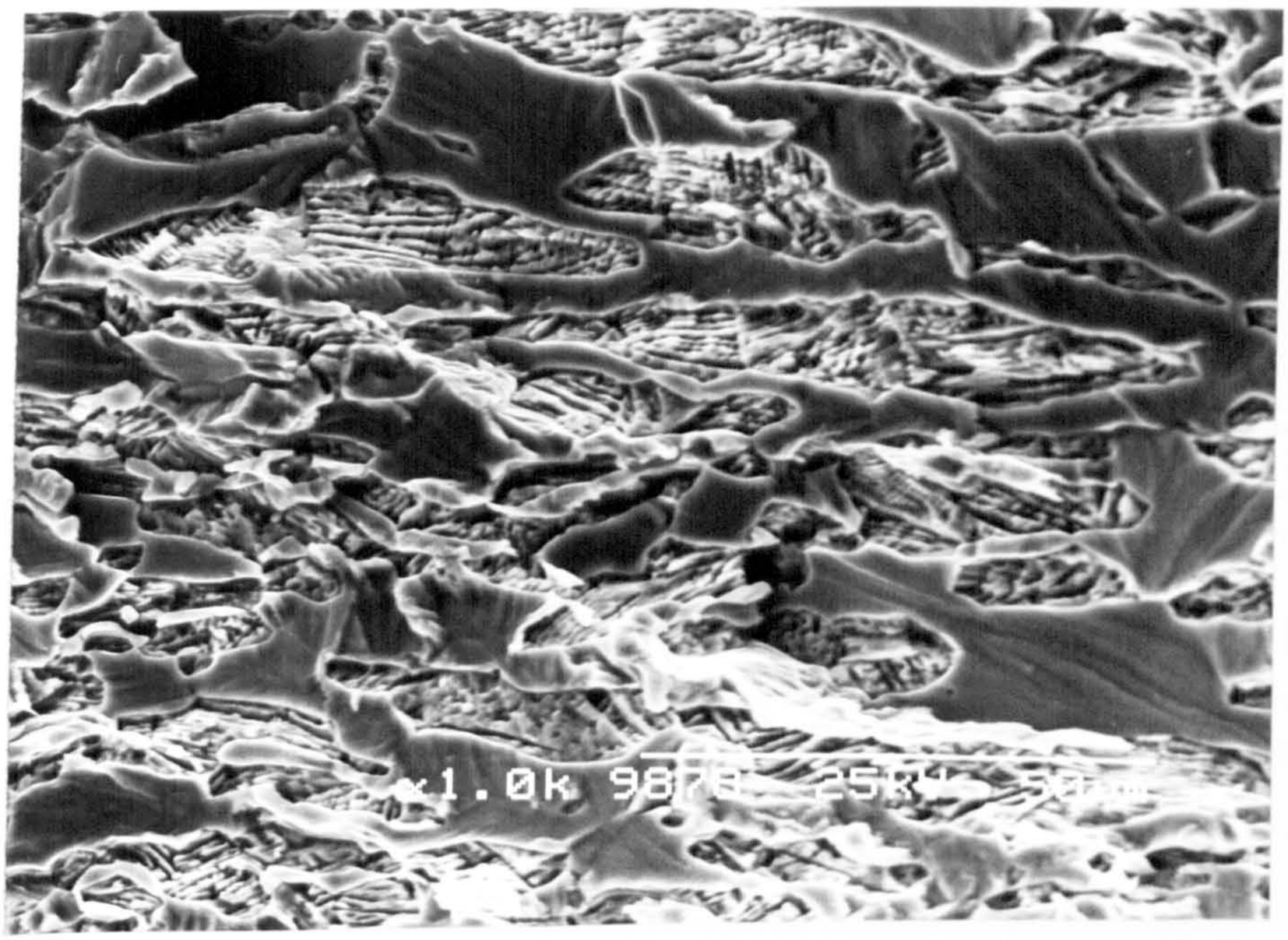

Figure 4.52 Fracture surface of duplex steel specimen strained to failure in NACE-01-77 solution at 40°C (same as Figure 4.50, after cleaning).

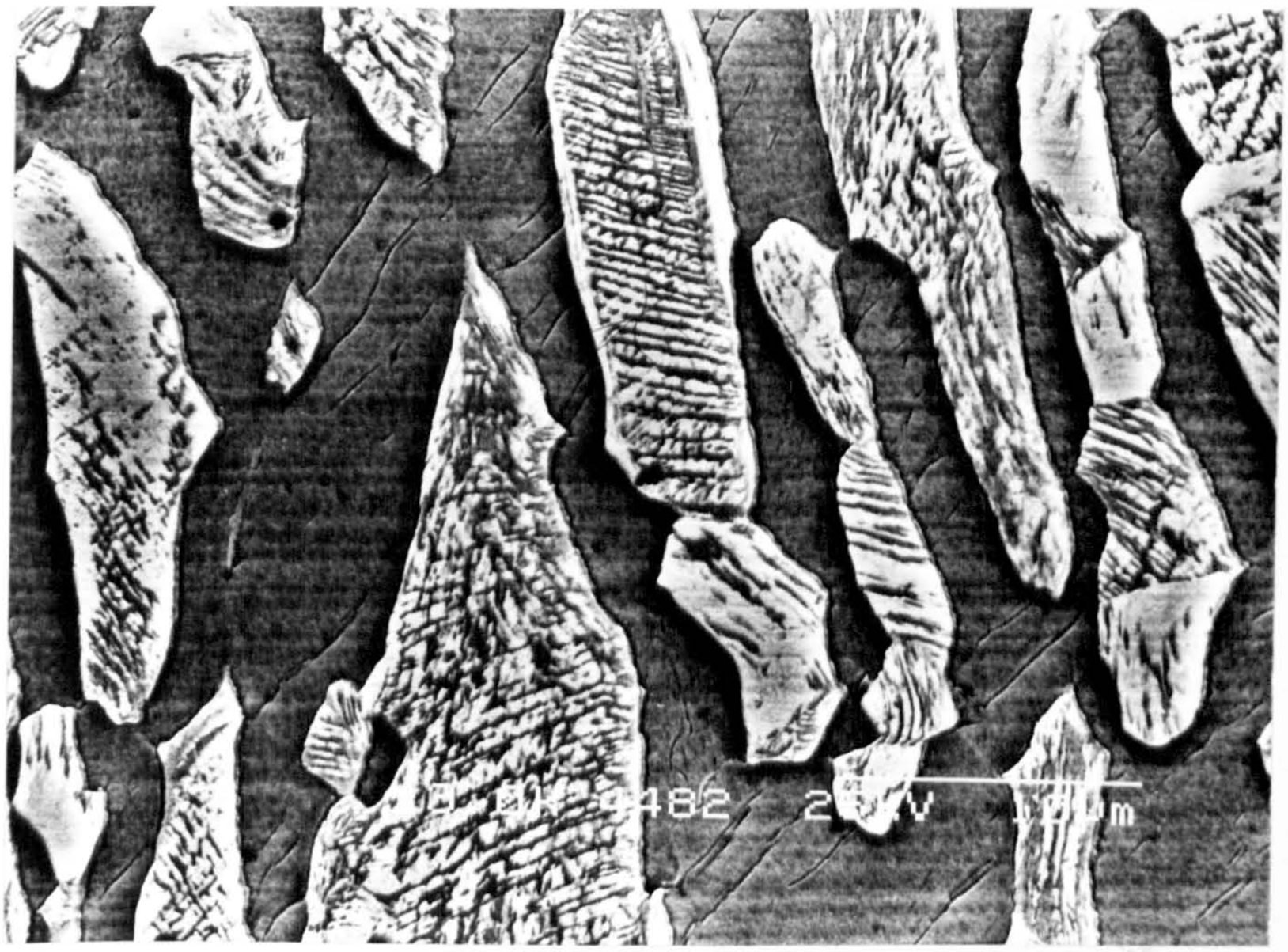

Figure 4.53 Fracture surface of duplex steel specimen strained to failure in NACE 01-77 solution at 40°C (same as figure 4.52 after polishing and etching).

4.2.2 The effect of Chloride ion concentration

Results of tests conducted in neutral aqueous solution, having various chloride ion concentrations ranging from 0 to 700 wppm and saturated with hydrogen sulphide, indicate that chloride ions play a significant role in the embrittlement mechanism. In distilled water (0% Cl) there was no significant loss in ductility but, as the concentration of chloride increased the sulphide scc susceptibility also increased until the chloride level reached ≈300 wppm. Increasing the Cl^- level beyond this limit seems to have little or no influence on the embrittlement (Figure 4.54). The chloride ion seems to play a significant role in the repassivation of the steel. Once the protective film is broken by straining a sufficient amount of chloride ion will inhibit the reformation of the film and hence hydrogen may enter the steel and produce a loss in ductility.

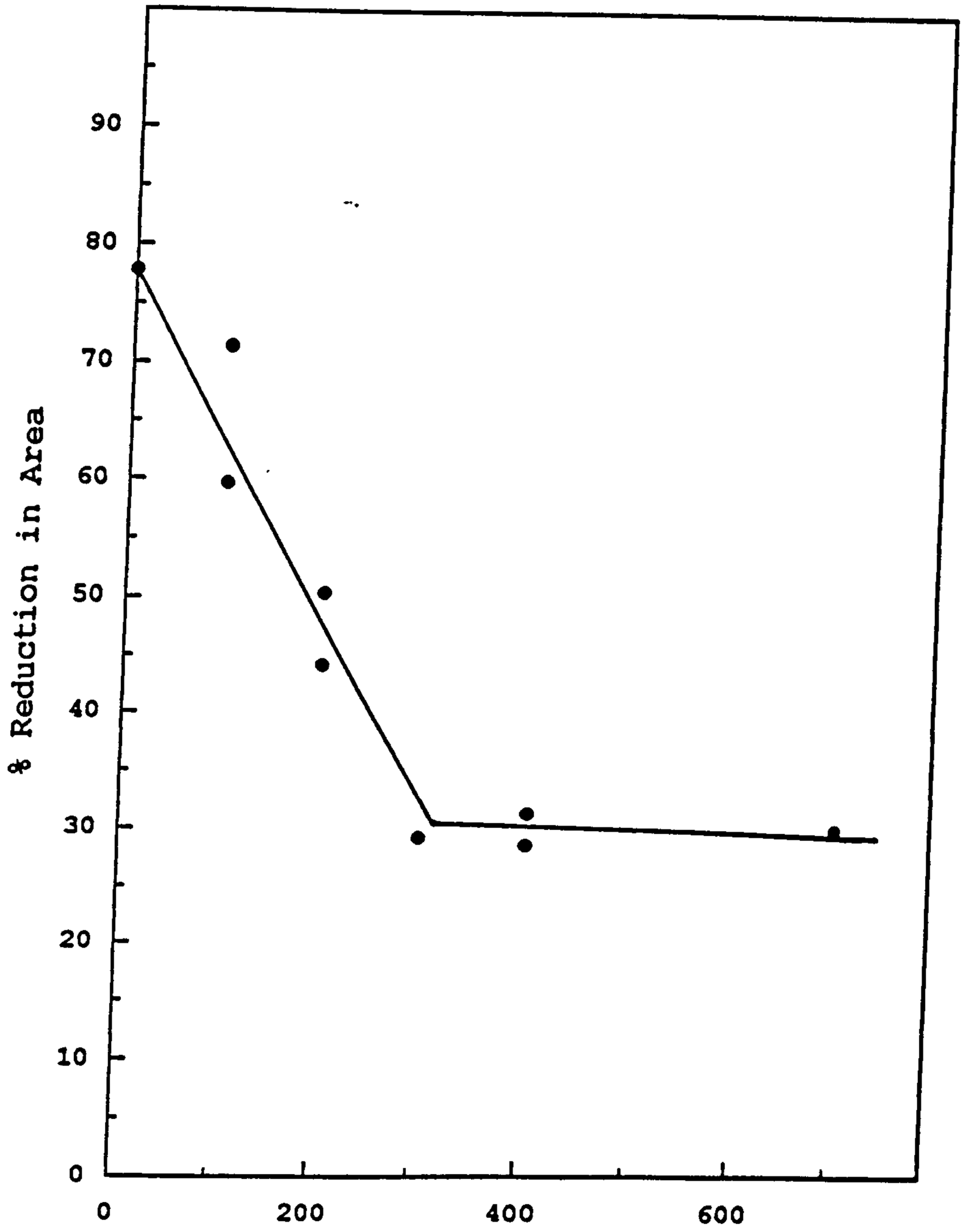

Figure 4.54 The effect of chloride ion concentration on the %RA of duplex steel "C" in solution saturated with hydrogen sulphide.

4.3 Straining cathodically polarized specimens

Straining of material C specimens while cathodically polarized in neutral 0.6 M aqueous sodium chloride (pH=6.5), at 2.0×10^{-6}/s and 70°C, revealed an increase in loss of ductility as the cathodic polarization was increased. No embrittlement is observed until an applied potential of -600 mV(sce) is reached, which coincides with the calculated hydrogen evolution voltage for a solution of such pH (6.5) (Figure 4.55). As the applied potential is further decreased, the loss in ductility observed increases progressively until the potential reaches -1000 mV(sce). At this potential the embrittlement appears to reach a maximum (26 %RA) and any further decrease in potential, in the range employed, seems to have little effect. When, however, the test solution is acified to a pH = 2.7, either by using NACE solution or by the addition of 7 ml/l HCl to the 0.6 M sodium chloride solution, the first embrittlement appears at the much higher potential of -400 mv(sce), which is again in good agreement with the hydrogen evolution voltage for a solution of pH = 2.7 (Figure 4.55). Moreover, no difference in the maximum level of embrittlement is observed between these two solution. The particular acid used to decrease pH seems unimportant and the important factor is the pH, which controls the amount of hydrogen produced at a certain potential.

The theoretical hydrogen fugacities created at the specimen surface during cathodic charging were calculated From the basic thermodynamic relationship between the applied potential, on the standard hydrogen electrode scale (E_H) and the hydrogen fugacity (f_H):

$$E_H = \frac{-RT \ln f_H}{2F} \qquad 4.2$$

Where, F, the Faraday constant = 96487 Coulomb and R is the gas constant = 8.314 $\frac{\text{Joules}}{\text{mol K}}$. The fugacity at which a significant loss of ductility occurred, for straining in all solutions employed, was 10^2 atm., while at the start of the maximum embrittlement plateau, the fugacity was 10^8 atm. (Figure 4.56). Scully and Moran /190/, obtained a similar trend for the dependence of the embrittlement on the applied potentials, and hence the hydrogen fugacities, for AISI 4340 steel in ASTM artificial ocean water (pH = 8.4). They observed a maximum loss in ductility at a hydrogen fugacity of 10^4 atm and this value is much lower than the value obtained for duplex stainless steels used in the present work (10^8 atm). This may be attributable to the higher susceptibility of the high strength 4340 steels to hydrogen embrittlement. The fact that less susceptible alloys require a much higher hydrogen fugacity to cause loss of ductility is evident in the present work. When polarized specimens of material B (which did not suffer any significant loss of ductility when strained in hydrogen, in air after thermal charging, or in the most severe environment containing hydrogen sulphide) were strained to failure with simultaneous cathodic charging, the loss in ductility was observed to begin at -900 mV(sce). This corresponds to an overpotential of -275.5 mV, which produces a hydrogen fugacity of 10^8 atm as compared to the other duplex steels A, C, and D where the embrittlement was observed at a fugacity of 10^2 atm (Figure 4.57, 4.58).

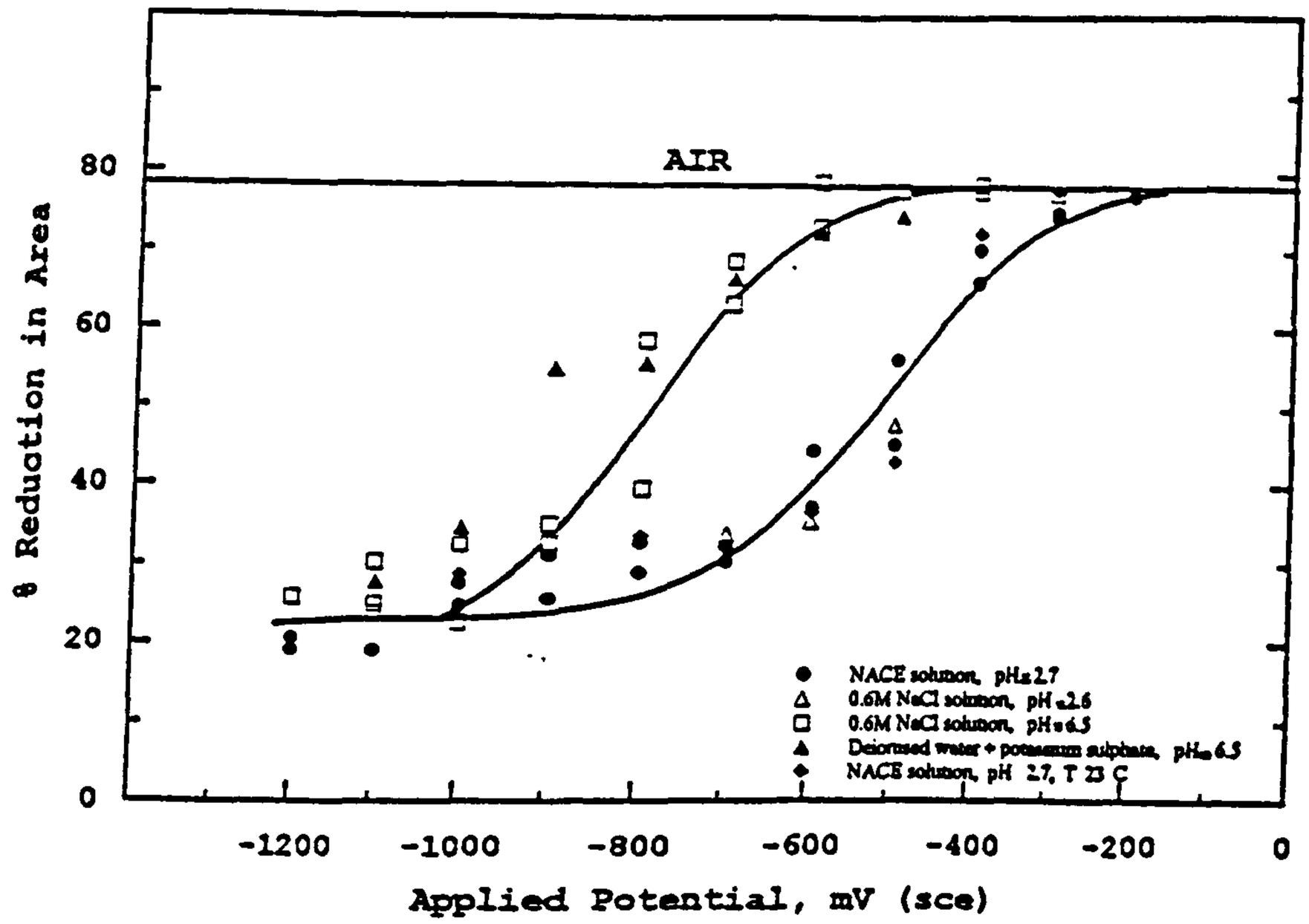

Figure 4.55 Variation of reduction in area with applied potential for cathodically polarized specimens strained to failure at 2.0×10^{-6}/s in aqueous solutions of different pH at 70°C.

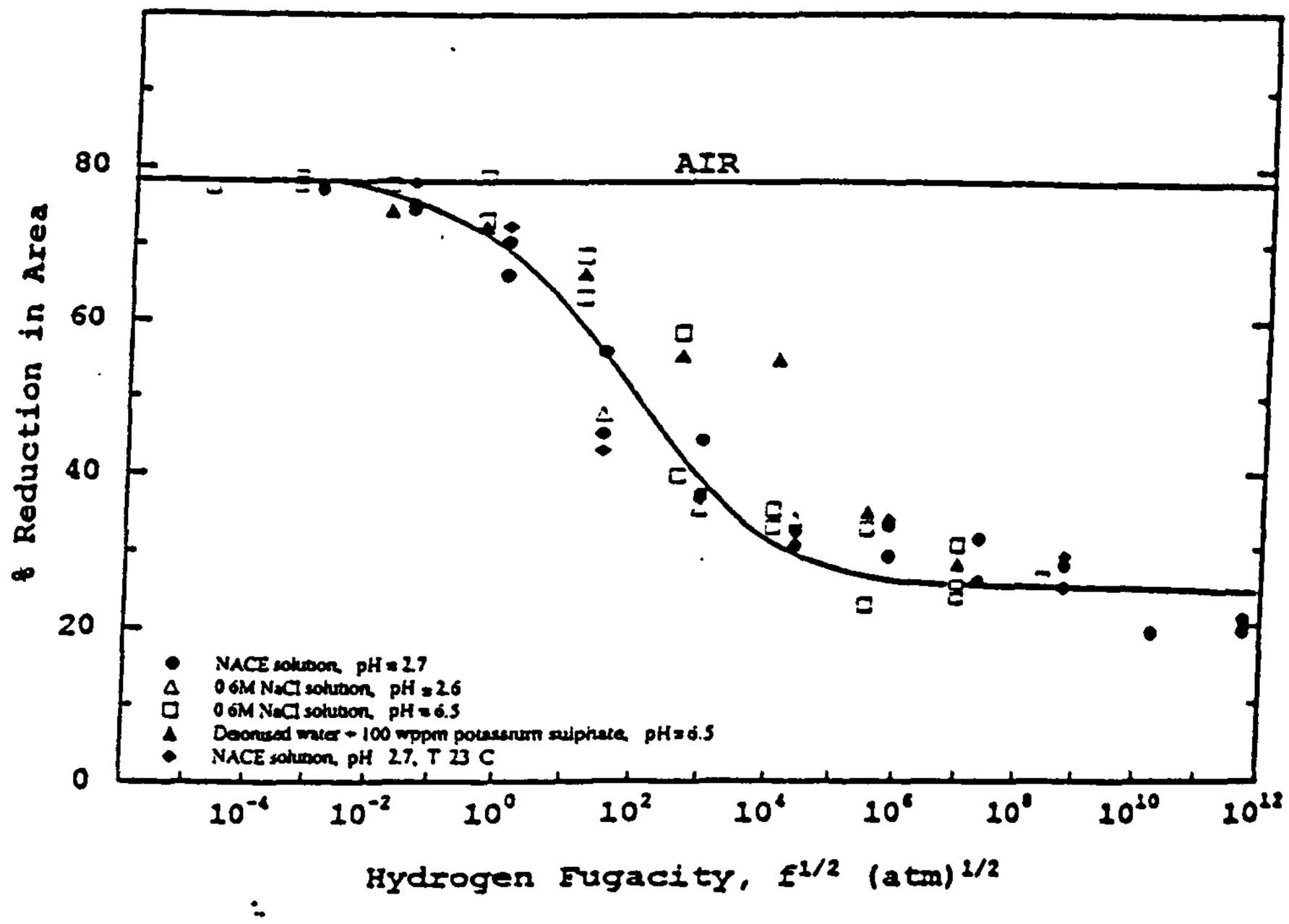

Figure 4.56 Relationship between relative hydrogen fugacity and ductility for duplex stainless steel C specimens strained to failure at 2.0×10^{-6}/s in aqueous solution of various pH at 70°C.

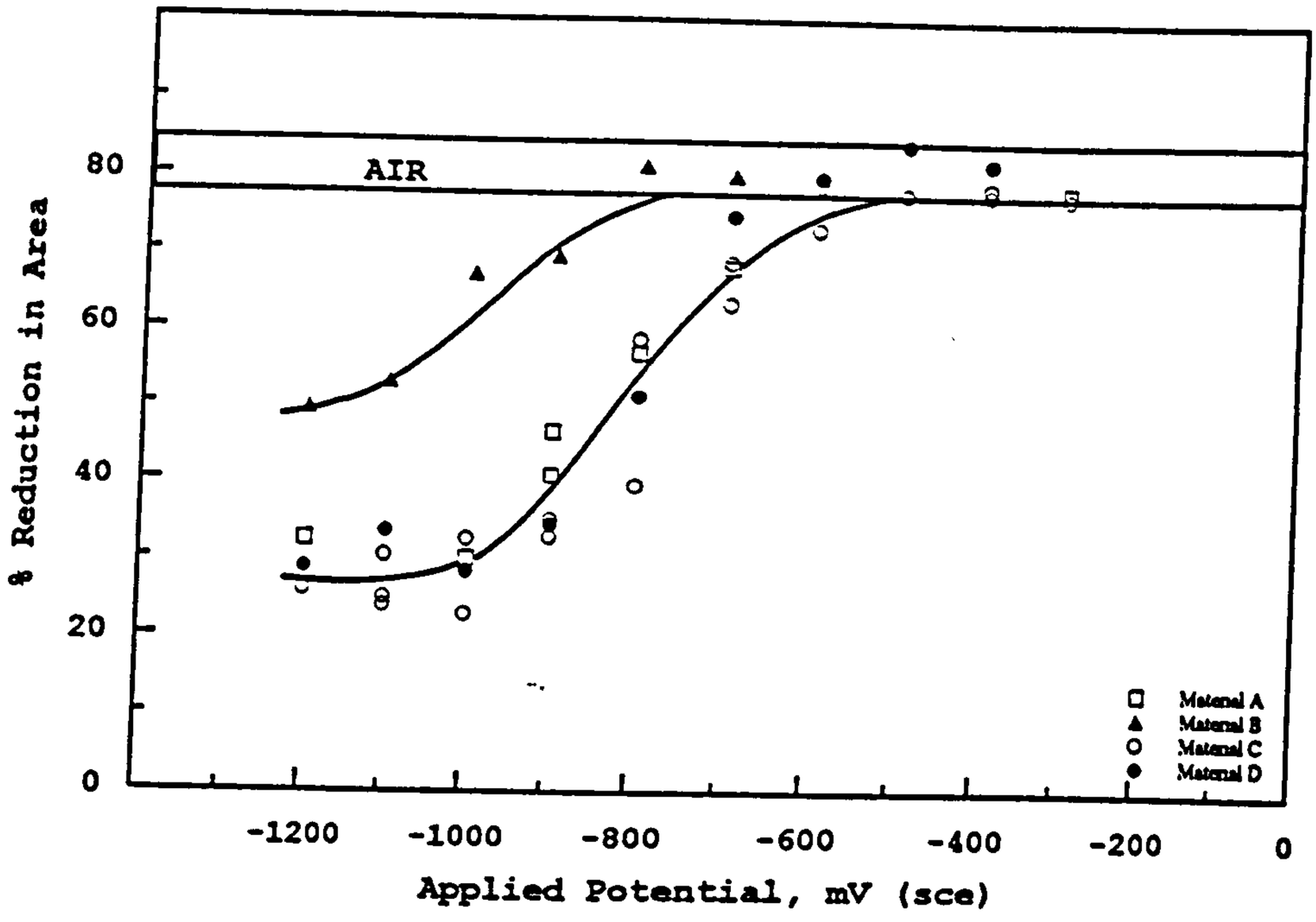

Figure 4.57 Variation of the reduction in area at fracture for the four duplex stainless steels A, B, C, and D strained at 2.0 x 10^{-6}/s whilst cathodically polarized in 0.6 M NaCl solution (pH = 6.5) at 70°C.

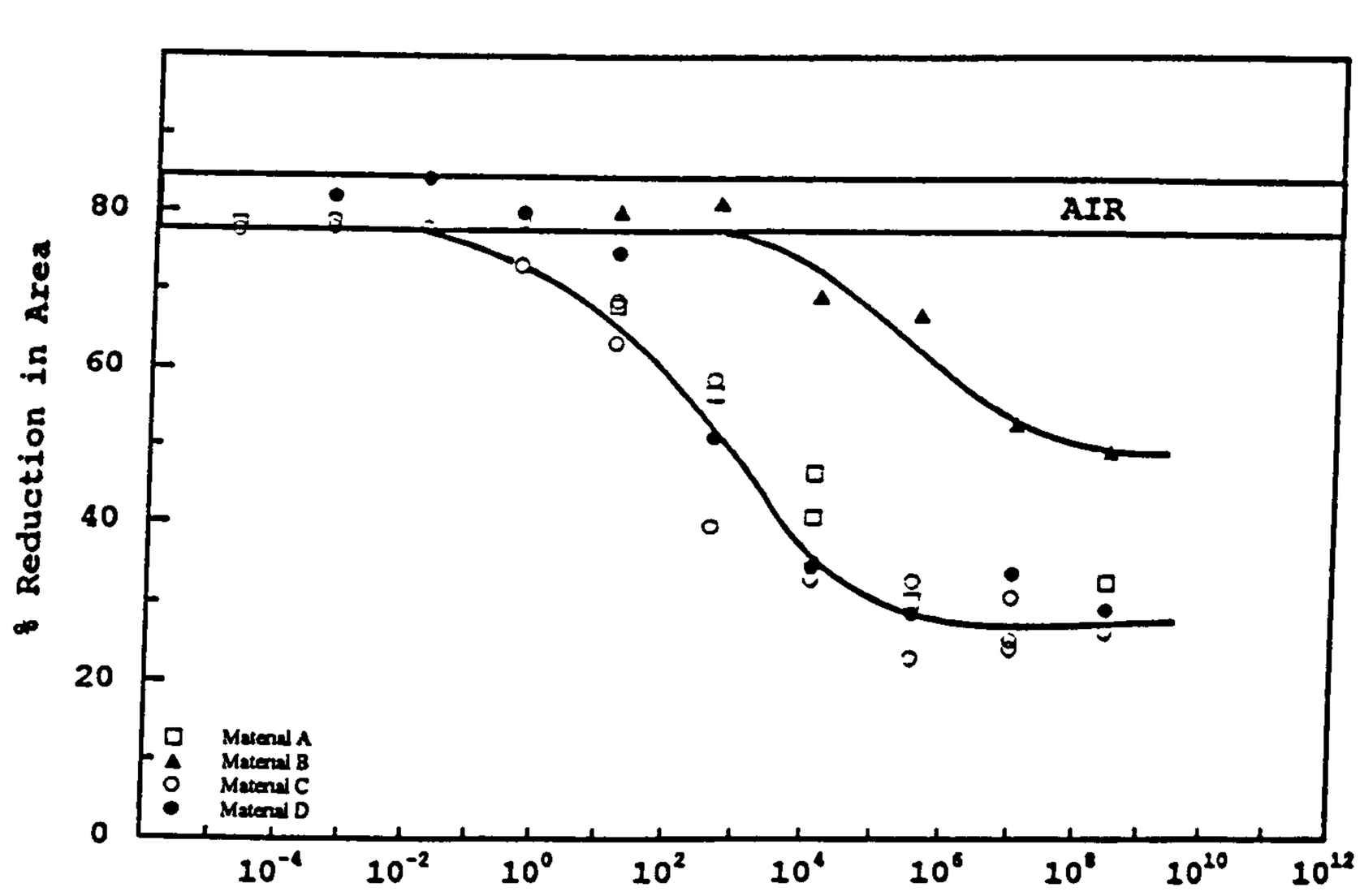

Figure 4.58 Relation between relative hydrogen fugacity and ductility of cathodically polarized material C at different potentials, while straining at 2.0 x 10^{-6}/s in 0.6 M NaCl solution (pH=6.5) at 70°C.

Although the microstructures of materials A, C, and D are significantly different, straining cathodically polarized specimens in 0.6M sodium chloride solution (pH=6.5) at 70°C revealed a similar embrittlement trend and the susceptibilities of all these steels (A, C, and D) were within the experimental error, (Figure 4.57) This is thought to be due to the extremely high hydrogen fugacities developed in this type of test compared with straining thermally charged specimens or straining in hydrogen gas. These high hydrogen fugacities provide high hydrogen concentrations and coverage on the specimen surface, and hydrogen will be continuously delivered to the crack tip during straining. In addition, the exceptionally high hydrogen fugacities associated with cathodic polarization can cause partial decomposition of the austenite phase into martensite (α (bcc) and ϵ (hcp)) above M_s temperatures /93, 126-128/. This is thought to negate the effectiveness of the austenite islands as obstacles to crack propagation. Cathodic charging, at a current density of 250 A/m^2 (at -1200 mv sce), of 1 mm thick, duplex steel C, sheets in NACE solution (pH=2.7) with 5 g/L sodium arsenate added as a recombination poison at 60°C has confirmed the formation of ϵ martensite (Figure 4.59) after a charging time of about 12h, which is shorter than the total time to failure T_f for tensile specimens strained to failure at the most severe cathodic potential of -1200 mv (T_f=25h). This suggests that martensite forms in the relatively early stages of the tensile straining. As the charging time increased the austenite phase developed more cracks (Figure 4.60) and these cracks appear to have a preferred orientation within specific grains and twin bands. The austenite diffraction lines progressively shift to a lower 2θ value, indicating a larger d spacing, as the charging time increases, which

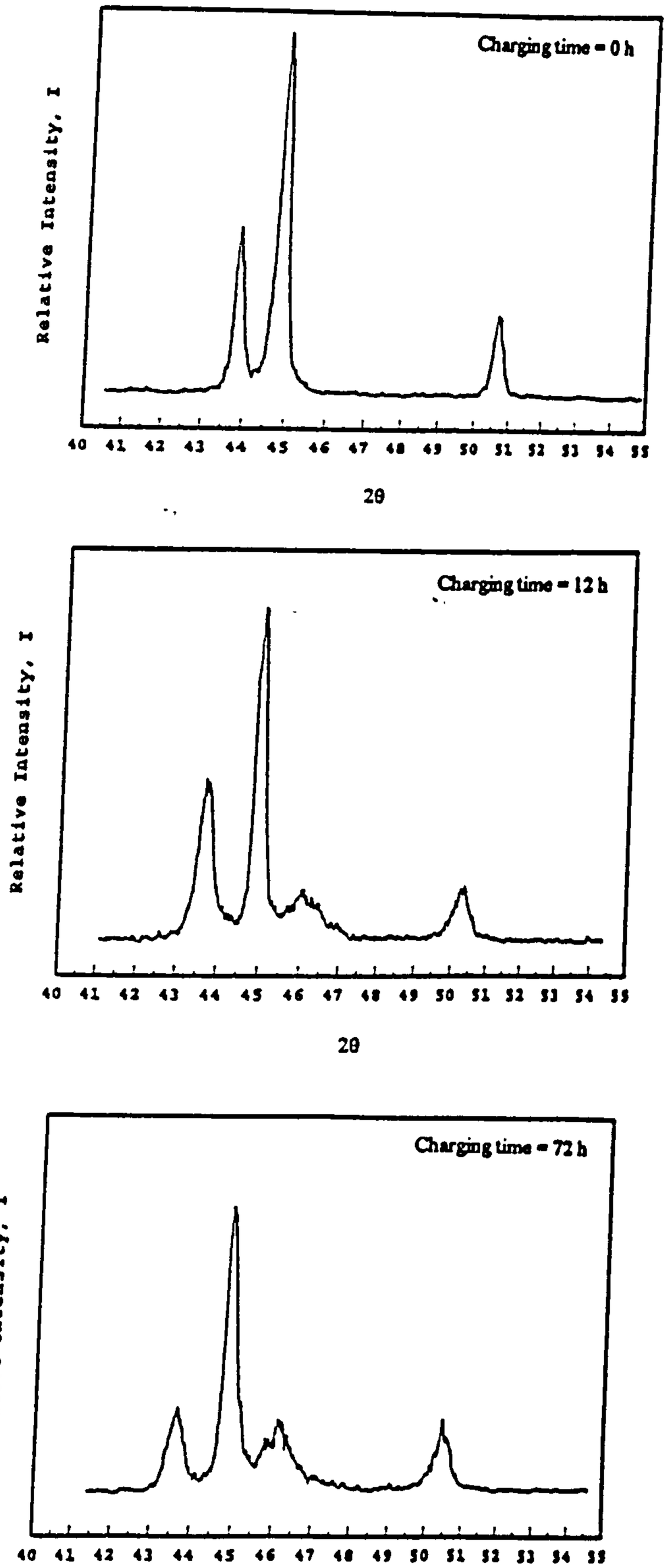

Figure 4.59 X-ray diffraction pattern for sample of material C cathodically charged in NACE solution (pH=2.7) , containing recombination poison at 60°C.

indicates expansion of the austenite unit cell due to the accommodation of the ingressd hydrogen. Moreover, it was observed that the ferrite phase also suffers some kind of surface damage (lenticular plates with midrib) which were crystallographic in nature (Figure 4.61 and 4.62). These plates were constrained by austenite islands (where no lenticular plates where observed) and also by slip lines. These features are very shallow and they were not observed if cathodically charged specimens are slightly polished using 1μm cloth to remove the black deposits formed during cathodic charging. Instead diluted nitric swabbing was employed to remove these deposits and enable the observation of these features. Some authors have observed similar midrib plates in their study of ferritic stainless steels of similar composition to the ferrite phase of the duplex stainless steel used here /191/ and duplex stainless steel /192/ and argued that these features are lenticular twins in the ferrite.

Straining of cathodically polarized specimens (material C) at 2.0×10^{-6}/s at 70°C in aqueous solution with varying chloride ion concentration ranging from tap water (25 wppm Cl^-) to 300 wppm indicated that varying the chloride ion concentration plays no significant role in the embrittlement attained at -1100 mV(sce) (Figure 4.63). Moreover, straining of specimens in deionized water (with 100 ppm potassium sulphate added) at 70°C revealed that, over the whole potential range employed (-1200 to -500 mV (sce)), the embrittlement closely follows that attained in 0.6M chloride solution of the same pH (pH=6.5)(Figure 4.55), which indicates that the presence of the chloride ion is not essential to prevent the reformation of the protective oxide film after it has been disrupted by

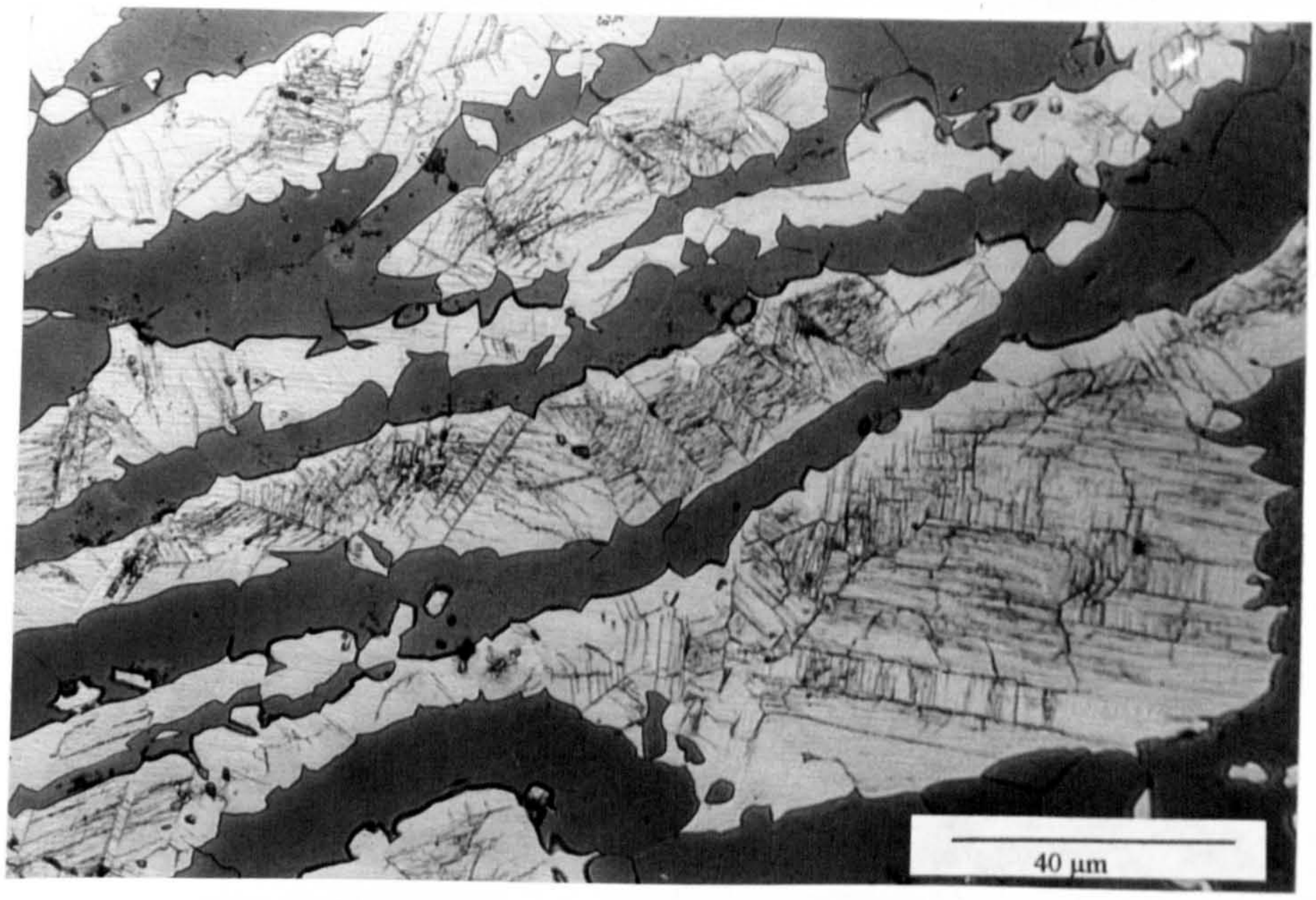

Figure 4.60 Microstructure of duplex material C cathodically polarized in NACE solution containing recombination poison at 60°C for 72h.

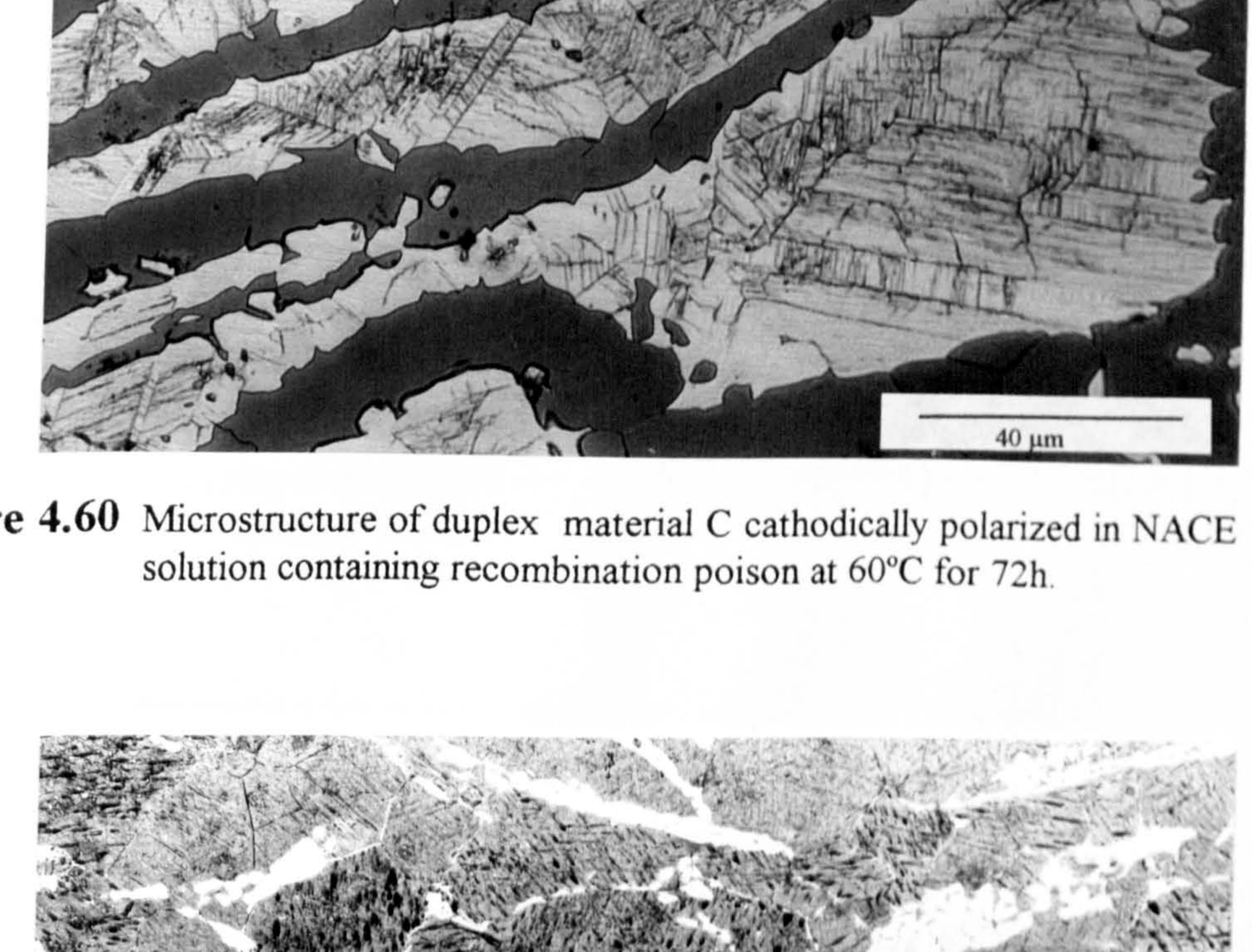

Figure 4.61 Optical micrograph of duplex stainless steel, material C, after cathodic charging at current density of 250 A/m^2 in NACE + 5g/L sodium arsenate Solution (pH=2.7) for 72h.

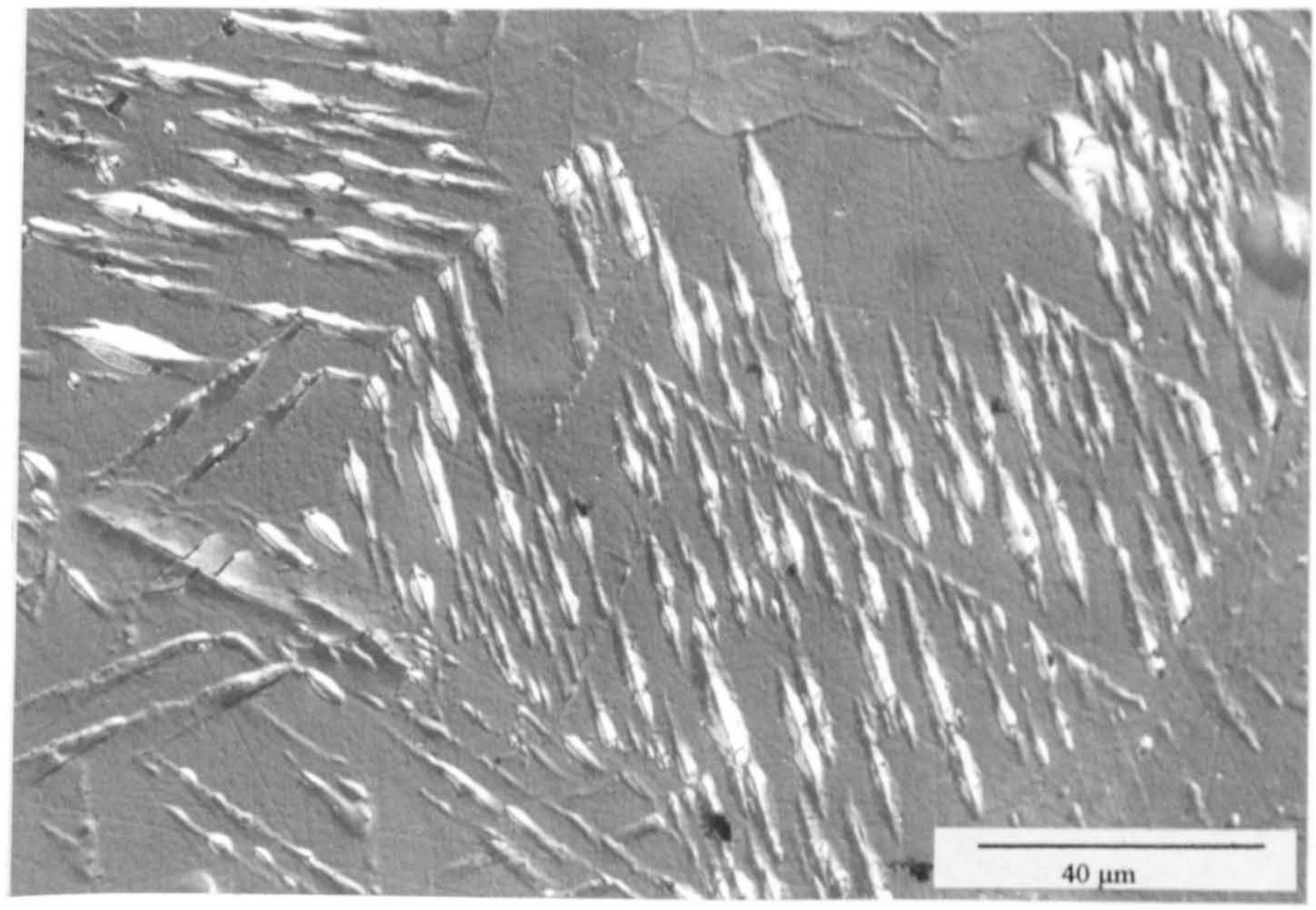

Figure 4.62 Dar .k field optical micrograph of a duplex stainless steel after catodic charging at current density of 250 A/m^2 in NACE + 5g/L sodium arsenate Solution (pH=2.7) at 60°C for 72h.

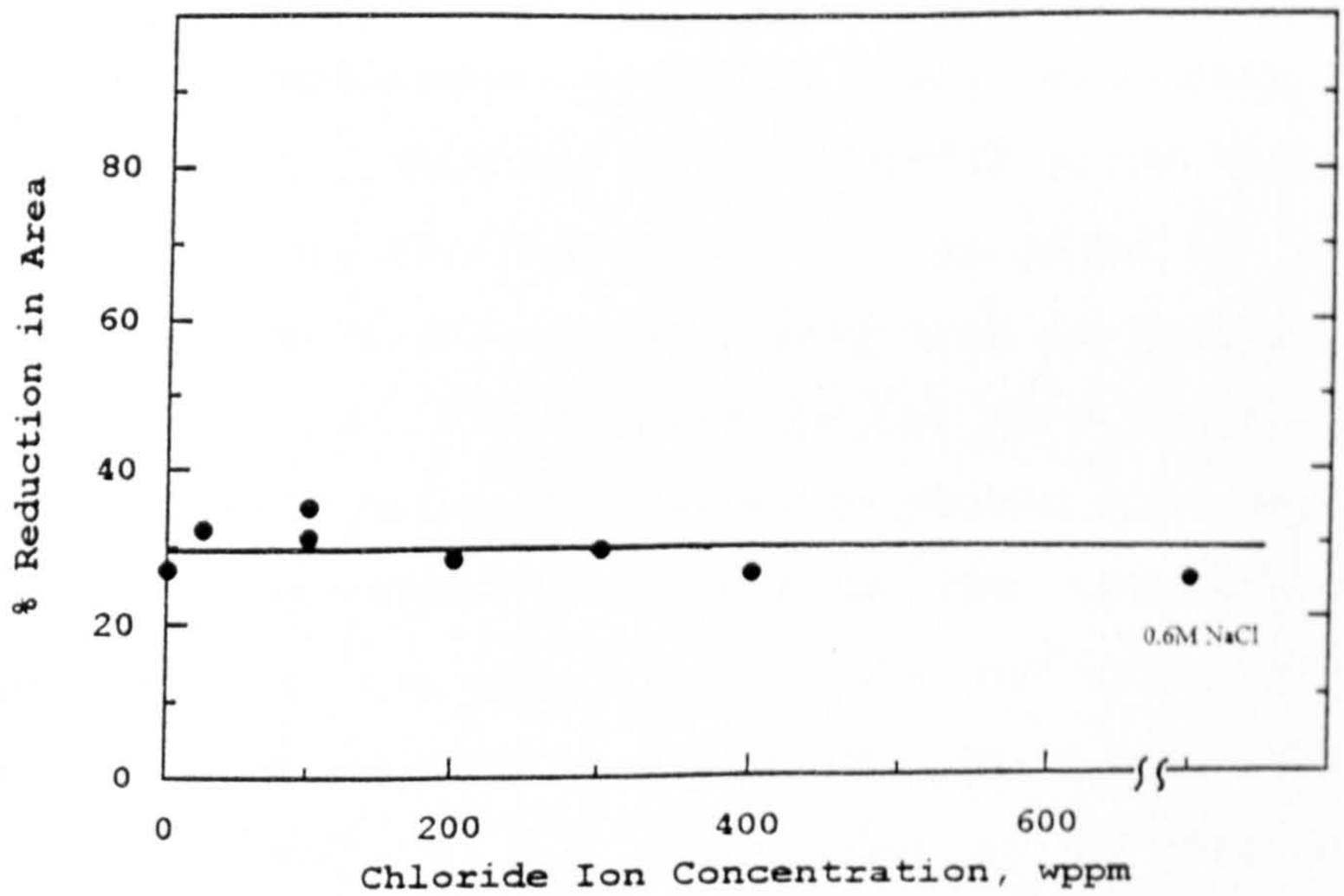

Figure 4.63 Variation of ductility with chloride ion concentration for material C cathodically polarized to -1100 mV(sce) whilst straining to failure in aqueous solution at 70°C.

straining. Applied potentials in the range from -500 to -1200 mV (sce) are sufficient to keep the duplex material away from the passive potential range and hence once the film is broken by straining it will not reform. In addition, straining a number of cathodically polarized specimens in NACE solution (pH=2.7) at room temperature of 23°C revealed no significant difference in the degree of embrittlement compared with straining at 70°C (Figure 4.55). This may also be attributed to the simultaneous effect of the extremely high fugacity and the continuous straining, which facilitates continuous delivery of hydrogen to the critical sites to cause embrittlement. In other words, the variation in diffusivity between 23°C and 70°C does not effect the delivery of hydrogen significantly.

Metallographic examination of the gauge lengths of the broken specimens revealed many secondary cracks initiated at the surface in the ferrite phase and running perpendicular to the tensile axis, as might be expected (Figure 4.64 and 4.65). These cracks tend to be arrested at austenite islands. The ferrite failed in a brittle manner with river marks while the austenite showed some ductility. An attempt was made to determine the crystallographic orientation of the fracture facets by using etch pit techniques. The solution used was 1N H_2SO_4 + 2g/l NH_4CNS and the etching voltage was maintained at 2V for 1 to 2 minutes. The etch pits are found to be square, which indicates that the crystallographic orientation of the cleavage planes of the ferrite are the {100} type (Figure 4.66).

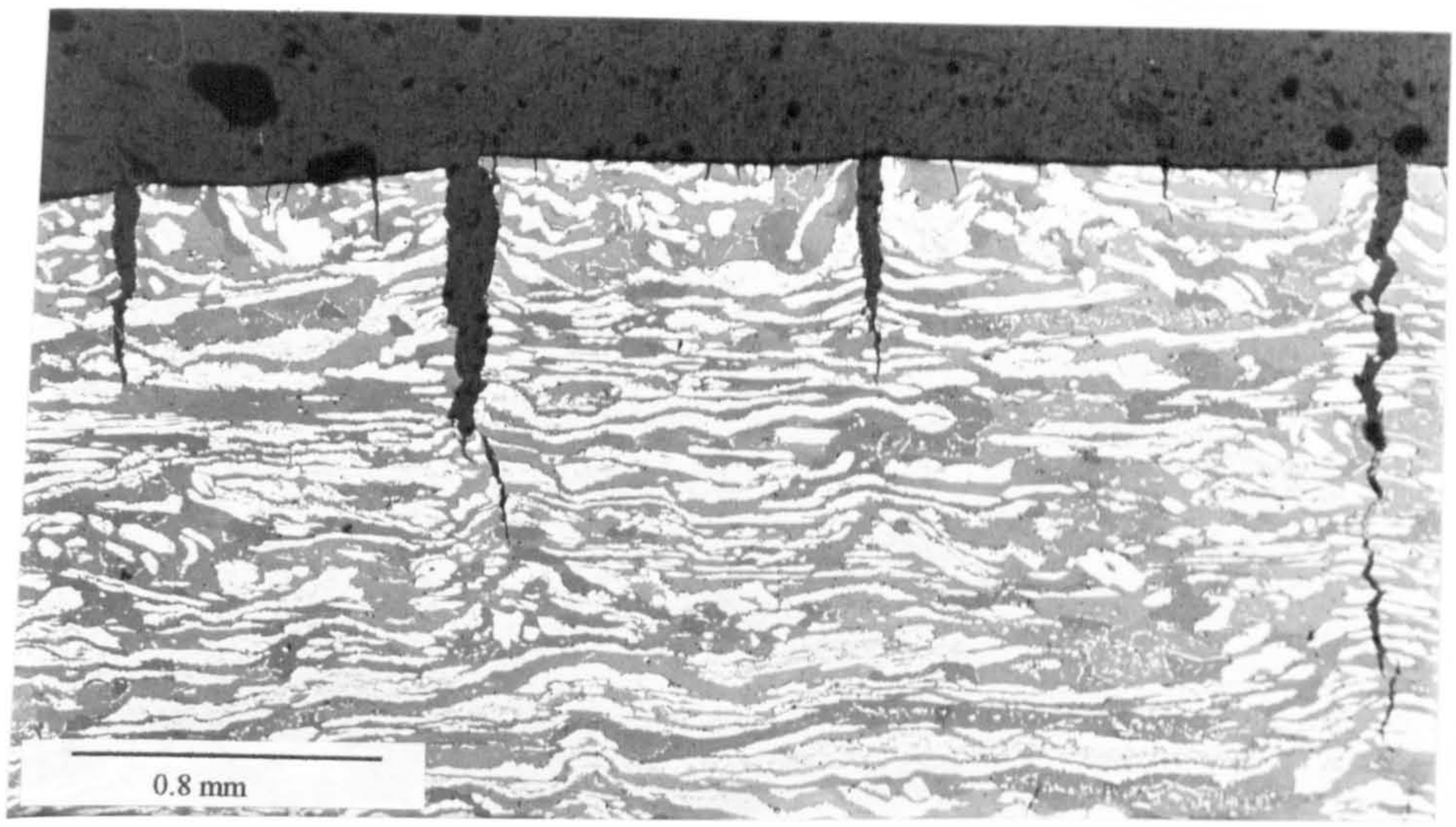

Figure 4.64 Polished section from the gauge length of duplex stainless steel material C specimen cathodically polarized at -1000 mV (sce) in 0.6M NaCl solution (pH=6.5), strained to failure at 2.0×10^{-6}/s.

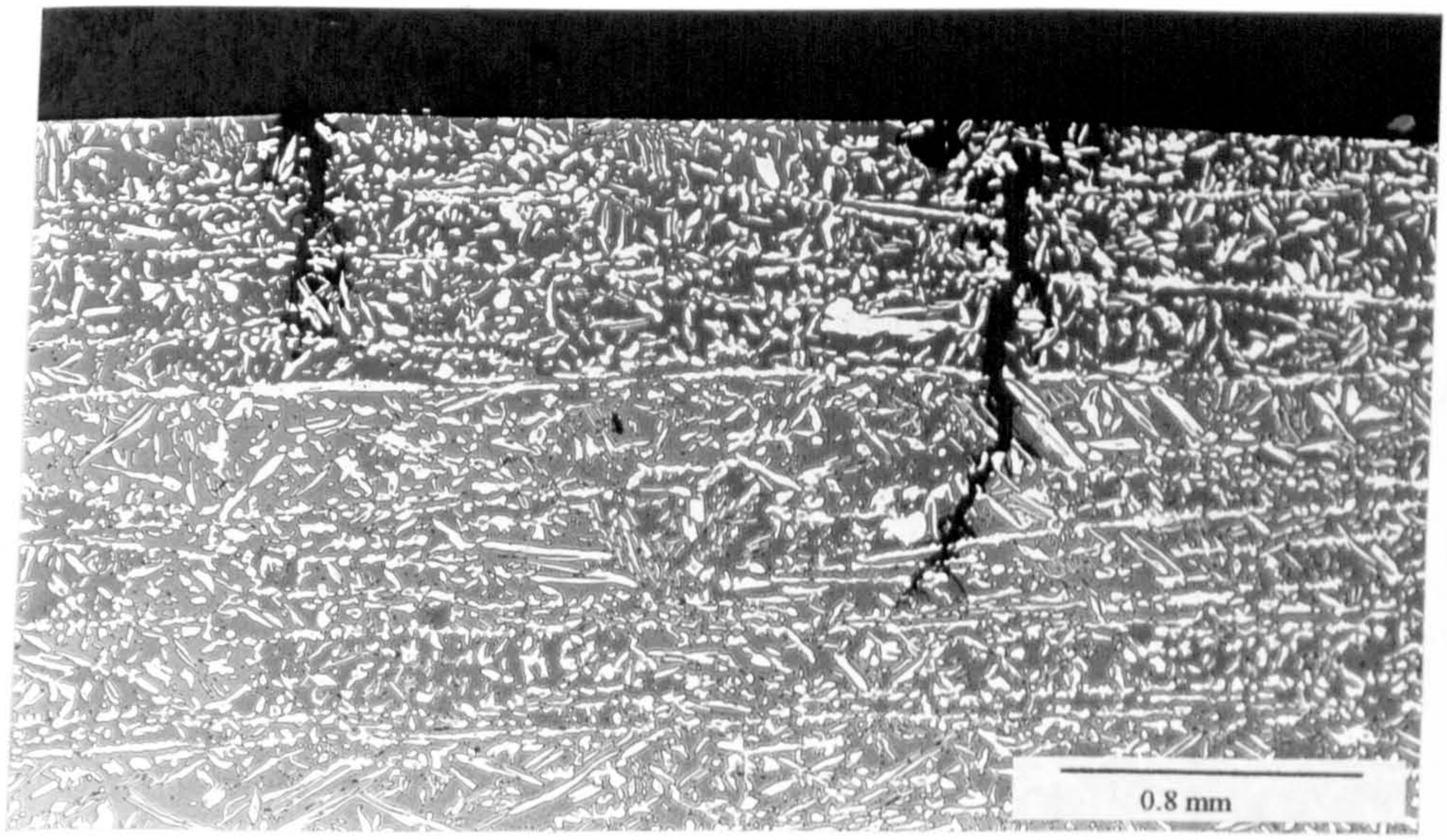

Figure 4.65 Polished section from the gauge length of duplex stainless steel material D specimen cathodically polarized at -1000 mV (sce) in 0.6M NaCl solution (pH=6.5), strained to failure at 2.0×10^{-6}/s.

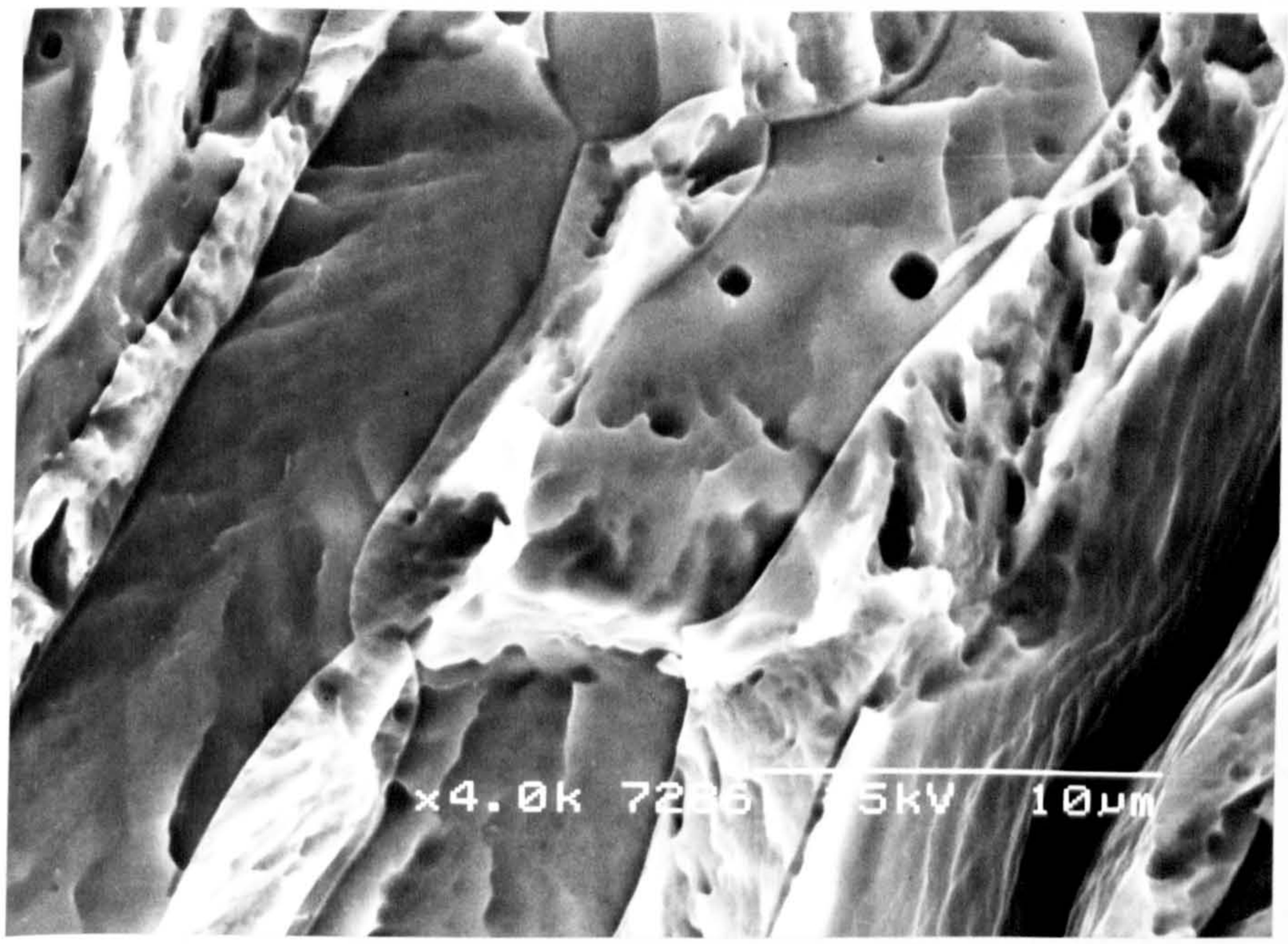

Figure 4.66 Fracture surface of duplex stainless steel material C specimen cathodically polarized at -1000 mV (sce) in 0.6M NaCl solution (pH=6.5), strained to failure at 2.0 x 10^{-6}/s showing square etch pits in the brittle ferrite phase.

4.4 Effect of microstructure

The different microstructures produced by the heat treatment of material C are shown in Figure 4.67. The first heat treatment (HT-1) involved heating the material to 1200°C for one hour and furnace cooling to 1000°C, at a rate of 5°C/min, to allow adequate time for the austenite to form in substantial proportion (≈50%), which is significantly more than the amount of the austenite in the as received material. The newly-formed austenite islands are much thicker and shorter than the previously banded structure. The second heat treatment (HT-2) produced 15% austenite and 85% ferrite by heating the material to 1250°C for one hour followed by ice-water quenching, which produced equiaxed austenite dispersed in a ferritic matrix. Both of these heat treatments produced no significant grain growth in either phase, but the third heat treatment (HT-3), in which the material was heated to 1300°C for one hour followed by ice-water quench and produced a fully ferritic structure, also had very large grains (up to 1 mm). This is more representative of the structure developed in the HAZ of welded material. Several attempts, were also made to produce a fully ferritic structure with a finer grain size, but failed because grain growth occurs extremely fast at such temperatures. Heating at 1300°C for only 5 min followed by ice-water quenching still produced large grains. On the other hand, heating at lower temperatures (e.g. 1280) for up to 24 hours failed to produce a fully ferritic structure and substantial grain growth still occurred.

It was found that the as received weld exhibited no inferior mechanical behaviour, in hydrogen, than that of the base material. This was attributed to the fact that this weld

a

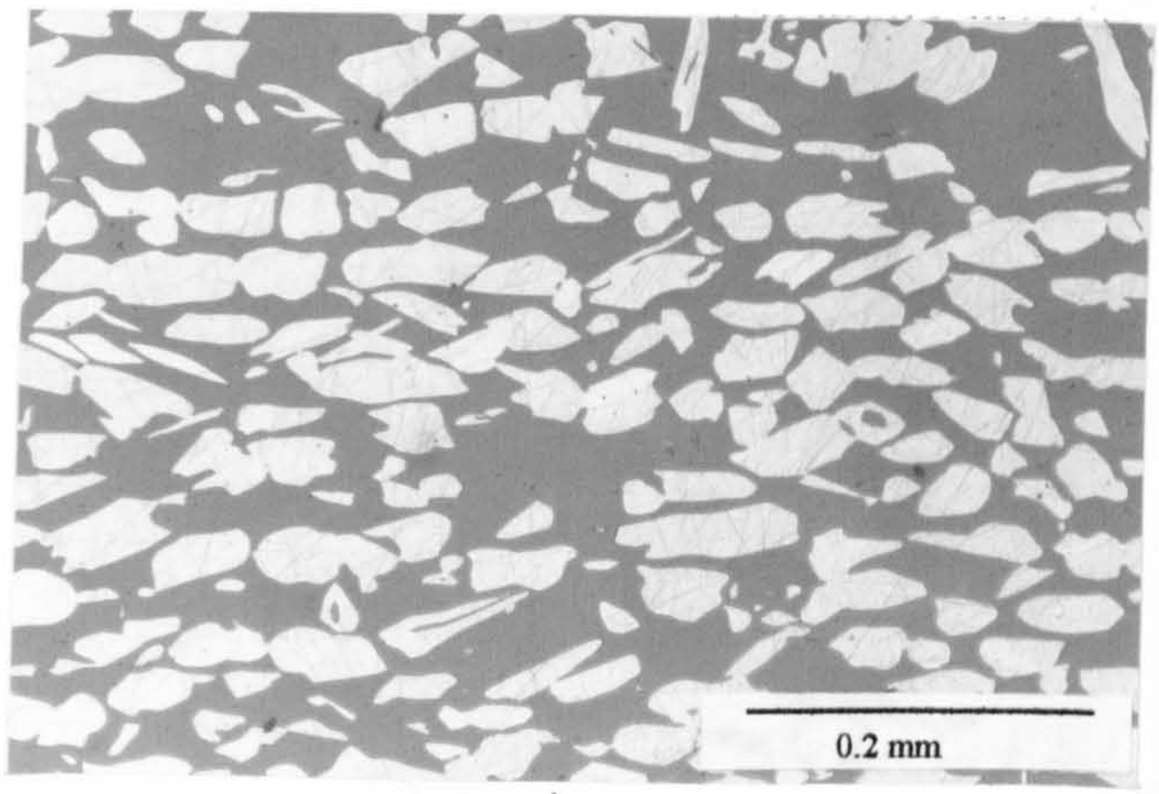

b

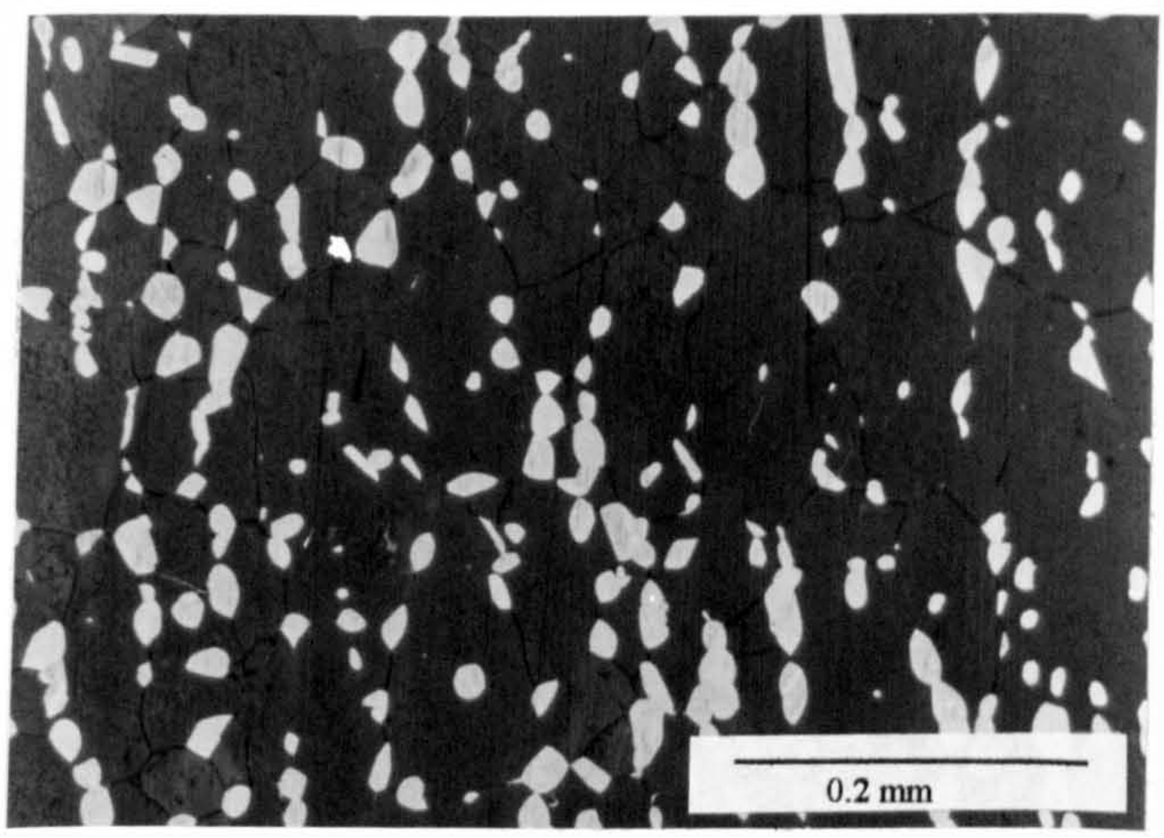

c

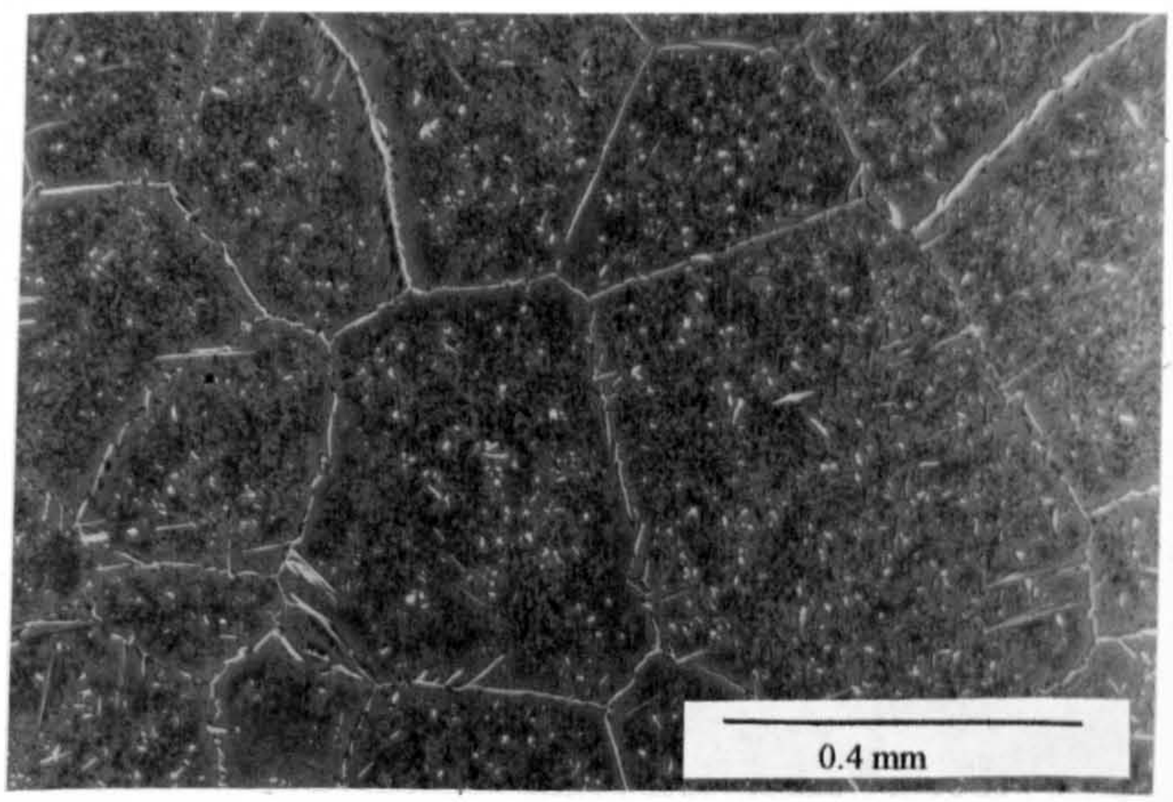

Figure 4.67 A representative sample of the microstructures achieved by heat treatment:

a) **HT-1** : 1 hour at 1200°C furnace cooled to 1000°C at 5°C/min followed by ice-water quenching.
b) **HT-2** : 1 hour at 1250°C followed by ice-water quenching.
c) **HT-3** : 1 hour at 1300°C followed by ice-water quenching.

was post-weld treated (annealed)(Figure 4.68). Therefore, heat treatment HT-3 was necessary in order to evaluate the effect of hydrogen uptake on the ductility of unannealed welds often practised in industries.

Changing the phase proportions in duplex stainless steels by heat treatment also produces a substantial change in the mechanical properties in air (Table 4.5), i.e. more ferrite in the resultant structure will result in higher proof stress, less strain hardening, and a significant change in the uniform strain because of the effect of work hardening on the point of instability.

Many attempts have been made to fit a mathematical equation to the true stress-true strain curve of metals. The most common, the Ludwik equation, is a power expression of the form:

$$\sigma = \sigma_0 + K\epsilon^n \qquad 4.2$$

where σ_0 is the yield stress, n is the strain-hardening exponent and K is the strength coefficient. A log-log plot of true stress-true strain up to maximum load should result in a straight line with slope n, and K is the true stress at $\epsilon = 1.0$. When results for the as received and heat treated materials are plotted in this way (Figure 4.69) a significant variation in the strain hardening exponent n is observed. Generally speaking n decreases with increase in the proportion of ferrite in the microstructure. The apparent discrepancy between results for as received and HT-1 may be due to the significant difference in the distrubution of the austenite phase.

Table 4.5 The mechanical properties of the heat treated material strained to failure in air.

Material	Strain rate/s	Reduction in Area (%)	Elongation (%)	Uniform Elongation (%)	0.2% Proof Stress (N/mm^2)	Ultimate Tensile Stregth (N/mm^2)
HT-1	1.3×10^{-3}	83.6	41.3	21.3	550.5	743.7
	3.7×10^{-6}	80.5	39.1	19.7	592.3	758.2
HT-2	1.3×10^{-3}	61.3	27.0	16.6	718	836.4
	3.7×10^{-6}	64.7	30.6	18.5	703.8	807.3
HT-3	1.3×10^{-5}	48.5	17.1	6.4	766.8	856.1
	3.7×10^{-4}	51.7	19.9	7.4	742.9	844.0

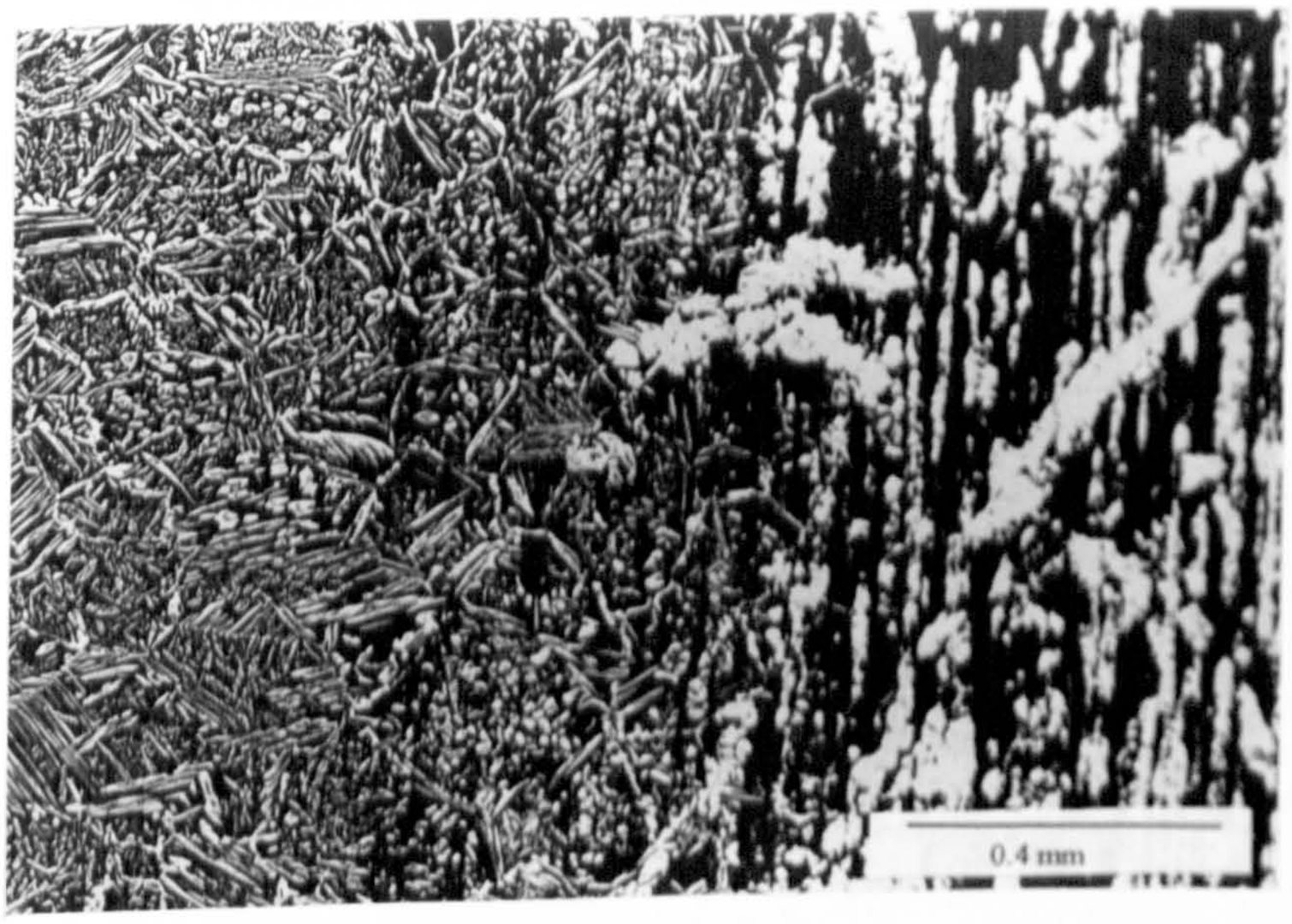

Figure 4.68 The microstructure of the as received weld.

In the light of these results, the embrittlement index based upon the percent elongation to fracture (El_e) provides a better representation of the hydrogen embrittlement of the different structures (Figure 4.70) than that based on reduction in area. The elongation is more influenced by the crack initiation whereas the the reduction in area becomes complicated by the effect of austenite on the crack propagation. It is clear from these results that as the proportion of ferrite is increased the material becomes more embrittled, simply because the ferrite phase is more susceptible to hydrogen embrittlement.

In addition, the amount of austenite in the structure plays a very important role as a hydrogen source in thermally charged specimens. Straining thermally charged tensile speimens of material HT-3 (with a fully ferritic structure) in air after room temperature degassing for 24 h produced significant recovery in the ductility from El_e= 80% to 38%(Figure 4.70), and this is understandable considering the high diffusivity and the low solubility of hydrogen in the ferrite phase. However, specimens with a substantially higher austenite content, e.g. material HT-2 with 15% austenite, displayed a much smaller recovery in ductility even after 48 h of room temperature degassing (from El_e= 61% to 49%). When these results are considred in association with the previous results for thermally charged longitudinal specimens (from as received material) strained to failure in air (where no significant recovery in ductility was detected after room temperature degassing for up to three years) support is provided for the role of the austenite phase as a reservoir of hydrogen. Hydrogen is retained for a long time in austenite when left at room temperature without straining, due to the very low diffusivity

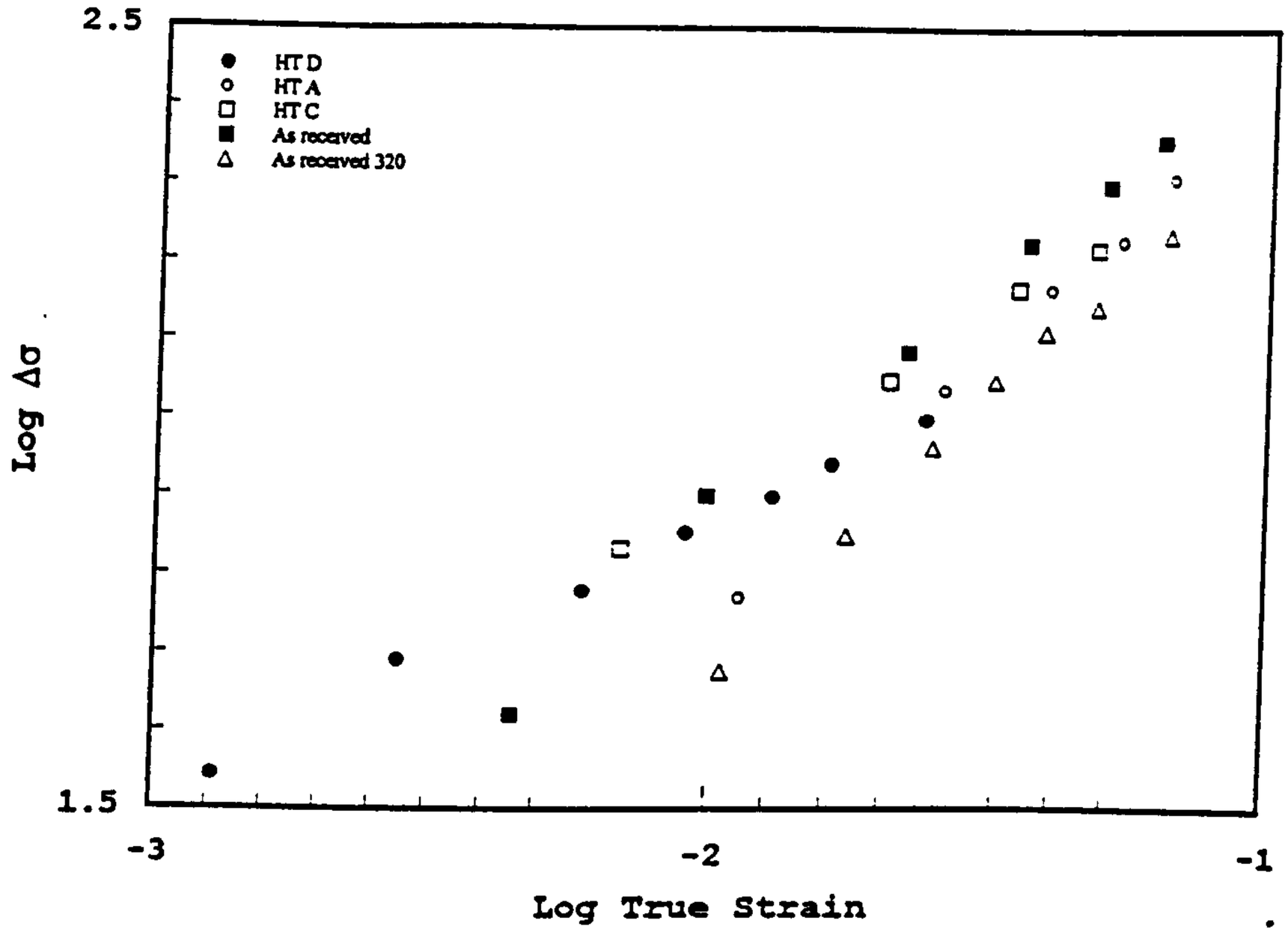

Figure 4.69 The true stress-true strain curve for tensile specimens made from the heat treated duplex steel (material C)

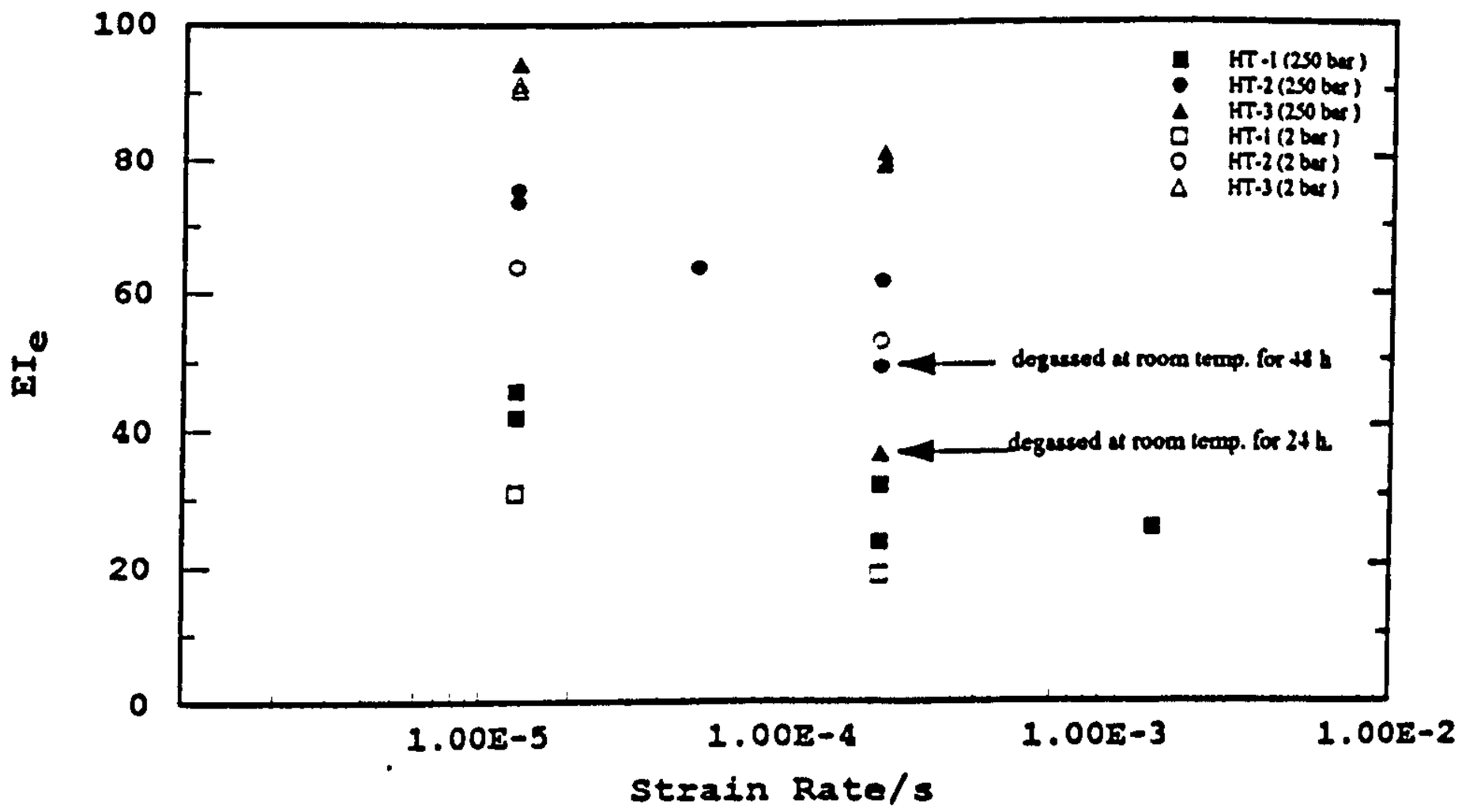

Figure 4.70 Embrittlement Index, based on % elongation (EI_e) vs strain rate of the heat treated duplex stainless steel (material C)

of hydrogen, but during straining hydrogen is delivered by dislocations to the ferrite in sufficient amounts to cause maximum embrittlement, if the structure contains an adequate amount of austenite e.g. 38% as in the as received structure (material C). The lower the austenite content of the material the lower the amount of stored hydrogen and when the amount of austenite in the structure falls below a certain proportion the hydrogen available to be delivered to the ferrite during straining is less than the critical amount needed to inflict maximum damage, as found in material HT-2 and HT-3.

Straining uncharged tensile specimens, of the heat treated materials in a 2 bar hydrogen atmosphere (Figure 4.70) again indicates maximum embrittlement for the fully ferritic structure and similar degrees of embrittlement for all structures to that observed after hydrogen charging.

Microscopic examination of the gauge lengths of the tensile specimens, HT-1 and HT-2, strained to failure in 2 bar hydrogen atmosphere has again emphasized the important role of the austenite phase as a barrier to crack propagation (Figures 4.71 and 4.72).

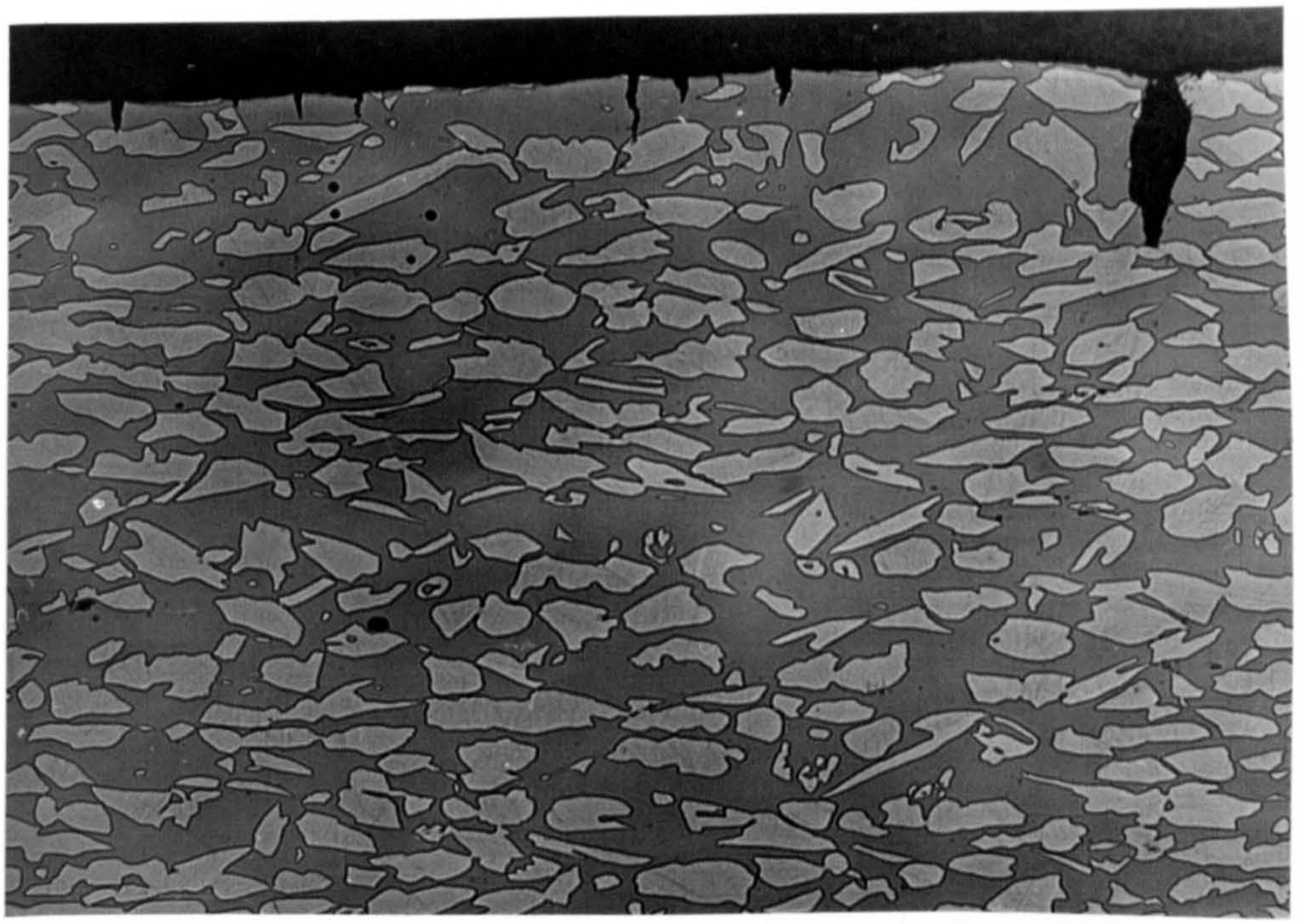

Figure 4.71 Polished section from the gauge length of duplex stainless steel (HT-1) tensile specimen strained to failure at 1.3×10^{-5}/s in 2.0 bar hydrogen.

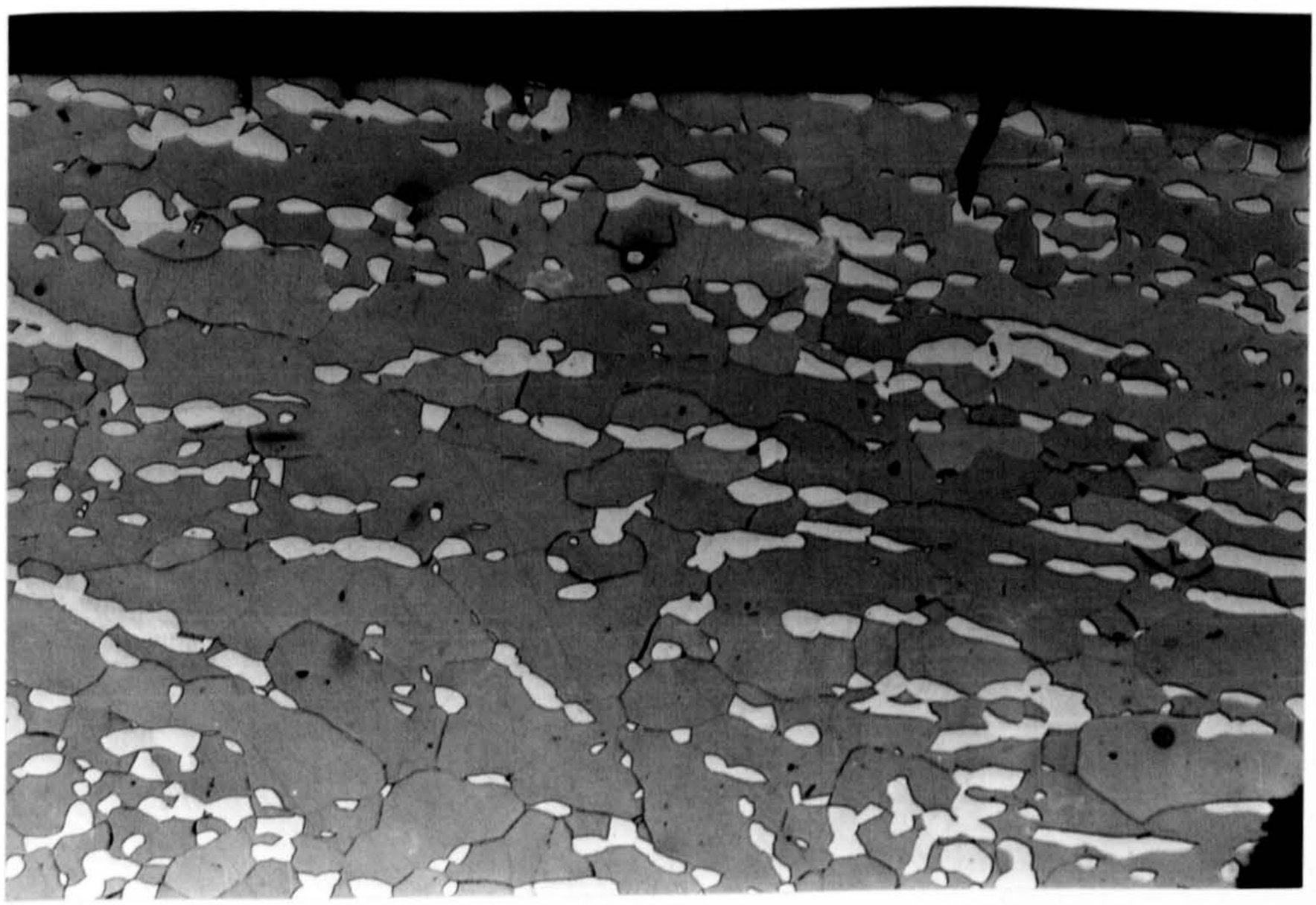

Figure 4.72 Polished section from the gauge length of duplex stainless steel (HT-2) tensile specimen strained to failure at 1.3×10^{-5}/s in 2.0 bar hydrogen.

Chapter 5

Conclusions

1- Hydrogen usually reduces the ductility of duplex stainless steel but the details of the effect on mechanical behaviour depend upon the source of hydrogen.

2- Straining in an atmosphere of hydrogen produces a reduction in ductility that increases with decrease in strain rate. At higher pressures the decrease is linear but when hydrogen is in short supply there is an intermediate ductility minimum around 10^{-4}/s which is attributable to ε martensite.

3- When specimens are thermally charged with hydrogen, there is a plentiful supply of hydrogen provided internally and the mechanical behaviour when subsequently straining in air is similar to that when straining in high pressure hydrogen. The ductility loss increases with charging pressure up to a maximum at about 200 bar.

4- Straining in solutions saturated with hydrogen sulphide at various temperatures revealed a loss in ductility that depended upon the solution pH; the greater the acidity the greater was the ductility loss.

5- Whatever the pH of the solution, maximum embrittlement occurred at some particular temperature between 0 and 95°C and this is attributed to the occurrence of two competing processes: hydrogen embrittlement and corrosion.

6- The effect of hydrogen on ductility increases with temperature as a result of breakdown of a passive film allowing easier excess to the metal, but rapid corrosion that occurs at higher temperatures causes crack blunting and hence an increase in measured ductility.

7- The presence of chloride ion in solution in excess of 300 wppm was essential to produce embrittlement in solutions saturated with hydrogen sulphide and this is thought to be necessary to prevent repassivation.

8- This is in contrast to the tests involving cathodic polarization during straining where the chloride ion was not essential to the embrittlement.

9- Provision of hydrogen at high fugacity by cathodic polarization during straining also introduces a ductility loss, which at a comparable strain rate gives a similar maximum embrittlement to that found straining in hydrogen or straining charged specimens in air.

10- The potential at which loss in ductility is first noted corresponds to the calculated hydrogen evolution potential for the particular solution pH concerned.

11- The microstructure, as affected by both composition and heat treatment, has a significant influence upon resistance to both hydrogen embrittlement and acid attack. This is important both from the point of view of the manufacturing process and welding.

12- The effect of microstructure is mainly reflected in the elongation to failure because the austenite, the less

embrittled phase, tends to resist the propagation of a brittle crack.

13- However, the austenite can provide a reservoir of hydrogen and therefore, if present in sufficient quantity, can cause loss in ductility over an extended period.

14- Duplex stainless steel B With 0.29 wt% Nitrogen and having a microstructure consisting of 50% ferrite and 50% austenite was not found to be susceptibility to hydrogen embrittlement or stress corrosion cracking in all of the environments tested.

REFERENCES

1- G.V. Karpenko and I. I. Vasilenko, "Stress Corrosion Cracking of Steels", Freund publishing House, Tel-Aviv, Israel (1977).

2- T. Sriskandarajah and A. C. Tseung,"Sulphide Stress Corrosion Cracking of Oil and Gas Well Equipment", Offshore Technology Report, HMSO BROOKS Publications Center (1987).

3- W. H. Johnson, Proc. Roy. Sco.,Vol.23 (1875), p. 168.

4- A. J. West and J. H. Holbrook, Proc. Conf. "Hydrogen in Metals", eds. I. M. Bernstein, A. W. Thompson, Warrendale, PA: Met. Soc. AIME (1981), p.607.

5- M. B. Whiteman and A. R. Troiano, Corrosion, Vol. 21 (1965), p. 53.

6- M. L. Holtzworth and M. R. Louthan, Corrosion, Vol. 24 (1968), p.110.

7- M. L. Mehta and J. Burke, Corrosion, Vol. 31 (1975), p. 108.

8- A. I. Asphahani, "Corrosion/80" (paper No 12), NACE, Chicago, Illinois, March (1980).

9- T. Nakayama, K. Fujiwara, Y. Torii, and T. Inoue, Corrosion, Vol. 45 (1990), p.749.

10- R. M. Vennett and G. S. Ansell, Trans. Amer. Soc. Met., Vol. 60 (1967), p. 242.

11- T. E. Truman, The Metallurgist and Material Technologist,(1980) January. p. 15; February. p. 75.

12- Anon. Steel and Coal, Vol.16 August (1963), p. 305.

13- J. Stodart and M. Faraday, Phil. Trans. Royal Soc., Vol.112 (1822), p. 253.

14- R. A. Hadfield, J. Iron and Steel Institute, Vol.2 (1892), p.49.

15- P. Monnartz, Metallurgie, Vol. 8 (1911), p.161.

16- M. A. Streicher, Proc. Conf. "Stainless Steels '77", ed.R. Q. Barr, climax Molybdenum company, London, UK, Sept.26-27 (1977).

17- L. Guillet, Revue de Metallurgie, Vol.3 (1906) p.412.

18- W. Geisen, ISI Carnegie Scholarship Memoirs, Vol.1 (1909), p.1.

19- A. M. Portevin, ISI Carnegie Scholarship Memoirs, Vol.1 (1906), p. 230.

20- E. C. Bain and W. E. Griffiths, Trans AIME, Vol.75 (1927), p.166.

21- J. W. Pugh and J. O. Nisbet, Trans AIME, Vol.188 (1950) p. 268

22- L.Colombier and J. Hochman, "Stainless Heat resisting Steels", St Martin's press, New York (1968).

23- ASM Metal Handbook, 8th Edition , vol. 8 (1973).

24- J. Charles, Proc. Conf."Duplex Stainless Steels", France (1991), p.3.

25- P. Payson, Trans AIME, Vol. 100 (1932), p.306.

26- R. F. Atkinson and R. W. King, Conf. Proc."Duplex Stainless Steel", ed R. A. Lula, ASM, St. Louis (1983), p. 399.

27- M. G. Fontana and F. H. Beck, Alloy Casting Institute project No. 44 Report 49, January (1964).

28- M. G. Fontana and F. H. Beck, Alloy Casting Institute Project No. 52, November (1965).

29- H. D. Solomon and T. M. Devine, Conf. Proc."Duplex Stainless Steels", ed R. A. Lula, ASM, St. Louis (1983), p. 693.

30- H. D. Solomon, "Treatise on materials science and technology", Vol. 25, ed. C. L. Briant and S. K. Banerji, Academic Press,New York (1983), p. 525.

31- A. Morini and G. Bettinelli, Conf. Proc. "Stainless Steels '84", Göteborg, Publ. I. O. M., London (1985), p.471.

32- H. F. Merrick, H. W. Hayden, and R. C. Gibson, Met. Trans., Vol. 4 (1973), p. 827.

33- J. C. Lippold, I. Varol, and W. A. Baeslack III, Proc. Conf."duplex stainless steel", France (1991), p. 383.

34- J. Charles, Proc. Conf."Duplex Stainless Steels", France (1991), p. 151.

35- E. O. Hall and S. H. Algie, Met. Rev. Vol.11 (1966), p.61.

36- J. S. Kasper, Act. Met., Vol.2 (1954), p. 456.

37- S. Rideout, W. D. Manly, El Kamen, and P. A. Beck, Tran. AIME, (1951), p. 872.

38- C. V. Roscoe, K. J. Gradwell, and G. W. Lorimer, Conf. Proc. "Stainless Steels '84", Göteborg, Publ. I.O.M., London (1984), p. 563.

39- Y. Maehara, N. Fujino, and T. Kunitaka, Tran. ISIJ, Vol. 23 (1983), p.247.

40- G. Herbsleb and P. Schwaab, Proc. Conf. "Duplex Stainless Steels", ed R. A. Lula, ASM, St. Louis (1983), p. 15, 1984.

41- A. Redjaimia, G. Metauer, and M. Gantois, Proc. Conf. "Duplex Stainless steels", France (1991), p.119.

42- T. Thorvaldsson, H. Eriksson, J. Kntka and A. Salwen, Proc. Conf."Stainless Steels '84" The Institute of Metals, London (1985).p.101.

43- J. O. Nilsson and P. Liu, Material Science and Technology, Vol.7 (1991), p.853.

44- T. Angel and J. of the Iron and Steel Institute, Vol. 177 (1954), p165.

45- K. Wakasa, T. Nakamura, J. Material science, Vol. 13 (1978), p. 21.

46- K. Wakasa, T. Nakamura, J. Material science, Vol. 13 (1978)p. 807.

47- A. L. Schaeffler, Metal Progress, Vol. 56 (1949), p.680.

48- C. J. Long and W. T. Delong, Welding J., Vol. 52 (1973), p. 2815.

49- T. A. Siewart, C. N. Mc Cowan, D. L. Olson, Welding J., Dec. (1988), p. 2895.

50- J. O. Nilsson, Material Science and Technology, Vol.8 (1992), p. 685.

51- W. T. Delong, Metal Progress, Vol. 77 (1960), p. 98.

52- F. B. Pickering, Int. Met. Rev., Vol.21 (1976), p. 227.

53- F. B. Pickering, Conf. Proc. "Stainless Steels '84", Goteborg, Pub. I.O.M., London (1985), p. 2.

54- S. Hertzman, W. Roberts, and M. Linderimo, Proc. Conf. "Duplex Stainless Steel", Netherland (1986) p. 257.

55- G. H. Eichelmann and F. C. Hull, Trans. ASM, Vol. 45 (1953), p. 77.

56- F. B. Pickering, " Physical Metallurgy and the Design of Steels", Applied Science Publisher, (1978).

57- J. W. Oldfield and W. H. Sutton, British Corrosion Journal, Vol.15 (1980), No.1, p 31.

58- J. Sakai, I Matsushima, Y. Kamemura, M. Tanimura, and T. Osuka, Proc. Conf. "Duplex stainless steels", ed. R. A. Lula, ASM, St. Louis (1983), p. 211.

59- H. Miyuki, T. Kudo, M. Koso, M. Miura, and T. Moroishi, proc. Conf. "Duplex stainless steels", ed. R. A. Lula, ASM, St. Louis (1983), p. 95.

60- M. Onoyama, N. Hayashi, K. Shitani, and T. Suehiro, Proc. Conf. "Duplex stainless steels", ed. R. A. Lula, ASM, St. Louis (1983), p. 191.

61- A. Poznansky, C. S. Nalbone, and J. D. Crawford, Proc. Conf. "Duplex stainless steels", ed. R. A. Lula, ASM, St. Louis (1983), p. 431.

62- P. Guha and C. A. Clark, Proc. Conf. "Duplex stainless steels", ed. R. A. Lula, ASM, St. Louis (1983), p. 355.

63- H. Tsuge, Y. Tarutani, T. Koudo, K. Fujwara, and T. Moroishi, Proc. Conf. "Duplex stainless steels", Netherland, (1986) preprints paper No 23, p 392.

64- S. Bernhardsson, Conf. Proc. "Duplex Stainless Steels", France (1991), p.185.

65- E. S.Sperry, Brass World, Vol. 2 (1906), p. 33.

66- C. E. Stromyer, J. Iron and Steel Institute, Vol.II, p. 404 (1909).

67- R. H. Jones, "Stress Corrosion Cracking", ed. R. H. Jones, ASM International, Materials Park Ohio (1992), p. 1.

68- R. W. Staehle, Conf. Proc. "Fundamental Aspects of Stress Corrosion Cracking", Ohio State University, Eds R. W. Staehle , A. J.Forty and D. Van Rooyan, NACE, Houston (1977) p. 1.

69- J. E. Truman, International Metals Reviews, No. 6 (1981), p. 301.

70- R. W. Staehle, "Theory of Stress Corrosion Cracking in Alloy" NATO, Brussels, 1971, Ed. J. C. Scully, p. 223.

71- A. J. Bursle and E. N. Pugh, Proc. Conf. "Environment Sensitive Fracture of Enginering Materials", ed. Z. A. Foroulis, Chicago, Met. Soc. of AIME (1977), p. 18.

72- F. A. Champion, "Symposium on Internal Stress in Metals and Alloys", Inst. of Metals, London, 1948, p. 468.

73- J. C. Scully, Corrosion Science, Vol. 15 (1975), p. 207.

74- R. W. Staehle, Proc. Conf. "Stress Corrosion Cracking and Hydrogen Embrittlement of Iron Base Alloys", ed. R. W. Staehle, J. Hochmann, R. D. McCright and J. E. Slater, NACE Houston, (1977),p. 180.

75- J. C. Scully, "Treatise on Materials Science and Technology", ed. J. C. Scully, Academic Press (London), Vol. 23 (1983), p. 103.

76- B.F. Brown, C. T. Fujii, and E. P. Dahlberg, J. Electrochemical Soc., Vol.116 (1969), p. 218.

77- E. H. Dix, Trans. Am. Ins. Min. Metal Engrs., Vol. 11, (1940), p. 137.

78- C. J. Cron, J. H. Payer, and R. W. Staehle, Corrosion, Vol. 27 (1971), p. 1.

79- N. J. Petch and P. Stables, Nature (London), Vol.169 (1952), p.842.

80- N. J. Petch, Phil. Mag, Vol.1 (1956), p.331.

81- A. A. Griffith, Phil. Trans. Roy. Soc. of London, Vol. A221 (1920), p.163.

82- E.G. Coleman, D. Weinstein, and W. Rostoker, Acta Metal, Vol. 9,(1961), p. 491.

83- E. Orowan, Welding Journal, Vol. 34 (1955), p. 1575.

84- A. R. Troiano, Tran. Amer. Soc. Metals, Vol.52 (1960), p. 54.

85- R. A. Oriani, and P. H. Josephic, Acta Metal, Vol.22 (1974), p.1065.

86- R.A. Oriani, Proc. Conf. "Stress Corrosion Cracking and Hydrogen Embrittlement of Iron Base Alloys" ed. R. W. Staehle, J. Hochmann, R.D. Mc Cright, and J. E. Slater, NACE Houston (1977), p. 351.

87- R. A. Oriani, BER. Bunsenges, Phys. Chem., Vol.76 (1973), p.848.

88- R. N. Parkins, Metall Review, Vol.9 (1964), p. 201.

89- R. N. Parkins, Brit. Corrosion J., Vol. 7 (1972)p. 15.

90- G. J. Theus, and R. W. Staehle, Proc. Conf. "Stress Corrosion Cracking and Hydrogen Embrittlement of Iron Base Alloys", eds. R. W. Staehle, J. Hochmann, R. D. McCright, and J. E. Slater, NACE, Houston, p. 845.

91- N. A Nielsen, Corrosion, Vol. 27 (1971), p.173.

92- R. E. Reed, and H. W. Paxton, "First International Conf. on Metallic Corrosion", Butterworths, London (1962), p. 301

93- M. L. Holzworth and M. R. Louthan, Corrosion, Vol.24 (1968) p. 110.

94- S. S. Birley and D. Tromans, Corrosion, Vol. 27 (1971) p. 63.

95- R. Liu, N. Narita, C. Altstetter, H. Birnbanm, and N. E. Pugh, Metal Trans., Vol. 11A (1980), p. 1563.

96- E. R. Jones and J. G. Hines, Corrosion Sci., Vol. 1 (1961), p. 1.

97- M. A. Scheil, "Symposium on SCC of Metals", STP 64, ASTM Ny (1945), p.395.

98- A. S. Couper, Material Protection, Vol. 8 (1969), p. 17.

99- C. Edeleanu, J. Iron and Steel Institute, Vol.173 (1953), p. 140.

100- L. Bednar, Corrosion, Vol. 35 (1979), p. 96.

101- M. A. Streicher, "Stress Corrosion of Ferritic Stainless Steels", Paper No. 68, Presented at "Corrosion'75" NACE, 1975.

102- A. P. Bond, and H. J. Dundas, Corrosion, Vol. 24, (1968), p. 344.

103- S. Shimodaira, M. Takano, Y. Takizawa, and H. Kamida, Proc. Conf. "Stress Corrosion Cracking and Hydrogen Embrittlement of Iron Base Alloys", eds. R. W. Staehle, J. Hochmann, R. D. Mc Cright, and J. E. Slater, NACE, Houston (1977), p. 1003.

104- R. T. Newberg, and H. H. Uhlig, J. Eloctochem. Soc., Vol. 119 (1972), p. 981.

105- J. D. Hartson and J. C. Scully, Corrosion, Vol. 26 (1970), p. 387.

106- J. W. Flowers, F. M. Beck, and M. G. Fontana, Corrosion, Vol. 19 (1963), p. 186t.

107- J. Hochmann, A. Desestret, P. Jolly, R. Mayard, Proc. Conf. "Stress Corrosion Cracking and Hydrogen embrittlement of Iron Base Alloys", Eds. R. W. Staehle, J. Hochmann, R. D. Mc Cright, and J. E. Slater, NACE, Houston (1977), p. 956.

108- S. Bernhardsson, Paper No. 177, "Corrosion 78", NACE, Houston (1978).

109- S. Bernhardsson, J. Oredsson, M. Tynell, Paper No. 14, "Corrosion 80", NACE, Chicago (1980).

110- S. Bernhardsson, P. Notberg, H. Eriksson, and O. Forsell, Paper No., "Corrosion /85", NACE, Boston, (1985).

111- T. Kudo, H. Tsuge, and A. Seki, Conf. Proc.,"Stainless Steels' 87" New York, Sept. 1987, Publ. I.O.M, London (1988), p. 168.

112- M. Marek and R. F. Hochman, Corrosion, Vol. 27 (1971), p. 361

113- J.P. Fraser and R. S. Treseder, Corrosion, vol. 8 (1952) p.342.

114- L. W. Vollmer, Corrosion, vol. 8 (1952), p. 326.

115- R. S. Treseder, and T. M. Swanson, corrosion, Vol. 24, (1968), p. 31.

116- A. I. Asphahani,"H_2S Corrosion in Oil & Gas Production ~ A Compilation of Classic Papers", eds. R. N. Tuttle and R. D. Kane, NACE Publication, USA, 1981, p. 369.

117- G. Herbsleb and R. Pöpperling, "Corrosion 80" paper No 13, NACE, Chicago, Illinois, March 1980.

118- C. M. Hudgins, R. L. McGlasson, P. Mehdizadeh, and W. M. Rosborough, Corrosion, Vol. 22 (1966) p. 238.

119- A. Ikeda, T. Kaneko and F. Terasaki, "Corrosion 80", paper no.8., NACE, Chicago, Illinois, March 1980.

120- H. E. Townsend, Corrosion, vol 28(1972), p.39.

121- J. Oredsson and S. Bernhardsson, Material Performance, January (1983), p. 35.

122- H. R. Gary, "Hydrogen Embrittlement Testing", ASTM, STP-543 (1972).

123- A. Sieverts, Z Metallk, Vol.12 (1929), p. 37.

124- L. S. Darken and R. P. Smith, Corrosion, Vol. 5 (1949), p. 1.

125- A. P. Bentley and G. C. Smith, Met. Trans, Vol. 17A (1986), p. 1593.

126- P. Maulik and J. Burke, Scripta Met,Vol.9 (1975), p.17.

127- H. Hanninen, T. Hakkarainen, and p. Nenonen, Proc. Conf. on " Hydrogen Effect in Metals", eds I. M. Bernsetien and A. W. Thompson, AIME,,(1981), p. 575.

128- D. Hardie and W. Zheng, Material Science and Technology, Vol 10 (1994), p. 817.

129- P. R. Rhodes, G. A. Welch, and L. Abrego, J. Materials for energy systems, Vol. 5 (1983), p. 3.

130- T. Perng and C. J. Altstetter, Acta metall. Vol.34 (1986), p. 1771.

131- R. A. Oriani, "Hydrogen in Metals", Proc. Symp. Stress Corrosion Cracking, (1967), p. 32.

132- H. G. Nelson, Hydrogen Embrittlement Testing, ASTM, STP 543 (1974), p. 152.

133- M. J. Gillan, Philosophical Magazine A, Vol. 58, No. 1, (1988), p. 257.

134- K. W. Kehr, Hydrogen in Metals, "Topics in Applied Physics, Springer, Berlin (1970), p. 197.

135- J. Volkl, G. Alefeld, Eds, "Hydrogen in Metals", Topics in Applied Physics, Springer, Berlin (1970), p. 321.

136- M. R. Luothan and R. G. Derrick, Corrosion Science, Vol. 15 (1975), p. 565.

137- J. K. Tien, Proc. Conf. "Effect of Hydrogen on Behaviour of Material", Wayoming (1975), p. 309.

138- J. K. Tien, A. W. Thompson, I. M. Bernstein, and R. J. Richard, Met. Trans., Vol. 7A (1976), p. 821.

139- A. H. Cottrell,"Dislocation and Plastic Flow in Crystals", The International Series of Monographs on Physics, Oxford University Press, Oxford (1953).

140- P. Bastien, and P. Azou, Compt. Revd Acad. sci., Paris Vol. 232 (1951), p. 1845.

141- P. Bastien, and P. Azou, Proceeding First World Metallurgist Congress, ASM, Cleveland Ohio (1951), p. 535.

142- M. Kurkela and R. M. Latanision, Scripta Met., Vol. 13 (1979), p. 927.

143- C. Hwang and I. M. Bernstein Scripta. Met.,Vol. 17 (1983), p. 1299.

144- G. S. Frankel and R. M. Latanision, Met. Trans, Vol. 17A (1986), p. 861.

145- G. S. Frankel and R. M. Latanision, Met. Trans, Vol. 17A (1986), p. 869.

146- M. R. Louthan and R. D. Mcnitt, Proc. Conf." Effects of Hydrogen on Behaviour of Material", Eds, A. W. Thompson, and I. M. Bernstein, AIME, NY (1976), p. 496.

147- C. Zapffe and C. Sims, Trans. AIME, Vol. 145 (1941), p. 225.

148- F. A. Dekazinczy, J. Iron and Steel Institute, Vol. 177 (1954), p. 85.

149- B. A. Bilby and J. Hewitt, Acta. Metall, Vol. 10 (1962), p. 587.

150- A. S. Tetelman and W. D. Robertson, Trans. Met. Soc. AIME, Vol. 224 (1962), p. 775.

151- R. Lagneborg, J. of Iron and Steel Institute,Vol. 207 (1969), p. 363.

152- H. H. Johnson and A. M. Willner, Applied Mat. Res. Vol. 4 (1973), p589.

153- J. T. Brown and W. M. Bladwin, J. Metals, Vol. 6 No. 2 (1954), p. 289.

154- G. R. Caskey, Scripta Met., Vol. 11 (1977), p.1077.

155- T. P. Perng and C. J. Altstetter, Met. Trans., Vol. 18A (1987), p. 123.

156- D. P. Williams and H. G. Nelson, Met. Trans., Vol. 1A (1970), p. 63.

157- H. G. Nelson, D. P. William and A. S. Tetelman, Met. Trans., Vol. 2A (1971), p. 935

158- J. P. Hirth, Met.Trans., Vol. 11A (1980), p.861.

159- J. G. Morlet, H. H. Johnson, and A. R. Troiano, J. Iron and Steel Inst., Vol. 189 (1958), p. 37.

160- H. H. Johnson, J. G. Morlet, and A. R. Troiano, Trans. Amer. Inst. Min. Met. Engr., Vol. 112 (1958), p. 326.

161- E. A. Steigerwald, F. W. Schaller, and A. R. Troiano, Trans AIME,Vol. 218 (1960), p. 832.

162- E. A. Stegerwald, F. W. Schaller, A. R. Troiano, Trans. Amer. Inst. Min. Met. Eng.,Vol.215 (1959), p. 1048.

163- R. A. Oriani, Scripta Met, Vol. 6, (1972), p. 681.

164- M. Cornet and S.Talbot-Bernard, Mat. Sci. J., Vol. 12 (1978), p. 335.

165- R. G. Frank, "Internal Stress Fatigue in metals", eds. G. M. Rassweilepand W. L. Grube, Elsevier, (1959), p411.

166- J. A. Donovan, Met. Trans., vol. 7A, (1976), p 1677.

167- M. R. Louthan , Proc. Conf." Hydrogen in Metals", eds, I. M. Bernstein and A. W. Thompson, ASM, Metal Park Ohio (1974), p. 53.

168- J. K. Tien, R. J. Richard, O. Buck and H. L. Marcus, Scripta Met., Vol. 9 (1975), p. 1097.

169- D. G. Westlake, Trans. ASM, Vol. 62 (1969), p. 1000.

170- G. M. Pressouyre, Acta Met., Vol. 28 (1980), p. 895.

171- G. M. Pressouyre, Met. Trans., Vol. 10A (1979), p. 1571.

172- B. E. Wilde, Corrosion, Vol. 27 (1971), p.326.

173- H. J. Bhatt and E. H. Phelps, corrosion, Vol. 17, (1961), p.430t.

174- J. E. Truman et al. ,J. Iron and Steel Institute, Vol. 202 (1964), p. 745.

175- JCPDS Powder Diffraction File, International Center for Diffraction Data, (1989).

176- E. Beraha, and B. Shpigler, "Color Metallography", ASM, Metal Park, Ohio, (1977).

178- W. Zheng and Hardie, Corrosion Science, Vol. 32 (1991), p. 23.

179- W. M. Robertson and A. W. Thompson, Metall. Trans. Vol. 11A (1975), p. 565.

180- L. S. Darken and R.W Gurry, "Phsical Chemistry of Metall", McGraw-Hill, New York, (1953).

181- S. Xiukui, X. Jian, and L. Yiyi, Acta. Met., Vol. 37 (1989), p. 2171.

182- W. Zheng and Hardie, Corrosion Science, Vol. 47 (1991), p.792.

183- J. R. Buckley, Ph.D. Thesis, University of Newcastle upon Tyne, 1991.

184- K. Van Gelder, J. G. Erlings, J. W. Damen, and A. Visser, Corrosion Sience, Vol. 27 (1987), p. 1271.

185- M. Barteri, F. Mancia, A. Tamba, and G. Montagna, Corrosion Sience, Vol. 27 (1987) p. 1239.

186- H. Miyuki,"Corrosion 84", paper No.293, New Orleans, (1984).

187- P. Gustafsson and H. Eriksson, Proc. Conf.,"Duplex Stainless Steels", Netherland (1986), p. 381.

188- F. F. Lyle and E. B. Norris, "H_2S Corrosion in Oil & Gas Production ~ A Compilation of Classic Papers", eds. R. N. Tuttle and R. D. Kane, NACE Publication, USA, 1981, p. 311.

189- S. Bernhardsson, R. Mellstrom, and J. Oredsson, "corrosion '81", Paper No.124, Toranto, Canada (1981).

190- J. R. Scully and P. J. Moran,"Hydrogen Embrittlement: Prevention and Controle", ASTM STP 962, ed. L. Raymond, ASTM, Philadelphia (1988), p. 387.

191- S. Tahtinen, P. Nenonen and H. Hanninen, Scripta Met., Vol. 21 (1987), p. 315.

192- L. J. Cohen, J. A. Charles and G. C. Smith, Conf. Proc.,"Stainless Steels' 87" Ny, Sept. 1987, Publ. I.O.M, London (1988), p. 363.